SCUOLA DI DOTTORATO
UNIVERSITÀ DEGLI STUDI DI MILANO-BICOCCA

Dipartimento di / Department of
Fisica “Giuseppe Occhialini”

Dottorato di Ricerca in / PhD program: Fisica e Astronomia Ciclo / Cycle: XXXVI

PRESENT AND FUTURE OF MULTI-MESSENGER ASTRONOMY

BINARY NEUTRON STAR AND BLACK HOLE NEUTRON - STAR MERGERS

Cognome / Surname: Colombo Nome / Name: Alberto

Matricola / Registration number: 778156

Tutore / Tutor: Prof. Monica Colpi

Co-tutore / Co-tutor: Dr. Om Sharan Salafia

Coordinatore / Coordinator: Prof. Stefano Ragazzi

ANNO ACCADEMICO / ACADEMIC YEAR 2023/2024

Abstract

The discovery of the gravitational wave signal GW170817, compatible with a binary neutron star system, by the LIGO and Virgo collaboration, along with the subsequent identification of its multi-wavelength electromagnetic counterparts, marked the beginning of the multi-messenger astronomy era. Notably, a second binary neutron star merger, GW190425, was also detected, yet it did not present any associated electromagnetic counterpart. Even black hole-neutron star mergers have the potential to produce electromagnetic emissions, but, although already detected through their GW signals, no electromagnetic counterpart has been associated with these events to date. During the third observing run of the gravitational wave detectors network, O3, and the initial phase of the fourth run, O4a, extensive electromagnetic follow-up campaigns were conducted. Despite significant investment in observational resources, these efforts predominantly yielded only contaminants, particularly supernovae Ia, providing limited insights into the properties of the gravitational wave-emitting binaries. As we progress towards the later stages of observing run O4, the forthcoming O5, and with the development of third-generation gravitational wave interferometers like the Einstein Telescope and Cosmic Explorer, the need for precise predictions becomes increasingly critical. These predictions are essential for refining follow-up strategies to maximize the likelihood of detecting associated, rapidly fading transient phenomena. This doctoral thesis presents a realistic projection of the number and characteristics of binary neutron star and black hole-neutron star mergers expected to be observable as multi-messenger sources during O4, O5, and by third-generation detectors. The objective is to provide strategic guidance for optimizing observational approaches. These predictions are grounded in a population synthesis model that incorporates various elements: the gravitational wave signal-to-noise ratio, inferred sky localization, kilonova optical and near-infrared light curves, peak photon flux of the relativistic jet gamma-ray burst prompt emission, and afterglow light curves across radio, optical, and X-ray wavelengths. Utilizing this approach, it is possible to delineate the expected distributions of electromagnetic observables for events detectable in the current and upcoming O4, O5 observing runs, and by future gravitational wave observatories. This study, therefore, addresses pivotal questions and offers an in-depth, contemporary perspective on the present and future of multi-messenger astronomy.

List of Abbreviations

aLIGO	Advanced LIGO
AdV	Advanced Virgo
BAT	Burst Alert Detector
BATSE	Burst And Transient Source Experiment
BBH	Binary Black Hole
BH	Black Hole
BHBH	Black Hole - Black Hole
BHNS	Black Hole - Neutron Star
BNS	Binary Neutron Star
CBC	Compact Binary Coalescence
CE	Cosmic Explorer
CGRO	Compton Gamma-Ray Observatory
DCO	Double Compact Object
EM	Electromagnetic
EoS	Equation of State
ET	Einstein Telescope
GRB	Gamma-Ray Burst
GRHD	General-Relativistic HydroDynamics
GROWTH	Global Relay of Observatories Watching Transients Happen
GW	Gravitational Wave
HMNS	Hyper-Massive Neutron Star
IFO	Interferometer
ISCO	Innermost Stable Circular Orbit
ISM	Interstellar Medium
KN	Kilonova
LGRB	Long Gamma-Ray Burst
LVC	LIGO-Virgo Collaboration
LVK	LIGO-Virgo-KAGRA Collaboration
MM	Multi-Messenger
NICER	Neutron Star Interior Composition Explorer
NIR	Near Infrared
NR	Numerical Relativity
NS	Neutron Star
NSNS	Neutron star - Neutron Star
sGRB	Short Gamma-Ray Burst
SMNS	Supra-Massive Neutron Star
SN	Supernova
S/N	Signal-to-Noise Ratio
TT	Transverse-Traceless
UVOT	UV-Optical Telescope
XRT	X-Ray Telescope

Contents

Preface

The advancement of the second-generation gravitational wave (GW) observatories, comprising the Advanced Laser Interferometer GW Observatory (LIGO [1]), Advanced Virgo [24], and KAGRA (from the third observing run O3, [38]), has revolutionized our ability to explore the cosmos through GWs. This revolution commenced with the landmark detection of GW150914 [12], the first observation of a compact binary coalescence (CBC) in GWs.

Throughout the initial three observing runs (O1, O2, and O3 – [5, 15, 17]) and the first half of the fourth (O4a), the collaborative network led by LIGO, Virgo, and KAGRA (LVK) has identified several tens of significant events ($p_{\rm astro} > 0.5$). These detections encompass a variety of sources, including numerous binary black hole (BHBH) mergers, two identified binary neutron star (NSNS) mergers, and even black hole-neutron star (BHNS) systems [18, 17].

To date, electromagnetic (EM) emissions have been definitively associated only with the NSNS merger GW170817 [6], heralding the era of multi-messenger (MM) astronomy. Virgo's inclusion in the network shortly before this event enabled a precise sky localization of GW170817 within a 28 deg^2 area [306]. This localization coincided with that of GRB170817A, a short gamma-ray burst (GRB) detected by Fermi and INTEGRAL [8] mere seconds post-GW chirp. Global telescopic efforts rapidly identified a faint, quickly evolving optical/near-infrared transient within the GW170817 localization error box in a nearby galaxy, NGC 4993 [84]. This transient was spectroscopically identified [234] as a kilonova (KN) – quasi-thermal emissions from the merger's expanding ejecta. Subsequently, a broadband (radio to X-rays) non-thermal source was discovered at the same location, identified weeks later as the afterglow of an off-axis relativistic jet, confirmed through very long baseline interferometry observations [208, 125].

On 25 April 2019, the LIGO-Virgo Collaboration (LVC) detected a second NSNS merger, GW190425 [4], but no confirmed EM counterpart was observed. Additionally, during the O3 observing run, four BHNS events were reported with a false-alarm-rate (FAR) of less than one per year: GW200115_042309, GW200105_162426, GW190917_114630, and GW190426_152155 [23], none of which were accompanied by detectable EM emissions.

In the last stages of the inspiral of a NSNS merger, the stars undergo partial tidal disruption, producing an emission of gravitationally unbound material, known as "dynamical ejecta", as well as a bound component, which forms an accretion disk around the remnant. The released neutron-rich material is an ideal site to synthesize heavy elements via rapid neutron capture and their nuclear decay can power the emission of a KN [176, 199]. Moreover, the accretion of the disk around the remnant can lead to the launch of a relativistic jet [102, 274]. BHNS mergers can also produce EM counterparts if the NS is tidally disrupted outside the BH innermost stable circular orbit (ISCO). If this condition is not satisfied the NS directly plunges into the BH and no material is ejected, precluding EM emissions [115, 162, 116].

Combined EM and GW data from NSNS and BHNS mergers can constrain various parameters, such as component masses, NS tidal deformabilities, viewing angle, and

distance, along with the equation of state (EoS) of supra-nuclear density matter [191, 7, 245, 247, 83, 224, 83, 44]. Moreover, these systems can help measuring the Hubble constant and understanding the production of heavy elements [277, 216, 105, 122, 132, 176, 177]. Such observations can be also critical in distinguishing the nature of merging systems that cannot be definitively classified through GW signals alone [190, 41, 42].

Although the detection of EM counterparts is crucial for a more comprehensive characterization of merging systems and an enhanced understanding of the physics involved, from an observational standpoint, MM astronomy remains a formidable challenge. The GW signal often yields only a large sky-localization, and when combined with distance uncertainty, the resultant volume error box may encompass thousands of galaxies and numerous other transients, especially supernovae Ia. Thus, identifying the transient associated with the GW signal is daunting, and rapidly fading EM counterparts risk being missed.

To optimize the scientific yield of forthcoming observing runs in a MM context, it is essential to anticipate joint detections and understand the properties of potential EM transients. This foresight will guide the establishment of instrumental scientific requirements and the formulation of optimal observational strategies.

In this work, I detail our projections for the EM emissions associated to NSNS [78] and BHNS [79] mergers detectable in the upcoming O4, O5 observing runs, as well as by third-generation (3G) GWs observatories like the Einstein Telescope (ET; [242]) and Cosmic Explorer (CE; [251]).

To achieve this, we developed a synthetic population of NSNS binaries, informed by GW detections and Galactic NSNS data, alongside a BHNS population based on the standard model in [68]. For each binary system, we simulated the signal-to-noise ratio of the GW signal within the detectors and the GW-determined sky localization using the `GWFAST` software [154].

We then assigned expected ejecta and accretion disk properties to each binary, derived from numerical-relativity-informed fitting formulae. Leveraging these properties, we calculated the observable characteristics of associated KN, GRB prompt, and GRB afterglow emissions employing a set of semi-analytical models, refining the approach described in [44]. This methodology enabled us to outline the distributions of EM observables for events detectable in O4, O5, and by 3G GW observatories. Consequently, this study addresses several key questions, offering a comprehensive and up-to-date overview of the evolving field of MM astronomy.

The thesis is organized as follow. In Chapter 1 we briefly describe the coalescence of compact binary systems and the related emission of GWs. In Chapter 2 we present the different mechanisms for ejecta production in NSNS and BHNS mergers and their properties. In Chapter 3 we discuss the physics of KNæ and we describe the emission model used in our work. In Chapter 4 we describe the basic physics of GRBs, as well as the GRB prompt and afterglow emission model used in the following analysis. In Chapter 5 and 6 we present our prospects for MM observations of NSNS and BHNS mergers in O4 and O5, based on Colombo et al. [78, 79]. In Chapter 7 we present a preliminary analysis for MM observations of NSNS and BHNS mergers in the ET era, which will be included in the Chapter of the Einstein Telescope Blue Book dedicated to MM observations. Finally, in Chapter 8 we summarize the main results of this thesis.

Chapter 1

Gravitational Waves

In this Chapter, we provide a concise overview of the merging process of compact binary systems and the resultant gravitational wave (GW) emissions. Section 1.1 outlines fundamental concepts in general relativity pivotal to the derivation of the GW equation [253, 186]. Section 1.2 delves into the inspiral and merger stages of a binary system, encapsulates key equations governing GW emissions [80]. Section 1.3 describe the detection of GWs, the intrinsic parameters of the binary that can be derived from GWs, and the main observing campaigns for present and future detections [80, 186]. In Section 1.4 and Section 1.5 we provide a brief description of the first two binary neutron star mergers [9, 11]. This Chapter is mainly based on the works by Riles [253], Maggiore [186], Colpi et al. [80] and references therein.

1.1 Fundamental physics of gravitational waves

The differential line element ds at space-time point $\overline{x}$ can be written as:

$$ds^2 = g_{\alpha\beta}(\overline{x})dx^\alpha dx^\beta, \tag{1.1}$$

where $g_{\alpha\beta}$ is the symmetric metric tensor [1]. Two examples of the metric tensor are a simple flat Cartesian-coordinate metric with $\alpha = (t, x, y, z)$:

$$g^{\text{Cart.}}_{\alpha\beta}(\overline{x}) = \begin{pmatrix} -1 & 0 & 0 & 0 \\ 0 & 1 & 0 & 0 \\ 0 & 0 & 1 & 0 \\ 0 & 0 & 0 & 1 \end{pmatrix}, \tag{1.2}$$

the so-called Minkowski metric, and a more complex curved, spherical-coordinate metric, with $\alpha = (t, r, \theta, \phi)$, outside of a spherically symmetric mass distribution of total mass M:

$$g^{\text{Schw.}}_{\alpha\beta}(\overline{x}) = \begin{pmatrix} -\left(1 - 2GM/c^2 r\right) & 0 & 0 & 0 \\ 0 & \left(1 + 2GM/c^2 r\right)^{-1} & 0 & 0 \\ 0 & 0 & r^2 & 0 \\ 0 & 0 & 0 & r^2 \sin^2\theta \end{pmatrix}, \tag{1.3}$$

also known as Schwarzschild metric. G is the gravitational constant, while c is the speed of light. One potential approach to measure the curvature of a metric involves employing the covariant equation of motion for a test particle:

$$\frac{d^2 x^\alpha}{d\tau^2} = -\Gamma^\alpha_{\beta\gamma}\frac{dx^\beta}{d\tau}\frac{dx^\gamma}{d\tau}, \tag{1.4}$$

[1] We are adopting Einstein notation, so repeated indices imply summation.

in which τ is the proper time and $\Gamma^{\alpha}_{\beta\gamma}$ is the Christoffel symbol defined as:

$$g_{\alpha\delta}\Gamma^{\delta}_{\beta\gamma} = \frac{1}{2}\left(\frac{\partial g_{\alpha\beta}}{\partial x^{\gamma}} + \frac{\partial g_{\alpha\gamma}}{\partial x^{\beta}} + \frac{\partial g_{\beta\gamma}}{\partial x^{\alpha}}\right). \tag{1.5}$$

The Riemann curvature tensor is defined as:

$$R^{\alpha}_{\beta\gamma\delta} = \frac{\partial \Gamma^{\alpha}_{\beta\delta}}{\partial x^{\gamma}} - \frac{\partial \Gamma^{\alpha}_{\beta\gamma}}{\partial x^{\delta}} + \Gamma^{\alpha}_{\gamma\epsilon}\Gamma^{\epsilon}_{\beta\delta} - \Gamma^{\alpha}_{\delta\epsilon}\Gamma^{\epsilon}_{\beta\gamma}. \tag{1.6}$$

Contracting the indices of the Riemann tensor, we obtain the so-called Ricci tensor:

$$R_{\beta\delta} = R^{\alpha}_{\beta\alpha\delta}. \tag{1.7}$$

The trace of the Ricci tensor with respect to the metric is the scalar curvature:

$$R = g^{\alpha\beta}R_{\alpha\beta} \tag{1.8}$$

With $T_{\alpha\beta}$ we indicate the stress-energy tensor, that represents the density and flux of energy and momentum in the space-time. The *time-time* component ($\alpha = \beta = 0$) indicates the energy density divided by c^2. The *time-space* components ($\alpha = 0$ and $\beta = i = 1, 2, 3$) indicate the density of the i-th component of the linear momentum. The diagonal *space-space* components ($\alpha = \beta = i = 1, 2, 3$) indicate the normal stresses, while the off-diagonal *space-space* components ($\alpha = i = 1, 2, 3$ and $\beta = j = 1, 2, 3$, with $i \neq j$) indicate the shear stresses. The stress-energy tensor is symmetric, so $T_{\alpha\beta} = T_{\beta\alpha}$.

Now we can write one of the most important and famous equations in physics, the Einstein Equation:

$$R_{\alpha\beta} - \frac{1}{2}g_{\alpha\beta}R = \frac{8\pi G}{c^4}T_{\alpha\beta}, \tag{1.9}$$

that describes how energy density provokes curvature and how curvature influences energy density. In order to derive the GW equation from this relation, it is possible to use a *perturbative approach*. Let us consider a small perturbation $h_{\alpha\beta}$ of the Minkowski metric $\eta_{\alpha\beta}$ given in (1.2) (a more general solution of Einstein equation $g^0_{\alpha\beta}$ could be considered as well), that is caused by some sources described by a stress-energy tensor $T_{\alpha\beta}$. The metric tensor of the perturbed space-time is:

$$g_{\alpha\beta}(\overline{x}) = \eta_{\alpha\beta} + h_{\alpha\beta}(\overline{x}). \tag{1.10}$$

Under the assumption that $|h_{\alpha\beta}| \ll |\eta_{\alpha\beta}| = 1$ (*linearized theory*), the left side of (1.9) can be simplified by keeping only leading order terms in $h_{\alpha\beta}$ and applying the Lorentz gauge condition:

$$\partial_{\beta}h^{\beta}_{\alpha}(\overline{x}) - \frac{1}{2}\partial_{\alpha}h^{\beta}_{\beta}(\overline{x}) = 0. \tag{1.11}$$

In vacuum ($T_{\alpha\beta} = 0$), we have the homogeneous wave equation:

$$\Box h_{\alpha\beta}(\overline{x}) = 0, \tag{1.12}$$

where $\Box$ is the D'Alambertian operator in flat spacetime,

$$\Box = \eta^{\alpha\beta}\frac{\partial}{\partial x^{\alpha}}\frac{\partial}{\partial x^{\beta}} = -\frac{1}{c^2}\frac{\partial^2}{\partial t^2} + \nabla^2, \tag{1.13}$$

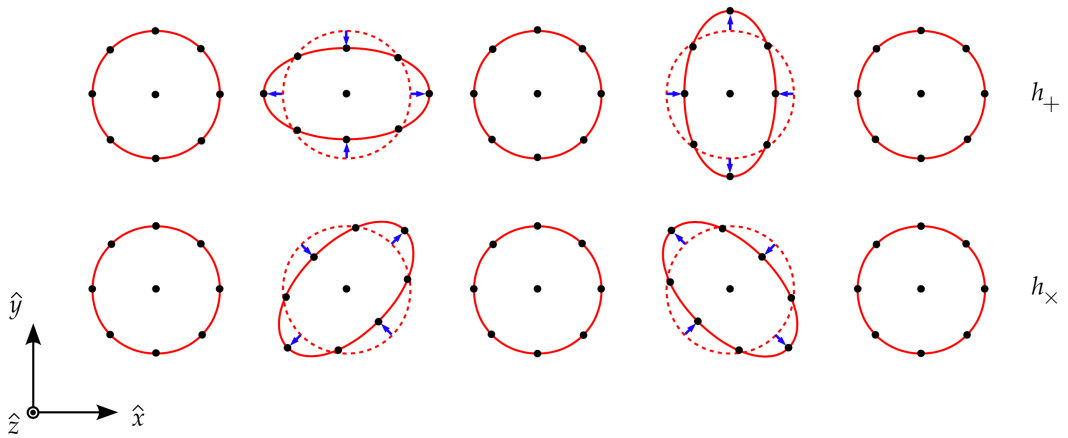

FIGURE 1.1: Representation of the two polarization modes of gravitational waves. Credit: [39].

which implies that GWs travel at the speed of light. Fixing a wave vector $\vec{k}$, a solution of (1.12) can be written as:

$$h_{\alpha\beta}(\bar{x}) = A_{\alpha\beta} e^{i(\vec{k}\cdot\vec{x}-\omega t)}, \tag{1.14}$$

where $\omega = kc$ and A is a symmetric 4×4 matrix. Assuming the previous gauge condition and the so called *transverse-traceless gauge* (TT-gauge) leads to a relatively simple form. Choosing a system in which the z axis lies along $\vec{k}$, we have:

$$h_{\alpha\beta}(\bar{x}) = \begin{pmatrix} 0 & 0 & 0 & 0 \\ 0 & h_+ & h_\times & 0 \\ 0 & h_\times & -h_+ & 0 \\ 0 & 0 & 0 & 0 \end{pmatrix} e^{i(kz-\omega t)}. \tag{1.15}$$

h_+ and $h_\times$ are called the amplitude of the *plus* and *cross* polarization of the wave, so a GW has only two physical degrees of freedom corresponding to the two possible polarization states (see Figure 1.1).

Choosing Cartesian spatial coordinates and the TT-gauge, the inhomogeneous wave equation can be written in the following way:

$$\Box h_{\alpha\beta}(\bar{x}) = -\frac{16\pi G}{c^4} T_{\alpha\beta}, \tag{1.16}$$

which has the same form of the wave equation for relativistic electrodynamic fields,

$$\Box A^\alpha = -\mu_0 J^\alpha, \tag{1.17}$$

where $A^\alpha = (\Phi/c, \vec{A})$ contains the scalar and vector potential functions, instead $J^\alpha = (c\rho, \vec{J})$ contains the electric scalar charge and current density. The electrodynamic vector potential solution can be written applying the Green function formalism [157]. We obtain:

$$\vec{A}(t,\vec{x}) = \frac{\mu_0}{4\pi} \int d^3x' \frac{\left[\vec{J}(\vec{x}',t')\right]_{\text{ret}}}{|x-x'|}, \tag{1.18}$$

where $[...]_{\text{ret}}$ indicates evaluation at the retarded time $t' \equiv t - |\vec{x} - \vec{x}'|/c$. In a similar way, we can write the solution of (1.16) as:

$$h_{\alpha\beta}(t, \vec{x}) = \frac{4G}{c^4} \int d^3x' \frac{\left[T_{\alpha\beta}\left(t', \vec{x}'\right)\right]_{\text{ret}}}{|x - x'|}. \tag{1.19}$$

The constant $4G/c^4$ is a very small value ($3.4 \cdot 10^{-49}\,\text{s}^2\,\text{g}^{-1}\,\text{cm}^{-1}$), making GWs very challenging to detect.

1.2 Gravitational waves from compact binaries

The term *compact binaries coalescence* (CBC) indicates the merger of binaries hosting the relics of massive stars evolution: binary neutron star (NSNS), black hole - neutron star (BHNS) and black hole - black hole (BHBH) binaries. In the current network detector (see Section 1.3), they are detectable at the time of their coalescence (from fractions of second before the merger for BHBH, to $\sim$ 100 seconds for NSNS), emitting a sizeable fraction of their reduced-mass-energy in GWs.

In Newtonian gravity, two binary point masses travel on circular or elliptical orbits around their common centre of mass. The motion is periodic with constant Keplerian frequency $f_{\text{K}} = \left(GM_{\text{tot}}/a^3\right)^{1/2}/(2\pi)$, where a is the semi-major axis of the relative orbit and $M_{\text{tot}} = M_1 + M_2$ is the total mass of the binary. In GR, binary systems emit GWs resulting in a loss of orbital energy and angular momentum. To compensate this radiative energy losses, binaries back-react gradually hardening, decreasing their semi-major axis a and increasing the orbital frequency f_{K}. The emission is initially weak and a phase of nearly adiabatic contraction anticipates the so called phase of *inspiral*, *merger* and *ringdown* (see Figure 1.2 for a schematic representation).

During the *inspiral* phase, that is the longer lasting, the two binary components can still be considered as structureless and their dynamics can be described by Post Newtonian (PN) theory [58]. During this phase the signal, called *chirp*, has a characteristic shape with both the amplitude and frequency of the wave slowly sweeping to higher values. The *inspiral* is fundamental in obtaining estimates of the binary parameters, which can be estimated by matching the observed signal with a catalogue of waveform templates. When the binary components are spinning, the signal is modulated by spin-orbit and spin-spin couplings. This modulation encodes the masses, orbit inclination, distance and sky location, but also the spins of the two interacting objects.

The word *merger* refers to the phase of very late inspiral and coalescence, which is no longer described by the PN formalism. The two objects experience extreme gravitational fields during this phase, moving at about one third of the speed of light, so that their dynamics and GW signal can be described only with Numerical Relativity (NR). The merger signal lasts for a shorter time (milliseconds) compared to the *inspiral*, and in this phase finite-size effects become important for mergers involving NSs, because they have a surface. In particular for a nearly equal mass NSNS coalescence, the merger resembles a slow collision, while if the primary object is substantially more massive than the secondary, the latter is tidally disrupted during the plunge and it essentially accretes onto the primary. NR simulations which account for the full non-linear structure of the Einstein Equation can accurately describe the dynamics and the GW radiation.

Finally, the system will eventually settle into a new stationary equilibrium solution of the Einstein field equations through a phase of *ringdown*, with a particular shape

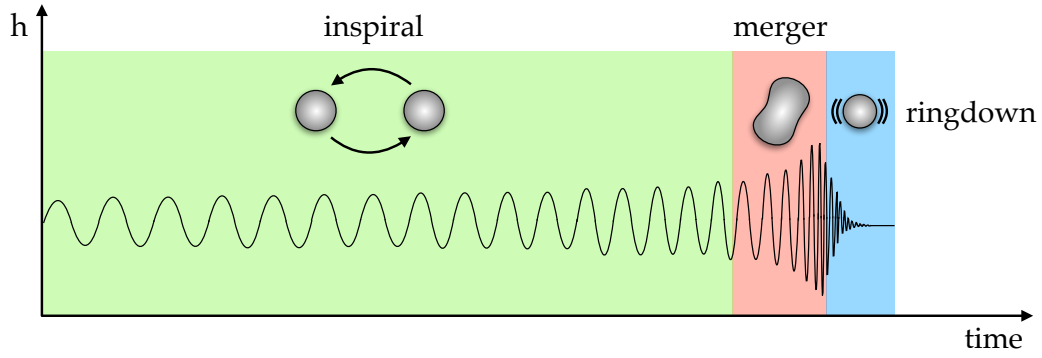

FIGURE 1.2: Representative waveform $h(t)$ from the coalescence of a compact binary and schematic representation of *inspiral*, *merger* and *ringdown* phases.

for the GW signal that depends on the remnant mass and rotational profile. After the merger, the remnant is always a BH for BHNS coalescences. Instead for NSNS mergers the remnant can be a BH, an unstable supramassive NS (SMNS) or a hypermassive NS (HMNS) that will collapse to a BH, or a stable NS. The fate of the remnant from NSNS merger primarily depends on the binary total mass and the equation of state of NS matter. In Fig. 1.2 we report a representative waveform $h(t)$ from a binary coalescence, highlighting the three phases.

1.2.1 Radiated energy and angular momentum

The reference frequency of GW at the time of coalescence is:

$$f_{\rm coal} = \frac{1}{(\pi 6^{3/2})}\frac{c^3}{GM} \tag{1.20}$$

that is twice the Keplerian frequency $f_{\rm K}$ of a test mass orbiting around a non-spinning BH of mass M at the innermost stable circular orbit $R_{\rm ISCO}$.

An important parameter for merging binaries is the so called *chirp mass* $M_{\rm c}$. For a binary with components masses M_1 and M_2, the chirp mass M_c is defined as:

$$M_{\rm c} \equiv \frac{(M_1 M_2)^{3/5}}{(M_1+M_2)^{1/5}} = \nu^{3/5} M_{\rm tot} = \mu^{3/5} M_{\rm tot}^{2/5}, \tag{1.21}$$

here also expressed in terms of the symmetric mass ratio $\nu = M_1 M_2 / M_{\rm tot}^2$ and of the reduced mass $\mu = M_1 M_2 / M_{\rm tot} = \nu M_{\rm tot}$. During the inspiral phase, $M_{\rm c}$ can be used to express, to the leading order, the power radiated by a circular binary averaged over an orbital period [232]:

$$\dot{E}_{\rm gw}^{\rm circ} = \frac{32}{5}\frac{c^5}{G}\left(\frac{GM_{\rm c}}{c^3}\pi f\right)^{10/3} = \frac{32}{5\cdot 6^5}\frac{c^5}{G}\nu^2 \tilde{f}^{10/3}, \tag{1.22}$$

where $f = 2f_{\rm K}$ is the frequency of the emitted GW and $\tilde{f} = f/f_{\rm coal}$ is the dimensionless frequency. Close to coalescence ($\tilde{f} \sim 1$), the luminosity $\dot{E}_{\rm gw}^{\rm circ}$ does not depend on the mass $M_{\rm tot}$ of the binary, but on the symmetric mass ratio ν only, reaching the value $\dot{E}_{\rm gw}^{\rm circ} \sim \nu^2 \left(c^5/G\right) \sim \nu^2 \left(3.6 \times 10^{59}\right)$ erg s^{-1}.

The binary orbital angular momentum L is radiated away at an orbit-averaged rate given by:

$$\dot{L}_{\rm gw}^{\rm circ,orb} = \frac{32}{5} M_{\rm c} c^2 \left(\frac{G M_{\rm c}}{c^3}\pi f\right)^{7/3} = \frac{32}{5\sqrt{6^7}} \nu^2 M_{\rm tot} c^2 \tilde{f}^{7/3} \tag{1.23}$$

in the L direction. Close to coalescence $\dot{L}_{\rm gw}^{\rm circ,orb} \sim \left[32/\left(5\sqrt{6^7}\right)\right] \nu^2 M_{\rm tot} c^2$, whose value depends on $M_{\rm tot}$ and ν.

The emission of GWs involves loss of orbital energy and angular momentum. According to the virial theorem in Newtonian dynamics, the orbital energy of the binary is

$$E_{\rm bin} = -\frac{G\nu M_{\rm tot}^2}{2a} = -\frac{1}{2}\nu M_{\rm tot}^2 (G M_{\rm tot})^{1/3} (\pi f)^{2/3}. \tag{1.24}$$

The total energy of the binary decreases adiabatically at a rate equal to $\dot{E}_{\rm bin} = -\dot{E}_{\rm gw}$, the semi-major axis decreases and the GW frequency increases at a rate:

$$\dot{f} = \frac{96}{5}\pi^{8/3}\left(\frac{G M_{\rm c}}{c^3}\right)^{5/3} f^{11/3}. \tag{1.25}$$

This last equation is obtained considering $\dot{E}_{\rm bin} = (dE_{\rm bin}/df)(df/dt)$, where $dE_{\rm bin}/df$ is derived using (1.24). Equation (1.25) expresses that to first order the frequency evolution of the GW emitted by a circular binary is determined by the chirp mass $M_{\rm c}$ only. The solution to (1.25),

$$f(t) = \frac{5^{3/8}}{(256)^{3/8}\pi}\left(\frac{G M_{\rm c}}{c^3}\right)^{-5/8} (t_{\rm coal} - t)^{-3/8}, \tag{1.26}$$

describes the rise of the frequency f of the GW emitted by the system while chirping, where $t_{\rm coal}$ gives the time of the merger.

Following (1.26), the remaining time to merger for binary observed at a frequency f is:

$$\tau_{\rm coal}^{\rm circ}(f) = \frac{5}{256\pi^{8/3}}\frac{1}{\nu}\left(\frac{c^3}{G M_{\rm tot}}\right)^{5/3}\frac{1}{f^{8/3}} \simeq \frac{7.4}{\nu}\left(\frac{\rm M_\odot}{M_{\rm tot}}\right)^{5/3}\left(\frac{1{\rm Hz}}{f}\right)^{8/3} {\rm days}, \tag{1.27}$$

which is a steep function of f. The late *inspiral*, *merger* and *ringdown* phases have a very short duration, in fact in terms of $\tilde{f} = f/f_{\rm coal} \sim 1$ this time is equal to:

$$\tau_{\rm coal}^{\rm circ}(\tilde{f}) = \frac{6480}{256}\frac{1}{\nu}\frac{G M_{\rm tot}}{c^3}\frac{1}{\tilde{f}^{8/3}} \simeq 1.25\times 10^{-4}\frac{1}{\nu}\frac{M_{\rm tot}}{M_\odot}\frac{1}{\tilde{f}^{8/3}}{\rm sec}. \tag{1.28}$$

Two other important quantities that describe circular compact binaries mergers are the energy spectrum $dE_{\rm gw}/df$ and the total energy radiated in GWs $E_{\rm gw}$. In the quadrupole approximation,

$$\frac{dE_{\rm gw}}{df} = \frac{\pi^{2/3}}{3G}(G M_{\rm c})^{5/3} f^{-1/3} \tag{1.29}$$

and

$$E_{\rm gw} \sim \frac{\pi^{2/3}}{2G}(G M_{\rm c})^{5/3} f_{\rm max}^{2/3}, \tag{1.30}$$

where $f_{\rm max}$ is the maximum frequency at which the inspiral is observed.

1.3 Detecting gravitational waves

For a circular binary at distance d the two independent polarisation states h_+ and $h_\times$ of a GW are given by [186]:

$$h_+(t) = \frac{4}{d}\left(\frac{GM_c}{c^2}\right)^{5/3}\left(\frac{\pi f\left(t_{\rm ret}\right)}{c}\right)^{2/3}\frac{1+\cos^2\iota}{2}\cos\Phi_{\rm N}\left(t_{\rm ret}\right), \tag{1.31}$$

$$h_\times(t) = \frac{4}{d}\left(\frac{GM_c}{c^2}\right)^{5/3}\left(\frac{\pi f\left(t_{\rm ret}\right)}{c}\right)^{2/3}\cos\iota\sin\Phi_{\rm N}\left(t_{\rm ret}\right), \tag{1.32}$$

where ι is the inclination angle between the line of sight and the unit vector parallel to the binary orbital angular momentum L, $f\left(t_{\rm ret}\right)$ is the instantaneous frequency given by (1.26), evaluated at the retarded time $t_{\rm ret} = t - d/c$ and $\Phi_{\rm N} \equiv 2\pi\int f\left(t'\right)dt'$ is the lowest order contribution to the orbital phase. $\Phi_{\rm N}$ evolves in time following:

$$\Phi_{\rm N}(t) = \Phi_0 - 2\left(\frac{5GM_c}{c^3}\right)^{-5/8}\left(t_{\rm coal}-t\right)^{5/8}, \tag{1.33}$$

with the constant Φ_0 giving the orbital phase at the epoch of merger, when f diverges nominally, but finite size effects impact on the waveform before this divergence is reached. Note that, using (1.21), at any given frequency, both h_+ and $h_\times$ scale as $\nu M_{\rm tot}^{5/3}$, namely faster than linear with respect to the total mass M and linear in ν. Therefore unequal mass binaries with total mass $M_{\rm tot}$ have weaker emission with respect to symmetric binaries with the same total mass. Furthermore the ratio of the two polarisation amplitudes depends on the inclination angle ι. Thus when the binary is seen edge-on ($\iota = \pi/2$) the radiation has only $+$ polarisation and the motion of the binary bodies projected on the sky is purely linear. Instead when the binary is seen face-on ($\iota = 0$) the polarisation component are out of phase by $\pi/2$ with equal amplitude, emitting a circularly polarised wave with the binary executing a circular motion in the sky. In conclusion, the polarisation has a direct relationship with the motion of the point masses projected on the observer's sky plane.

A single GW detector can measure just a linear combination of the polarisations amplitudes, the so-called *strain amplitude*:

$$h(t) = F_+(\alpha,\delta,\psi)h_+ + F_\times(\alpha,\delta,\psi)h_\times, \tag{1.34}$$

where F_+ and $F_\times$ are the detector antenna pattern functions [275], α and δ are the right ascension and declination, the angles that describe the binary's position in the sky, and ψ the polarisation angle [278]. It is possible to write the response $h(t) = F(t)\left(\cos\xi h_+ + \sin\xi h_\times\right)$ with $F = \left(F_+^2 + F_x^2\right)^{1/2}$ and $\tan\xi = F_\times/F_+$. In this way $F(t)$ is independent of the polarisation angle and supplies a measure of the detector sensitivity to different locations in the sky.

If the signal is extracted via matched filtering techniques, what is measured is the *effective strain amplitude*, that is [80]:

$$h_{\rm eff} = \mathcal{N}_{\rm cycles}^{1/2}h, \tag{1.35}$$

where $\mathcal{N}_{\rm cycles} = \int_{f_{\rm min}}^{f_{\rm max}} df (f/\dot{f})$ represents the number of cycles spent by the source within the detector bandwidth $[f_{\rm min}, f_{\rm max}]$. Using (1.25), we can write:

$$\mathcal{N}_{\rm cycles} = \frac{1}{32\pi^{8/3}} \left(\frac{GM_{\rm c}}{c^3}\right)^{-5/3} \left(f_{\rm min}^{-5/3} - f_{\rm max}^{-5/3}\right). \tag{1.36}$$

$\mathcal{N}_{\rm cycles}$ can be written in a compact form using the dimensionless frequency $\tilde{f} = f/f_{\rm coal}$ and the in-band cycles can be estimated with the minimum frequency of the detector sensitivity $f_{\rm min} \ll f_{\rm max}$,

$$\mathcal{N}_{\rm cycles}\left(\tilde{f}_{\rm min}\right) = \frac{6^{5/2}}{32\pi} \frac{1}{\nu} \tilde{f}_{\rm min}^{-5/3}. \tag{1.37}$$

In order to compare theoretical waveforms with experimental sensitivity and to compute the signal-to-noise ratio (S/N) we need to write the signal in the frequency domain. The Fourier transform of the two polarisation amplitudes are described by the following formulae:

$$\tilde{h}_+(f) = A \frac{c}{d} \left(\frac{G\mathcal{M}_{\rm c}}{c^3}\right)^{5/6} e^{i\varphi_+^{\rm PN}(f)} \frac{1}{f^{7/6}} \left(\frac{1+\cos^2\iota}{2}\right), \tag{1.38}$$

$$\tilde{h}_\times(f) = A \frac{c}{d} \left(\frac{G\mathcal{M}_c}{c^3}\right)^{5/6} e^{i\varphi_{\rm X}^{PN}(f)} \frac{1}{f^{7/6}} \cos\iota, \tag{1.39}$$

with $A = \pi^{-2/3}(5/12)^{1/2}$ and $\varphi_+^{\rm PN}(f) = \varphi_\times^{\rm PN}(f) - \pi/2$. Calculating the Fourier transform of the strain amplitude $\tilde{h}(t)$ (in units of Hz^{-1}) that includes the antenna pattern response of the detector, we can compute the square of the S/N:

$$\mathrm{S/N}^2 = \int_0^\infty d\ln f \frac{|2\tilde{h}(f)\sqrt{f}|^2}{S_{\rm n}}, \tag{1.40}$$

where $\sqrt{S_{\rm n}}$ is the *spectral strain sensitivity* with dimension $\mathrm{Hz}^{-1/2}$, describing the noise in the detector (see Figure 1.3).

1.3.1 Parameter estimation

The GW signal originating from the coalescence of a compact binary is contingent upon intrinsic parameters that delineate the system's dynamics and waveform characteristics. Additionally, extrinsic parameters encapsulate the spatial orientation of the source relative to the detector network.

For BHBH systems, intrinsic parameters include the masses $M_{\rm i}$ and spin vectors $\vec{S}_{\rm i}$. These spin vectors, denoted as $\vec{\chi}_{\rm i} = c\vec{S}_{\rm i}/\left(GM_{\rm i}^2\right)$, are dimensionless and exhibit magnitudes within the $[0,1]$ range. Although the individual spins are not precisely ascertainable from the GW signal, the combined parameter, effective aligned spin $\chi_{\rm eff}$ is more constrained. $\chi_{\rm eff}$ represents the projection of the mass-weighted mean spin along $\hat{L}_{\rm N}$, the normal to the orbital plane, and it is defined as:

$$\chi_{\rm eff} = \frac{(M_1\vec{\chi}_1 + M_2\vec{\chi}_2)}{M_1+M_2} \cdot \hat{L}_{\rm N}. \tag{1.41}$$

The extrinsic parameters are the time of the merger $t_{\rm c}$, the luminosity distance $d_{\rm L}$, the viewing angle ι, the right ascension α, the declination δ, the polarization angle ψ and the phase at coalescence $\phi_{\rm c}$.

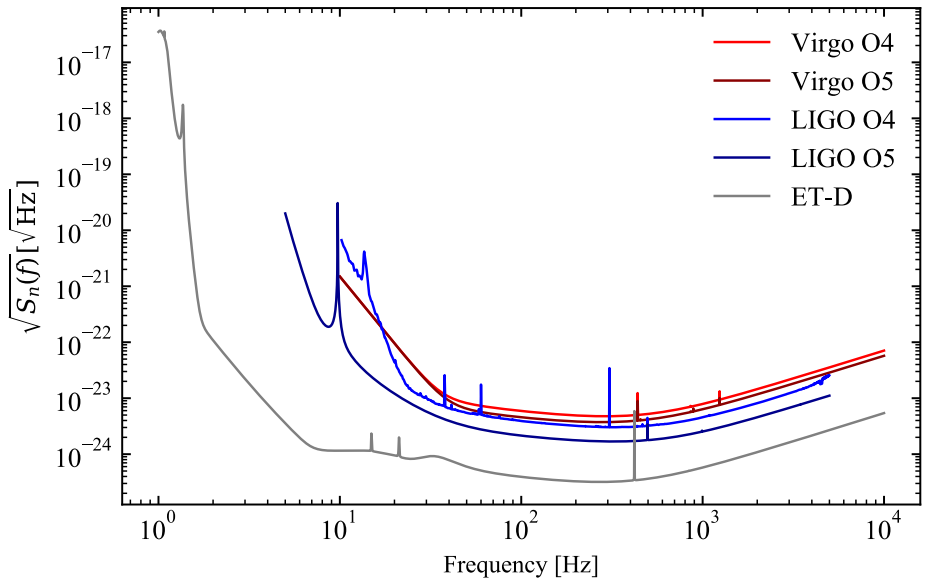

FIGURE 1.3: Spectral strain sensitivity $\sqrt{S_{\rm n}(f)}$ of present and future detectors. We show the expected strain sensitivity of Virgo and LIGO during O4 (red and blue) and O5 (dark red and dark blue). We show in grey the expected strain sensitivity for the Einstein Telescope in D configuration [187].

The chirp mass $M_{\rm c}$ is one of the most precisely measured parameters from the GW signal. Due to its importance in controlling the inspiral phase, $M_{\rm c}$ is well measured for low mass binaries (long inspiral), but is less well measured for higher mass systems (short inspiral). The conversion of $M_{\rm c}$ into the component masses M_1 and M_2 is not easy, because the mass ratio $q = M_1/M_2$ is degenerate with the components spins.

Neutron stars are deformable bodies and they have a surface. As already mentioned, in the final phase of the inspiral of a NSNS or a BHNS binary the tidal interaction becomes important.

In the case of NSNS binaries, additional parameters come into play, and these are associated with the deformation of the stars within a tidal field. The effect of the tidal interaction, in the final phase of the inspiral, is measured by a quantity known as *tidal Love number* λ [111], defined for each binary component. Intuitively, the first body (either a NS or BH) can be treated as a point mass sourcing the external monopole potential $U_{\rm ext}$. The deformed mass distribution can be described using the quadrupolar deformation Q_{ij} that turns out to be proportional to the external tidal field $T_{ij} = -\partial_i\partial_j U_{\rm ext}$. The proportionality constant is the tidal Love number λ. Dimensional analysis needs $Q_{ij}/T_{ij} = -2\kappa_2 R^5/(3G) = \lambda$, where R is the NS radius and k_2 is is the tidal apsidal constant [111] that lies in the range $\sim [0.05 - 0.15]$ [147, 148]. The external gravitational potential, relative to the centre of mass of the deformed object, is:

$$U = \frac{GM_2}{r} - \frac{1}{2}\left[1 + 2\kappa_2\left(\frac{R}{r}\right)^5\right] T_{ij}x^i x^j. \tag{1.42}$$

The first term in (1.42) represents the monopole contribution, the second one the gravitational potential by the point mass sourcing the tide and the third one the correction to the gravity field caused by the distorted mass distribution.

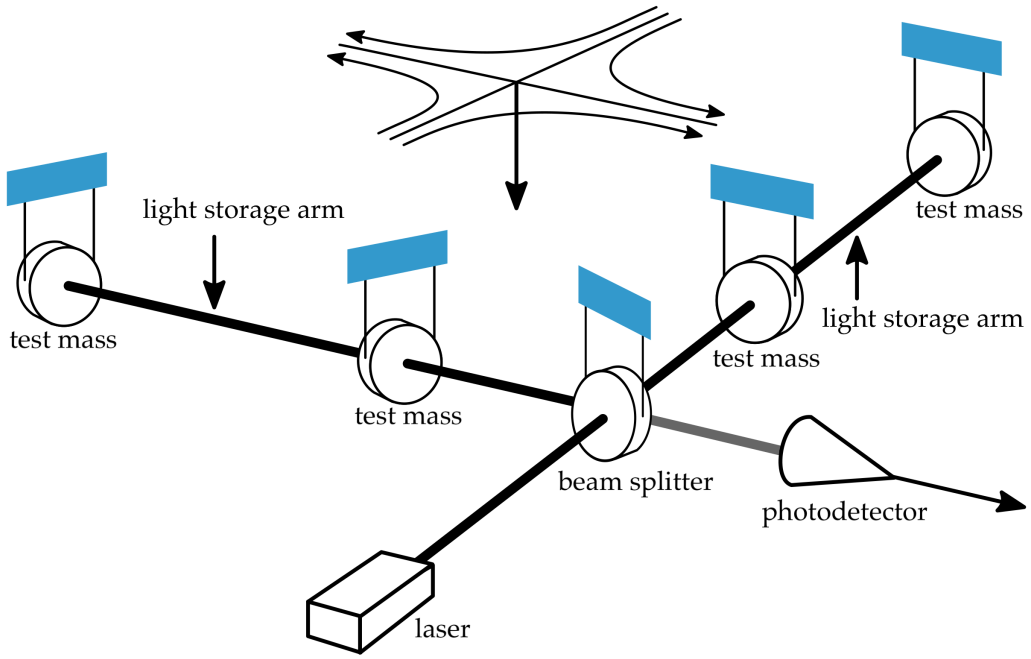

FIGURE 1.4: Schematic representation of a basic interferometer design. Credit: LIGO.

We can also define the dimensionless quadrupolar tidal deformability Λ of a star as

$$\Lambda = \frac{2}{3} k_2 C^{-5}, \tag{1.43}$$

where C is the star compactness,

$$C = \frac{GM}{Rc^2}. \tag{1.44}$$

The individual Love number for a binary component can not be directly inferred from the observed gravitational signal. Instead, what is measured is the effective tidal deformability of the binary $\widetilde{\Lambda}$, a mass-weighted combination of the λ of the binary components [247], given by:

$$\widetilde{\Lambda} = \frac{16}{13} \frac{(M_1 + 12M_2)M_1^4 \Lambda_1 + (M_2 + 12M_1)M_2^4 \Lambda_2}{(M_1 + M_2)^5}. \tag{1.45}$$

Clearly a BH is not deformable so, for a BHNS binary, $\Lambda_1 = \Lambda_{\rm BH} = 0$.

1.3.2 Observing runs and second-generation detectors

GWs are currently being detected using second-generation (2G) GW detectors: Advanced LIGO (aLIGO) [2] and Advanced Virgo (AdV) [25]. The Kamioka Gravitational Wave Detector (KAGRA) has also become part of this network, initiating data collection in February 2020 [38, 13]. Soon, a third aLIGO detector (LIGO-India) will be located in India [300].

These detectors are large Michelson interferometers (see Figure 1.4). when a GW traverses a detector, it induces variations in the relative arm lengths, leading to fluctuations in power output from the laser, which is then captured by the photodetector. Operational within the frequency range of 10 Hz to 5 kHz, these detectors are

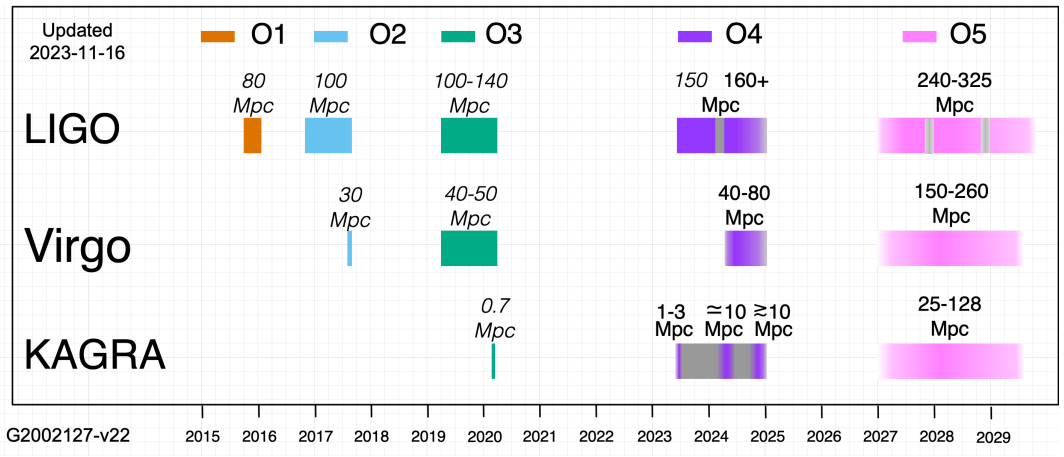

FIGURE 1.5: Planned sensitivity evolution of the Advanced LIGO, Advanced Virgo and KAGRA from O1 to O5. The colored bars show the observing runs, with achieved and planned sensitivities as BNS range for a single-detector S/N threshold of 8 in each observing run (see https://observing.docs.ligo.org/plan/ for further updates).

sensitive to GW chirp frequencies associated with the merger of stellar mass compact objects like BHs and NSs.

The aLIGO detectors, comprising identical designs with 4 km-long arms, are situated in Livingston (Louisiana, USA) and Hanford (Washington, USA). AdV, located in Cascina (Italy), shares a similar design but with 3 km-long arms, as well as KAGRA, situated in Kamioka (Japan), which was instead constructed underground with cryogenic mirrors.

The first observing run (O1) of aLIGO spanned from mid-September 2015 to mid-January 2016. Subsequently, the second observing run (O2) for aLIGO commenced at the conclusion of November 2016 and continued until the end of August 2017. During O2, the AdV detector officially initiated observations in early August 2017, facilitating the first three-detector observations of GWs [10]. The third observing run (O3) of LIGO-Virgo detectors lasted from April 2019 until March 2020.

The fourth observing run (O4) started on 24 May 2023 and it is scheduled to span a duration of 20 calendar months, encompassing potential breaks of up to 2 months allocated for commissioning and maintenance activities. In the first period of this run, O4a, which ended on 16 January 2024, just the LIGO Hanford and Livingston detectors were online, operating at BNS ranges between 140 and 170 Mpc. Recent commissioning endeavors have enabled the Virgo detector to attain a BNS range exceeding 45 Mpc[2]. Virgo will join the network in the second part of O4, O4b, which is planned to start on 10 April 2024. KAGRA recommenced its commissioning phase on July 3 2023, and is anticipated to reintegrate into the observing run during the spring of 2024, featuring a BNS range of approximately 10 Mpc.

The commencement dates, duration, and sensitivities for O5 are currently under discussion, with LIGO-India expected to join the global network of detectors.

1.3.3 Third-generation detectors

The third generation (3G) of GW detectors represents a "quantum leap" in our ability to explore the universe through GWs. Unlike the current 2G detectors, these

[2] https://observing.docs.ligo.org/plan/

advanced instruments incorporate groundbreaking technological concepts to significantly enhance their sensitivity. Two prominent proposals leading the way are the Einstein Telescope (ET) in Europe [242] and Cosmic Explorer (CE) in the USA [251].

The European-based ET is envisioned as a singular triangular observatory situated $200 - 300$ meters underground, a strategic measure to significantly mitigate seismic noise. Its triangular configuration, consisting of three nested detectors with $10 - 15$ km-long arms, offers redundancy, the ability to distinguish GW polarizations, and a null stream, achieved through a combination of outputs where the GW signal cancels, which serves as a veto against disturbances. The xylophone configuration of ET is another distinctive feature. Each of the three detectors comprises two interferometers: one tuned for high frequencies utilizing high laser power, and the other tuned for low frequencies operating at cryogenic temperatures and low laser power.

An alternative configuration, distinct from the single triangular layout, involves the deployment of two well-separated L-shaped detectors, referred to as the "2L" configuration. This arrangement retains all other innovative concepts integral to the ET design. The effect of variations in the geometry and the impact on the science output are currently under study [64].

With a sensitivity increase of one order of magnitude and a significant expansion of the bandwidth encompassing both low and high frequencies, these detectors are poised for remarkable potential in scientific discovery. Specifically, in the context of coalescing binaries, they promise substantial advancements in detection distances, the number of identified events, the precision of signal reconstructions, and the scope of mass exploration. The data generated by these detectors have the potential to instigate transformative developments in fundamental physics, cosmology, and astrophysics. Leveraging insights from numerous prior studies, the scientific rationale for 3G detectors is currently under comprehensive investigation [187, 159].

1.4 GW170817

On August 17, 2017, aLIGO and AdV detected a NSNS coalescence event, designated GW170817, with the merger time recorded at 12:41:04 UTC [9]. The *Fermi* Gamma-ray Burst Monitor independently detected a gamma-ray burst (GRB 170817A [19].) with an approximately 1.7-second delay from the merger (see Figure 1.6). The GW signal allowed for a localization of the source to a 31 deg^2 region of the sky at a distance of 40^{+8}_{-14} Mpc. The component masses were consistent with neutron stars. Following the merger, an extensive observation campaign was launched across the electromagnetic spectrum. Less than 11 hours post-merger, a bright optical transient, AT2017gfo [11], was discovered in the galaxy NGC 4993 by the One-Meter, Two Hemisphere (1M2H) team using the 1 m Swope Telescope. The discovery was rapidly followed by observations from various teams. These collective observations reinforced the hypothesis that GW170817 was the result of a NSNS merger in NGC 4993, followed by a short GRB and a kilonova, powered by the radioactive decay of *r*-process nuclei in the ejecta.

The gravitational signal GW170817, detected with a combined S/N of 32.4 across the three-instrument network, was analyzed using a coherent Bayesian approach [306]. This analysis, accounting for calibration uncertainties, assumed the signal to be from a quasi-circular orbit compact binary system and incorporated waveform models considering component spins and tidal effects [9].

The choice of spin priors significantly influences the estimated source properties, except for the chirp mass. The GW170817 analysis utilized low-spin ($|\chi| \leq 0.05$) and

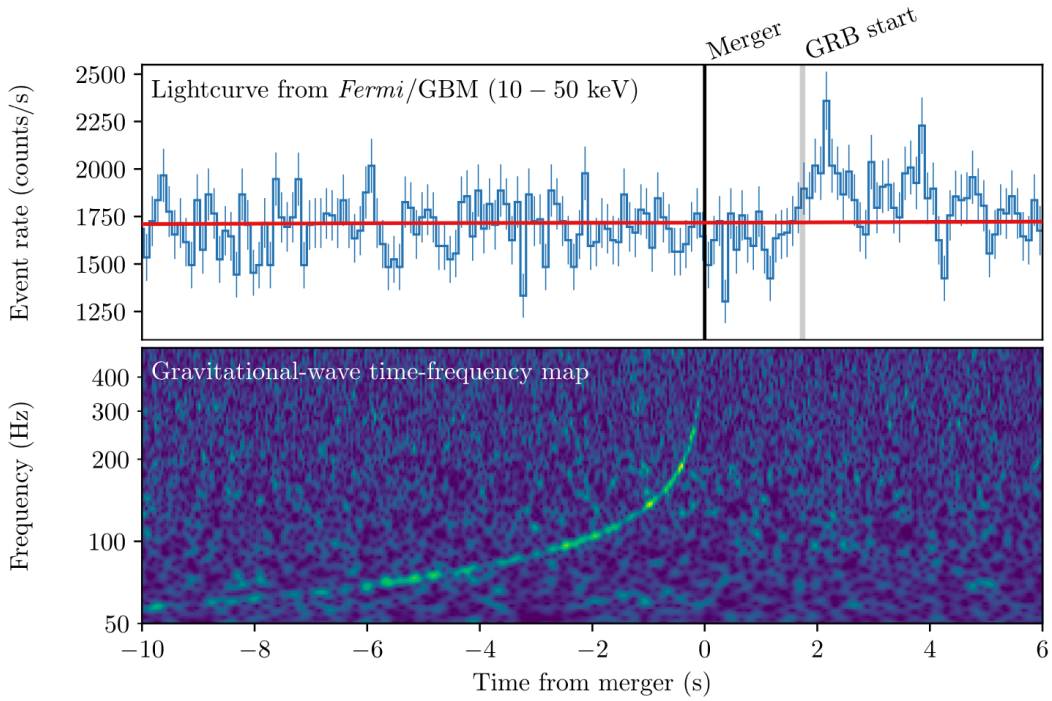

FIGURE 1.6: Multi-messenger detection of GW170817 and GRB 170817A. The top panel shows the GBM light curve between 10 and 50 keV. The red line represents the background estimate.The bottom panel shows the time-frequency map of GW170817, obtained by combining aLigo Hanford and Livingston data. Credit: [8].

high-spin ($|\chi| \leq 0.89$) priors. The estimated masses[3] for the primary and secondary objects (M_1 and M_2, respectively) were $M_1 \in 1.36 - 2.26 M_\odot$ and $M_2 \in 0.86 - 1.36 M_\odot$ under high-spin priors ($M_1 \in 1.36 - 1.60 M_\odot$ and $M_2 \in 1.17 - 1.36 M_\odot$ for low-spin priors). The chirp mass M_c, the most precisely measured parameter, was $M_c = 1.118^{+0.004}_{-0.002} M_\odot$. The total binary mass was estimated as $M_{tot} = 2.82^{+0.47}_{-0.09} M_\odot$ for high-spin priors ($M_{tot} = 2.74^{+0.04}_{-0.01} M_\odot$ for low-spin priors), and the mass ratio q was bounded between 0.4 - 1.0 for high-spin priors (0.7 -1.0 for low-spin priors). These findings align with a BNS system; white dwarfs were excluded due to the GW signal sweeping through 200 Hz in the sensitivity band, indicating an orbit of size $\sim$ 100 km, much smaller than a typical white dwarf radius [282].

1.5 GW190425

On 25 April 2019, 08:18:05 UTC, aLIGO and AdV detected a CBC, GW190425, during O3 [4]. At the time of GW190425, the Hanford detector was temporarily offline with only Livingston and AdV taking data. The Livingston detector observed the event with S/N 12.9. AdV did not contribute to detection due to a low S/N (2.5), but its data were used for subsequent parameter estimation. The LIGO and Virgo Collaboration (LVC) assigned GW190425 a $>$ 99% probability of being a NSNS merger. LVC sent out an alert $\sim$43 minutes after the trigger, which included a sky map computed using a rapid Bayesian algorithm [286]. The initial sky map had a 90% credible region of 10200 deg^2. This large area is due to the fact that the signal was observed with high confidence only in a single interferometer. LVC generated an improved sky

[3]The following mass values are quoted in the frame of the source.

map using a Bayesian analysis [306] that sampled over all binary system parameters, producing a 90% credible sky area of 8284 deg^2 and a distance constrained to 159^{+69}_{-71} Mpc (as a comparison GW170817 was localized to within 28 deg^2 at a 90% credible level). The broad probability region in the sky map for this event presented a difficult challenge for follow-up searches of EM counterparts. Indeed no firm detection of a counterpart has been reported in coincidence with GW190425.

The inferred chirp mass was $M_c = 1.44^{+0.02}_{-0.02} M_\odot$. From the chirp mass and inferred mass ratio ($q \in 0.8 - 1.0$ for low-spin priors and $q \in 0.4 - 1.0$ for high-spin priors) LVC constrained the primary and secondary mass to the range $M_1 \in 1.61 - 2.52 M_\odot$ and $M_2 \in 1.12 - 1.68 M_\odot$ for high-spin priors ($M_1 \in 1.60 - 1.87 M_\odot$ and $M_2 \in 1.46 - 1.69 M_\odot$ for low-spin prior). The total binary mass was $M_{\mathrm{tot}} = 3.4^{+0.3}_{-0.1} M_\odot$ for high-spin priors ($M_{\mathrm{tot}} = 3.4^{+0.1}_{-0.1} M_\odot$). The inferred effective spin parameter was $\chi_{\mathrm{eff}} = 0.058^{+0.11}_{-0.05}$ for high-spin priors ($\chi_{\mathrm{eff}} = 0.012^{+0.01}_{-0.01}$ for low-spin priors).

The chirp mass and the total mass of GW190425 are significantly larger than those of any other known NSNS system. The possibility that one or both binary components of the system are BHs can not be ruled out from gravitational-wave data [172, 145]. For these *ambiguous* systems the detection of an electromagnetic counterpart could be pivotal to infer the nature of the binary [43, 42].

The formation of GW190425's source is challenging to understand within standard formation scenarios. For example it might have involved a phase of stable or unstable mass transfer from a post helium main-sequence star onto a NS, or the stellar companion of a massive NS might have been replaced with another NS through a dynamical encounter [257].

Chapter 2

Ejecta

In this Chapter, we introduce the various mechanisms responsible for ejecta production and detail the characteristics of each ejecta component resulting from neutron star-neutron star and black hole-neutron star mergers. In Section 2.1 we describe the main mechanism for ejecta production. In Section 2.2, we introduce the characteristics of the dynamical component and the fitting formulae used in this work [245, 171]. In Section 2.3, we analyze the components associated to the accretion disks and we present the relatively fitting formulae [42, 171, 163]. The works on which this Chapter is based are specified in the text.

2.1 Ejecta production

In the concluding stages of a binary neutron star (NSNS) merger, tidal forces lead to a partial disruption of the stars, leading to a significant outflow of neutron-rich material. When the crusts of the merging NSs collide, compression, shock heating, and possibly neutrino ablation cause an additional outflow [48, 246].

The released material from these mergers can be categorized into two main components. First, there are the *dynamical ejecta*, gravitationally unbound and rapidly exiting the merger region. This ejection happens on a short, dynamical timescale (milliseconds) due to the initial violent interactions, including partial NS disruption and shock heating when the NS surfaces collide.

The second component comprises the bound material, which does not immediately fall onto the central remnant but has enough angular momentum to form an *accretion disk* around the merger remnant. On longer timescales, this accretion disk becomes the source of additional outflows. These include faster *wind ejecta*, produced by magnetic pressure and neutrino-matter interactions during the initial neutrino-cooling-dominated accretion phase [88, 200, 229, 158]. Additionally, there are slower but more massive *secular ejecta*, produced by viscous processes within the disk [285].

In the context of a NSNS merger, the properties of the resulting ejecta are highly dependent on the eventual fate of the merger remnant. This fate, in turn, is closely linked to the total mass of the original NSNS binary, denoted as $M_{\rm tot}$. As discussed in various studies [283, 48], for $M_{\rm tot}$ exceeding a critical threshold mass ($M_{\rm crit}$) of approximately $2.6 - 3.9 M_\odot$, which accounts for a range of soft and stiff Equations of State (EoS), the remnant immediately collapses into a BH within the dynamical timescale of milliseconds or less.

Bauswein et al. [48] proposed an empirical fitting formula for $M_{\rm crit}$ in relation to the Tolman–Oppenheimer–Volkoff (TOV) mass ($M_{\rm TOV}$) of a non-rotating NS and the NS compactness. This relationship is found to be relatively insensitive to the binary mass ratio ($q = M_2/M_1$) for $q \gtrsim 0.7$ [165].

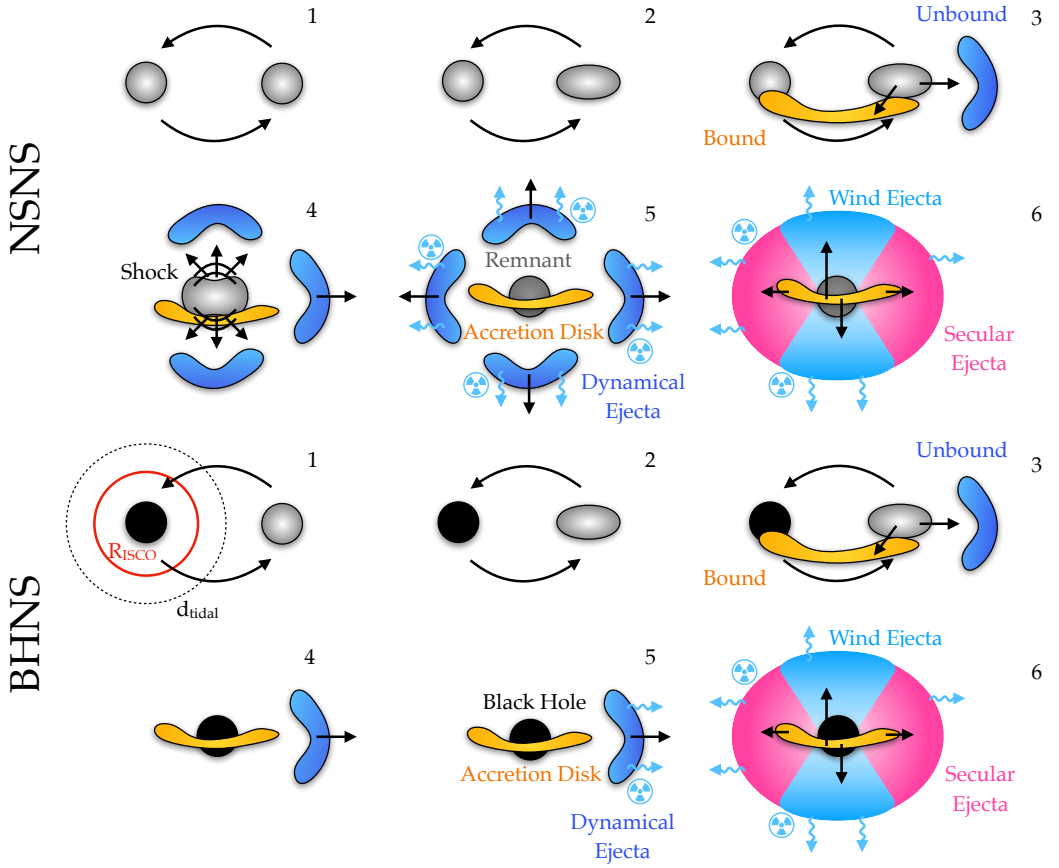

FIGURE 2.1: Schematic representation of the main stages leading to ejecta production in NSNS and BHNS mergers (upper panel and lower panel, respectively). For further details, see the text.

If the total mass of the binary ($M_{\rm tot}$) is less than $M_{\rm crit}$, prompt collapse is avoided. Typically, this results in the formation of a rapidly-spinning NS remnant, with a mass approximately equal to $M_{\rm tot}$ after accounting for losses due to neutrino and gravitational wave (GW) emissions and dynamical ejecta. This remnant is at least temporarily stable against gravitational collapse to a BH. Different studies [47, 219] show that the maximum stable mass of a NS exceeds $M_{\rm TOV}$ when the NS is rapidly spinning near its break-up velocity.

The remnant may be categorized as either a *hypermassive* NS (HMNS) or a *supramassive* NS (SMNS). An HMNS, which is supported only by differential rotation, is unlikely to survive more than a few tens to hundreds of milliseconds post-merger before collapsing to a BH due as differential rotation is damped due to viscous angular momentum transport. On the other hand, SMNS remnants, which can be supported by solid body rotation, may spin down through less efficient processes like magnetic dipole radiation or GW emissions due to minor non-axisymmetric distortions of the NS. Consequently, SMNS can potentially survive much longer before collapsing. Finally, as Giacomazzo et al. [126] noted, the merger of a particularly low-mass binary that leaves a remnant with a mass below $M_{\rm TOV}$ will result in an indefinitely stable NS remnant.

In BHNS mergers, the key condition for the production of ejecta is based on the relationship between the distance at which tidal disruption occurs, $d_{\rm tid}$, and the radius of the black hole's (BH) innermost stable circular orbit (ISCO), $R_{\rm ISCO}$. To elaborate, if $d_{\rm tid} < R_{\rm ISCO}$, any material that is released during the merger is inevitably

destined to be absorbed by the BH. This is a critical factor in determining whether the merger will produce any observable ejecta and, consequently, an electromagnetic (EM) counterpart.

As outlined by Foucart [115], $R_{\rm ISCO}$ is proportional to $M_{\rm BH}$ for a given BH spin $\chi_{\rm BH}$, and $d_{\rm tid}$ scales with $R_{\rm NS}\left(M_{\rm BH}/M_{\rm NS}\right)^{1/3}$. Therefore, significant tidal disruption of the NS is more likely if the BH is of low mass and/or rapidly spinning. In scenarios where the BH is not sufficiently low-massive or rapidly spinning, the NS may directly plunge into the BH without producing any ejecta. Consequently, such events would lack an EM counterpart, limiting the observational opportunities to understand these phenomena fully.

2.2 Dynamical ejecta

As explained before, in NSNS mergers, the ejection of unbound matter on dynamical timescales primarily occurs via two processes. Initially, tidal interactions during the late inspiral and merger phase create spiral arms. These arms expand outwards, predominantly along the equatorial plane, driven by angular momentum transfer through hydrodynamic processes. Additionally, hydrodynamic forces at the contact interface between the merging stars lead to the expulsion of shock-heated material. The neutron-rich material can be also ejected due to quasi-radial pulsations of the remnant, as detailed by Bauswein et al. [48] and Hotokezaka et al. [151].

The extent and nature of these ejection processes are influenced by several factors, including the total mass of the binary system, its mass ratio, and the equation of state (EoS) of the NSs. Notably, shock-driven ejection is less pronounced in scenarios leading to prompt collapse, while greater mass ejection is observed in asymmetric mergers due to the tidal disruption of the lightest star[48, 55]. With softer EoS, which corresponds to less deformable NSs, tidal disruption becomes less effective, resulting in less massive dynamical ejecta. Conversely, higher dynamical ejecta masses are associated with rapidly spinning NSs [89, 209].

Typically, the total mass of dynamical ejecta in NSNS mergers ranges between 10^{-4} and $10^{-2}M_{\odot}$, with velocities between 0.1 and 0.3 times the speed of light (c), as outlined by Radice et al. [246] and Bovard et al. [63]. The composition of NSNS dynamical ejecta varies depending on the fate of the remnant. If there is a supramassive or hypermassive NS (SMNS/HMNS) phase before collapse to a black hole, strong neutrino irradiation can increase the electron fraction Y_e, defined by (3.1), and lower the opacity, especially near the polar axis where neutrino wind is more intense. In the absence of such a phase, the ejecta have higher opacity due to their neutron-rich composition.

In BHNS mergers, dynamical ejecta result solely from the tidal disruption of the NS, given that the BH lacks a crust and therefore no shock is produced at the point of 'collision'. As a consequence, these systems tend to generate dynamical ejecta predominantly near the equatorial plane, and largely across approximately half of the azimuthal angle [162, 108, 116].

Simulations of BHNS mergers have identified dynamical ejecta masses reaching up to $\sim 0.1\mathrm{M}_{\odot}$, with velocities comparable to those in NSNS cases. The mass of the BHNS dynamical ejecta primarily depends on variables such as $\chi_{\rm BH}$, the mass ratio $q = M_1/M_2$, and the NS EoS. For instance, low mass or rapidly spinning BHs, which have smaller $R_{\rm ISCO}$, are more likely to satisfy the condition $d_{\rm tid} > R_{\rm ISCO}$, thus favoring the production of substantial dynamical ejecta. Tidal disruption is more likely with a lower q, which enhances the mass of dynamical ejecta, except in cases of

large NS masses corresponding to lower deformabilities. Furthermore, for stiffer EoS, NSs are more deformable, leading to more massive dynamical ejecta. The absence of an intermediate/stable NS remnant that could produce strong neutrino irradiation means that BHNS dynamical ejecta generally have lower values of Y_e, thus a higher opacity.

2.2.1 Fitting formulae

In order to calculate the dynamical ejecta mass for NSNS mergers, we use a fitting formula calibrated on a set of high-resolution general-relativistic hydrodynamics (GRHD) simulations [171]:

$$\frac{M_{\rm dyn}^{\rm NSNS}}{10^{-3}M_\odot} = \left[\alpha\left(\frac{M_1}{M_2}\right)^{\frac{1}{3}}\frac{1-2C_1}{C_1} + \beta\left(\frac{M_2}{M_1}\right)^n + \gamma\left(1-\frac{M_1}{M_1^{\rm B}}\right)\right]M_1^{\rm B} + (1\leftrightarrow 2) + \delta, \tag{2.1}$$

where the symbol $\leftrightarrow$ indicates the same expression, but with inverted indices (1 and 2 refer to primary and secondary component, respectively). The best-fit parameters are $\alpha = -1.35695$, $\beta = 6.11252$, $\gamma = -49.4355$, $\delta = 16.1144$ and $n = -2.5484$. C is the star's compactness defined by (1.44), $M^{\rm B}$ is the NS baryonic mass

$$M^{\rm B} = E_b + M_{\rm NS}, \tag{2.2}$$

where E_b is the binding energy of the NS. E_b can be expressed as a function of the NS mass and compactness through a fitting formula [175]:

$$E_b = M_{\rm NS}\frac{0.6C_{\rm NS}}{1-0.5C_{\rm NS}}, \tag{2.3}$$

so (2.2) becomes:

$$M^{\rm B} = M_{\rm NS}\left(1+\frac{0.6C_{\rm NS}}{1-0.5C_{\rm NS}}\right). \tag{2.4}$$

We also use a similar fitting formula to calculate the ejecta velocity in units of the speed of light [245]:

$$v_{\rm dyn}^{\rm NSNS} = \left[\alpha\left(\frac{M_1}{M_2}\right)(1+\gamma C_1)\right] + (1\leftrightarrow 2) + \beta, \tag{2.5}$$

with fitting coefficients $\alpha = -0.287$, $\beta = 0.494$ and $\gamma = -3.000$.

Regarding BHNS mergers, we employ the following fitting formula for dynamical ejecta [171]:

$$\frac{M_{\rm dyn}^{\rm BHNS}}{M_{\rm NS}^b} = a_1\left(\frac{M_{\rm BH}}{M_{\rm NS}}\right)^{n_1}\frac{1-2C_{\rm NS}}{C_{\rm NS}} - a_2\left(\frac{M_{\rm BH}}{M_{\rm NS}}\right)^{n_2}\frac{R_{\rm ISCO}}{M_{\rm BH}} + a_3\left(1-\frac{M_{\rm NS}}{M_{\rm NS}^b}\right) + a_4, \tag{2.6}$$

with coefficients $a_1 = 0.04464$, $a_2 = 0.002269$, $a_3 = 2.431$, $a_4 = -0.4159$, $n_1 = 0.2497$, and $n_2 = 1.352$. $R_{\rm ISCO}(\chi)$ is the BH dimensionless innermost stable circular orbit, where $\chi = \chi_{\rm BH}\cos\iota_{\rm tilt}$ with $\iota_{\rm tilt}$ the angle between the binary angular momentum and the BH spin, and it is given by [45, 163]

$$R_{\rm ISCO}(\chi) = 3 + Z_2 - {\rm sign}(\chi)\sqrt{(3-Z_1)(3+Z_1+2Z_2)}, \tag{2.7}$$

where

$$Z_1 = 1 + \left(1-\chi^2\right)^{1/3}\left\{(1+\chi)^{1/3} + (1-\chi)^{1/3}\right\} \tag{2.8}$$

and

$$Z_2 = \sqrt{3\chi^2 + Z_1^2}. \tag{2.9}$$

For the dynamical ejecta velocity we use the formula [163]

$$\frac{v_{\rm dyn}^{\rm BHNS}}{c} = (aq+b), \tag{2.10}$$

where $a = 1.533 \times 10^{-2}$ and $b = 0.1907$.

2.3 Accretion disk

An accretion disk is formed in most NSNS mergers, and in those BHNS mergers where the NS is tidally disrupted outside the BH horizon. Merger simulations have identified disk masses ranging from $\sim 10^{-3} - 0.3 M_\odot$ [245, 165, 162, 113]. In NSNS cases, the disk mass is mainly dependent on the binary's total mass and mass ratio, as well as the NS EoS. Massive binaries that undergo prompt collapse to a BH tend to produce relatively low-mass disks. This is because the production of massive disks is intimately tied to the internal redistribution of remnant mass and angular momentum during the transition from differential to solid body rotation; in prompt collapses, this process does not have time to occur. Asymmetric mergers, as shown by Kiuchi et al. [165], lead to more massive accretion disks, a trend also observed with stiff EoS. For BHNS mergers, the disk mass primarily depends on the BH spin, the binary's mass ratio, and the NS EoS.

Disk outflows are a significant source of material over seconds or more. Shortly after disk formation, when the accretion rate is high, thermal neutrinos are emitted copiously, and mass loss is driven by neutrino heating [239, 196]. Spiral density waves, induced by oscillations in the NS remnant, may contribute to mass ejection and outward angular momentum transport [213]. Time-dependent models of disk evolution, including neutrino emission and absorption, show that in prompt collapse scenarios, only a small fraction of mass is ejected [107, 158, 230]. However, if the remnant is a HMNS or a SMNS, the higher neutrino luminosity results in more significant mass ejection [88, 229, 193, 252], enhanced by a strongly magnetized NS remnant [201].

The disk evolves from a neutrino-cooled to a radiatively inefficient state over seconds, driven by spiral waves or MRI [196]. This transition results in neutron-rich winds due to the freeze-out of weak interactions [167, 196]. Later hydrodynamical models indicated electron fractions $Y_e \sim 0.2 - 0.4$ in disk outflows for prompt collapses, sufficient to produce the entire range of r-process elements [107, 158]. The fraction of disk mass ejected ranges from 5% to $\sim$ 30% depending on the BH spin [158]. 3D GRMHD simulations confirmed large disk ejecta fractions and high Y_e, predicting up to 40% of the torus to be unbound [285, 109], with outflow properties sensitive to the magnetic field's strength and geometry [109].

In cases with a HMNS or SMNS remnant, up to 90% of the disk mass can be unbound due to higher neutrino irradiation and the hard surface of the star [200]. The electron fraction of the ejecta increases with the remnant's lifetime [200, 161]. Even in prompt collapses, early-stage disk evolution can produce high Y_e material [203].

2.3.1 Fitting formulae

Kiuchi et al. [165] observed that the fitting formula from Radice et al. [245] tends to underestimate the accretion disk mass in asymmetric NSNS mergers. In order to account for both symmetric and asymmetric mergers, we use the formula for the accretion disk mass from NSNS mergers presented by Barbieri et al. [42]

$$M_{\rm disk}^{\rm NSNS} = \frac{1}{4}\,(2+x_1)\,(x_1-1)^2\,M_2 + (1 \leftrightarrow 2), \tag{2.11}$$

where

$$x_1 \sim 2\left[\left(1+\frac{M_2}{M_1}\right)^{-1} + \lambda_1^{-1} - 1\right] \tag{2.12}$$

is limited between 0 and 1, and

$$\lambda_1 = \left(\frac{\tilde{\Lambda}}{\Lambda_0}\right)^{\alpha}\left(\frac{M_2}{M_1}\right)^{\beta} \tag{2.13}$$

with $\Lambda_0 = 245$, $\alpha = 0.097$ and $\beta = 0.241$. We do not assume any minimum disk mass.

Foucart et al. [116] provided a formula to estimate the mass remaining outside the remnant BH following a BHNS merger

$$\frac{M_{\rm out}^{\rm BHNS}}{M_{\rm NS}^{\rm B}} = \left[\max\left(\alpha\frac{1-2C_{\rm NS}}{\eta^{1/3}} - \beta\frac{R_{\rm ISCO}}{M_{\rm BH}}\frac{C_{\rm NS}}{\eta} + \gamma, 0\right)\right]^n, \tag{2.14}$$

where η is the symmetric mass ratio defined as $\eta = M_{\rm BH}M_{\rm NS}/(M_{\rm BH}+M_{\rm NS})^2$ and the best-fit parameters are $\alpha = 0.406$, $\beta = 0.139$, $\gamma = 0.255$ and $n = 1.761$. We obtain the disk mass by subtracting $M_{\rm dyn}^{\rm BHNS}$ from $M_{\rm out}^{\rm BHNS}$:

$$M_{\rm disk}^{\rm BHNS} = \max(M_{\rm out}^{\rm BHNS} - M_{\rm dyn}^{\rm BHNS}, 0). \tag{2.15}$$

We assume that $M_{\rm dyn}$ can not exceed $50\%M_{\rm out}$ [250, 113].

Chapter 3

Kilonovae

In this Chapter, we delve into the essential physics of kilonovae. Section 3.1 is dedicated to discussing r-process nucleosynthesis in the cosmos and summarizing the historical development of kilonova research [199]. Section 3.2 presents the kilonova emission model employed in our analysis [230, 44]. Lastly, Section 3.3 briefly describes the discovery of the kilonova associated to GW170817 [11]. This Chapter is mainly based on the works by Metzger [199], Perego et al. [230], Barbieri et al. [44, 43] and references therein.

3.1 Background of kilonovae

3.1.1 *r*-process nucleosynthesis

The *rapid neutron-capture process*, commonly known as *r*-process, serves as a mechanism for the formation of heavy elements extending beyond iron, specifically the lanthanides and actinides. This process is characterized by the capture of neutrons by lighter seed nuclei and typically unfolds in dense and neutron-rich environments, where the β-decay timescale is longer than the neutron capture timescale. The *r*-process results in the creation of neutron-rich nuclei that are inherently unstable, existing far from the valley of stable isotopes.

In 1957, pioneering works by Burbidge et al. [70] and Cameron [73] identified the *r*-process as the primary synthesis mechanism responsible for approximately half of the heavy elements in the Universe. For decades, the astrophysical environments conducive to the *r*-process remained uncertain.

One crucial factor determining the feasibility of the *r*-process is the material *electron fraction*:

$$Y_e \equiv \frac{n_p}{n_n + n_p}, \tag{3.1}$$

where n_p and n_n are the densities of protons and neutrons. Ordinary stellar material usually has more protons than neutrons ($Y_e \geq 0.5$), while matter with more neutrons ($Y_e < 0.5$) is typically needed for the *r*-process.

Neutrino-heated winds emanating from proto-NSs formed during core collapse supernovae (SNæ) have historically been considered as promising sites for the r-process, as discussed in earlier studies such as Duncan et al. [98] and Takahashi et al. [293]. However, more recent investigations, as exemplified by works like Arcones et al. [37] and Roberts et al. [255], have cast doubt on this hypothesis. An exception to this trend could be hyper-energetic core collapse SNæ, characterized by the presence of very massive proto-NSs and ultra-strong ordered magnetic fields. It is worth noting that such hyper-energetic events are rare, accounting for only 1/1000 of all core collapse SNæ. To match Galactic abundances, each of these events should release approximately $\gtrsim 10^{-2} M_\odot$ of *r*-process material, which subsequently mixes with the outer SN ejecta containing ^{56}Ni responsible for the optical luminosity of the SN.

However, this large amount of *r*-process material mixing with the outer ejecta would theoretically redden the SN light curve. Unfortunately, this expectation is inconsistent with observations of hyper-energetic SNæ, as discussed by Metzger [199].

The discovery of the first binary pulsar by Hulse and Taylor in 1975 [153] spurred new proposals in the field. Lattimer and Schramm in 1974 and 1976 [176, 177] suggested that mergers of compact binaries, particularly BHNS, could serve as plausible environments for *r*-process nucleosynthesis. Simultaneously, Symbalisty and Schramm in 1982 [292] put forth the hypothesis of NSNS mergers. Following these proposals, the link between NSNS mergers and Gamma-Ray Bursts (GRBs) was introduced by Blinnikov et al. in 1984 [61] and Paczynski in 1986 [220]. This was followed by more comprehensive studies of the model by Eichler et al. in 1989 [102] and the first numerical simulations of such events conducted by Davies et al. in 1994 [86] and Rosswog et al. in 1999 [261]. One notable advantage of this emerging scenario regarding compact binaries is that the system geometry and dynamic nature prevent a portion of the unbound ejecta from being exposed to neutrino fluxes. This results in lower electron fraction, typically $Y_e \lesssim 0.2$. In contrast, in the context of core-collapse SNæ, the acceleration of matter resulting from the neutrino-driven wind occurs more gradually. Processes such as $\nu_e + n \rightarrow p + e^-$ are permitted to significantly increase Y_e.

The required production rate of heavy *r*-process nuclei ($A > 140$), averaged over the age of the Galaxy, is $\sim 2 \cdot 10^{-7} M_\odot\,\mathrm{yr}^{-1}$ [243]. Given a detection rate R_{NSNS} by Advanced LIGO/Virgo at design sensitivity [1], the required *r*-process mass yield per merger event to explain the Galactic abundances is roughly given by [197]:

$$\langle M_r \rangle \sim 10^{-2} M_\odot \left(\frac{R_{\mathrm{NSNS}}}{10\,\mathrm{yr}^{-1}} \right)^{-1}. \tag{3.2}$$

Numerical simulations of NSNS and BHNS mergers show a range of total ejecta masses of $\langle M_r \rangle \sim 10^{-3} - 10^{-1} M_\odot$, consistent with $\langle M_r \rangle \sim 0.03 - 0.06 M_\odot$, inferred from the KN of GW170817. Although large uncertainties remain[2], NSNS and BHNS mergers are likely the major sources of *r*-process in the Universe.

3.1.2 History of kilonovae

The pioneering work that first introduced the concept of radioactively-decaying ejecta from NSNS or BHNS mergers as potential sources of thermal transient emission, akin to SNæ, was conducted by Li and Paczynski in 1998 [180]. They postulated that this emission would reach its peak on timescales of approximately 1 day, significantly shorter than the timescales observed in SNæ cases, which typically extend over weeks or months. This conclusion was drawn from the characteristics of the ejecta, specifically their low mass and high velocity, leading to rapid transparency to their own radiation.

The initial model proposed by Li and Paczynski was ill-defined, leading to overly optimistic heating rates. Consequently, they predicted peak luminosities in the range of $\sim 10^{43} - 10^{44}$ erg s^{-1}, surpassing even the ones observed in SNæ. The refinement

[1] With a horizon distance of 200 Mpc for NSNS mergers.

[2] SN kicks could potentially displace the NSNS or BHNS binary systems far from the galaxy core, thereby preventing the contamination of *r*-process nuclei within the galaxy. Additionally, recent studies [248, 302] propose that SNæ may offer a more suitable explanation for the abundances of *r*-process elements in low-metallicity environments compared to NSNS/BHNS mergers. These considerations lend support to the idea of an alternative *r*-process source at low metallicity, possibly arising from collapsars—massive rotating stars whose collapse also gives rise to long-duration GRBs [241, 284].

of the luminosity scale for this transient was introduced by Metzger et al. in 2010 [197]. In their study, light curve models were computed with self-consistent radioactive heating rates, derived for the *r*-process using a nuclear reaction network calculation.

This work revealed that the peak luminosities of this emission were approximately three orders of magnitude brighter than typical novae. In light of this, the authors coined the term *kilonovae* (KNæ) to describe these emissions. Importantly, this study was one of the first to allude to the connection between KNæ, short GRBs, gravitational waves (GWs) from NSNS or BHNS mergers, and the sites where the *r*-process nucleosynthesis takes place.

Following the confident determination of the radioactive heating rate, attention shifted towards addressing the issue of ejecta opacity κ. It was discovered that the opacity of *r*-process elements could surpass values significantly greater than those of iron, contrary to previous assumptions (including those in Metzger et al. 2010) that relied on grey opacities typical of iron-rich ejecta from Type-Ia supernovae. This novel finding stemmed from the intricate atomic structures of certain lanthanides and actinides, which exhibit a high density of line transitions, as demonstrated by different works [160, 294].

These increased opacities have implications for the light curve characteristics, suggesting bolometric peaks at later times (weeks instead of days) and lower luminosities [46]. Additionally, factoring in the increased optical opacity due to line blanketing, the spectral peak shifted from the optical/UV range to the near-infrared band. Shortly after, Tanvir et al. [295] and Berger et al. [54] presented evidence from Hubble Space Telescope observations of GRB130603B, revealing an infrared excess emission approximately one week after the GRB.

Conversely, if the ejecta possess a relatively high electron fraction ($0.25 \lesssim Y_e \lesssim 0.4$), they are incapable of producing lanthanide with atomic mass numbers $A > 140$. As a result, the emission from such ejecta evolves more rapidly and is shifted towards the UV band. In a study by Metzger and Fernàndez in 2014 [200], this emission from high Y_e, lanthanide-poor ejecta was termed *blue* KN, in contrast to the emission from low-Y_e, lanthanide-rich ejecta, referred to as *red* KN.

Metzger and Fernàndez also proposed the possibility of observing both types of KNæ following the same merger event, arising from emissions by distinct ejecta components. These hybrid KN models played a crucial role in the interpretation of GW170817.

3.2 Kilonova model

3.2.1 NSNS

The kilonova emission model used in this work and described in [78] is based on a work by Barbieri et al. [41], following Perego et al. [230]. They introduce a semi-analytical model that assumes axially symmetric ejecta, with the axis corresponding to the direction of the total angular momentum of the binary prior to merger. The polar plane is discretized into 30 slices, evenly distributed in $\cos\theta$, where θ is the polar angle. Within each slice, the model assumes homologous expansion and calculates the thermal emission at the photosphere using a methodology akin to the approaches described by Grossman et al. [141] and Martin et al. [193].

Numerical simulations [259] and analytical arguments [309] propose a mass distribution that is contingent on velocity and takes the form of

$$\frac{dm}{dv} \propto \left(1 - \left(\frac{v}{v_{\max}}\right)^2\right)^3 v^2, \tag{3.3}$$

where $v_{\max}$ is the maximum velocity of the ejecta. From now on the velocity v is considered as a Lagrangian coordinate and the term "shell" indicates the ejecta moving at the same velocity. For each ejecta component i, the bolometric luminosity emitted at time t in the angular slice j is:

$$L_{ij}^{\rm bol}\left(t, m_{ij}, Y_{{\rm e},ij}\right) = \dot{\epsilon}_{\rm nuc}\left(t, Y_{{\rm e},ij}\right) m_{{\rm rad},ij}\left(t, m_{ij}, Y_{{\rm e},ij}\right), \tag{3.4}$$

where m_{ij} and $Y_{{\rm e},ij}$ are the mass and electron fraction of the i-th component (dynamical, wind or secular) in the j-th angular slice, $\dot{\epsilon}_{\rm nuc}$ is the nuclear heating rate for r-process products radioactive decay and $m_{{\rm rad},ij}$ is the mass of the radiating shell.

The quantity m_{ij} is computed with the consideration that dynamical and secular ejecta exhibit higher concentration near the equatorial plane. Perego et al. [230] described their mass distributions in the polar plane as a function $F(\theta) \propto \sin^2\theta$, where θ is the polar angle measured from the polar axis (the direction of the binary's total angular momentum). In contrast, the wind ejecta propagates along the polar axis, maintaining a uniform mass distribution within its opening angle $\theta_{\rm w} = 60$ deg. Consequently, its angular mass distribution can be expressed as $F(\theta) = $ const. for $\theta \leq 60$ deg. Therefore, the expression for m_{ij} for dynamical and secular ejecta is given by

$$m_{ij} = \frac{m_{i,\,\rm tot}}{16}\left(\cos 3\theta_{j+1} - 9\cos\theta_{j+1} - \cos 3\theta_j + 9\cos\theta_j\right), \tag{3.5}$$

and for wind ejecta by

$$m_{ij} = \frac{m_{i,\,\rm tot}}{2\left(1-\cos\theta_{\rm w}\right)}\left(\cos\theta_j - \cos\theta_{j+1}\right) \quad \text{for } \theta < \theta_{\rm w}, \tag{3.6}$$

with θ_{j+1} and θ_j indicate the upper and lower bound of the j-th angular slice, respectively.

In the subsequent discussion, the treatment remains identical for all angular slices and ejecta components, so we can simplify the notation by dropping the indices ij.

The nuclear heating rate can be described described by the following fitting formula (based on detailed nucleosynthesis calculations [169]):

$$\dot{\epsilon}_{\rm nuc}(t) = \epsilon_0 \frac{\epsilon_{\rm th}}{0.5}\left[\frac{1}{2} - \frac{1}{\pi}\arctan\left(\frac{t-t_0}{\sigma}\right)\right], \tag{3.7}$$

where $\sigma = 0.11$ s, $t_0 = 1.3$ s and $\epsilon_{\rm th} = 0.5$ is the thermalization efficiency, assumed constant. Since there are large uncertainties in the decay models and nuclear mass, ϵ_0 is assumed in the range $10^{18} \lesssim \epsilon_0 \lesssim 2\times10^{19}{\rm erg}^{-1}\ {\rm s}^{-1}$ [194, 260].

Perego et al. [230] incorporated an additional term ϵ_{Y_e} in the expression of $\dot{\epsilon}_{\rm nuc}$, depending on the electron fraction Y_e of the ejecta. This term considers that ejecta with large Y_e (low opacity) exhibit a decay half-life of only a few hours, resulting in enhanced emission at early times:

$$\epsilon_{Y_e}(t) = \begin{cases} 0.5 + 2.5\left\{1 + e^{\left[4\left(\frac{t}{1\,\rm d}-1\right)\right]}\right\}^{-1} & \text{if } Y_e \geq 0.25, \\ 1 & \text{otherwise.} \end{cases} \tag{3.8}$$

The quantity $m_{\rm rad}$ in (3.4) represents the mass of the radiating shell, referring to the ejecta region situated between the diffusion surface and the photosphere. The diffusion surface is identified as the shell with optical depth $\tau = c/v$. Below this surface, the diffusion timescale is greater than the dynamical timescale, rendering photons unable to escape. On the other hand, the photosphere corresponds to the shell with $\tau = 2/3$, above which photon thermalization is inefficient. Assuming homologous expansion, where the ejecta mass distribution remains stationary in velocity space, the mass of ejecta with a velocity greater than a specified value v can be expressed as:

$$m_{>v}(v) = m_{\rm ej}\left[1 + F\left(\frac{v}{v_{\rm max}}\right)\right], \tag{3.9}$$

where, assuming (3.3), $F(x)$ is:

$$F(x) = \frac{35}{112}x^7 - \frac{105}{80}x^5 + \frac{35}{16}x^3 - \frac{35}{16}x. \tag{3.10}$$

Diffusion becomes effective when the optical depth is below c/v,

$$\tau = \kappa\bar{\rho}\Delta r = \frac{\kappa m_{>\rm v}}{4\pi(vt)^2} \leq \frac{c}{v}. \tag{3.11}$$

The times at which the diffusion surface and the photosphere correspond to the shell with velocity v are, respectively,

$$t_{\rm diff}\,(v) = \sqrt{\frac{\kappa m_{>v}}{4\pi v c}}, \tag{3.12}$$

$$t_{\rm phot}(v) = \sqrt{\frac{3\kappa m_{>v}}{8\pi v^2}}. \tag{3.13}$$

The time evolution of the diffusion and photospheric shells can be found by inverting these relations. The effective radiating mass is given by:

$$m_{\rm rad} = m_{>v_{\rm diff}(t)} - m_{>v_{\rm phot}(t)}. \tag{3.14}$$

The KN emission is assumed to be described by a blackbody. At the point of their launch, the ejecta exhibit a temperature exceeding 10^4 K, gradually cooling as they expand. As the temperature T reaches the first ionization temperature of lanthanides, denoted as $T_{\rm La}$, the ejecta opacity decreases due to the recombination of lanthanides[3] [46]. The front of recombination moves backward, causing the photosphere to shift along with it. However, the temperature of the photosphere remains constant ($T = T_{\rm La}$) The photospheric radius before recombination is given by:

$$R_{\rm phot} = v_{\rm phot}t. \tag{3.15}$$

After recombination, using the Stefan-Boltzmann law $L_{\rm bol} = A\sigma_{\rm SB}T^4 = R^2\Omega\sigma_{\rm SB}T^4$, the photospheric radius at costant temperature $T_{\rm La}$ is given by:

$$R_{\rm phot} = \sqrt{\frac{L_{\rm bol}}{\Omega\sigma_{\rm SB}T_{\rm La}^4}}, \tag{3.16}$$

[3]This is based on the assumption of local thermal equilibrium. Observations of the KN associated to GRB230307A [178] are in tension with this assumption.

where σ_{SB} is the Stefan-Boltzmann constant and Ω is the subtended solid angle. At each time the photospheric radius is the minimum of the two expressions. Let us summarize the two cases with the following expressions:

$$\begin{cases} R_{\rm phot} = v_{\rm phot}\, t, T = \left(\frac{L_{\rm bol}}{\Omega \sigma_{\rm SB} R_{\rm phot}^2}\right)^{1/4} & \text{before recombination} \\ T = T_{\rm La}\,, R_{\rm phot} = \sqrt{\frac{L_{\rm bol}}{\Omega \sigma_{\rm SB} T_{\rm L3}^4}} & \text{after recombination} \end{cases} \tag{3.17}$$

In order to evaluate the observed spectral flux by superposing Planckian distributions, we follow [193], projecting the emitting surface in each angular bin along the line of sight. The total observed spectral flux for a given time t and frequency ν, given the blackbody spectrum in each bin and the observer direction $\mathbf{w}$, is:

$$F_v(\mathbf{w}, t) = \sum_j B_v\left(T_j(t)\right) \int_{\hat{\mathbf{n}}_\mathbf{j}\cdot\mathbf{w}>0} \mathbf{w}\cdot d\mathbf{\Omega}, \tag{3.18}$$

where $\hat{\mathbf{n}}_\mathbf{j}$ is the unit vector perpendicular to the photosphere in the j-th angular slice. The integral gives time independent projection factors, so they can be computed in advance and used as weighting factors $p_j(\mathbf{w})$:

$$F_\nu(\mathbf{w}, t) = \sum_j p_j(\mathbf{w}) B_\nu\left(T_j(t)\right). \tag{3.19}$$

At any time B_ν is given by:

$$B_\nu = \left(\frac{R_{\rm phot}}{d_{\rm L}}\right)^2 \frac{2h\nu^3}{c^2} \frac{1}{e^{h\nu/(k_{\rm B}T)} - 1}, \tag{3.20}$$

where $d_{\rm L}$ is the luminosity distance, h the Planck constant, ν the considered frequency and $k_{\rm B}$ the Boltzmann constant.

3.2.2 BHNS

Concerning the KN emission from BHNS mergers, the model for the wind and secular ejecta is the same as in the NSNS case. In BHNS mergers, the dynamical ejecta exhibit a distribution close to the equatorial plane, forming a crescent-like geometry. Specifically, they span a region defined by $\theta_{\rm dyn} \sim 0.2 - 0.5$ rad in the latitudinal direction and $\phi_{\rm dyn} \sim \pi$ in the azimuthal direction [163, 108]. Given that in BHNS mergers, the dynamical ejecta are not axisymmetric relative to the direction of the binary's total angular momentum, a different model is required compared to the one adopted for other components. In this work, the semi-analytical model is based on the one presented by Barbieri et al. [44].

In this model the dynamical ejecta mass is assumed to be distributed in velocity space as in equation 3.9. Each dynamical ejecta shell can emit from its latitudinal photosphere or towards the radial photosphere, based on which diffusion time is the shortest. Defining θ as the angle measured from the equatorial plane, dynamical ejecta extend from $\theta = -\theta_{\rm dyn}$ to $\theta = \theta_{\rm dyn}$. The discussion can be limited to the region above the equatorial plane ($\theta > 0$), because the same results hold for the region below. The diffusion time, in the latitudinal direction for photons diffusing upwards in the

shell and produced at an angle θ, can be expressed as:

$$t_{\rm d,lat} \sim \frac{\left(\theta_{\rm dyn}-\theta\right)^2 \kappa_{\rm dyn} dm/dv}{c\theta_{\rm dyn}\phi_{\rm dyn} t}, \tag{3.21}$$

where $\kappa_{\rm dyn}$ is the dynamical ejecta opacity. The diffusion time in the radial direction is given by:

$$t_{\rm d,rad} \sim \frac{\kappa_{\rm dyn} m_{\rm dyn,>v}\left(v_{\rm max}-v\right)}{c\theta_{\rm dyn}\phi_{\rm dyn} v^2 t}. \tag{3.22}$$

The angle $\theta_{\rm lat}(v)$ above which the diffusion time in the latitudinal direction is shorter than that in radial direction is given by:

$$\theta_{\rm lat}\left(v\right) = \theta_{\rm dyn} - \min\left(\theta_{\rm dyn}, \sqrt{\frac{m_{\rm dyn,>v}\left(v_{\rm max}-v\right)}{v^2 dm/dv}}\right). \tag{3.23}$$

By using this angle, three regions can be identified in the ejecta, each one emitting only in the direction for which the diffusion time is the shortest. Two regions emit in the latitudinal direction above and below the equatorial plane (from now on region A and B), while a third one is the region emitting in the radial direction (from now on region C).

Inside region A, the diffusion time is equal to the elapsed time at an angle:

$$\theta_{\rm d}(v,t) = \theta_{\rm dyn} - t\sqrt{\frac{c\theta_{\rm dyn}\phi_{\rm dyn}}{\kappa_{\rm dyn} dm/dv}}. \tag{3.24}$$

Assuming a uniform density distribution in the latitudinal direction and that the nuclear heating energy release that happens above $\theta_{\rm d}$ instantaneously contributes to the latitudinal emission, the latitudinal luminosity per unit velocity can be expressed as:

$$\frac{dL_{\rm lat}}{dv}(v,t) = \frac{1}{2}\dot{\epsilon}(t)\frac{dm}{dv} \times \max\left(1-\frac{\theta_{\rm lat}\left(v\right)}{\theta_{\rm dyn}}, 1-\frac{\theta_{\rm d}(v,t)}{\theta_{\rm dyn}}\right), \tag{3.25}$$

where the factor $1/2$ takes into account that only the region above the equatorial plane has been considered. The latitudinal surface, for a given shell, is

$$\frac{dS_{\rm lat}}{dv}(v,t) = \phi_{\rm dyn}\, v dv t^2, \tag{3.26}$$

while the black-body effective temperature of the latitudinal annulus above the shell is

$$T_{\rm BB,lat}(v,t) = \left(\frac{dL_{\rm lat}/dv}{\sigma_{\rm SB}\left(dS_{\rm lat}/dv\right)}\right)^{1/4}. \tag{3.27}$$

Considering the effect of lanthanides recombination described above, the latitudinal surface effective temperature is:

$$T_{\rm lat}\left(v,t\right) = \max\left(T_{\rm BB,\,lat}\left(v,t\right), T_{\rm La}\right). \tag{3.28}$$

A similar approach can be followed for region C, but the relative speed between the shell and the emitting surface must be considered. The condition for which radiation can escape from a given region is that the radial diffusion speed is larger than the local velocity. This happens beyond a *diffusion velocity* $v_{\rm d}$, obtained through the implicit

equation:

$$t = \sqrt{\frac{\kappa_{\rm dyn} m_{\rm dyn,>v_d}}{\theta_{\rm dyn}\phi_{\rm dyn} v_{\rm d} c}}. \tag{3.29}$$

Thus the radial luminosity is

$$L_{\rm rad}(t) = \dot{\epsilon}(t) m_{\rm rad,>v_d}(t), \tag{3.30}$$

where $m_{\rm rad,>v_d}$ is the mass moving faster than v in region C:

$$m_{\rm rad,>v} = \int_v^{v_{\rm phot}} \frac{\theta_{\rm lat}(v)}{\theta_{\rm dyn}} \frac{dm}{dv} dv. \tag{3.31}$$

The radial emission surface is

$$S_{\rm rad}(t) \sim \phi_{\rm dyn}\theta_{\rm dyn} v_{\rm phot}^2 t^2, \tag{3.32}$$

where the photospheric velocity is obtained by solving

$$\tau = \frac{2}{3} = \frac{\kappa_{\rm dyn} m_{>v_{\rm phot}}}{\theta_{\rm dyn}\phi_{\rm dyn} v_{\rm phot}^2 t^2}. \tag{3.33}$$

The radial photospheric effective temperature is

$$T_{\rm rad}(t) = \max\left[\left(\frac{L_{\rm rad}(t)}{\sigma_{\rm SB} S_{\rm rad}(t)}\right)^{1/4}, T_{\rm La}\right]. \tag{3.34}$$

Assuming that the dynamical ejecta is geometrically thin, for an observer whose line of sight forms an angle $\theta_{\rm v}$ with the polar axis the projection factor for latitudinal emission is:

$$f_{\rm lat} = \cos(\theta_{\rm v}). \tag{3.35}$$

Instead, for radial emission, the projection factor is:

$$f_{\rm rad} = \pi \cos(\theta_{\rm v}) \sin^2(\theta_{\rm dyn}) + 2\sin(\theta_{\rm v})\left[\theta_{\rm dyn} + \sin(\theta_{\rm dyn})\cos(\theta_{\rm dyn})\right]. \tag{3.36}$$

3.3 AT2017gfo

On Aug 17, 2017, several groups of astronomers, from all over the world, who previously signed agreements with the LIGO-Virgo Collaboration to receive alerts about GW candidates, initiated extensive broadband observing campaigns in search for an electromagnetic counterpart to a NSNS merger candidate, GW170817 [9, 11]. The event, whose sky localization was relatively tight thanks to all three GW detectors in the network being online, was particularly interesting also because Fermi/GBM detected a short GRB with a delay of only 1.7 s after the GW signal. Teams worldwide, utilizing both ground- and space-based telescopes, were mobilized to observe the region pinpointed by the GW detection. Positioned in the southern sky, GW170817 was only visible to Chilean telescopes about 10 hours post-merger, making it initially inaccessible to most northern hemisphere telescopes. The One-Meter Two-Hemispheres (1M2H) team was the first to identify and report [84] a bright optical transient in the *i*-band, marking the beginning of a series of observations by various teams within the following hour [11].

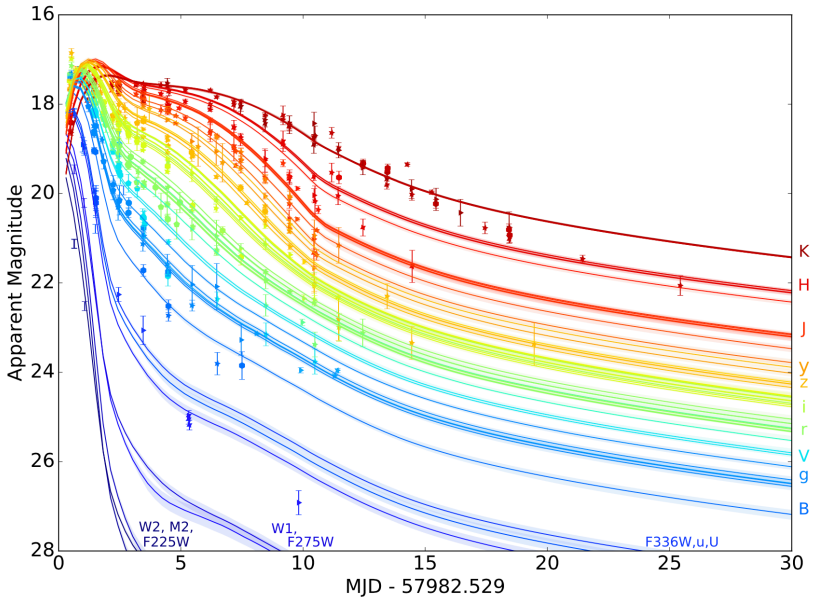

FIGURE 3.1: Ultraviolet, optical, infrared light curves of AT2017gfo from the data set with a best-fit spherically symmetric three-component kilonova model. Credit: [307].

AT2017gfo initially exhibited a distinct blue hue and a featureless thermal spectrum peaking at UV frequencies [215], rapidly evolving over several days to emission dominated by near-infrared (NIR) wavelengths [234]. This rapid color transformation was markedly different from other extragalactic transients, solidifying the link between AT2017gfo and GW170817. By day 2.5, observations indicated separate optical [215] and NIR [75] emission components, with spectra featuring absorption lines around 1.5 and 1.75 μm, associated with light r-process elements such as CsI and TeI [289].

Bolometric luminosity observations of AT2017gfo aligned closely with power-law-like decay predictions for r-process isotopes [197], with required total ejecta mass to match the luminosity falling in the range of $\sim 0.02 - 0.06 M_\odot$. This range aligns with NSNS merger predictions and independent GW170817 modeling estimates.

Fig. 3.1 shows a comprehensive dataset of photometric observations of AT2017gfo compiled by Villar et al. [307], highlighting the rapid fade of blue/UV bands (F225W, F275W) post-11 hours, contrasted by a more gradual decline in NIR bands. The early blue emission suggests the outer ejecta layers comprised light r-process elements with low opacity, synthesized from higher $Y_e \gtrsim 0.25$ ejecta. In contrast, the persistent NIR emission implies inner layers with higher opacity, likely containing lanthanides or actinides [200].

Many groups described AT2017gfo using two or three separate ejecta components with varying lanthanide abundances [230]. For instance, Fig. 3.1 features a best-fit model from [307], combining three spherically symmetric KN models with opacities $\kappa = (0.5, 3, 10)\,\mathrm{cm^2\,g^{-1}}$. The inferred ejecta masses were $M_{\rm ej} \sim 0.02$, 0.047 and 0.011 $M_\odot$ with average velocities $v_{\rm ej} \sim 0.27$, 0.15 and 0.14 c. Most ejecta exhibited intermediate $Y_e \approx 0.25 - 0.35$, leading to nucleosynthesis up to the second r-process peak, with smaller portions reaching either higher or lower Y_e values.

The dynamical ejecta alone are insufficient to account for the observed emission. The bulk of the ejecta, especially the low-Y_e component, is more likely attributed to outflows from the post-merger accretion disk [285, 109]. The source of the early-time blue emission, consistent with shock-heated dynamical ejecta properties, remains

debated.

Chapter 4

Gamma-Ray Bursts

In this Chapter, we delve into the physics of gamma-ray bursts (GRBs). In Section 4.1 we summarize the fundamental concepts on the physics of GRB and the salient moments that led to the discovery of these sources [195, 236]. In Section 4.2 we analyze the necessary conditions in binary mergers to launch a successful relativistic jet, describing also its launch mechanism and structure [44]. In Sections 4.3 and 4.4 we report the GRB prompt and afterglow emission model used in our analysis [44, 43]. Lastly, in Section 4.5 we briefly describe the GRB associated to GW170817 [8]. The first Section is mainly based on the works by Meszaros [195] and Piran [236], while the Sections regarding the model are mainly based on Barbieri et al. [44, 43], Salafia et al. [267, 266] and references therein.

4.1 Background of gamma-ray bursts

4.1.1 Fundamental concepts of GRBs

Gamma-ray bursts (GRBs) are short and intense pulses of gamma-rays. The bursts last from a fraction of a second to several hundred seconds. Their isotropic luminosity of $10^{51} - 10^{52}$ erg/s makes GRBs the most luminous events in the Universe.

GRBs are categorized based on the observed duration of gamma-ray emission into two main types: *short* GRBs (sGRBs), which last less than 2 seconds, and *long* GRBs (LGRBs), characterized by a more prolonged emission. The origin of GRBs lies in the accretion of matter from a disk onto a compact object. Specifically, LGRBs are associated with the core collapse of massive stars, while sGRBs are typically linked to mergers between neutron stars (NSNS) and black hole-neutron star (BHNS) binaries, under certain conditions outlined later. This accretion process results in the creation of a collimated, unsteady, relativistic jet, which can be visualized as a series of shells traveling at varying speeds. In the simplest scenario, when these shells collide, they generate *internal shocks* that transform a portion of the jet kinetic energy into photons. These internal shocks are thought to be responsible for the GRB *prompt emission*, although alternative mechanisms like magnetic reconnection have also been proposed. Following the prompt emission, the relativistic jet expands into the interstellar medium (ISM). This interaction decelerates the jet, leading to the formation of a strong relativistic forward shock that propagates into the ISM, known as the *external shock*. Near this shock, electrons in the ISM are accelerated through the Fermi process, resulting in synchrotron radiation that powers the so-called GRB *afterglow emission*.

The jet's journey, however, begins with its propagation through matter surrounding its birthplace. For LGRBs, the jet pierces through through the dense stellar wind resulting from the core collapse, while in sGRBs, it must pass through ejecta from the merger. A jet that possesses sufficient kinetic energy to break through this surrounding matter is termed a *successful jet*, producing the emissions described above.

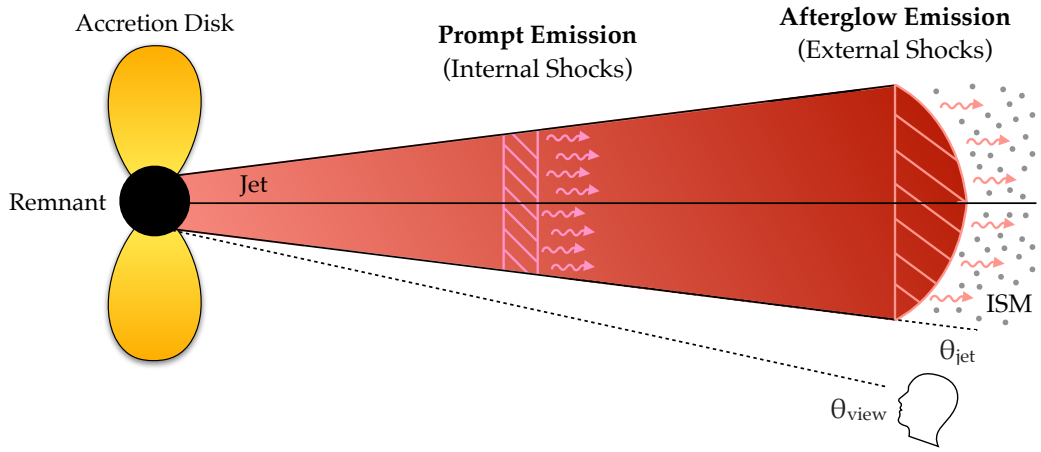

FIGURE 4.1: Schematic representation of a GRB jet. θ_{jet} is the jet half opening angle, while θ_{view} is the viewing angle.

In contrast, a jet that fails to penetrate this matter is known as a *choked jet*, which does not generate GRB emissions.

4.1.2 History of GRBs

GRBs were first detected in 1967 by the Vela satellites, but they were not publicly announced until 1973 [166]. The Vela satellites were carried with all-sky gamma-ray detectors and they were flown by the U.S. Department of Defense to monitor for nuclear explosions which could violate the *Partial Test Ban Treaty*, which prohibited nuclear test explosions in the atmosphere, outer space and underwater. When these gamma-ray flashes were first detected, it was determined that they did not come from the Earth's direction and it was soon realized that they constituted a new class of astrophysical sources and this phenomenon led to a huge interest in all the scientific community.

It was realized that a high spatial and temporal resolution instrument dedicated only to study GRBs was necessary. For this reason, the Compton Gamma-Ray Observatory was launched in 1991 with Burst And Transient Source Experiment (BATSE) on board. The all-sky survey from the BATSE instrument showed that GRBs were isotropically distributed, strongly suggesting their cosmological origin. At cosmological distances, the observed GRB fluxes involved huge energies, which emerged in a small volume in a very short time (due to the the fast time variability). Therefore, the formation of a relativistically expanding fireball was proposed as the main emitting mechanism of GRBs [220, 131].

In 1997 the Italian-Dutch satellite Beppo-SAX detected an X-ray emission associated with a GRB [82], representing the first afterglow detection. This led to the possibility of identifying the candidate host galaxies, measuring redshift distance and confirming that GRBs were cosmological sources [202, 90]. The detection of other GRB afterglows followed in rapid succession, in some cases extending to radio wavelengths [118] and over timescales of months [305]. Sometimes it was possible to identify candidate host galaxies [263]. These studies of afterglows have provided strong confirmation for the fireball model of GRB.

4.1.3 Swift and Fermi

The Swift multi-wavelength afterglow satellite (launched in 2004) brought many advancements in the observation of GRBs, particularly in terms of the enhanced sensitivity of its Burst Alert Telescope (BAT) compared to earlier instruments. Additionally, Swift boasts a rapid response capability, being able to reorient itself within less than 100 seconds towards the location identified by BAT. This quick positioning is performed by detectors with superior angular resolution, namely the X-Ray Telescope (XRT) and the UV-Optical Telescope (UVOT). This satellite achieved the long-awaited purpose of accurately localize afterglows starting about a minute after the burst trigger, in gamma-ray, X-ray and optical bands [124]. This unveiled the previously unexplored afterglow behaviour from minutes to hours, allowing a study of the transition from the prompt emission to the following long term afterglow, discovering a range of X-ray early behaviours.

Over the past ten years, the Fermi satellite has emerged as a pivotal player in the study of GRBs. Launched in 2008, this satellite was specifically engineered to conduct comprehensive gamma-ray observations across the entire sky. The satellite has significantly advanced gamma-ray astronomy through enhancements in angular resolution, effective area, field-of-view, energy resolution and range, and temporal resolution. Onboard, Fermi is equipped with two primary instruments: the Large Area Telescope (LAT) and the Gamma-ray Burst Monitor (GBM). LAT is an imaging gamma-ray detector that operates within the photon energy range of 20 MeV to greater than 300 GeV and captures about 20% of the sky in its field-of-view. GBM, comprising 14 scintillation detectors, is adept at detecting gamma-rays in the energy range of 10 keV to 25 MeV across the entire sky, with the exception of areas blocked by the Earth. Notably, it was the Fermi GBM, in conjunction with the space telescope INTEGRAL, that detected GRB170817A, marking a significant contribution to the emergence of multi-messenger astronomy.

4.2 Relativistic jet

4.2.1 Launch and breakout conditions

Jets launched by NSs have been observed in our galaxy [227, 303]. Several studies have postulated that a rapidly rotating, highly magnetized proto-NS formed from a merger could potentially launch a relativistic jet [198, 210]. Conversely, the neutrino-driven winds [229] and the magnetically-driven winds [77] from a proto-NS during its early evolutionary stages are likely to saturate the surrounding area with an excessive number of baryons. This baryon-rich environment, might hinder any nascent jet from achieving relativistic velocities [76].

At the time of merger, the magnetic field is amplified due to Kelvin-Helmholtz instabilities [164, 27]. If the remnant is a BH, or it collapses into one in a timeframe significantly shorter than the accretion timescale, several processes come into play. The development of a large-scale ordered magnetic field with a significant poloidal component enables the Blandford-Znajek jet-launching mechanism (see next Section) [60] to function.

Given the challenges associated with a proto-NS central engine, this work assumes that for NSNS mergers only a BH remnant, which may or may not evolve through a hypermassive neutron star (HMNS) phase, is capable of launching a relativistic jet. To ensure the formation of a HMNS we can impose a simple condition on the binary

and ejecta masses [136, 67, 270]:

$$M_{\rm rem} = M_1 + M_2 - M_{\rm dyn} - M_{\rm disk} - M_{\rm GW} > 1.2 M_{\rm TOV}, \tag{4.1}$$

where M_1 and M_2 are the masses of the binary components, $M_{\rm dyn}$ is the dynamical ejecta mass, $M_{\rm disk}$ is the disk mass, $M_{\rm GW} = E_{\rm GW}/c^2$ is the mass loss associated to GWs emission with total energy $E_{\rm GW}$ and $M_{\rm TOV}$ is the maximum mass of a non-spinning NS. The latter multiplied by 1.2 represents the maximum mass that can be supported by uniform rotation (the factor 1.2 can be considered independent from the NS EoS [67]). We compute $E_{\rm GW}$ using the public available repository `bns_lum`[1], that implements numerical-relativity fitting formulae from Zappa et al [312], including GW mass loss from the inspiral to the early post-merger phase [270].

Even if the remnant is a BH the jet needs enough energy to successfully break out of the ejecta cloud. Following Duffell et al. [97], we can compare the total jet energy $E_{\rm jet}$ with the minimum energy required for successful breakout $E_{\rm bkt}$, requiring $E_{\rm jet} > E_{\rm bkt}$. Given the initial opening angle of the injected jet $\theta_{\rm jet}$ and the isotropic equivalent kinetic energy of the ejecta $E_{\rm ej}$, we can write $E_{\rm bkt}$ as:

$$E_{\rm bkt} = \kappa E_{\rm ej} \theta_{jet}^2, \tag{4.2}$$

with $\kappa = 0.05$. If the total jet energy is smaller than $E_{\rm bkt}$, all its energy is given to the ejecta.

Obviously, as far as BHNS mergers are concerned, the remnant is always a BH.

4.2.2 Jet launch

When the NS is tidally disrupted and some of the released material forms a disk, its accretion on the remnant can induce the launch of a relativistic jet through the so called Blandford-Znajek mechanism [60, 168], producing a luminosity [296]:

$$L_{\rm BZ} \propto \frac{G^2}{c^3} M_{\rm BH}^2 B^2 \Omega_{\rm H}^2 f\left(\Omega_{\rm H}\right), \tag{4.3}$$

where B is the amplitude of the magnetic field at the BH horizon, $0 \leq \Omega_{\rm H} \leq 1/2$ is the dimensionless angular velocity evaluated at the horizon,

$$\Omega_{\rm H} = \frac{\chi_{\rm BH}}{2(1+\sqrt{1-\chi_{\rm BH}^2})}, \tag{4.4}$$

and $f\left(\Omega_{\rm H}\right) = 1 + 1.38\Omega_{\rm H}^2 - 9.2\Omega_{\rm H}^4$ is a correction for high-spin values. For NSNS we compute the remnant spin following Zappa et al. [312], while for BHNS we follow Pannarale et al. [223] (see their equation 11).

After the merger, the magnetic field B can be amplified by Kelvin-Helmholtz and magneto-rotational instabilities up to a given fraction of the rest mass energy density of the disk [127] and we can write:

$$B^2 \propto \frac{c^5}{G^2} \dot{M} M_{\rm BH}^{-2}, \tag{4.5}$$

[1] https://git.tpi.uni-jena.de/core/bns_lum

with $\dot{M}$ the rate of mass accretion on the remnant BH. Then it follows:

$$L_{\rm BZ} \propto \dot{M} c^2 \Omega_{\rm H}^2 f\left(\Omega_{\rm H}\right), \tag{4.6}$$

where the scaling is consistent with general-relativistic hydrodynamic (GRHD) simulations of compact binary mergers where a jet is launched [281].

The jet kinetic energy is:

$$E_{\rm jet} = L_{\rm BZ} \times t_{\rm acc}, \tag{4.7}$$

with $t_{\rm acc}$ the duration of disk accretion,

$$t_{\rm acc} = \left(1 - \xi_{\rm w} - \xi_{\rm s}\right) M_{\rm disk} / \dot{M}. \tag{4.8}$$

$\xi_{\rm w}$ and $\xi_{\rm s}$ represent the fraction of the disk mass lost in wind and secular ejecta. Therefore

$$E_{\rm jet,0} = \epsilon \left(1 - \xi_{\rm w} - \xi_{\rm s}\right) M_{\rm disc} c^2 \Omega_{\rm H}^2 f\left(\Omega_{\rm H}\right), \tag{4.9}$$

where ϵ is a dimensionless constant, fixed by imposing the accretion-to-jet energy conversion efficiency $\eta = \epsilon\, \Omega_{\rm H}^2 f(\Omega_{\rm H})$ to be $\eta = 10^{-3}$ when $\chi_{\rm BH} = 0.71$, therefore matching the inferred efficiency in GW170817 [264]. This leads to $\epsilon = 0.022$.

Part of this energy is spent by the jet in its propagation through the ejecta cloud as explained before. If $E_{\rm jet,0} \leq E_{\rm bkt}$, where $E_{\rm bkt}$ is defined by (4.2), we consider the jet to be choked during the propagation and we neglect its emission; otherwise, we assume the jet to successfully break out, with an available energy $E_{\rm jet} = E_{\rm jet,0} - E_{\rm bkt}$.

4.2.3 Jet structure

We assume jets that successfully break out to be endowed with a jet structure (angular energy and bulk Lorentz factor profiles) featuring a uniform core of half-opening angle $\theta_{\rm j}$, surrounded by "wings" with power-law decreasing energy density and Lorentz factor. Explicitly

$$\frac{dE}{d\Omega}(\theta) = \frac{\epsilon_{\rm c}}{1 + (\theta/\theta_{\rm j})^{s_{\rm E}}}, \tag{4.10}$$

$$\Gamma(\theta) = 1 + \frac{\Gamma_{\rm c} - 1}{1 + (\theta/\theta_{\rm j})^{s_\Gamma}}, \tag{4.11}$$

where $\epsilon_{\rm c} = (E_{\rm jet} - E_{\rm bkt})/\pi\theta_{\rm c}^2$ is the core energy per unit solid angle and $\Gamma_{\rm c}$ is the core Lorentz factor. We keep the structure parameters identical across the population, fixing $\theta_j = 3.4^\circ$, $s_{\rm E} = 5.5$, $\Gamma_{\rm c} = 251$ and $s_\Gamma = 3.5$, which are the best-fit values for the GRB170817A afterglow from Ghirlanda et al. [125].

It is crucial to recognize that the typical structures of jets from NSNS and BHNS mergers could potentially differ. This variation primarily arises from the different environments in which the jets are launched. Specifically, the process of jet self-collimation, which involves the formation of a hot, over-pressured cocoon, might be less effective in BHNS post-merger systems. This is due to the comparatively lower density expected in the polar region of a BHNS system, as compared to a NSNS system [144, 133, 269].

In NSNS systems, the collision of the two stars typically results in shock-driven ejecta, leading to a more isotropic distribution of dynamical ejecta, as opposed to the BHNS scenario. The latter, according to Foucart et al. [114], primarily produces dynamical ejecta near the equatorial plane due to the tidal disruption of the neutron star, as evidenced in studies like Kawaguchi et al. [163]. Additionally, the intermediate

state of a supra-massive (SMNS) or HMNS in NSNS mergers, known for generating strong post-merger winds [108], is absent in BHNS mergers. Therefore, in this work, a larger jet half-opening angle, $\theta_c = 15°$, is also considered as a second variation for the jet structure in BHNSs, to account for these differences. Figure 4.2 shows the rest-frame SED peak photon energy $E_{\rm peak}$ (left panel) and the isotropic-equivalent energy $E_{\rm iso}$ (right panel) as functions of the viewing angle θ_v, for the two assumptions on the jet half-opening angle.

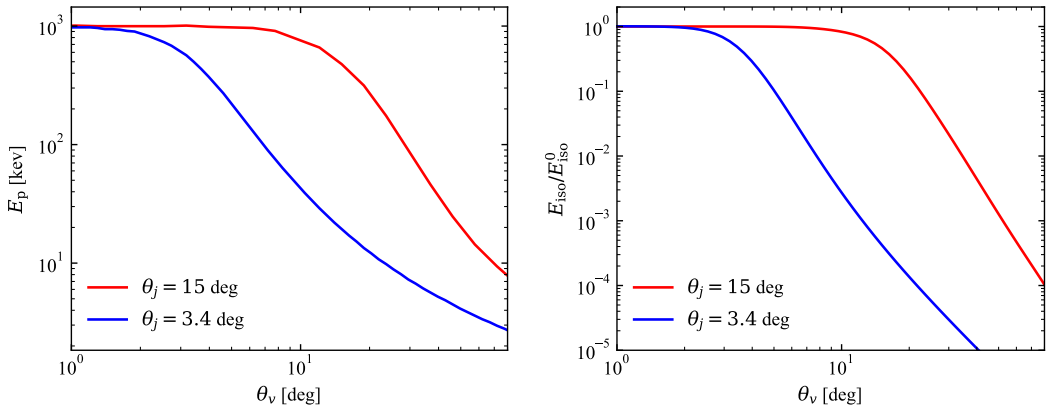

FIGURE 4.2: Rest-frame SED peak photon energy $E_{\rm peak}$ (left panel) and isotropic-equivalent energy $E_{\rm iso}$ normalized to the value $E^0_{\rm iso}$ measured by an on-axis observer (right panel), as functions of the viewing angle θ_v. Blue and red colors refer to a different assumption on the jet half-opening angle, $\theta_j = 3.4°$ and $\theta_j = 15°$, respectively.

4.3 GRB prompt model

We compute the prompt emission spectrum following Salafia et al. [267, 266], assuming the conversion efficiency of jet energy into radiation to be $\eta_\gamma = 0.15$ in regions of the jet with $\Gamma \geq 10$, and zero otherwise. The isotropic equivalent specific luminosity at observer frequency ν, as measured by an observer who sees the jet under a viewing angle $\theta_{\rm v}$, and under the assumption of a viewing-angle-independent emission duration T, is then given by Salafia et al. [267]

$$L_\nu, {\rm iso}(\nu, \theta_v) = \frac{\eta_\gamma}{T} \int_0^{\theta_\gamma} \sin\theta \, {\rm d}\theta \int_0^{2\pi} {\rm d}\phi \, S_{\nu'}(\nu(1+z)/\delta) \frac{\delta^2}{\Gamma} \frac{{\rm d}E}{{\rm d}\Omega}, \tag{4.12}$$

where z is the source redshift, θ_γ is the angle such that $\Gamma(\theta_\gamma) = 10$ (which is $\theta_\gamma = 8.7°$ with our parameters), δ is the relativistic Doppler factor of material located at spherical angular coordinates (θ, ϕ), and $S_{\nu'}$ is the comoving spectral shape, which we assume to be a power law with an exponential cut-off, $S_{\nu'} \propto (\nu')^a \exp\left[-(1+a)\nu'/\nu'_{\rm p}\right]$, with $a = 0.24$ and $h\nu'_{\rm p} = 3\,{\rm keV}$ (h here is Planck's constant), similarly as in [266], and the normalization is such that $\int S_{\nu'} d\nu' = 1$.

From the specific luminosity we obtain the photon flux in the $[h\nu_0, h\nu_1]$ observing band as

$$p_{[h\nu_0, h\nu_1]} = \frac{1}{4\pi d_{\rm L}^2} \int_{\nu_0}^{\nu_1} \frac{L_{\nu,{\rm iso}}(\nu(1+z))}{h\nu(1+z)} {\rm d}\nu, \tag{4.13}$$

where d_L is the source luminosity distance. Figure 4.3 shows the inverse cumulative distributions of photon fluxes in the [10,1000] keV (blue) and [15,150] keV (red) bands

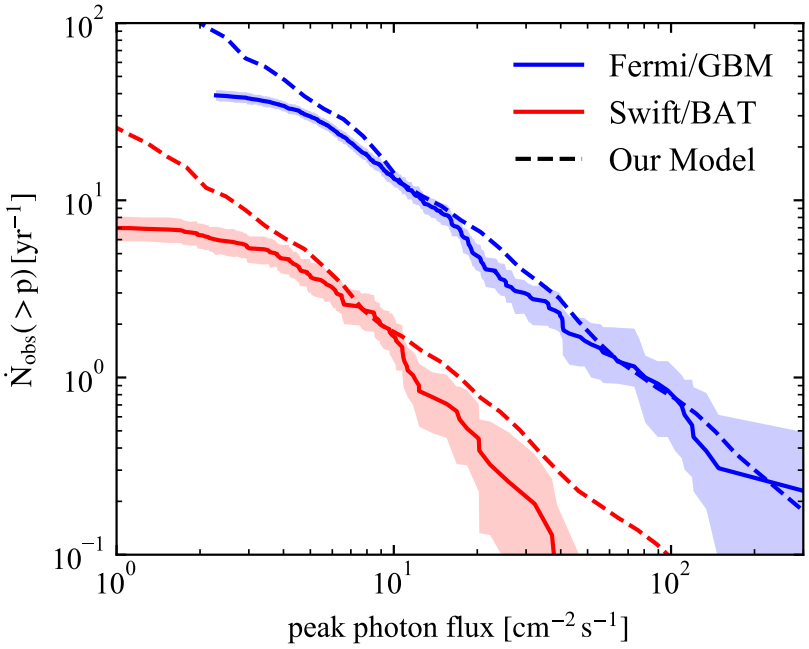

FIGURE 4.3: *Fermi*/GBM (*Swift*/BAT) observed inverse cumulative distribution of 64ms (20ms)-binned photon fluxes in the 10–1000 (15–150) keV band (the colored band shows the 90% confidence band due to Poisson and measurement uncertainties) compared with our model (dashed line).

for our population (dashed lines), and the corresponding distributions for short GRBs observed by *Fermi*/GBM and *Swift*/BAT, respectively (solid lines, with the shaded area showing the 90% confidence regions, including both measurement uncertainties and Poisson count statistics) (see [78]). The distributions for our model are computed accounting for the duty cycle and field of view factors for each instrument, for a fair comparison.

4.3.1 Cocoon shock breakout

As the jet head progresses, it pushes aside the ambient material it encounters. This action creates an over-pressured region around the jet, commonly referred to as a *cocoon*. This cocoon is a critical aspect of the jet's structure and dynamics, playing a significant role in the jet's evolution and interaction with its surroundings.

The cocoon around a jet can originate from two distinct scenarios. First, it may be formed by a choked jet that fails to produce a sGRB in any direction. Alternatively, a cocoon can also be generated by a successful jet, one that does create a regular sGRB. In this latter case, the sGRB is emitted along the system's axis, but in a direction that points away from us, rendering it undetectable from our vantage point [135, 265].

To account for the contribution of a putative shock breakout emission component, for viewing angles $\theta_v < 60^\circ$ we include an additional emission component with identical properties as GRB170817A, namely an isotropic-equivalent luminosity $L_{iso} = 10^{47}$ erg/s and a cut-off power law spectrum (same shape as the assumed prompt emission spectrum) with $h\nu_p = E_{peak} = 185$ keV and $a = 0.38$ [19].

4.4 GRB afterglow model

As already mentioned, after the prompt emission the jet expands into the ISM, starting to decelerate when it has swept a quantity of material whose rest mass energy times the jet Lorentz factor squared is comparable to its kinetic energy. This provokes the formation of a strong forward shock (*external shock*). ISM electrons are accelerated, near the shock, producing synchrotron radiation, that is the source of the GRB afterglow emission. Behind the forward shock, in the so called *downstream region*, electrons are accelerated through the Fermi process resulting in a non-thermal energy distribution, that is generally represented by a power-law of index p. We assume $p = 2.3$, following Fermi acceleration simulations in weakly magnetised relativistic shocks [287]. We can obtain the total energy density behind the shock using shock jump conditions from [59]. We consider that a fraction ϵ_e of this energy is given to the electrons and that a fraction ϵ_B is given to the magnetic field. A typical value for ϵ_e seems to be ~ 0.1 according to analysis of radio-to-GeV emission energy ratio in LGRBs [53, 212]. Instead ϵ_B lies in the range $10^{-4} - 10^{-1}$ [52, 140]. The forward shock dynamics and its synchrotron emission can be calculated with the model used in [266], based on [85, 125]. Following [222] we can also compute the synchrotron self-absorption. We consider a constant ISM density $n = 10^{-3}\,\mathrm{cm}^{-3}$, consistent with the analysis of GRB 170817A and SGRBs with a modelled afterglow emission [112].

4.4.1 Dynamics

Let us consider a jet whose axis is aligned with the z axis of a spherical coordinate system. θ and ϕ are respectively the latitudinal and azimuthal angles. We define the viewing angle θ_v as the angle between the observer's line of sight and the jet axis. We also define *annulus* each jet's head sub-region with latitudinal angle lying in the range $[\theta, \theta + d\theta]$. We do not consider energy exchanges among adjacent annuli, that would result in lateral expansion. Therefore we assume the annuli to be independent from each other. For each annulus the kinetic energy per unit solid angle and initial Lorentz factor are $dE/d\Omega$ and $\Gamma(0, \theta)$. The ISM mass per unit solid angle that the shock has swept per unit solid angle as a function of the distance from the jet's launch site is:

$$\mu(R) = \frac{R^3}{3} n m_p, \tag{4.14}$$

where m_p is the proton mass assuming the ISM to be composed of hydrogen only. Following [138, 222] and imposing energy conservation, we evaluate the shock dynamics, resulting in a Lorentz factor of material right behind the shock that evolves as

$$\Gamma(R, \theta) = \frac{\mu_0}{2\mu} \left[\sqrt{1 + \frac{4\mu \left(dE/d\Omega c^{-2} + \mu + \mu_0 \right)}{\mu_0^2}} - 1 \right], \tag{4.15}$$

where μ_0 is defined as

$$\mu_0(\theta) = \frac{dE/d\Omega(0, \theta)}{\Gamma(0, \theta) c^2}. \tag{4.16}$$

The shocked material lies behind the shock in a thin layer [59]. If we assume a uniform density distribution in the radial direction inside this layer, it is possible to compute its thickness ΔR using electron number conservation. Imposing shock jump conditions from [59] the number density of electrons in the shocked region is then

given by:

$$n_{\rm s} = n\frac{\gamma_{\rm a}\Gamma + 1}{\gamma_{\rm a} - 1}, \tag{4.17}$$

where $\gamma_{\rm a}$ is the post-shock adiabatic index [228]. Therefore the thickness ΔR is:

$$\Delta R = \frac{R\left(\gamma_{\rm a} - 1\right)}{3\left(\gamma_{\rm a}\Gamma + 1\right)\Gamma}. \tag{4.18}$$

The forward shock is faster than the shocked material, thus the tickness ΔR increases. The relation between the forward shock Lorentz factor $\Gamma_{\rm s}$ and Γ [59] is:

$$\Gamma_{\rm s} = \left[\gamma_{\rm a}(\Gamma - 1) + 1\right]\sqrt{\frac{\Gamma + 1}{\gamma_{\rm a}\left(2 - \gamma_{\rm a}\right)\left(\Gamma - 1\right) + 2}}. \tag{4.19}$$

Photons emitted at a given time in the shocked region are detected by the observer at different times. If we consider that the emitting region thickness is small with respect to the radius ($\Delta R \ll R$), then we can assume that photons are emitted from the shock surface. The photon arrival time is then given by:

$$t_{\rm obs}\left(R, \theta_{\rm v}, \theta, \phi\right) = (1 + z)\int_0^R \frac{1 - \beta_{\rm s}\cos\alpha}{\beta_{\rm s} c} dR, \tag{4.20}$$

where $\beta_{\rm s} = \sqrt{1 - \Gamma_{\rm s}^{-2}}$ is the shock velocity, z is the redshift and α is the angle between the observer line of sight and the unit vector perpendicular to the surface element, that is $\cos\alpha = \cos\theta\cos\theta_\nu + \sin\theta\sin\phi\sin\theta_\nu$. The shock surface brightness is given by:

$$I_\nu(\nu, \theta, \phi, R) = \Delta R' j'_{\nu'}(\nu/\delta)\delta^3, \tag{4.21}$$

with primed quantities calculated in the comoving frame, $j'_{\nu'}$ is the synchrotron emissivity (see the following subsection), and $\Delta R' = \Gamma(R, \theta)\Delta R$. The term $\delta\left(R, \theta_{\rm v}, \theta, \phi\right) = 1/\left\{\Gamma(R, \theta)[1 - \beta(R, \theta)\cos\alpha]\right\}$ is the Doppler factor of the shocked material.

Let us divide the jet emitting surface in sub-regions and consider N bins for the latitudinal angle θ in the range $[10^{-4}, \pi/2]$ and M bins for the azimuthal angle ϕ in the range $[-\pi/2, \pi/2]$. We calculate the emission only from one half of the surface, because the contribution from the other half is the same for symmetry. For each sub-region we compute I_υ at radii that correspond to a given $t_{\rm obs}$. Inverting equation (4.20) we can evaluate these radii $R\left(\theta, \phi, t_{\rm obs}\right)$. We obtain the total flux density at time $t_{\rm obs}$ by integrating over θ and ϕ:

$$F_\nu\left(\nu, t_{\rm obs}\right) = 2\frac{1 + z}{d_1^2}\int_0^1 d\cos\theta \int_{-\pi/2}^{\pi/2} d\phi R^2 I_\nu(\nu(1 + z), R), \tag{4.22}$$

where the factor 2 is due to the symmetry argument.

4.4.2 Radiation

We follow a shocked material synchrotron emission model described in [222, 274]. We assume that the forward shock accelerates the ISM electrons generating a power law γ distribution:

$$\frac{dn_{\rm s}}{d\gamma} \propto \gamma^{-p}, \tag{4.23}$$

with $p > 2$. As already mentioned, we assume that a fraction ϵ_e of the total energy density e behind the shock is given to the electrons:

$$e_e = \epsilon_e e = \epsilon_e(\Gamma - 1) n_s m_p c^2. \tag{4.24}$$

We can then define the minimum electron Lorentz factor [274] as:

$$\gamma_m = \max\left[1, \frac{p-2}{p-1}(\Gamma - 1)\frac{m_p}{m_e}\right], \tag{4.25}$$

where m_e is the electron mass. The γ distribution is a decreasing power law, so the majority of electrons have $\gamma = \gamma_m$. Before the shock the magnetic field is amplified by small-scale instabilities. The magnetic energy density e_B can be expressed as a fraction ϵ_B of the total energy density e:

$$e_B = \frac{B^2}{8\pi} = \epsilon_B e. \tag{4.26}$$

Following [304, 287] we evaluate the peak synchrotron emissivity of electrons *downstream*, in the comoving frame:

$$j'_{\nu',\max} \approx 0.66 \frac{q_e^3}{m_e^2 c^4} \frac{p-2}{3p-1} \frac{B\epsilon_e e}{\gamma_m}, \tag{4.27}$$

where q_e is the electron charge. Using (4.21) we can write the surface brightness:

$$I_\nu(\nu) = \delta^3 \Delta R' j'_{\nu',\max} S\left(\nu'\right), \tag{4.28}$$

with $\nu' = \nu/\delta$ and $S\left(\nu'\right)$ the normalized spectral shape. $S\left(v'\right)$ can be evaluated as a sequence of power laws, including all spectral orderings [139]. The different power laws are connected at break frequencies: ν_m, ν_c, ν_a and ν_{ac}. ν_m is the synchrotron frequency related to γ_m,

$$\nu_m = \frac{\gamma_m^2 q_e B}{2\pi m_e c}. \tag{4.29}$$

ν_c is the synchrotron frequency related to γ_c, the electron Lorentz factor above which they loose energy through synchrotron emission on a timescale shorter than the dynamical timescale of expansion,

$$\gamma_c = \frac{6\pi m_e c^2 T\beta}{\sigma_T B^2 R}, \tag{4.30}$$

where σ_T is the Thomson cross section.

When $\nu_m < \nu_c$ most of the electrons have a Lorentz factor smaller than γ_c, thus their synchrotron emission energy loss occurs on a timescale larger than the expansion timescale (*slow cooling* regime). Instead when $\nu_m > \nu_c$ the electrons loose their energy faster than their expansion, the shocked region is refilled with fresh electrons (*fast cooling* regime). Before leaving the shocked region in free-free transitions, emitted photons can be re-absorbed by electrons (synchrotron self-absorption). Below the frequency ν_a the emission is self-absorbed [222].

4.5 GRB 170817A

The initial announcement of GRB 170817A was issued through a Gamma-ray Coordinates Network (GCN) Notice, automatically generated by *Fermi*-GBM at 12:41:20 UTC, approximately 14 seconds after the GRB detection at $T_0 = 12:41:06$ UTC. This GRB was also detected by the *International Gamma-Ray Astrophysics Laboratory* (*INTEGRAL*) spacecraft using the Anti-Coincidence Shield (ACS) of the spectrometer of *INTEGRAL* (SPI), prompted by an offline search triggered by the LIGO-Virgo and *Fermi*-GBM reports. The last *Fermi*-GBM localization placed GRB 170817A at $\alpha(\text{J2000.0}) = 12^{\text{h}}28^{\text{m}}$, $\delta(\text{J2000.0}) = -30^{\circ}$, covering a 90% probability region of $\sim 1100\,\text{deg}^2$ [128]. The time difference between the merger and GRB was $T_0 - t_c = 1.734 \pm 0.054$s [8]. The discrepancy in gamma-ray signal arrival times between *Fermi*-GBM and *INTEGRAL* SPI-ACS provided additional constraints on the gamma-ray localization area. The interplanetary network (IPN) localization will be crucial for future GW events that may not be well-localized by LIGO-Virgo.

Follow-up analyses of the *Fermi*-GBM trigger determined the burst duration, $T_{90} = 2.0 \pm 0.5\,\text{s}$, where T_{90} is the time interval over which 90% of the burst's fluence is accumulated in the 50-300 keV range. Based on the T_{90} measurement, GRB 170817A was classified as a sGRB, with 3:1 odds against being a LGRB. This classification is reinforced by considering the burst's hardness ratio compared to the *Fermi*-GBM catalog [128]. The SPI-ACS recorded duration for GRB 170817A of 100 ms aligns with a sGRB classification within its historical sample [276]. The sGRB peaked at 64 ms with a photon flux of 3.7 ± 0.9 photons $\text{s}^{-1}\text{cm}^{-2}$ and a T_{90} fluence of $(2.8 \pm 0.2) \times 10^{-7}$ erg cm^{-2}. GRB 170817A is the closest observed sGRB with a measured redshift. A detailed analysis of the *Fermi*-GBM data for GRB 170817A identified two components: a main pulse from $T_0 - 0.320\,\text{s}$ to $T_0 + 0.256\,\text{s}$, followed by a weaker tail starting at $T_0 + 0.832\,\text{s}$ and extending to $T_0 + 1.984\,\text{s}$. The main pulse's spectrum is best described by a Comptonized function (a power law with an exponential cutoff) with a photon index of -0.62 ± 0.40, peak energy $E_{\text{peak}} = 185 \pm 62\,\text{keV}$, and a time-averaged flux of $(3.1 \pm 0.7) \cdot 10^{-7}$ erg $\text{cm}^{-2}\text{s}^{-1}$. The tail, consistent in location with both the main pulse and GW position, contributed 34% of the main pulse's fluence and exhibited a softer, blackbody spectrum with $kT = 10.3 \pm 1.5\,\text{keV}$ [128].

The *Fermi*-GBM spectral parameters of the main peak and T_{90} interval were used to estimate the integrated fluence measured by *INTEGRAL* SPI-ACS as $(1.4 \pm 0.4) \cdot 10^{-7}\text{erg}\,\text{cm}^{-2}$.

X-ray and radio observations of GRB afterglows play a crucial role in constraining the outflow geometry, energy output, and system orientation relative to the observer's line of sight. The first targeted X-ray observations of GW170817, conducted by the X-Ray Telescope on the *Swift* satellite ($T_0 + 0.62$ days), did not detect any emission. *Swift* was succeeded by follow-up observations from *INTEGRAL* and *Chandra*. Nine days after the trigger, [298] detected a significant X-ray counterpart with *Chandra*, coinciding with the optical/IR counterpart's position. The first radio detection was achieved by the Very Large Array (VLA) on September 2 and 3, 2017, at two different frequencies ($\approx$3 GHz and $\approx$6 GHz) through two independent observations [207]. Subsequent repeated detections across multiple frequencies confirmed an evolving transient [142].

The observed X-rays and radio emissions were characterized by a non-thermal spectrum, following a single power-law across more than eight orders of magnitude in frequency. This suggested a common origin for the emissions, consistent with an afterglow produced by a relativistic jet. Continuous monitoring revealed an unusual increase in afterglow luminosity over time, deviating from the typical behavior of

GRBs. This observation led to the exclusion of simple models such as the off-axis jet and isotropic fireball [208]. Late-time radio observations ($\sim$ 200 days post-event) of the GRB afterglow by [125] provided insights into the apparent source size. Their findings indicated that GW170817 resulted in a structured relativistic jet [266].

Chapter 5

Multi-Messenger Observations of Binary Neutron Star Mergers in the O4 and O5 Runs

This Chapter is primarily a copy of the original publication [78], with an additional section regarding prospects for the O5 run. The main change from the original paper is that the gravitational wave model is now based on a different software for consistency with subsequent Chapters, as specified in the text. This results in only minor variations in the rates, and the key points of the work remain unchanged. Some plots have been modified to provide more information or for consistency with other Chapters. A detailed description of the population used can be found in Appendix A.

5.1 Introduction

The second generation of gravitational wave detectors – now including the Advanced Laser Interferometer Gravitational-Wave Observatory (LIGO, [1]), Advanced Virgo [24] and, starting with the third observing run O3, KAGRA [38] – led to a revolution in our capability to listen to the Universe, that started with the discovery of GW150914 [12], the first compact binary coalescence (CBC) detected in gravitational waves (GWs). During the first three observing runs (O1, O2 and O3 – [5, 15, 17]), the network, operated by the LIGO, Virgo and KAGRA (LVK) Collaborations, detected ninety significant ($p_{\rm astro} > 0.5$) events comprising signals from merging binary black holes (BHBH, the vast majority), binary neutron stars (NSNS, with only two confident identifications) and even black hole-neutron star (BHNS) coalescences [18, 17]. The latter detections, performed during the second part of O3, marked the first ever observation of this new type of sources. So far, electromagnetic (EM) emission was observed only in association to the NSNS merger GW170817 [6]. Thanks to Advanced Virgo joining the network shortly before, GW170817 was localized in the sky within an area of 28 deg^2 (at 90% credible level, high-latency – [306]; [6]). Remarkably, the localisation was consistent with that of GRB170817A, a short gamma-ray burst (GRB) detected by Fermi and INTEGRAL [8] two seconds after the GW170817 chirp. Telescopes all over the world soon discovered an intrinsically faint, rapidly evolving optical/near-infrared transient in a nearby galaxy within the GW170817 localisation error box [84], which was then spectroscopically classified [234] as a kilonova (KN), that is, quasi-thermal emission from the expanding ejecta produced during and after the merger, powered by the nuclear decay of heavy elements synthesized by rapid neutron capture. In the second week after the merger an additional, broadband (radio to X-rays), non-thermal source was detected at the same position: after a few months, the debate about the nature of the source was settled by very long

baseline interferometry observations [208, 125], which provided conclusive evidence in support of its interpretation as the afterglow of a relativistic jet seen off-axis.

The O3 observing run did not see any new EM counterpart detection (except for a controversial association to the BHBH merger GW190521, see [137]), despite the significant increase in sensitivity. The EM follow up campaigns in response to potentially EM-bright O3 events proved generally difficult, in some cases due to the poor sky localisation of the GW signal (e.g. in the case of GW190425, [4]) or to the relatively large distance (e.g. GW190814, for which the non-detection of an EM counterpart did not lead to strong constraints on the progenitor – see for example [26] – despite the good localisation and the massive observational effort).

The fourth observing run (O4)[1] started in May 2023. The first half of the run O4a ended on January 16th and the second half O4b is currently expected to begin on April 10, 2024. The improvements in the sensitivity of the LIGO Hanford and Livingston, Virgo and KAGRA (LVK) interferometers will let us explore a wider volume of the Universe, with a large predicted increase in the detection rate with respect to O3 [14, 233]. The optimisation of EM follow-up strategies will be fundamental in order to enhance the probability of discovering rapidly fading transients in association to these detections. Indications about the predicted GW and EM properties of the population accessible during O4 would be extremely valuable to this task (see [41] for an application using the expected kilonova light curve range).

In this Chapter we present our predictions[2] for the observational appearance of the EM emission associated to NSNS mergers that will be detected during O4, focusing on KN and jet-related emission. For completeness, we also provide a brief description of the prospects for the O5 run, although the start date and operational detectors are still subject to discussion[3]. To this purpose, we built a synthetic population of merging NSNS binaries, with a mass distribution informed by both GW and Galactic NSNS binaries (see Appendix A.1.1), and computed the expected properties of their ejecta and accretion disks through numerical-relativity-informed fitting formulae. Using these properties as inputs, we then computed the observable properties of their associated KN, GRB prompt and GRB afterglow emission through a suite of semi-analytical models, updating the methodology described in [44]. This allowed us to construct the distributions of the EM observables for O4 and O5 GW-detectable events, and to address a number of fundamental questions, such as: *what is the fraction of NSNS mergers that produce an EM counterpart? Which counterpart is best detected in wide-area surveys or in targeted observations? How diverse is the kilonova emission in terms of brightness and other properties? How long after the merger do we expect the detection of most of the GRB afterglows in the radio, optical and X-ray bands?*

5.2 Observing scenarios and detection limits

We consider two representative sets of detection limits (see Table 5.1) based on the typical depth that can be reached during an EM follow up in response to a GW alert. In particular, the 'counterpart search' set is representative of the search for an EM counterpart over the GW localization volume (or of online triggering algorithms in the case of space-based gamma-ray detectors), while the 'candidate monitoring' set

[1] https://observing.docs.ligo.org/plan/

[2] When needed, in this work we assume a ΛCDM cosmology, with Planck Collaboration et al. [237] parameter, namely $\Omega_M = 0.3065$, $\Omega_\lambda = 0.6935$, $\Omega_k = 0.005$, $h = 0.679$. Errors due to the uncertainty in cosmological parameters are negligible in comparison to intrinsic rate density uncertainties and modelling systematics.

[3] https://observing.docs.ligo.org/plan/

consists of deeper limits typical of the monitoring of a candidate counterpart with arc-second localisation (or of off-line sub-threshold searches in gamma-ray detector data). In addition to discussing the expected rates of GW+EM events that exceed (some combinations of) these limits, we also briefly discuss the prospects for joint GW+EM detections in off-line sub-threshold searches in GW data triggered, for example, by a GRB detection by an EM facility [we call this a 'sub-threshold GW search', see e.g. 3].

LVK [14] predicted an optimistic 90% credible O4 GW localization area of 33^{+5}_{-5} deg^2 assuming a LVK network configuration, while Petrov et al. [233] proposed a higher and more realistic value of 1820^{+190}_{-170} deg^2, considering a different minimum number of detectors and a different minimum signal-to-noise ratio (S/N) threshold (based on O3 public alerts). Given these expected GW localization areas in O4, optical/infrared counterpart searches covering a significant fraction of the localization probability will be only feasible with large, wide-field telescopes or in a galaxy-targeted approach with smaller facilities. In both cases, the typical realistic depth of EM counterpart search observations is down to 21 – 22 AB magnitudes in the J, z, g bands [e.g. 83, 26], in part limited by the availability of deep templates. Radio telescopes with a sufficiently fast survey speed can conduct searches for an EM counterpart over a significant fraction of the GW error box [91], either by means of an unbiased survey of the area or by preferentially targeting galaxies, realistically reaching detection limits of 0.1 mJy at a representative frequency of 1.4 GHz [e.g. 92, 28]; X-ray searches have been attempted with the Neil Gehrlels *Swift* Observatory [221] and typically reached a 10^{-13} erg cm^{-2} s^{-1} keV^{-1} limiting flux at 1 keV. Despite not representing technically a search, we include in this category the gamma-ray sky monitoring by *Fermi*/GBM and *Swift*/BAT, with representative 64-ms peak photon flux limits of 4 and 3.5 ph cm^{-2} s^{-1} (these limits are based on a visual comparison of the flux distribution predicted by our model with those observed by these instruments, see Figure 4.3 in Chapter 4).

Once a promising candidate is localized with arc-second accuracy, longer exposures become feasible, and deeper limits can be reached: our deeper 'candidate monitoring' detection limit set assumes a detection to be possible down to 28 AB magnitudes in the J, z, g bands, representative of deep space-based observations or of ground-based ones with large adaptive-optics-equipped facilities [e.g. 184]; in X-rays down to 10^{-15} erg cm^{-2} s^{-1} keV^{-1} at 1 keV, representative of the limits that can be reached by *Chandra* or XMM-Newton with long ($\gtrsim 10^4$ s) exposures [e.g. 192, 85]; in radio down to 10 μJy, representative of limits that can be reached after hour-long exposures with a large facility such as the Karl Jansky Very Large Array [e.g. 142]. We also include in this category the off-line, sub-threshold detection of gamma-ray emission by *Fermi*/GBM and *Swift*/BAT, with a representative flux limit of 1 ph cm^{-2} s^{-1}, for both.

Based on the above considerations, we defined the set of representative detection limits given in Table 5.1. For the GW detection, we assumed a network S/N threshold $S/N_{net} \geq 12$ (see next sub-section for the definition) for a confident detection, following [14]. They also assume an S/N threshold larger than 4 in at least two detectors, but this condition would decrease our rate of about 0.1%. We also tested the condition that the S/N of each single detector should be at least larger than 5, resulting in a decreasing of the rate lower than 5%. For the sub-threshold GW search we assume a less stringent $S/N_{net} \geq 6$.

5.3 GW-EM population model

Our synthetic cosmological population of NSNS mergers is characterized by power-law chirp mass and mass ratio probability distributions, assumed independent and fitted to currently available observational constraints from both GW-detected and Galactic NSNS binaries (see Appendix A.1.1). We assumed a cosmic merger rate density (Appendix A.1.2) obtained by convolving a simple $P(t_{\rm d}) \propto t_{\rm d}^{-1}$ delay time distribution (here $t_{\rm d}$ represents the delay between the formation of the binary and its GW-driven merger), with a minimum delay $t_{\rm d,min} = 50\,{\rm Myr}$, with the cosmic star formation rate from Madau and Dickinson [185], and normalized (see Appendix A.1.3) to a local rate density $R_0 = 347^{+536}_{-256}\,{\rm Gpc^{-3}\,yr^{-1}}$ to self-consistently reproduce the actual number of significant NSNS mergers observed so far [17]. For each event we computed the expected S/N in the LIGO[4], Virgo[5] and KAGRA[6] detectors with the projected O4 [7] and O5 (including LIGO-India) sensitivities, adopting the `IMRPhenomD_NRTidalv2` waveform model through the software package `GWFAST`[8] [154] to model the GW signal [14], and computed the network S/N following (1.40). We performed the analyses with the inclusion of a 70% uncorrelated duty cycle for each detector. Only the LIGO Hanford and Livingston detectors were operational in O4a, with a BNS range between 140 and 170 Mpc. Virgo is expected to join the network in O4b, with a target sensitivity of 40-80 Mpc. KAGRA will join the run in the spring of 2024, featuring a BNS range of approximately 10 Mpc [9]. Assuming a network consisting of only two aLIGO detectors would decrease our detection rates by about 10%.

For all events in the population we then computed the expected ejecta mass, ejecta average velocity and accretion disk mass using numerical-relativity-informed fitting formulae [41, 171, 245] and assuming the SFHo equation of state [291], which satisfies the current astrophysical constraints [e.g. 203]. This equation of state predicts a maximum non-rotating NS mass of $M_{\rm TOV} = 2.06\,M_\odot$[10].

We used the results as inputs to compute KN light curves from 0.1 to 50 days in the g (484 nm central wavelength), z (900 nm) and J (1250 nm) bands, using the multi-component model of [230] with updates based on [66] (see Chapter 3).

In cases of mergers with final mass $M_{\rm rem} \geq 1.2 M_{\rm TOV}$, corresponding to remnants that collapse promptly or after a short-lived hyper-massive neutron star phase to a black hole, we assumed the system to launch a relativistic jet, with an energy set by the mass of the accretion disk and the spin of the remnant (see Chapter 4). In cases in which the jet energy exceeded a threshold defined following [97], we assumed the relativistic jet to be able to break out of the ejecta cloud and produce GRB prompt and afterglow emission (a 'successful jet'). In our population, 53% of the events launch a successful jet, satisfying the current observational constraints on the incidence of jets in NSNS mergers [270].

For these cases, we assumed a jet angular structure[11] inspired by GRB170817A [125] (see Chapter 4 for more details) and computed afterglow light curves from 0.1

[4] https://www.ligo.caltech.edu/

[5] https://www.virgo-gw.eu/

[6] https://gwcenter.icrr.u-tokyo.ac.jp/en/

[7] For LIGO, Virgo and KAGRA we considered, respectively, a target sensitivity of 190 Mpc, 120 Mpc and 10 Mpc (https://dcc-lho.ligo.org/LIGO-T2000012/public).

[8] Note that we changed the GW model adopted in [78] to be coherent with the next Chapters, however this affects our rates by about 5%.

[9] Updates are available at https://observing.docs.ligo.org/plan/.

[10] This implies that the secondary component of GW190814 [21] is most likely a black hole.

[11] Angular dependence of the jet energy density and bulk Lorentz factor.

to 1000 days in the radio (1.4 GHz), optical (g band)[12] and X-rays (1 keV), fixing the interstellar medium density at $n = 5 \times 10^{-3}\,\mathrm{cm}^{-3}$ (the median density in the [112] sample) and the afterglow microphysical parameters at $\epsilon_e = 0.1$, $\epsilon_B = 10^{-3.9}$ and $p = 2.15$ (representative of GW170817, [125]).

Given the uncertainty on the detailed physical processes involved in the GRB prompt emission, to compute its properties we adopted a semi-phenomenological model similar to that used in [44] and [266], where a constant fraction $\eta_\gamma = 0.15$ [52] of the jet energy density at each angle (restricting to regions with a bulk Lorentz factor $\Gamma \geq 10$) is assumed to be radiated in the form of photons with a fixed spectrum in the comoving frame. The observed spectrum was then obtained by integrating the resulting radiation over the jet solid angle, accounting for relativistic beaming.

To account for a putative wider-angle cocoon shock breakout component [135], for systems observed within a viewing angle $\theta_v \leq 60^\circ$ we also included an additional component in the GRB emission whose properties reproduce those observed in GRB170817A [8], namely a luminosity $L_{SB} = 10^{47}\,\mathrm{erg/s}$ and a cut-off power-law spectrum with νF_ν peak photon energy $E_{p,SB} = 185\,\mathrm{keV}$ and low-energy photon index $\alpha = -0.62$.

The photon fluxes in the 10-1000 keV (*Fermi*/GBM) and 15-150 keV (*Swift*/BAT) energy bands were then computed assuming a fixed rest-frame duration $T = 2\,\mathrm{s}$ for all bursts. We provide more details on the model in Chapter 4. To compute the final GRB prompt emission detection rates we took into account the limited field of view and duty cycle of *Fermi*/GBM and *Swift*/BAT by multiplying the resulting rates by 0.60 and 0.11 respectively [71].

5.4 Prospects for EM counterpart in O4

5.4.1 Detection rates with the 'counterpart search' limit set

In the left-hand panel of Figure 5.1 we show our predictions for the EM counterpart search scenario in O4, assuming the 'counterpart search' limits set. The light grey line ("All NSNS") represents the intrinsic cumulative merger rate, with the underlying light grey band showing its uncertainty (Poissonian uncertainty on the rate density normalization assuming our mass distribution, see Appendix A.1.3), which propagates as a constant relative error contribution to all the other rates shown in the figure. The black line ("GW LVK O4") is our prediction for the cumulative detection rate of NSNS mergers by the GW detector network in O4. The blue, red and orange lines are the all-sky cumulative rates for the joint detection of GW and g band KNæ ("Kilonova+GW"), GW and GRB radio afterglows ("GRB Afterglows+GW"), GW and GRB prompt emission ("GRB Prompt+GW"), respectively. For the latter we show the rate for a GRB detection by *Fermi*/GBM. The result for all the other bands is reported in Table 5.1. The redshift (or luminosity distance) values at which the curves saturate clearly show that the horizons are currently set by the GW detection.

We find that, in the O4 run, NSNS merger GW signals will be detectable out to ~ 300 Mpc ($z \sim 0.07$), with a detection rate of $7.4^{+11.3}_{-5.5}$events per calendar year. Joint GW+EM detection rates for the various counterparts considered are reported in Table 5.1. These rates show that the vast majority of KNæ associated to O4 events will be brighter than the assumed limits at peak, and therefore in principle within the reach of current EM counterpart search facilities and strategies. As shown in Figure 5.2 and detailed in sec. 5.5.1, though, the extremely fast evolution of these

[12] We do not consider the dust extinction in computing the optical KN and GRB afterglow emission.

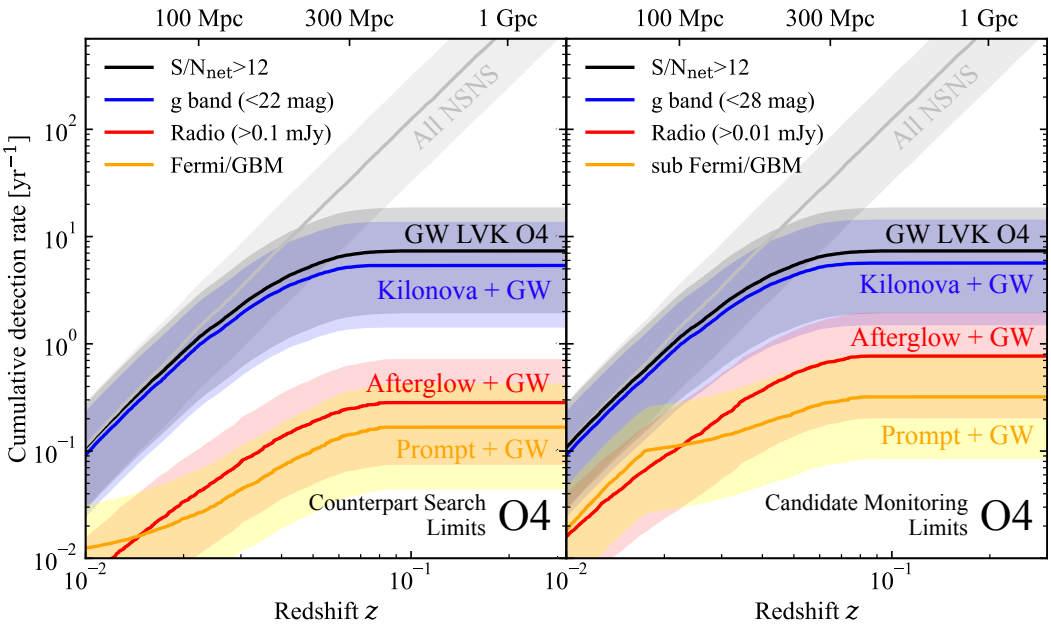

FIGURE 5.1: Cumulative multi-messenger detection rates as a function of redshift (luminosity distance) for our NSNS population. The left-hand panel assumes the 'counterpart search' detection limits, representative of a search for an EM counterpart over the GW localization volume (see Tab. 5.1). The light grey line ("All NSNS") represents the intrinsic merger rate in a cumulative form, with the grey band showing its assumed uncertainty [16], which propagates as a constant relative error contribution to all the other rates as shown in the figure by the colored bands. The black ("GW LVK O4") line is the cumulative GW detection rates (events per year with network S/N $\geq$ 12, accounting for the single detector duty cycles) in O4. The blue ("Kilonova+GW"), red ("GRB Afterglow+GW") and orange ("GRB Prompt+GW") lines are the cumulative detection rates for the joint detection of GW and a KN, GRB afterglow or GRB prompt in O4 (in one of the considered bands, all-sky except for the GRB prompt, which accounts for the *Fermi*/GBM duty cycle and field of view). The right-hand panel assumes deeper detection limits (see Tab. 5.1) representative of the monitoring of a well-localized candidate (and a sub-threshold search for the GRB prompt).

TABLE 5.1: Assumed detection limits and predicted detection rates in our observing scenarios. Below each rate we also report in parentheses the fraction over the total O4 NSNS GW rate ("LVK O4"). The GW detection limits refer to the S/N_{net} threshold. Near infrared and optical limiting magnitudes are in the AB system; radio limiting flux densities are in mJy @ 1.4 GHz; X-ray limiting flux densities are in erg cm^{-2} s^{-1} keV^{-1} @ 1 keV; gamma-ray limiting photon fluxes are in photons cm^{-2} s^{-1} in the 15–150 keV (*Swift*/BAT) or 10–1000 keV (*Fermi*/GBM) band. Detection rates are in yr^{-1}. The reported errors, given at the 90% credible level, stem from the uncertainty on the overall merger rate (hence they cancel out in the fractions), while systematic errors are not included.

	GW	Kilonova + GW O4			GRB Afterglow + GW O4			GRB Prompt + GW O4	
	LVK O4	*J*	*z*	*g*	Radio	Optical	X-rays	*Swift*/BAT	*Fermi*/GBM
Count. Search									
Limit	12	21	22	22	0.1	22	10^{-13}	3.5	4
Rate	$7.4^{+11.3}_{-5.5}$	$2.4^{+3.7}_{-1.8}$	$4.9^{+7.6}_{-3.6}$	$5.4^{+8.3}_{-4.0}$	$0.28^{+0.44}_{-0.21}$	$0.04^{+0.07}_{-0.03}$	$0.32^{+0.49}_{-0.24}$	$0.03^{+0.04}_{-0.02}$	$0.17^{+0.26}_{-0.13}$
(% of O4 GW)	(100%)	(33%)	(67%)	(73%)	(4%)	(0.6%)	(4%)	(0.4%)	(2%)
Cand. Monitoring									
Limit	/	28	28	28	0.01	28	10^{-15}	1	1
Rate	/	$5.7^{+8.7}_{-4.2}$	$5.7^{+8.7}_{-4.2}$	$5.7^{+8.7}_{-4.2}$	$0.77^{+1.23}_{-0.57}$	$0.47^{+0.71}_{-0.35}$	$0.55^{+0.85}_{-0.41}$	$0.05^{+0.06}_{-0.04}$	$0.32^{+0.50}_{-0.24}$
(% of O4 GW)	/	(77%)	(77%)	(77%)	(10%)	(6%)	(8%)	(0.6%)	(4%)
GW subthreshold									
Limit	6	21	22	22	0.1	22	10^{-13}	3.5	4
Rate	60^{+92}_{-44}	$3.9^{+6.1}_{-2.9}$	$15^{+23}_{-11.1}$	23^{+35}_{-17}	$1.08^{+1.68}_{-0.80}$	$0.25^{+0.39}_{-0.18}$	$1.46^{+2.26}_{-1.08}$	$0.15^{+0.23}_{-0.11}$	$0.90^{+1.38}_{-0.66}$

sources will make their actual identification very challenging, and will require a coordinated global effort and the use of large facilities. Our predicted joint GW and GRB rates for EM searches are instead much lower ($0.32^{+0.49}_{-0.24}$ yr^{-1} for the GRB afterglow and $0.17^{+0.26}_{-0.13}$ yr^{-1} for the GRB prompt[13]), and they reflect the faintness of these components for the considered flux thresholds, mainly because of the large abundance (97%) of off-axis jets (i.e. with $\theta_v \geq 2\theta_j$, where θ_j is the core angle as defined in Chapter 4).

5.4.2 Detection rates with the 'candidate monitoring' limit set

In the right-hand panel of Figure 5.1 we show the results for the scenario simulating the monitoring of a well-localized candidate and the GRB prompt sub-threshold detection, assuming the 'candidate monitoring' limits set. These rates represent the hypothetical maximum detection rates that can be achieved in the limiting situation in which all events are localised to arc-second accuracy, allowing for observations as deep as the assumed limits. The KN rate in this panel is therefore shown mostly for reference, as the most likely scenario is one in which the arc-second localisation is obtained through the identification of the KN in a shallower wide-area search. Still, given that all jet-producing events in our population also produce a KN, and given that almost all our KNæ exceed the 'couterpart search' limit set, the rates reported for the afterglow in this panel do represent actual achievable rates.

The light grey and black lines in the panel are the same as the left panel. The blue and red lines are the all-sky cumulative detection rates for the Kilonova+GW and GRB Afterglow+GW detectable sources with this limit set.

In this panel we also show with orange lines the rates of joint GW+GRB detections assuming a detection threshold (see Table 5.1) representative of an off-line sub-threshold search in the gamma-ray detector data.

The fact that the deeper optical and infrared limits do not increase significantly the KN detection rate reflects the fact that the majority of KNæ associated to O4 events in our population are already brighter (at peak) than the limits adopted in the search scenario. As far as the GRB afterglow is concerned, we find that the deeper limits allow to increase the detection rate in the radio, optical and X-ray bands by factors of $\sim$ 3, 10 and 2, respectively, with the highest detection rate in the radio, reaching $0.77^{+1.23}_{-0.57}$ yr^{-1}. Also for the GRB prompt sub-threshold detection we find a small increase in the rates up to $0.32^{+0.50}_{-0.24}$ yr^{-1}. All detection rates are reported in Table 5.1.

5.4.3 Sub-threshold GW search in response to an external EM trigger

The bottom group of rows in Table 5.1 report the detection rates predicted by our model adopting a lower GW detection threshold $S/N_{net} \geq 6$, which we take as representative of a sub-threshold GW search for events coincident with an external EM trigger. The most relevant external trigger, in our context, is a GRB, as it allows for the search to focus on a short time interval and on a relatively small sky area, therefore increasing significantly the sensitivity with respect to an all-sky, all-time search [3]. Thanks to the expanded GW horizon in the sub-threshold search, the rate of joint GRB+GW detections increases to a more promising $0.90^{+1.38}_{-0.66}$ yr^{-1} (for *Fermi/GBM*), which is in good agreement with the rate predicted by the LVK Collaboration for the same kind of search [19] and would mean a relatively high chance of a new

[13]These values can be scaled for different detection limits using Figure 5.6 in Section 5.6

GRB-NSNS association. Sub-threshold searches may in principle be conducted also in response to the EM detection of a KN or GRB orphan afterglow candidate: for that reason, we also report the joint GW+KN and GW+afterglow rates in the table, but we caution that these are not representative of a real expected rate, as the serendipitous discovery of KNæ and orphan GRB afterglows in current all-sky surveys is hampered by limited cadence, depth, and availability of time at large facilities for spectroscopic classification of candidates.

5.5 EM Properties in O4

In the following section, we characterize the EM properties of the GW-detectable (with $S/N_{net} \geq 12$) NSNS mergers in our population. Our purpose is mainly that of informing EM follow up strategies, by constructing expected distributions of source brightness at various times and frequencies and for different EM counterparts.

5.5.1 Kilonova

In Figure 5.2 we show the time evolution of the distribution of KN brightness for binaries in our population that are GW-detectable in O4. In particular, in the left-hand panel we show the bands that contain 50%, 90% and 99% of the light curves at each time. Blue (upper panel) and red (lower panel) colors refer to the g and J band, respectively. When scaled to the median distance ($\sim$ 174 Mpc) of these events, AT2017gfo (colored circles) lies at the top of the 50% band, showing that our assumptions are conservative in that they predict KNæ that are on average slightly dimmer than AT2017gfo, but with a similar temporal evolution. While the peaks of these KNæ span a relatively wide apparent magnitude range $17 - 24$, 50% are concentrated in the relatively narrow interval $20 - 22$. In the right-hand panel we show the cumulative apparent magnitude distributions at peak (solid line) and also 3 and 5 days after the merger (dashed and dotted lines), which clearly display the very rapid evolution, especially in the g band.

The detection of the KN in the g and J band seems particularly probable (73% and 67% of GW events, respectively) for current all-sky EM campaign. However, the rapid evolution, underlined by Figure 5.2, suggests that the observation should take place within the first night for the g band and within about two nights for the z band. While the J band, even if it evolves more slowly, could be too faint to be detected with current all-sky facilities (33% of GW events).

5.5.2 GRB afterglow

In Figure 5.3 we show the properties of GRB afterglows associated to GW-detectable binaries in our population by showing the contours containing 50% (solid lines) and 90% (dashed lines) of GRB afterglow peaks on the (F_ν, t) plane. We also report on the right the apparent AB magnitude and νF_ν at 1 keV. The red, green and blue colors refer to our radio, optical and X-ray bands, respectively. Most peak times are at $\gtrsim 10^2$ days (we note that we restricted the light curve computation between 10^{-1} and 10^3 rest-frame days), with a tail at shorter peak times. We also show 500 randomly sampled optical light curves (thin grey lines) in the background, to help visualizing the underlying light curve behavior. For comparison, we also show GRB170817A data [188, small circles] at the median distance of our population ($\sim$ 174 Mpc), whose peak lies within the 50% contours in all three bands.

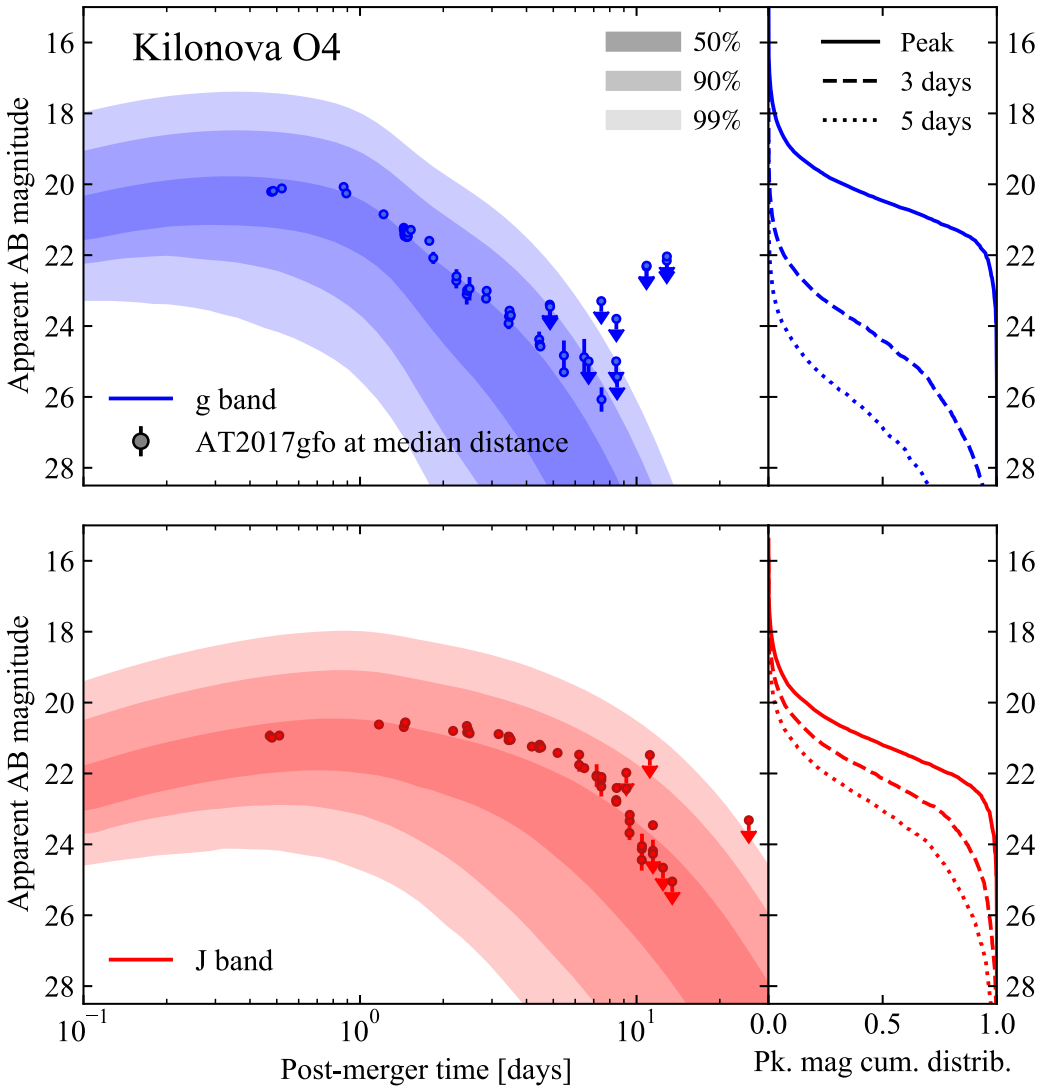

FIGURE 5.2: Distribution of O4 KN optical and infrared magnitude as a function of time. The left-hand panel shows the apparent AB magnitude versus post-merger time for our simulated KN light curves, restricting to O4 GW-detectable sources. The shaded regions contain 50%, 90% and 99% of the KN light curves. Blue (upper panel) and red (lower panel) colors refer respectively to the g (484 nm) and J (1250 nm) band. Colored circles show extinction-corrected AT2017gfo data rescaled to the median distance of our population ($\sim$ 174 Mpc). The right-hand panel shows the cumulative distributions of apparent magnitude at peak, at 3 days and at 5 days after the merger (solid, dashed and dotted lines, respectively)

.

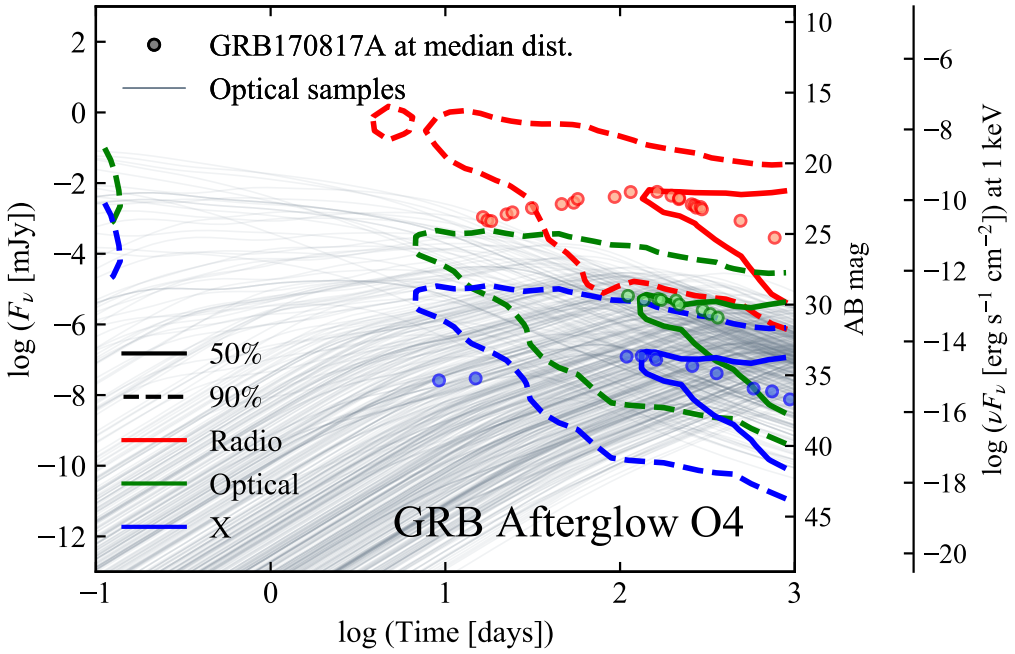

FIGURE 5.3: F_ν, AB magnitude and νF_ν versus time for the GRB afterglow light curves associated to O4-detectable sources in our population. Solid and dashed contours contain 50% and 90% of the peaks, respectively. Red, green and blue colors indicate the radio (1.4×10^9Hz), optical (4.8×10^{14}Hz), X-ray (2.4×10^{17}Hz) bands, respectively. The colored circles are the observed data of GRB170817A [188] at the median distance of our population. The grey lines in the background are 500 randomly sampled optical light curves.

These results stem from the strong dependence of the GRB afterglow light curve on the viewing angle, combined with the GW-detection-induced bias on the viewing angle distribution (which skews the distribution towards smaller viewing angles with respect to the isotropic case, with a peak at $\sim 30^\circ$ – [278]). This places the majority of the peaks months to years after the GW event, with a small sub-sample peaking at early times (∼hours) in the optical and X-rays, producing very bright emission, thanks to a smaller viewing angle.

The GRB afterglow properties highlighted in Figure 5.3 and the low rates shown in Table 5.1, suggest that the preferred candidate for an all-sky observing campaign is the KN, at least in the first days after the GW event. Once the KN is detected, it seems convenient to wait weeks or months after the event, to proceed in search of a GRB afterglow with deeper detection limits.

5.5.3 GRB prompt

In Figure 5.4 we show the distribution of rest-frame spectral energy distribution (SED) peak energy $E_{\rm peak}$ versus the isotropic-equivalent energy $E_{\rm iso}$ of events for which both the GW signal and the GRB prompt emission meet our detectability criteria (considering the O4 LVK network and *Fermi*/GBM, green filled contours), and separately those that are detectable in GW (black dashed contours) or by *Fermi*/GBM (magenta contours). In particular, different shades in the green regions progressively contain 50%, 90% and 99% of joint GRB prompt- and O4-detectable binaries[14]. The

[14]The detection rate corresponding to this region is shown by orange lines in Figure 5.1 and reported in Table 5.1.

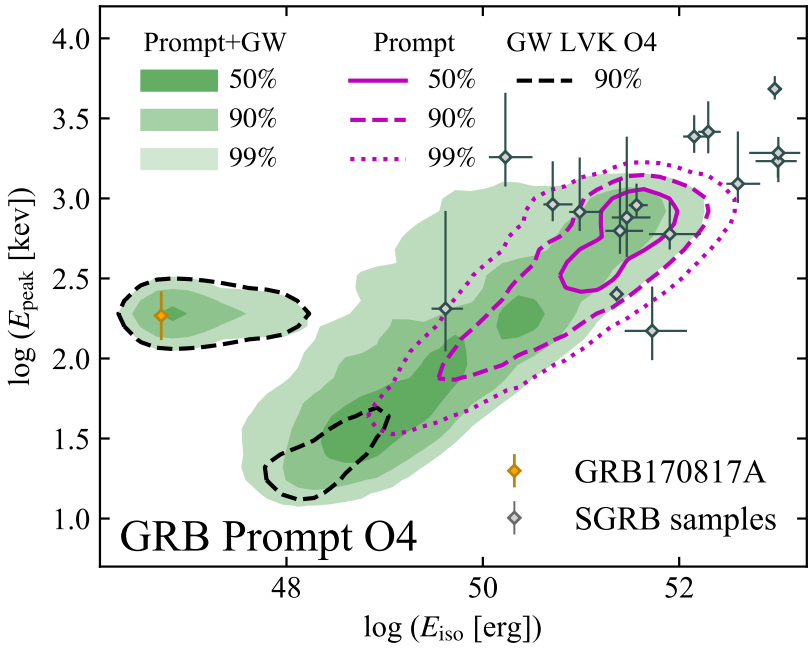

FIGURE 5.4: Rest-frame SED peak photon energy E_{peak} versus the isotropic-equivalent energy E_{iso} for our NSNS population. The filled green colored regions contain 50%, 90% and 99% of the binaries both GRB Prompt- and O4-detectable. The magenta lines contain 50%, 90% and 99% (solid, dashed and dotted, respectively) of the GRB Prompt-detectable binaries. The black dashed line contains 90% of the O4-detectable binaries. The black dots with error bars represent a sGRB sample for comparison [268]. The orange dot is GRB170817A.

dashed black line is the 90% confidence region for the O4-detectable binary without the constrain on the GRB prompt detectability. The comparison between the GRB prompt detections by *Fermi*/GBM and the known cosmological population shows a broad consistency with the sample of short GRBs (sGRBs) with known redshift [268, grey diamonds]. The position of GRB170817A in this plane [19] is shown by the orange diamond, which is consistent by construction with the position of the small island in the left-most part of the plot, which represents events whose emission is dominated by the cocoon shock breakout component. Differently from [78], where for events with viewing angles (θ_v) less than 60 degrees, we computed the peak energy E_{peak} as a weighted average based on the isotropic energy E_{iso} both with and without shock breakout, in our current approach, we adopt a fixed value of $E^{sb}_{peak} = 185$ keV whenever the shock breakout photon flux exceeds that of the GRB prompt photon flux. The expansion of the green island on the plot is due to the application of a Gaussian filter, a choice made to facilitate clearer interpretation of the data. While this methodology introduces some variations in the plot's contours, the overall qualitative insights remain consistent with previous findings.

5.5.4 Viewing angle versus redshift

In Figure 5.5 we show the distribution of some sub-samples of our population in the viewing angle θ_v versus redshift z plane. Grey filled contours refer to GW LVK O4-detectable binaries, while empty contours refer to joint GW and EM detectable binaries: in particular the blue, orange and red lines refer to KN+O4, GRB Prompt+GW O4 and GRB Afterglow+GW O4 detectable binaries, respectively. The detection rates

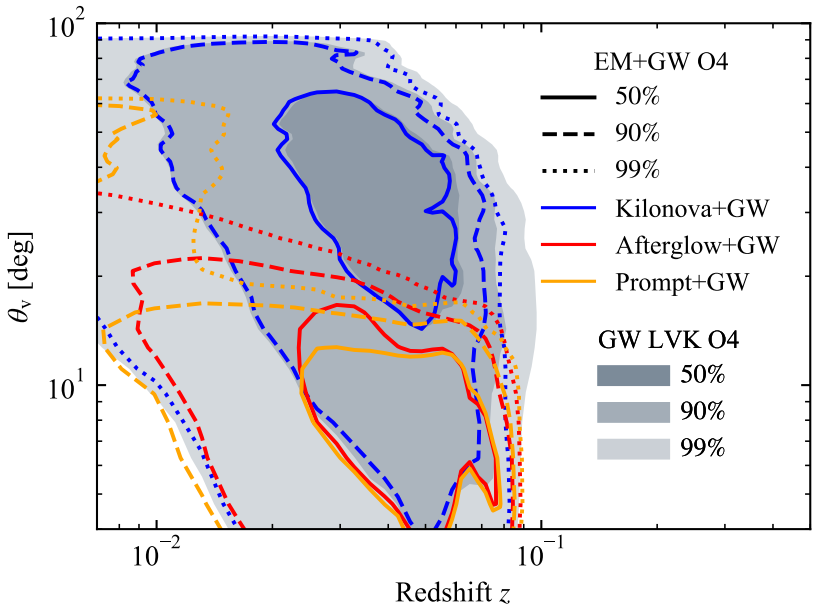

FIGURE 5.5: Viewing angle θ_v versus redshift z for our NSNS population. The filled grey regions contain 50%, 90%, 99% of the GW O4-detectable binaries. Solid, dashed and dotted contours contain 50%, 90%, 99% of the binaries that exceed both the O4 GW S/N_{net} limit and any one of the 'couterpart search' limits relevant to the particular counterpart considered (blue: KN; red: GRB afterglow; orange: GRB prompt). The corresponding detection rates are reported in Figure 5.1.

corresponding to these regions are shown by lines of the same color in Figure 5.1 and are reported in Table 5.1. The figure clearly shows the weak dependence on redshift for the jet-related emission, whose luminosity is strongly dependent on the viewing angle. Moreover, 90% (50%) of the GRB Prompt+GW O4 and GRB Afterglow+GW O4 events have relativistic jets seen under a viewing angle lower than $\sim 15\,(10)$ degrees.

5.6 Detection rate versus detection limit

In section 5.4 we report the detection rates for joint GW and EM events considering two representative detection limit sets based on the two main scenarios considered in this work. In order to allow the community to explore alternative observing configurations that correspond to different detection limits, we show in Figure 5.6 the distribution of the detection rates as a function of the detection limit for the GRB Prompt+GW O4 (upper panel, orange) and GRB Afterglow+GW O4 (lower panel, red) detectable binaries (for KNæ, such information is already contained in the right-hand panels of Figure 5.2).

For the GRB Prompt+GW O4 detection we show the rates assuming an all-sky field of view and a 100% duty cycle (solid line) and accounting for the duty cycle and field of view of *Fermi*/GBM (dashed line) and *Swift*/BAT (dotted line). The figure shows how the GRB prompt+GW detection rate increases with the prompt emission detector sensitivity: if it were possible to reach photon flux threshold values of $\sim$0.1 ph cm^{-2} s^{-1}, the cocoon emission would start to be detected in essentially all jet-launching binaries (this produces the bump in the orange lines at the low-flux-limit end).

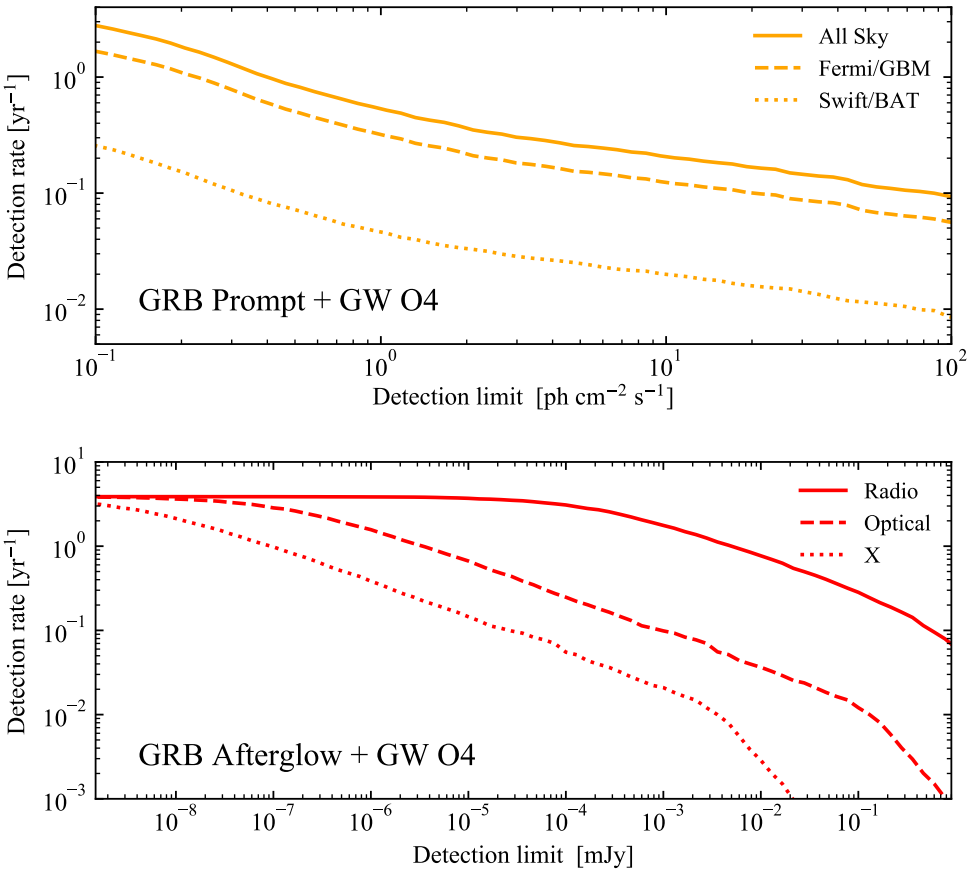

FIGURE 5.6: Detection rates as a function of the detection threshold limit for our NSNS population. The upper panel refers to GRB Prompt + GW O4 detectable binaries. The solid line indicates an all-sky field of view with a 100% duty cycle, the dashed and dotted lines accounts for the *Fermi*/GBM and *Swift*/BAT duty cycle and field of view, respectively. The lower panel refers to GRB Afterglow + GW O4 detectable binaries. The solid, dashed and dotted lines indicate the radio, optical and X band, respectively.

For the GRB Afterglow+GW O4 events, we show individually the rates for the radio (solid), optical (dashed) and X (dotted) bands. The detection limit value at which the curves saturate indicates the sensitivity needed to detect all the GRB Afterglow+GW O4 events, with a corresponding detection rate of $4.0^{+6.1}_{-3.0}$ yr^{-1} (that is the GW O4 detection rate of $7.4^{+11.3}_{-5.5}$ yr^{-1} times the 53% fraction of jet-launching system).

5.7 Prospects for EM counterpart in O5

For the O5 run, assuming a complete network at design sensitivity including LIGO-India, we expect an increase in the rate of about an order of magnitude, thanks to the increasing sensitivity of the detectors and the expansion of the GW horizon (see Figure 5.7). In particular, we find a GW detection rate of $67.1^{+104}_{-49.5}$ yr^{-1}, with a horizon around redshift $z \sim 0.2$.

Among these GW-detectable events, the fraction of events with an observable EM counterpart is similar to what was described in O4. Therefore, considering the set of 'counterpart search' limits, we expect a rate of potentially detectable KNæ of $24.9^{+38.6}_{-18.4}$ yr^{-1} up to redshift $z \sim 0.08$. As for the emissions related to the relativist jet, also in this case the rates are less promising, with a rate of prompt and afterglow emissions respectively at $1.03^{+1.6}_{-0.76}$ and $1.2^{+1.9}_{-0.9}$ yr^{-1}. Although much lower compared to the KN, these rates would already be a huge improvement compared to O4, ensuring at least one joint detection of GW+GRB per year.

Assuming the 'candidate monitoring' limit set, we expect for the KN an increase in the rate of about a factor of 2, bringing their horizon to be limited only by the GW horizon. For GRB prompt and afterglow, we expect an increase of about a factor of 1.5 and 3 respectively. This can be particularly relevant for the afterglow, ensuring some observation every year, under the assumption of being able to reach deeper limits following the identification of the KN.

All the detection rates are reported in Table 5.2.

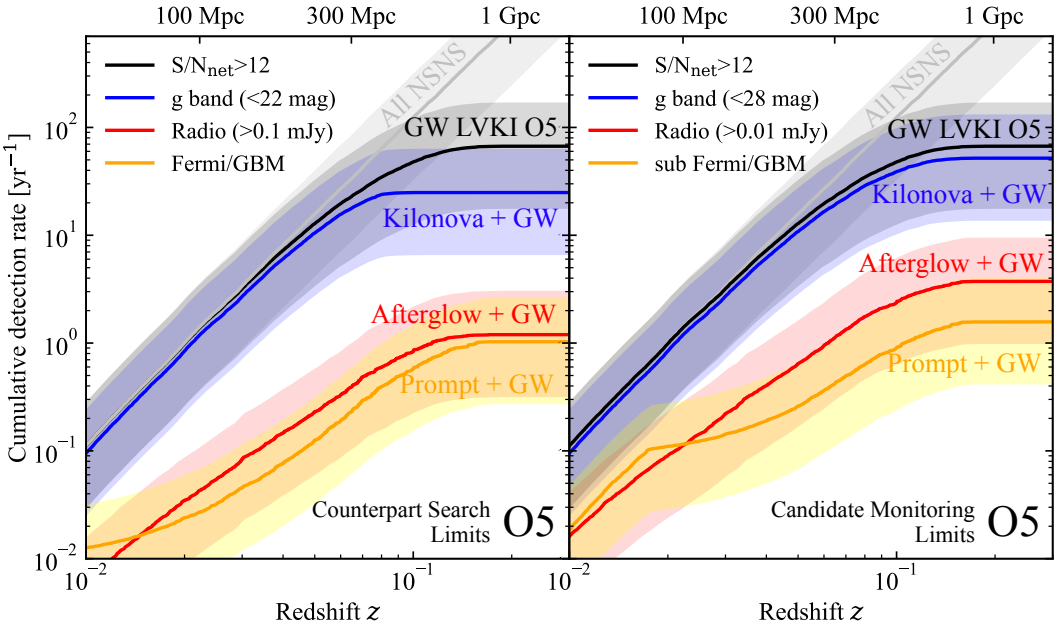

FIGURE 5.7: Same as Figure 5.1, but assuming the LVKI O5 network.

TABLE 5.2: Same as Table 5.1, but assuming the LVKI O5 network.

	GW	Kilonova + GW O5			GRB Afterglow + GW O5			GRB Prompt + GW O5	
	LVKI O5	J	z	g	Radio	Optical	X-rays	*Swift*/BAT	*Fermi*/GBM
Count. Search									
Limit	12	21	22	22	0.1	22	10^{-13}	3.5	4
Rate	$67.1^{+104}_{-49.5}$	$4.1^{+6.3}_{-3.0}$	$16.0^{+24.5}_{-11.8}$	$24.9^{+38.6}_{-18.4}$	$1.2^{+1.9}_{-0.9}$	$0.25^{+0.39}_{-0.18}$	$1.6^{+2.6}_{-1.2}$	$0.17^{+0.26}_{-0.13}$	$1.03^{+1.6}_{-0.76}$
(% of O5 GW)	(100%)	(6%)	(24%)	(37%)	(1.8%)	(0.4%)	(2.5%)	(0.3%)	(1.5%)
Cand. Monitoring									
Limit	/	28	28	28	0.01	28	10^{-15}	1	1
Rate	/	$52.9^{+79.1}_{-39.3}$	$52.9^{+79.1}_{-39.3}$	$52.9^{+79.1}_{-39.3}$	$3.7^{+5.8}_{-2.7}$	$2.4^{+3.7}_{-1.8}$	$2.8^{+4.3}_{-2.1}$	$0.25^{+0.38}_{-0.18}$	$1.57^{+2.43}_{-1.16}$
(% of O5 GW)	/	(77%)	(77%)	(77%)	(5.6%)	(3.6%)	(4.2%)	(0.4%)	(2.3%)
GW subthreshold									
Limit	6	21	22	22	0.1	22	10^{-13}	3.5	4
Rate	547^{+844}_{-404}	$4.5^{+6.8}_{-3.3}$	$21^{+32.6}_{-15.5}$	$36^{+55.3}_{-26.6}$	$3.1^{+4.6}_{-2.3}$	$0.93^{+1.5}_{-0.69}$	$8.1^{+12.6}_{-6.0}$	$0.89^{+1.38}_{-0.66}$	$5.3^{+8.1}_{-3.9}$

5.8 Discussion and conclusions

In this Chapter we presented our predictions for the detection rates and properties of KNæ and GRBs (including both prompt and afterglow emission) that will be associated to double neutron star binary mergers to be detected during the next GW detector network run O4, started in May 2023. These predictions are based on a synthetic population of events with an observationally motivated mass distribution and event rate density, for which we computed GW signal-to-noise ratios, KN light curves, GRB afterglow light curves and prompt emission peak photon fluxes, enabling the direct evaluation of the detectability of each emission component for each event in the population.

KNæ are produced in 77% of mergers in our population, the remaining fraction being massive events that result in a prompt black hole collapse with neither disk nor ejecta (see Figure A.4 in Appendix A.1.1). We find light curves that are intrinsically similar to, but on average slightly dimmer than, AT2017gfo (Fig. 5.2). Despite the larger median distance with respect to events detected in the previous runs, their apparent brightness in most cases (95% of events with an associated KN) will still exceed the typical limits reached in previous optical counterpart searches, but for a limited time (only the first night in the g band, few nights in the z band), making the detection and identification of these sources more challenging than it had been for AT2017gfo. Our result that most O4 KNæ will be accessible down to current typical EM counterpart search detection thresholds is in line with e.g. Chase et al. [74], Setzer et al. [280] and Sagués Carracedo et al. [262].

Relativistic jets are produced in 53% of the events in our population. Their GRB prompt emission exceeds our assumed limits in only a few percent of the events, with only a minor improvement when considering the deeper thresholds representative of a sub-threshold search in the gamma-ray detector data. A more promising route for the association of a GRB with a NSNS event in O4 will be that of a sub-threshold GW event search in response to a gamma-ray trigger, which results in a joint detection rate of $0.90^{+1.38}_{-0.66}$ yr^{-1} in our model, thanks to the expanded GW horizon.

Radio observations represent the best route for the detection of the relativistic jet afterglow when monitoring a well-localised event. Indeed, radio afterglows are brighter than our 'candidate monitoring' detection limits in around one tenth of the simulated events, corresponding to a detection rate of $0.77^{+1.23}_{-0.57}$ yr^{-1} (achievable if all candidates are localised to arc-second accuracy through the detection of their KN emission). These predictions indicate that one new relativistic jet counterpart in O4, which would constitute an important new piece of information on these sources, is not unlikely, yet not guaranteed.

For what concerns the observable properties of the relativistic jet counterparts, if a fortunate GRB prompt emission event will be detected, we expect it to be dominated by either the cocoon shock breakout emission component (for events closer than ~ 100 Mpc), or more likely by emission from the slower, less energetic material that surrounds the jet core, if a mechanism similar to that which produces the prompt emission of cosmological GRBs extends to two-three times the jet core opening angle (Fig. 5.4). A due caveat here is that it is unclear to which extent the (poorly known) prompt emission mechanism of GRBs operates outside the jet core and, conversely, the current understanding of shock breakout emission does not extend to highly anisotropic, highly relativistic cases, making any statement on the observable properties of the shock breakout from parts of the cocoon closer to the jet axis highly uncertain. The observable GRB afterglows (Fig. 5.3) are expected to display similar properties as those of GRB170817A, that is, a shallow increase in flux density over a

few months after the merger, followed by a peak and a relatively fast decay afterwards. Still, a few percent of the detectable events in our population feature an earlier peak, corresponding to a smaller viewing angle, which would constitute an interesting case study that would bridge the gap between the viewing angles of cosmological GRBs and that of GRB170817A.

In the last years, several works predicting the joint GW+EM detection rates during O4 have been published or circulated as pre-prints, each focusing on a single or at most two EM counterparts [119, 314, 205, 272]. Factoring in the lower local NSNS merger rate density assumed in this work with respect to studies that used the O2 estimate (which was higher by a factor of around three), our joint GW+EM detection rate predictions are in general agreement with most of these previous works. In particular, Frostig et al. [119], Zhu et al. [314] and Mochkovitch et al. [205] find a similarly large fraction 60-80% of KNæ detectable with similar thresholds as ours; factoring in the different fraction of jet-launching events (53% in this work, compared to 100% in the others), our estimate, that up to 10% of the afterglows will be detectable in radio, is in agreement with the 20% estimated by Duque, Daigne, and Mochkovitch [100] and Saleem et al. [272]. The prediction that only few percent of the NSNS events detectable in O4 through GW emission will have a detectable short GRB is in line (again factoring in our 53% fraction of jet-launching systems) with, e.g., Belgacem et al. [51], Howell et al. [152] and Yu et al. [311], while Patricelli et al. [226], Saleem [271] and Mogushi, Cavaglià, and Karelle [206] find somewhat higher fractions (but note that the estimate for sub-threshold GW detections triggered by GRB detections from [271] is in good agreement with ours).

It is worth stressing the fact that the entirety of these models either assume identical properties for all counterparts, or use empirical parametrizations for the distributions of their properties. The strength of our approach lies in computing the ejecta properties and EM emissions directly from the binary parameters, instead of e.g. extracting EM model parameters randomly from given distributions.

In this work we worked under the assumption that the GW sky localization areas of O4 NSNS mergers will always be covered down to our assumed representative thresholds by EM counterpart searches. This is clearly not feasible when considering single facilities (due to limitations in the accessible sky and in the time that can be dedicated to each search), but we note that the combined coverage of different facilities can probe very large localization areas, as demonstrated by the searches for EM counterparts of the single-detector event GW190425, e.g. [36, 83, 183, 150]. A more refined assessment of the detection rates that can be realized in practice would require facility-specific simulations of the GW localization and of the actual search strategy (as done e.g. in [119]), which is out of the scope of this work.

As a final remark, our estimates make GRB170817A an extremely lucky event (in line with, e.g., [205], but see also [231]), which is not going to repeat soon. Given the excellent agreement of our model predictions with the short GRB cumulative peak flux distribution observed by *Fermi*/GBM and *Swift*/BAT (see Figure 4.3 in Chapter 4), we consider this a robust statement. Still, we caution that all our predictions are based on loose observational constraints, and carry systematic uncertainties that have not yet been explored, due to the complexity of the full population modeling. The synergy between gravitational and electromagnetic telescopes in future runs will provide us with more observations, allowing to get closer and closer to the real physics of these events.

The data produced in this Chapter are publicly available on Zenodo through the link https://doi.org/10.5281/zenodo.6900865. All scripts and files to reproduce the main figures in the text are publicly available at https://github.com/

acolombo140/O4NSNS.

Chapter 6

Multi-Messenger Observations of Black Hole - Neutron Star Mergers in the O4 and O5 Runs

This Chapter is primarily a copy of the original work [79], accepted for publication in Astronomy & Astrophysics. Some plots and part of the text may differ to accommodate minor revisions from the peer review process. Part of the Appendix has been moved to the main text.

6.1 Introduction

The first detections of binary compact objects composed of a black hole and a neutron star (BHNS binaries) through gravitational waves (GWs) recently accelerated the study of BHNS physics [22]. To date, there are four BHNS events detected with false-alarm-rate (FAR) $< 1\ \mathrm{yr}^{-1}$; GW200115_042309, GW200105_162426, GW190917_114630, and GW190426_152155 [23], by the LIGO-Virgo-KAGRA Scientific Collaboration (LVK) consisting of the two Advanced Laser Interferometer Gravitational wave Observatories [aLIGO, 2], the Advanced Virgo [25], and KAGRA detector [38].

BHNS observations provide novel and complementary information on the formation pathways of compact objects to be compared with those of binary black hole (BBH) and binary neutron star (BNS) mergers [e.g., 170, 273]. The first detections of mergers suggest that BHNS binaries are a population hosting highly asymmetric binaries with a large mismatch between the BH and NS mass compared to BBHs and BNSs, suggesting different progenitor stars and formation avenues [e.g., 68, 130].

In a BHNS merger, the NS undergoes one of two faiths: It is either partially or completely torn apart by the tidal forces of the BH outside the innermost stable circular orbit (ISCO), or it is directly engulfed by the BH [e.g., 162, 116, 113]. The outcome of the NS hinges on the relative position between the BH ISCO $R_{\rm ISCO}$ and the distance $d_{\rm tidal}$ at which the BH gravitational field is capable of causing tidal disruption of the star. The condition $d_{\rm tidal} > R_{\rm ISCO}$ depends on several factors, and it is favored for larger values of the NS tidal deformability, larger BH spins, and lower BH masses [e.g., 162, 41]. When the NS is disrupted in a BHNS merger, neutron-rich material is released. This tidal debris is comprised of two distinct components: one is a gravitationally bound portion that forms an accretion disk around the BH remnant, the other is an unbound component, commonly referred to as the "dynamical ejecta" [e.g., 162, 116, 113]. The presence of this matter outside the BH can potentially power a kilonova (KN) and launch a relativistic jet, which can in turn produce 'prompt' and 'afterglow' emission possibly contributing a sub-class of gamma-ray bursts (GRB) [e.g., 180, 199]. Detecting EM emission from a BHNS merger would help in constraining the equation of state (EoS) of matter at nuclear densities [173, 95], measuring the

Hubble constant [e.g., 277, 216], and understanding the role of BHNS mergers in the production of heavy elements [176, 177].

When compared with expectations from numerical relativity, the signals from the two BHNSs detected in January 2020 suggest that these mergers did not lead to significant ejection of matter [22, 57, and references therein]. This is consistent with the non-detection of EM signals during the follow-up campaign [e.g. 31][1], although the uncertainties in the distance and GW sky localization region disallow completely excluding the possibility of a potentially detectable EM emission. Moreover, the fraction of BHNS bright events is commonly considered low [117], as the possibility of highly rotating BHs and stiff NS EoS is disfavored by LVK constraints [20, 13]. However, the possibility of BHNS mergers with BHs in the lower mass gap ($M_{\rm BH} < 5M_{\odot}$) would allow for EM counterparts even under the assumption of non-rotating BHs and soft EoSs. In particular, the hypothesis of events in the mass gap is suggested both by LVK observations [21, 313] and by "delayed" supernova model theories [120, 94, 68], upon which the population considered in this study is based. The current and upcoming observation runs of the global network of GW interferometers (IFOs), with an ever-improving sensitivity, open the doors to elucidating the elusive properties of BHNS systems, detecting their GW signals and, for a subclass of these, their joint GW and EM signals.

This study is an attempt to infer realistic prospects of the rate of BHNS mergers as multi-messenger (MM) sources during the current O4 and upcoming O5 runs and to explore their properties. Our study is based on population synthesis models for the BHNS systems, numerical-relativity-informed prescriptions for the properties of the materials expelled from the mergers, and semi-analytical models to compute the observable properties of the associated KN, GRB prompt, and GRB afterglow emission.

Before run O4 started (in May 2023), a number of papers appeared in the literature, which anticipated estimates of the MM detection rates of BHNS mergers. Boersma and van Leeuwen [62] focused on the observation of GRB radio afterglows with the SKA1 radio array finding that a joint detection is unlikely within O5, even with such a sensitive instrument. They point out how current uncertainties on the BH spin hugely affect the results, as expected from the role that the BH spin plays in the disruption of the NS. Similarly, Zhu et al. [315] focused on the KN and GRB afterglow counterparts of BHNS mergers and find a prominence of plunging systems with negligible EM emission for a population of low-spinning BHs. Consequently, they suggest relying on searches in data streams from optical surveys as a strategy to discover KN and afterglow counterparts of BHNS systems (so-called 'blind searches', e.g., [32, 33]), rather than dedicating target-of-opportunity (ToO) time after GW triggers with low chances of a successful outcome. Regarding the GRB prompt counterpart, Zhu et al. [316] was the first to derive a population model for BHNS systems starting from three long-duration GRBs (including GRB211211A), under the hypothesis of a BHNS origin. They estimate a joint GW+KN+GRB detection rate of BHNS mergers of $\sim 0.1\ \mathrm{yr}^{-1}$ during O4, though large uncertainties remain.

In this study, we extend the analysis of the MM properties of BHNS mergers considering GRB prompt, multi-wavelength GRB afterglow, and KN emissions for BHNS systems detectable above the GW network threshold. Furthermore, we study the impact of the EoS of NS matter and of the BH spin distribution on the expected population of MM events. This enables us to account for two of the main sources of

[1] A summary of the follow-up campaigns of these two events can be evinced from the Global Coordinates Network circulars at https://gcn.gsfc.nasa.gov/other/S200105ae.gcn3, and https://gcn.gsfc.nasa.gov/other/S200115j.gcn3.

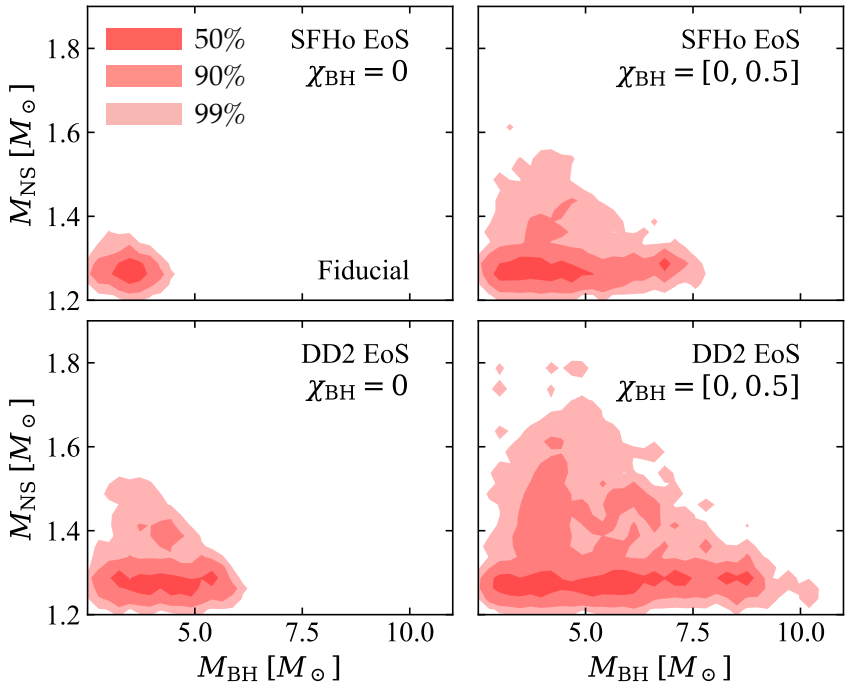

FIGURE 6.1: Distribution of BHNS binaries in our population on the NS mass versus BH mass plane, restricted to events for which the mass m_{out} remaining outside the remnant is larger than zero [171, Eq. 9], the fundamental condition for an EM emission. In each panel, the red shaded regions contain 50%, 90% and 99% of the binaries (darker to lighter shades). Upper panels assume the SFHo EoS, while lower panels assume the DD2 EoS. Left-hand panels assume all BH spins are negligible, while right-hand panels assume uniformly distributed BH spin parameters in the interval [0,0.5].

uncertainty on BHNS systems. Also, our predictions for detectable EM counterparts are based on the follow-up performance expected for existing or planned instruments across the EM spectrum. Finally, our predictions for the MM signals allow us to derive follow-up strategies tailored to BHNS events.

The paper is organized as follows. In Section 6.2, we describe the distribution of binary parameters in our BHNS population model, the emission models for the GW and EM signals, and the assumed MM representative detection limits for O4 and O5. In Section 6.3, we present our results for the MM detection rates, and in Section 6.4 we detail the expected properties of the different EM counterparts. In Section 6.5 we report Appendix C of the original work [79], regarding variations on the detection limits and a brief discussion on the GW-inferred sky localization. We discuss these results in Section 6.6, specifically comparing our results with similar studies in the literature. We also discuss observing strategies that would best target the BHNS mergers. Finally, in Section 6.7 we summarize our results and conclude.

Throughout this work, we assume a flat cosmology with cosmological parameters drawn from Planck Collaboration et al. [237].

6.2 GW and EM population models

6.2.1 Progenitor binary population

Given the scarcity of observational constraints, we chose to build our population based on binary population synthesis models. In particular, we assumed the BH

and NS mass distributions resulting from the fiducial parameter set (model A) from Broekgaarden et al. [68]. We assumed the fiducial metallicity specific star formation rate density from the same work, based on the phenomenological model described in Neijssel et al. [214], and normalized to an observationally-derived merger rate density of $R_0 = 149^{+153}_{-87}\mathrm{Gpc}^{-3}\mathrm{yr}^{-1}$ at redshift $z = 0$. We computed this value to self-consistently reproduce four BHNS events detected with FAR $\leq 1\ \mathrm{yr}^{-1}$ [17], following a similar procedure to the one described in Appendix A.1.3. For the BH spin parameter χ_{BH} prior to the merger, we considered two different configurations: a conservative one with $\chi_{\mathrm{BH}} = 0$ for all binaries and a more optimistic one with a uniform distribution in the interval $\chi_{\mathrm{BH}} \in [0, 0.5]$, which corresponds to the typical spin range found in several simulations [121, 49].

In order to explore the dependence of our results on the uncertain NS EoS, we computed the NS tidal deformabilities assuming two EoS models: the soft SFHo EoS [146], with a maximum non-rotating NS mass $M_{\mathrm{TOV}} = 2.06\,\mathrm{M}_\odot$ and a $1.4\ \mathrm{M}_\odot$ NS radius $R_{1.4} = 11.30\,\mathrm{km}$; and the stiff DD2 EoS [291], with $M_{\mathrm{TOV}} = 2.46\,\mathrm{M}_\odot$ and $R_{1.4} = 13.25\,\mathrm{km}$. Both EoS are in agreement with current constraints from GW170817 and the Neutron star Interior Composition Explorer [NICER, e.g. 203, 204, 244], with a slight tension for the DD2, which we therefore consider as optimistic regarding the emission of EM radiation. Hereafter, we take the conservative set-up with non-spinning BHs and the SFHo EoS as our fiducial population and consider the other pairs of BH spin distributions and NS EoS as variations on this fiducial model.

In Figure 6.1 we show, for all the four variations, the regions containing 50%, 90%, and 99% of the binaries with a mass remaining outside the remnant $m_{\mathrm{out}} > 0$, that is the fundamental condition for having an EM emission. Here, we determine this mass using numerical-relativity-informed fitting functions from Krüger and Foucart [171, Eq. 9], see section 6.2.3. Our fiducial scenario, which assumes no spins for the BH and a soft EoS for the NS, is therefore the most pessimistic scenario in terms of EM emission. Indeed, in the fiducial model, only events with a $M_{\mathrm{BH}} \lesssim 4.5 M_\odot$ can emit an EM counterpart. By varying the spin and the EoS with more optimistic assumptions, it is possible to find EM counterparts associated to events with a $M_{\mathrm{BH}} \lesssim 11 M_\odot$. These variations also correspond to a different fraction of BHNS events with $m_{\mathrm{out}} > 0$. We find a range between $2.2\% - 13\%$ of GW triggers that satisfied the previous condition, in agreement with different estimates in the literature [256, 57].

Figure 6.1 shows that, in our fiducial population model (upper-left panel), all the BHNS systems susceptible to emit EM radiation have a small-mass BH, with $M_{\mathrm{BH}} < 5\,M_\odot$, due to their zero spins. Until the first discoveries of GW from merging compact objects, the existence of BH with such low masses was largely doubted. Indeed, the observation of galactic X-ray binaries suggested a sharp cutoff of BH masses below around $5\ M_\odot$ [219, 103], leading to the existence of a 'lower mass gap' in BHs masses between $5\,M_\odot$ and the most massive NS at $M_{\mathrm{TOV}} \sim 2.2 - 2.5\,M_\odot$ (according to EoS analysis and various observational constraints; for a review, see [217]). In addition, this mass gap had theoretical support from binary evolution scenarios such as the 'rapid' core-collapse supernova mechanism [120, 50].

However, recent GW observations could suggest the lower mass gap could not be as empty as anticipated, through the detection of the merger of a system with a secondary component likely in the bounds of the purported lower mass gap [21, 313]. A mass distribution overlapping with the mass gap, such as ours, is supported in theory by the 'delayed' supernova explosion model from which our population is drawn [68].

Future GW observations will continue to test the robustness of the lower mass gap. If these observations do not support the lower mass gap, then BHNS systems such

as in our fiducial model, with low-mass and non-spinning BHs, would be a viable channel for EM radiation from BHNS mergers, in addition to the high-mass, high-spin systems identified previously and included in our population model variations. In this case, the requirements on the SN scenario to produce EM-bright BHNS mergers would not be as stringent as anticipated by Xing et al. [310]. In any case, including a population of systems with BHs in the mass gap, such as our fiducial model, is a novelty of our work and contributes to shifting the focus from high-spin BHs to low-mass BHs as progenitors for EM-bright BHNS mergers.

Finally, we checked that our prescription for the binary masses are consistent with the current (yet weak) constraints deduced from the first observations of BHNS mergers. To this effect, as reported in Appendix A.2.1, we compared the mass distributions of the NS and BH component of the systems in our BHNS population model with the constraints derived by [57] from the first detections of mergers in the GW domain. We find that, indeed, our prescriptions are consistent with the first constraints deduced from GW data, though these remain quite uncertain.

6.2.2 GW model

For each merger event, as a detection statistic, we computed the expected network matched-filter signal-to-noise ratio defined as (see e.g. Chap. 7 of [186] for a formal derivation)

$$(\mathrm{S/N})^2 = \sum_i (\mathrm{S/N})_i^2 \,, \quad (\mathrm{S/N})_i^2 = 4 \int_{f_{\min}}^{f_{\mathrm{cut}}} \frac{|\tilde{h}_{(i)}(f)|^2}{S_{n,i}(f)} \mathrm{d}f \,, \tag{6.1}$$

with the index i running over the detectors in the network, $f_{\min} = 10$ Hz, f_{cut} being a cutoff frequency determined by the events' parameters, $\tilde{h}_{(i)}(f)$ denoting the Fourier-domain GW strain projected onto the detector i and $S_{n,i}(f)$ the i^{th} IFO's noise power spectral density. We also computed the 90% credible sky localization area $\Delta\Omega_{90\%}$ for each signal. For O5, we assumed a network consisting of the two aLIGO, Advanced Virgo, KAGRA and LIGO-India (LVKI) with the projected O5 sensitivities Abbott et al. [14][2]; for O4 we did not consider LIGO-India (hence we assumed an LVK network) and we assumed the O4 sensitivities from Abbott et al. [14][2]. Both for the O4 and O5 scenarios, we performed the analyses with the inclusion of a 70% uncorrelated duty cycle for each detector (this is the same value adopted in [14]). The S/N and sky localization area computations were carried out through the `GWFAST` software package [155, 154], using the `IMRPhenomNSBH` waveform model [225, 89] which, in `GWFAST`, depends on the detector-frame chirp mass, the mass ratio, the dimensionless spins of the two binary components projected along the orbital angular momentum, the luminosity distance, the sky position, the binary inclination angle with respect to the line of sight, the polarization angle, the time of coalescence, the phase at coalescence and the tidal deformability of the neutron star [155]. For the parameters not discussed in Section 6.2.1, we draw the values from uninformative priors limited to their relevant physical range. We refer to Iacovelli et al. [155] for details on the prior ranges and definitions. `GWFAST` computes forecasts for the statistical uncertainty on the measurement of the source parameters resorting to the Fisher matrix approximation, which is valid in the high S/N limit [301]. The full likelihood is approximated by a multivariate Gaussian in the parameters, with covariance equal to the inverse of the

[2]The projected noise amplitude spectral densities we used can be found at https://dcc.ligo.org/LIGO-T2000012/public. For KAGRA we considered a target sensitivity of 10 Mpc in O4 and 127 Mpc in O5. For the other detectors we assumed the highest target sensitivity.

Fisher matrix. The error on the sky localization is computed as [40]

$$\Delta\Omega_{90\%} = 2\pi \ln 10 \, |\sin\theta| \sqrt{C_{\theta\theta} C_{\phi\phi} - C_{\theta\phi}^2}, \tag{6.2}$$

where θ and ϕ here represent the polar and azimuthal angles of the source position in the sky in a geocentric frame (they are related to the right ascension and declination as RA $= \phi$ and dec $= \pi/2 - \theta$, respectively), and $C_{\theta\theta}$, $C_{\theta\phi}$ and $C_{\phi\phi}$ are the relevant elements of the covariance matrix as estimated from the Fisher information matrix.

To keep the inversion error of the Fisher matrix under control in the subspace $\{\theta, \phi\}$, we resort to a Singular Value Decomposition (SVD) and eliminate from the inversion singular values below a threshold value of 10^{-10} [99]. This allows in particular to avoid numerical instabilities in presence of strong correlations between distance and inclination. This is particularly relevant for GW events with an associated GRB emission, which are usually close to face-on. We refer to Section 2 and App. D of Iacovelli et al. [154] for a detailed discussion of this issue and for a comparison of different inversion methods.

6.2.3 EM emission models

For all events in our population we computed the expected mass in dynamical ejecta $m_{\rm dyn}$ and the average velocity $v_{\rm dyn}$, and the mass $m_{\rm out}$ remaining outside the remnant BH, using the numerical relativity-informed fitting formulae from Krüger and Foucart [171, their Eq. 9], Kawaguchi et al. [163, their Eq. 1] and Foucart, Hinderer, and Nissanke [116, their Eq. 4]. In cases where $m_{\rm dyn} > 0.5 m_{\rm out}$ as predicted by these formulae, we imposed $m_{\rm dyn} = m_{\rm dyn}^{\rm max}(m_{\rm out}) = 0.5 m_{\rm out}$ [113, 250]. Finally, we computed the mass of the accretion disk as $M_{\rm disk} = m_{\rm out} - m_{\rm dyn}$.

We utilized the obtained outcomes as inputs to calculate the observable properties of the EM counterparts associated with each binary in our population, following a procedure analogous to Colombo et al. [78] and Barbieri et al. [44, 41]. In particular, we computed the KN light curves in the g (484 nm central wavelength), z (900 nm), and J (1250 nm) bands, employing the anisotropic multi-component model presented in Breschi et al. [66], based on Perego, Radice, and Bernuzzi [230]. For events with $M_{\rm disk} > 0$, we assumed the system to launch a relativistic jet whose energy $E_{\rm c}$ was computed following the method described in Colombo et al. [78]. This method relies only on estimates of the post-merger physical quantities of remnant and disk mass and is applicable to both BHNS and BNS systems. If the ratio of jet energy to ejecta mass surpassed the threshold based on Duffell et al. [97, their Eq. 20], we assumed that the relativistic jet successfully breaks out from the ejecta cloud, leading to the production of both GRB prompt and afterglow emissions.

In order to compute the observables associated to the relativistic jet, the jet's angular structure has to be specified, i.e. the angular profile of the jet isotropic-equivalent energy $E(\theta)$ and bulk Lorentz factor $\Gamma(\theta)$, as a function of the latitude θ of the material from the jet axis [e.g. 270]. We considered two variations. In the first we assumed the same structure used in Colombo et al. [78], inspired by the GRB 170817A structure as inferred by Ghirlanda et al. [125]. It features a uniform jet core of half-opening angle $\theta_j = 3.4^\circ$ outside of which the energy falls off as a power law $E \propto \theta^{-5.5}$ and the bulk Lorentz factor as $\Gamma \propto \theta^{-3.5}$. The bulk Lorentz factor in the core was fixed at $\Gamma_{\rm c} = 250$. The core isotropic-equivalent energy was set based on the requirement that the total jet energy equals a fraction of the accretion disk rest-mass energy, following the method described in [44, 78]. In brief, such fraction is $\sim 10^{-3}$ if the remnant BH spin is $a_{\rm BH,rem} \sim 0.7$ [based on the accretion-to-jet

energy conversion efficiency of GW170817 as estimated in 264], and the dependence on $a_{\rm BH,rem}$ is based on the [60] mechanism efficiency as derived in Tchekhovskoy, Narayan, and McKinney [296].

In order to compute the photon flux in the gamma-ray detector band, an additional assumption on the spectrum is needed. We obtained it by assuming a latitude-independent comoving spectral shape that is a power law with an exponential cut-off, with a comoving νF_ν peak photon energy $E'_{\rm peak} = 3.2\,{\rm keV}$ (similar to [266] and identical to [78]), and summing the contributions from all jet latitudes after accounting for relativistic beaming, as done in Salafia et al. [267]. We defer the reader to Appendix B of Colombo et al. [78] for more details on the computation of the prompt emission properties.

While the choice of such a structure facilitates the comparison with our BNS results from Colombo et al. [78], the typical jet structure of BNS and BHNS jets could arguably differ, due to the distinct environments in which the corresponding jets are launched. In particular, the jet self-collimation due to the development of a hot, over-pressured cocoon may be less effective owing to the presumably lower density in the polar region of the BHNS post-merger system, with respect to a BNS system [69, 96]. Indeed, in the latter, shock-driven ejecta arising from the collision of the two stars are expected to lead to a more isotropic distribution of dynamical ejecta compared to to the BHNS case [114], in which dynamical ejecta are primarily produced near the equatorial plane due to tidal disruption of the NS [163]. In addition, the intermediate supra- or hyper-massive NS state in BNS mergers, which is expected to generate strong post-merger winds [e.g. 107, 158], is absent in the BHNS case. For these reasons, we also considered a larger jet half-opening angle $\theta_j = 15^\circ$, which is our second variation for the choice of the jet structure. In this case, we left all the other jet structure parameters unchanged, with the exception of the jet core isotropic-equivalent energy $E_{\rm c} = E(0)$, which was rescaled to keep the total jet energy constant (see Figure 4.2).

For each jet structure, we generated afterglow light curves spanning from 0.1 to 1000 days in the radio (1.4 GHz), optical (g band), and X-rays (1 keV) assuming a fixed interstellar medium number density of $n = 5 \times 10^{-3}, {\rm cm}^{-3}$ (the median density in the [112] sample) and employing afterglow microphysical parameters of $\epsilon_{\rm e} = 0.1$, $\epsilon_{\rm B} = 10^{-3.9}$, and $p = 2.15$, representative values for GW170817, as reported in Ghirlanda et al. [125]. These physical parameters pertain to the microphysical behavior in the shock system formed when the jet decelerates in the circum-burst medium. Therefore, they are set solely by the jet's energy and Lorentz factor, which we have chosen to be as inferred in GW170817, hence our choice of microphysical parameters as in GW170817. Concerning the GRB prompt, we employed a semi-phenomenological model, similar to the approach utilized in previous studies such as Barbieri et al. [44] and Salafia et al. [266]. This model assumes that a constant fraction $\eta_\gamma = 0.15$ [52] of the jet energy density, limited to regions with a bulk Lorentz factor $\Gamma \geq 10$, is radiated in the form of photons with a fixed spectrum in the jet comoving frame [78, Section B.3]. The observed spectrum was then derived by integrating the resulting radiation across the solid angle of the jet, accounting for relativistic beaming at the relevant viewing angle.

6.2.4 Multi-messenger detection criteria

The sub-population of BHNS systems that will be detectable and that can provide MM datasets is determined by the instruments available for the GW observations and the follow-up efforts.

For the detection of the GW signals in both O4 and O5, we applied a network S/N threshold of 12. This limit is the same as that assumed in our previous study of BNS systems [78] and it is representative of the S/N threshold for a confident detection by the LVK Collaboration [14]. Such relatively high S/N cut also makes the `GWFAST` Fisher-information-matrix-based parameter estimation forecast more reliable [154].

For EM follow-up during O4, we adopted the same limits in the radio, optical, X-ray and gamma-ray bands as in Colombo et al. [78], that is, a limiting radio flux density of 0.1 mJy at 1.4 GHz, representative of the limits for current radio arrays adopting the 'galaxy targeted' or 'unbiased' search strategies [e.g. 92]; optical and near-infrared limiting AB magnitudes of $g < 22$, $z < 22$ and $J < 21$ respectively, in line with the typical depths reached in EM counterpart searches during the O3 run [e.g., 83, 26, 34] and with new wide-field instruments [87, 182]; X-ray limiting flux of 10^{-13} erg/cm^2/s/keV at 1 keV, representative of the limits that can be reached by Chandra or XMM-Newton with long exposures ($\sim 10^4$ s, e.g., [192]; [85]); in the gamma-ray band for the detection of the GRB prompt emission, a limiting 10-1000 keV average photon flux of 4 ph cm^{-2} s^{-1}, as deduced from the cumulative distribution of photon fluxes of GRBs in *Fermi*/GBM which is our reference instrument [78, Appendix B.3].

From O4 to O5, we expect a significant improvement in the depth of the search for counterparts in the radio and optical bands, owing to new instruments coming online. In the radio band, we considered an order of magnitude improvement with a limiting flux of 0.01 mJy [92]. We note that this flux level was approximately that of the afterglow in GW170817 upon discovery in the $3-6$ GHz bands in deep searches at the location of the KN transient [11, 188], but this level could be reached by the next-generation instruments in untargeted counterpart searches, such as the SKA2 [65], Next-Generation VLA [81] or DSA-2000 [143].

In the optical band, we accounted for the arrival of new large field of view (FoV) instruments such as the Vera Rubin Observatory [aka, 'the Rubin Observatory' 156]. For this purpose, we considered a magnitude threshold of 26 in the g band and 24.4 in the z band, corresponding to the limit reached in the preferred follow-up strategy suggested for the target-of-opportunity program of Rubin Observatory [180 s exposure, 35].

However, for the X-ray and gamma-ray bands, we considered the same limits in O5 as in O4, due to the later launching of the next generation of high-energy instruments with significant improvements in both the FoV and sensitivity, such as *THESEUS* [30], *HERMES* [110] or the *Gamow Explorer* [308, pp. 2030+]. Although we did not consider these instruments for follow-up in O4 and O5, in Section 6.6.2 we developed new follow-up strategies tailored to BHNS mergers inspired by recently proposed strategies for upcoming large-FoV X-ray instruments, such as *ATHENA*/WFI [211] which could tile the GW localization skymap in search for the X-ray afterglow counterpart [258].

We stress that, in this work, we operated on the premise that the GW sky localization areas of O4 and O5 BHNS mergers will consistently be surveyed to the assumed detection thresholds by the combined efforts of various observatories, as evidenced by the EM counterpart searches following the BNS event GW190425 [83, 150]. A more detailed evaluation of the actual detection rates attainable in practical terms would necessitate conducting simulations that mimic the search strategies implemented by individual facilities. In Section 6.5, we explore how our prospects for the detection rates change by varying our assumptions about the detection limits and the events sky localization.

6.3 Multi-messenger detection prospects

Using the synthetic population described in Section 6.2, we can determine the detection rates of BHNS mergers in the GW domain and in the various EM counterparts by applying S/N and peak brightness cuts to each of the events in the population. We start by presenting the results for our fiducial set of assumptions and then study the variations on the EoS, BH spin distribution, and jet core opening angle.

In Figure 6.2, we present cumulative detection rates as a function of redshift, with error propagated from the uncertainty on the intrinsic merger rate as described in Section 6.2.1 and from the uncertainty on the jet opening angle for the related emissions (see Figure 6.3 and below for the uncertainty on the assumptions of our population model).

In total, we expect a BHNS GW detection rate of $15.0^{+15.4}_{-8.8}$ yr^{-1} (90% confidence interval) for our assumed BHNS mass distribution and detection thresholds during O4. The cumulative rate of GW-detectable sources with an EM-detectable KN[3] (blue curve) follows the same trend as the distribution of GW detections up to a distance of 200 Mpc, indicating that the majority of KNæ in our population is luminous enough to be detected within this distance. Up to 200 Mpc, we expect 2.2% of GW triggers to give rise to a detectable KN. At $d_{\rm L} \gtrsim 200$ Mpc the cumulative rate of KNæ flattens out as an increasing number of KNæ fail to exceed the assumed detection thresholds, with the cumulative rate saturating at $0.16^{+0.17}_{-0.10}$ yr^{-1}, about two orders of magnitude lower than the total GW detections.

The cumulative rate of GW-detectable BHNS with an afterglow counterpart detectable in the radio band (red curve) features a shallower slope with respect to the GW or GW+KN cumulative rates, owing to the strong dependence of the afterglow peak brightness on the inclination angle. The total rate of radio afterglow detection is predicted to be $0.015^{+0.015}_{-0.009}$ yr^{-1}.

Concerning the GRB prompt emission (orange curve), we find a cumulative rate of GW-detectable events with an EM-detectable counterpart that increases with redshift with the same slope as that of GW events, hence with a constant ratio between the two rates on the order of 10^3. This is due to the fact that the prompt emission luminosity drops rapidly for viewing angles outside the jet core opening angle, such that the selection of the prompt emission boils down to simply a selection of solid angle, which does not vary appreciably with distance, on top of the GW detectability selection. The latter dominates in determining the GW+EM horizon, because the distance up to which the prompt emission is detectable for an on-axis observer largely exceeds the GW horizon.

It's important to emphasize that in the O4 scenario, we considered a full network with high target sensitivities as reported in Section 6.2.2. However, at the time of writing, only the LIGO Hanford and Livingston detectors are operational, with a BNS range between 140 and 170 Mpc. Virgo is expected to join the network in the second part of O4, scheduled to begin on March 27, 2024, with a target sensitivity of 40-80 Mpc. KAGRA will join the run in the spring of 2024, featuring a BNS range of approximately 10 Mpc [4]. Assuming a network consisting of only two aLIGO detectors would decrease our detection rates by about 14%. However, since the joint detection rates are low, even an optimistic assumption for the network does not change the general sense of our analysis. The effects of different network assumptions on the sky localization are discussed in Section 6.5.

[3] In the case of all EM+GW events, we display only one band in Figure 6.2 for clarity. The results for the other bands considered in the study can be seen in Table 6.1.

[4] Updates are available at https://observing.docs.ligo.org/plan/

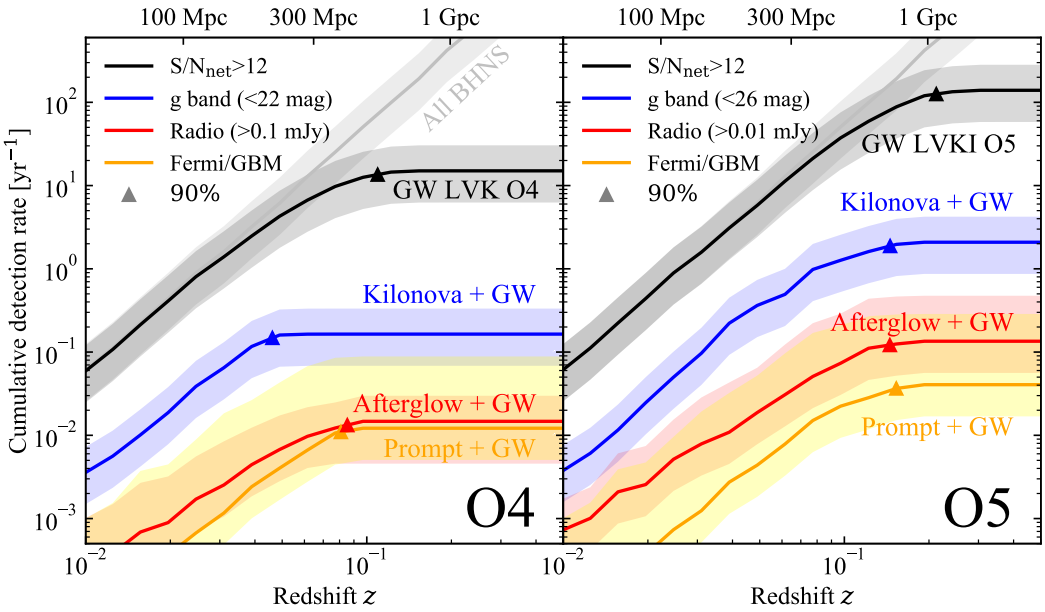

FIGURE 6.2: Cumulative MM detection rates as a function of redshift (luminosity distance) for our fiducial BHNS population (SFHo EoS, non-spinning BHs) and assuming a jet core half-opening angle $\theta_j = 3.4°$ for the jet-related emissions. Triangles indicate the 90$^{\text{th}}$ percentile of the cumulative detection rate (Figure 6.3 shows how this is affected when varying our assumptions). *Left-hand panel*: assumes the LVK network configuration and the O4 projected sensitivities. The light grey line ("All BHNS") represents the intrinsic merger rate, with the grey band showing its uncertainty drawn from that on the local merger rate. This uncertainty propagates as a constant relative error contribution to all the other rates shown in the figure. The error region for the jet-related emissions takes also into account a possible larger core half-opening angle $\theta_j = 15°$. The black ("GW LVK O4") line is the cumulative GW detection rate (events per year with network S/N $\geq$ 12) in O4. The blue ("Kilonova+GW"), red ("Afterglow+GW") and orange ("Prompt+GW") lines are the cumulative detection rates for the joint detection of GW plus either a KN, a GRB afterglow or a GRB prompt in O4 (all-sky except for the orange line, which accounts for the *Fermi*/GBM duty cycle and field of view). The assumed thresholds are shown in the legend. *Right-hand panel:* similar to the left-hand panel, but assuming an LVKI GW detector network with the O5 projected sensitivities, and deeper EM detection thresholds (see text).

Moving to O5, we find an overall increase in detection rates by one order of magnitude, which stems from both the better GW sensitivity and the deeper EM detection limits assumed. For the KN (blue curve), whose detection horizon is primarily determined by the EM threshold, the larger median distance of the GW-detected events is largely compensated by the expected increase in sensitivity of the optical searches, such that the KN detections track the GW detections up to a higher redshift. The GW detection rate increases up to 140^{+143}_{-81} yr^{-1}. The total detection rate of KN signals in O5 reaches a promising value of $2.1^{+2.1}_{-1.2}$ yr^{-1}, despite our conservative assumptions about the EoS and BH spin. The joint detection rate of GW along with GRB jet prompt emission (orange curve) and radio afterglow (red curve, whose horizon is mostly set by the GW sensitivity) also increases, but not as dramatically. GW-detectable systems with a detectable radio afterglow reach a total rate of $0.14^{+0.14}_{-0.08}$ yr^{-1}, similar to that of GW+KN in O4.

Intriguingly, some GW-detectable BHNS mergers with a detectable afterglow feature a KN whose peak brightness is below our assumed thresholds, opening the possibility for the afterglow being the primary counterpart to some BHNS systems

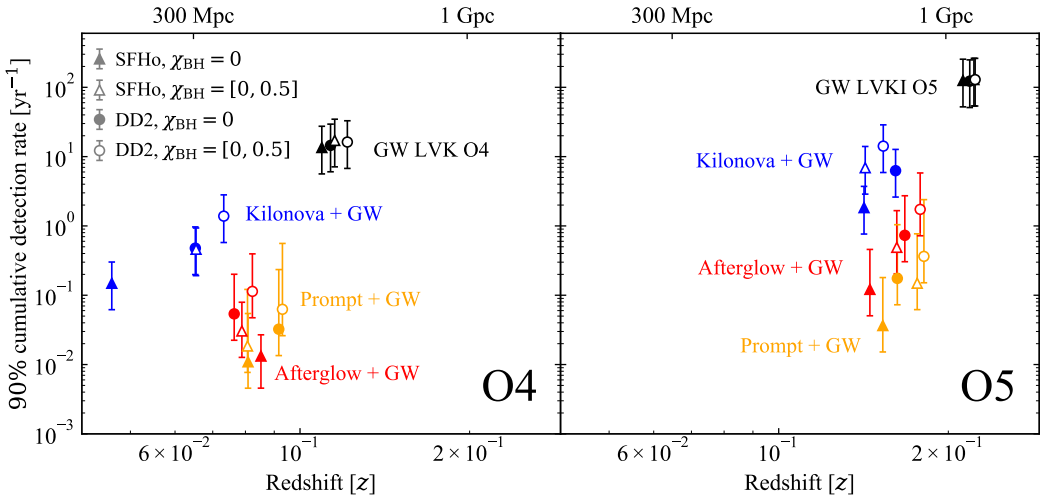

FIGURE 6.3: Predicted 90$^{\text{th}}$ percentile of the cumulative MM detection rates for our four population model variations, assuming a jet core half-opening angle $\theta_j = 3.4°$ for the jet-related emissions. Different marker shapes indicate different adopted EoSs (triangle: SFHo; circle: DD2). Filled markers are for $\chi_{BH} = 0$, while empty markers are for a uniform spin parameter distribution between 0 and 0.5. The error bars indicate the uncertainty on the local merger rate. For GRB afterglow and prompt they also take into account a variation on the jet core half-opening angle ($\theta_j = 15°$). Similarly as in Figure 6.2, the left-hand panel assumes an LVK GW-detector network and the O4 projected sensitivities, while the right-hand panel assumes an LVKI network and the O5 sensitivities. EM bands and detection thresholds are the same as in Figure 6.2.

in O5. We come back to this point in Section 6.6.2. Even in O5, the rate of GW-detectable BHNS with a detectable GRB prompt emission remains lower than one in 10 years, making the prospects for such events not particularly promising. Under the assumption of a larger opening angle for the jet, as explored in Secs. 6.4.2 and 6.4.3 with $\theta_j = 15°$ instead of $\theta_j = 3.4°$, we would expect a larger rate of GRB prompt counterparts, up to 1 yr^{-1}. Indeed the horizon for GRB prompt emission detection largely exceeds the GW horizon, such that GRB prompt detection is ensured for lines of sight looking into the jet.

We stress that the start dates, duration, and sensitivities projected for the O5 run are based on the best current estimates. Therefore, there is a possibility that the target sensitivities might be overestimated, as well as the inclusion of LIGO-India in the network from the beginning of the run. Removing LIGO-India from the network would decrease the detection rates by about 42%.

In both O4 and O5, the distance of the horizon for GW+EM events, i.e., the value of the redshift corresponding to the saturation of the curves, is smaller compared to the curve requiring just the GW detection. This is because only the lighter events, and therefore those with a smaller intrinsic S/N, are capable of emitting an EM counterpart, as highlighted in Figure 6.1. Thus, the GW+EM horizon is set by the GW detection of events with a BH smaller than a certain value.

The results in Figure 6.2 are affected by the uncertainty in the intrinsic BHNS merger rates. Moreover, they are affected by the uncertainty on the BHNS formation pathway that determines the binary parameter distribution (e.g., BH mass, mass ratio, and spins) and on the NS EoS. In Figure 6.3, we study the effect of this uncertainty through the variations of two assumptions of our population model. For simplicity, we only show the 90 percentile of the cumulative detection rate for GW and EM signals at the redshift where this value is reached for visualization purposes.

Concerning the GW detections (black symbols with black error bars), the variations of the NS EoS and $\chi_{\rm BH}$ prior induce a negligible change in detection rate and distance, in line with the marginal effect of both the component spins and tidal deformability in the inspiral signal. In O4, the variations induce a large uncertainty of one order of magnitude in KN detection rate (blue symbols), which largely surpasses the intrinsic uncertainty on the BHNS merger rate that we normalize our population to. This increase in KN detection rate follows with a large increase in redshift distance to which they are observable. This shows the crucial role of formation channel and NS properties in the MM detection prospects and, in turn, the potential to constrain these with MM data in the future. The choice of the NS EoS, with the stiffer DD2, leads to a factor of a few more KN detections than SFHo, due to the larger ejecta mass. The spin distribution plays another significant role, with higher spins favoring the disruption of the NS and a significant amount of ejecta in the post-merger phase.

For the afterglow counterpart in the radio band (red symbols), the effect of a stiffer EoS is also present due to its influence on the disk mass. One must keep in mind that, beyond the binary parameters, the afterglow is also largely determined by the microphysics parameters of the jet's forward shock and the density of the circum-merger medium. The possible variation of these is another source of uncertainty. However, we focus here on the effects of EoS and BH spin distribution, because the effects of the afterglow parameters and of the density on MM population models have already been explored for BNSs, and are expected to be similar for BHNSs [e.g., 134, 101].

Considering the O5 run, the trends for O4 are reproduced in all the counterparts. However, the role of the EoS and BH spin in determining the detection rate of KNæ (blue symbols) is less important. This is due to the better optical limits we consider in O5, such that an overall larger fraction of KNæ is detectable (as discussed in Figure 6.2), hence a lesser sensitivity to the secondary effects.

To summarize these results, we present in Tab. 6.1 the total detection rates of BHNS mergers in the O4 and O5 runs for our fiducial population model and the three variations. In addition, in Section 6.5, we briefly consider the prospects of GW sky localization of the sources to discuss the MM results presented in this section. For a more detailed discussion of how to leverage the potential for source localization, see Section 6.6.2.

TABLE 6.1: Detection limits and predicted detection rates for O4 and O5, assuming our fiducial population model (SFHo EoS and $\chi_{\rm BH} = 0$) and three variations. For the jet-related emissions, we assume a half-opening angle $\theta_j = 3.4°$, while in parenthesis we report the rate assuming $\theta_j = 15°$. The GW detection limits refer to the $S/N_{\rm net}$ threshold. Near infrared and optical limiting magnitudes are in the AB system; radio limiting flux densities are in mJy @ 1.4 GHz; X-ray limiting flux densities are in erg cm^{-2} s^{-1} keV^{-1} @ 1 keV; gamma-ray limiting photon fluxes are in photons cm^{-2} s^{-1} in the 15–150 keV (*Swift*/BAT) or 10–1000 keV (*Fermi*/GBM) band. Detection rates are in yr^{-1}. The reported errors, given at the 90% credible level, stem from the uncertainty on the overall merger rate, while systematic errors are not included.

	GW	KN + GW			GRB Afterglow + GW			GRB Prompt + GW	
		J	z	g	Radio	Optical	X-rays	*Swift*/BAT	*Fermi*/GBM
LVK O4									
Limit	12	21	22	22	0.1	22	10^{-13}	3.5	4
Rate SFHo, $\chi_{\rm BH} = 0$	$15.0^{+15.4}_{-8.8}$	$0.05^{+0.05}_{-0.03}$	$0.16^{+0.17}_{-0.10}$	$0.16^{+0.17}_{-0.10}$	$0.015^{+0.015}_{-0.009}$	$0.002^{+0.002}_{-0.001}$	$0.02^{+0.02}_{-0.01}$	$0.002^{+0.002}_{-0.001}$	$0.012^{+0.013}_{-0.007}$
($\theta_j = 15°$)					$(0.011^{+0.011}_{-0.006})$	$(0.001^{+0.001}_{-0.001})$	$(0.05^{+0.05}_{-0.03})$	$(0.007^{+0.007}_{-0.004})$	$(0.044^{+0.045}_{-0.026})$
Rate SFHo, $\chi_{\rm BH} = [0, 0.5]$	$16.1^{+16.6}_{-9.4}$	$0.29^{+0.30}_{-0.17}$	$0.54^{+0.55}_{-0.31}$	$0.53^{+0.55}_{-0.31}$	$0.06^{+0.06}_{-0.03}$	$0.014^{+0.015}_{-0.008}$	$0.08^{+0.08}_{-0.04}$	$0.006^{+0.006}_{-0.004}$	$0.04^{+0.04}_{-0.02}$
($\theta_j = 15°$)					$(0.10^{+0.11}_{-0.06})$	$(0.02^{+0.02}_{-0.01})$	$(0.22^{+0.23}_{-0.13})$	$(0.04^{+0.04}_{-0.02})$	$(0.20^{+0.21}_{-0.12})$
Rate DD2, $\chi_{\rm BH} = 0$	$19.0^{+19.5}_{-11.1}$	$0.30^{+0.31}_{-0.18}$	$0.56^{+0.57}_{-0.33}$	$0.54^{+0.56}_{-0.32}$	$0.03^{+0.04}_{-0.02}$	$0.007^{+0.007}_{-0.004}$	$0.04^{+0.04}_{-0.02}$	$0.003^{+0.003}_{-0.002}$	$0.02^{+0.02}_{-0.01}$
($\theta_j = 15°$)					$(0.04^{+0.05}_{-0.03})$	$(0.004^{+0.004}_{-0.002})$	$(0.11^{+0.11}_{-0.06})$	$(0.2^{+0.02}_{-0.01})$	$(0.12^{+0.12}_{-0.07})$
Rate DD2, $\chi_{\rm BH} = [0, 0.5]$	$18.0^{+18.5}_{-10.5}$	$0.97^{+0.99}_{-0.56}$	$1.57^{+1.61}_{-0.92}$	$1.55^{+1.60}_{-0.91}$	$0.13^{+0.13}_{-0.07}$	$0.03^{+0.03}_{-0.02}$	$0.16^{+0.16}_{-0.09}$	$0.012^{+0.012}_{-0.007}$	$0.07^{+0.07}_{-0.04}$
($\theta_j = 15°$)					$(0.21^{+0.21}_{-0.12})$	$(0.03^{+0.03}_{-0.02})$	$(0.55^{+0.57}_{-0.32})$	$(0.09^{+0.09}_{-0.05})$	$(0.5^{+0.5}_{-0.3})$
LVKI O5									
Limit	12	21	24.4	26	0.01	26	10^{-13}	3.5	4
Rate SFHo, $\chi_{\rm BH} = 0$	140^{+143}_{-81}	$0.08^{+0.08}_{-0.05}$	$1.5^{+1.6}_{-0.9}$	$2.1^{+2.1}_{-1.2}$	$0.14^{+0.14}_{-0.08}$	$0.05^{+0.05}_{-0.03}$	$0.07^{+0.07}_{-0.04}$	$0.008^{+0.008}_{-0.005}$	$0.04^{+0.04}_{-0.02}$
($\theta_j = 15°$)					$(0.23^{+0.24}_{-0.14})$	$(0.07^{+0.08}_{-0.04})$	$(0.18^{+0.19}_{-0.11})$	$(0.03^{+0.03}_{-0.01})$	$(0.15^{+0.15}_{-0.09})$
Rate SFHo, $\chi_{\rm BH} = [0, 0.5]$	136^{+140}_{-80}	$0.48^{+0.49}_{-0.28}$	$5.6^{+576}_{-3.3}$	$7.0^{+7.2}_{-4.1}$	$0.81^{+0.83}_{-0.47}$	$0.23^{+0.24}_{-0.14}$	$0.33^{+0.34}_{-0.20}$	$0.04^{+0.05}_{-0.02}$	$0.20^{+0.20}_{-0.11}$
($\theta_j = 15°$)					$(1.46^{+1.50}_{-0.85})$	$(0.73^{+0.75}_{-0.43})$	$(1.22^{+1.25}_{-0.71})$	$(0.17^{+0.19}_{-0.09})$	$(0.92^{+0.94}_{-0.54})$
Rate DD2, $\chi_{\rm BH} = 0$	144^{+148}_{-84}	$0.53^{+0.54}_{-0.31}$	$6.8^{+6.9}_{-3.9}$	$7.9^{+8.1}_{-4.6}$	$0.55^{+0.56}_{-0.32}$	$0.21^{+0.21}_{-0.12}$	$0.27^{+0.27}_{-0.15}$	$0.03^{+0.03}_{-0.02}$	$0.17^{+0.17}_{-0.10}$
($\theta_j = 15°$)					$(0.92^{+0.95}_{-0.54})$	$(0.42^{+0.43}_{-0.25})$	$(0.92^{+0.94}_{-0.53})$	$(0.12^{+0.16}_{-0.06})$	$(0.64^{+0.65}_{-0.37})$
Rate DD2, $\chi_{\rm BH} = [0, 0.5]$	144^{+147}_{-84}	$1.6^{+1.7}_{-0.9}$	$13.4^{+13.8}_{-7.8}$	$15.9^{+16.4}_{-9.3}$	$1.9^{+2.0}_{-1.1}$	$0.47^{+0.49}_{-0.28}$	$0.71^{+0.73}_{-0.41}$	$0.07^{+0.08}_{-0.04}$	$0.4^{+0.4}_{-0.2}$
($\theta_j = 15°$)					$(3.2^{+3.3}_{-1.9})$	$(1.7^{+1.8}_{-1.0})$	$(2.8^{+2.9}_{-1.6})$	$(0.4^{+0.5}_{-0.2})$	$(2.2^{+2.2}_{-1.3})$

6.4 Detailed study of the detectable EM signals

We now turn to detailed studies of the different EM counterparts.

6.4.1 Kilonova

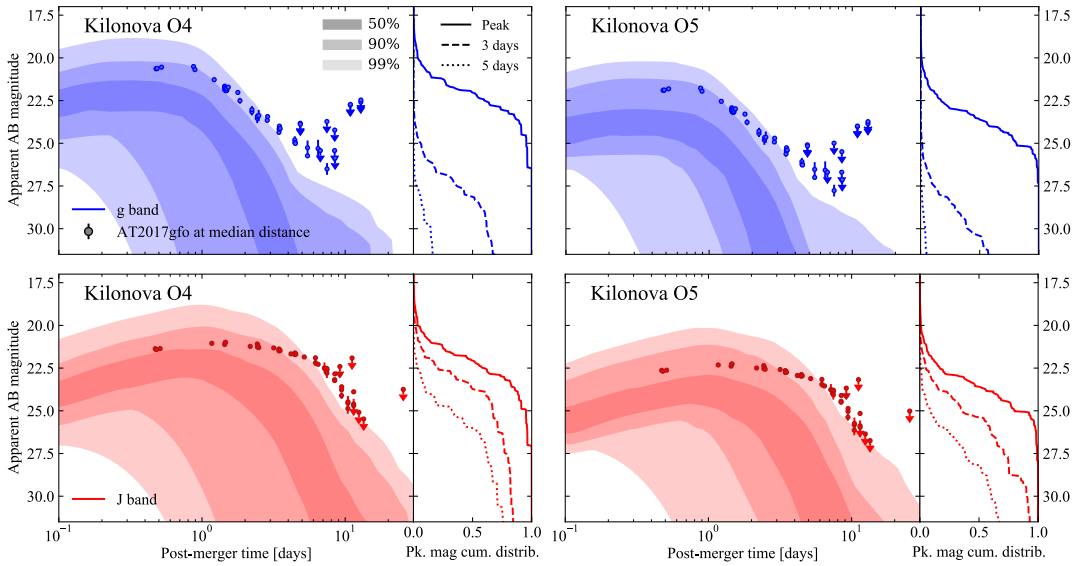

FIGURE 6.4: Distribution of O4 (left-hand panel) and O5 (right-hand panel) KN g band (484 nm, upper panel in blue) and J band (1250 nm, lower panel in red) magnitudes as a function of time. The shaded regions show the apparent AB magnitude versus post-merger time for 50%, 90% and 99% of our simulated KN light curves GW-detectable sources. Colored circles show extinction-corrected AT2017gfo data rescaled to the median distance of the GW triggers ($\sim$ 212 Mpc in O4, $\sim$ 381 Mpc in O5). The solid, dashed and dotted lines show the cumulative distributions of apparent magnitude at peak, at 3 days and at 5 days after the merger, respectively.

In Figure 6.4, we plot the distributions of the g and J band KN light curves of the GW-detectable events for the O4 and O5 runs, with the photometry of the KN signal associated with GW170817, AT2017gfo, at the median distance of the GW-detectable events with $m_{\rm out} > 0$ ($\sim$ 212 Mpc in O4, $\sim$ 381 Mpc in O5). We took the photometric data from Villar et al. [307]. We note that, for the first few days, the typical BHNS KN light curve is at least two magnitudes dimmer than AT2017gfo, signaling the intrinsic weakness of the BHNS KN with respect to BNS KN sources at the origin of the low detection prospects described in Section 6.3.

By applying the detection threshold we considered in O4 and O5 (22 and 26 magnitudes for the g band, respectively and 21 for the J band), we find that most of the KNæ are undetectable in O4, whereas a majority of them are detectable in O5 in the g band. Indeed, the magnitude threshold is slightly above the median peak magnitude of O4 and largely below for O5. This explains the jump in KN-detectable fraction that was found in Figure 6.2 and the lesser effect of the EoS and spin distributions in Figure 6.3.

However, the distribution of magnitudes at 3 days post-merger shows that, even the deep limits considered in O5 are too shallow to detect the signal by this time. In fact, the distribution of light curves suggests that the post-peak dimming is even faster than for AT2017gfo. This poses the well-known issue of detecting the KN counterpart in time before it dims away, which has been a limiting factor in follow-up

searches, notably because of the large GW skymaps. This issue is partially solved by considering infrared bands, where the signal is longer-lived. However, our numbers show that the weaker sensitivity of instruments, e.g. in the z and J bands, hinders the detectability prospects in these bands. This can be solved by large-FoV optical instruments such as the dedicated ZTF or survey instruments with a ToO program such as the Rubin Observatory [35]. An additional solution to the recession of the GW horizon and the dimming KNæ is to search for the non-thermal counterparts such as the radio afterglow directly with tiling instruments, a strategy that is available to upcoming radio surveys and that we will study further in Section 6.6.2.

6.4.2 GRB afterglow

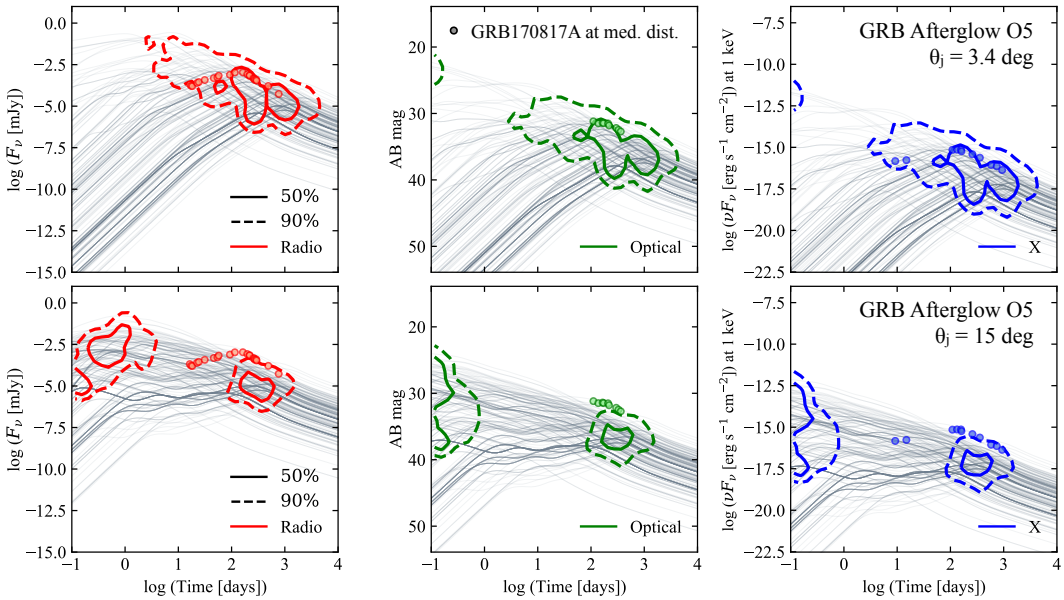

FIGURE 6.5: F_ν, AB magnitude and νF_ν versus time for the GRB afterglow light curves associated to O5-detectable sources in our population. In the top panel we assume a jet core half-opening angle $\theta_j = 3.4°$, in the lower panel we assume $\theta_j = 15°$. Solid and dashed contours contain 50% and 90% of the peaks, respectively. Red, green and blue colors indicate the radio (1.4×10^9Hz), optical (4.8×10^{14}Hz), X-ray (2.4×10^{17}Hz) bands, respectively. The colored circles are the observed data of GRB170817A [188] at the median distance of the GW triggers. The gray lines in the background are 300 randomly sampled light curves in the respective bands.

In Figure 6.5 we show the properties of GRB afterglows associated with O5 GW-detectable binaries in our population by showing the contours containing 50% (solid lines) and 90% (dashed lines) of GRB afterglow peaks on the F_ν (AB magnitude, νF_ν) versus observer time plane. The red, green, and blue colors refer to the radio, optical, and X-ray bands, respectively. In the upper panel, we assume a jet half opening angle of $\theta_j = 3.4°$ and in the lower panel of $\theta_j = 15°$. In the narrow jet population, most peak times are at ≥ 10 days, with a small subsample peaking at early times ($\sim$ hours) in the optical and X-rays, producing very bright emission, due to on-axis events with small viewing angles. In the population with a larger opening angle of 15°, more jets can fall within the viewing angle of the observer. As a result, the number of on-axis events will increase compared to the narrow jet population, leading to the bimodality of the distribution of afterglow peaks at short and long times apparent in the bottom panels of Figure 6.5. In order to help visualize the underlying light-curve

behavior, we display 300 randomly sampled afterglow light curves from our GW triggers (thin gray lines) in the background (the band is the same as the respective contours). The small circles indicate GRB 170817A data [188] at the median distance of our population of GW triggers with $m_{\rm out} > 0$ ($\sim$ 381 Mpc in O5), whose peak lies within the 50% (90%) contours in all three bands, assuming $\theta_j = 3.4^\circ$ ($\theta_j = 15^\circ$).

6.4.3 GRB prompt

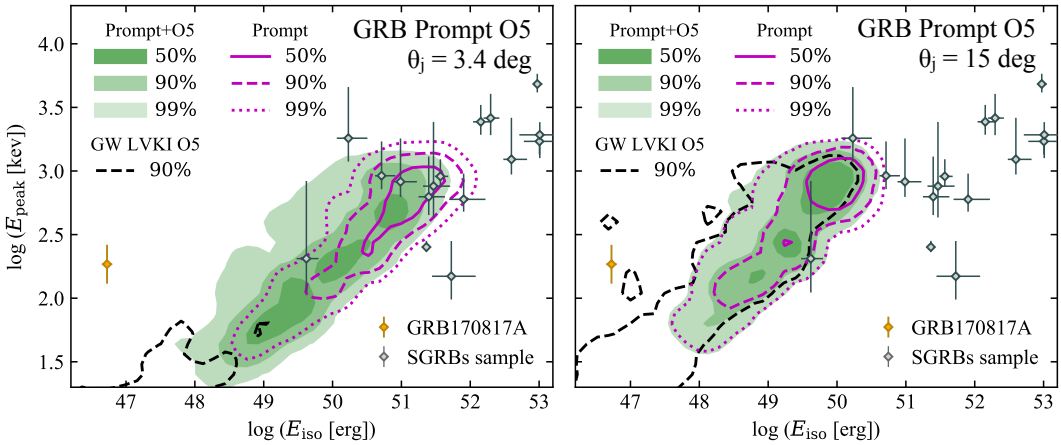

FIGURE 6.6: Rest-frame SED peak photon energy $E_{\rm peak}$ versus the isotropic-equivalent energy $E_{\rm iso}$ for our BHNS population. In the top panel we assume a jet core half-opening angle $\theta_j = 3.4^\circ$, in the lower panel we assume $\theta_j = 15^\circ$. The filled green colored regions contain 50%, 90% and 99% of the binaries both GRB Prompt- and LVKI 05-detectable. The magenta lines contain 50%, 90% and 99% (solid, dashed and dotted, respectively) of the GRB prompt-detectable binaries. The black dashed line contains 90% of the O5-detectable binaries. The black dots with error bars represent a SGRB sample for comparison [268]. The orange dot is GRB170817A.

In order to visualize the GRB prompt emission parameter space accessible by multi-messenger observations, in Figure 6.6 we show how the rest-frame spectral energy distribution (SED) peak energy $E_{\rm peak}$ and the isotropic-equivalent energy $E_{\rm iso}$ are distributed for events that satisfy our detectability criteria for the GW signal, the GRB prompt emission, or both. The two variations in the jet half-opening angle are displayed in two separate panels: $\theta_j = 3.4^\circ$ (right panel) and $\theta_j = 15^\circ$ (left panel). Green filled contours refer to events that can be jointly detected by the O5 LVKI network and *Fermi*/GBM: different shades of green contain a progressively higher fraction (50%, 90%, and 99%) of the joint GRB prompt- and O5-detectable binaries. The black dashed contour contains 90% of the events that are detectable in GW. The magenta contours contain 50%, 90% and 99% of events detectable by *Fermi*/GBM.

For comparison with the known cosmological population, we show with gray diamonds the properties of a sample of short GRBs (SGRBs) with known redshift [268]. The orange diamond in the plot corresponds to the position of GRB 170817A.

Given the monotonic dependence on the viewing angle of both $E_{\rm iso}$ and $E_{\rm peak}$, as shown in Figure 4.2, the GRBs in our model naturally feature an "Amati" correlation [29, 299], with events on the upper-right part of the plane observed close to on-axis and events with lower $E_{\rm iso}$ and $E_{\rm peak}$ observed farther from the jet axis [see 268, for a detailed explanation of why and how this kind of correlation is induced by the presence of an angular jet structure]. The contours show clearly that Fermi/GBM preferentially detects events close to on-axis (actually, close to $\theta_{\rm j}$ where the accessible

solid angle is maximised); the GW detectors preferentially detect events with a larger viewing angle (peaking at around 30° due to a trade-off between the larger solid angle and the weaker GW strain with increasing viewing angle, e.g. [278]); joint GRB plus GW detections occupy a region in between these two, especially for $\theta_j = 3.4^\circ$ where the peaks of the GW and GRB distributions are more widely separated.

The main impact of the two different jet core half-opening angle assumptions on these distributions consists in a horizontal shift towards lower E_{iso} for increasing θ_j. This is a consequence of the fact that we keep the total jet energy fixed when varying the opening angle, which implies that the maximum attainable E_{iso} for each jet (which corresponds to that measured by an on-axis observer) scales as θ_j^{-2}. This shows that, if the average opening angle of BHNS jets were indeed larger than that of BNS jets, and if the spectral properties of the prompt emission were otherwise similar as we assumed, then BHNS-associated GRBs would follow a distinct Amati correlation with respect to BNS-associated ones. This statement clearly rests on very uncertain assumptions and must therefore be taken with a grain of salt.

Inspection of Table 6.1 additionally shows that a larger θ_j positively impacts the joint GRB plus GW detection rate, despite the GRBs being dimmer overall. This is a consequence of the fact that, for the current generation of GW detectors, the horizon for a joint detection is set by the GW than by the GRB: while the latter can be detected in principle out to $z \gtrsim 2$, the former are currently accessible only out to $z \sim 0.1 - 0.3$ (see Figure 6.2).

6.5 Sky localization and detection limits

In Section 6.3 we show the detection rates for joint GW and EM events considering representative detection limits based on the typical depth that can be reached during a wide-field EM follow-up in response to a GW alert in O4 and O5, without information on the GW sky localization. In order to provide the community with the opportunity to explore alternative observing configurations that correspond to varying detection limits as well as constraining the sky localization, we report in Figure 6.7 and in Figure 6.8 the distribution of detection rates as a function of the detection limit for the joint EM+GW channels considered in this work, in O4 (upper panels) and O5 (lower panels).

In particular, in Figure 6.7 we show the detection rates for the GRB prompt+GW (left panel, orange) and GRB afterglow+GW (right panel, red) detectable binaries for our BHNS fiducial population (for KNæ this information is already displayed in Figure 6.4). For the GRB Prompt+GW detections, we showcase the rates under three different assumptions: we assume an all-sky field of view and a 100% duty cycle (solid line), we account for the duty cycle and field of view of *Fermi*/GBM (dashed line) and Swift/BAT (dotted line). Both in O4 and O5 the curves tend to flatten after a value of about 10 ph cm^{-2} s^{-1}, as the GRB prompt detection is limited by the GW detection. For the GRB afterglow+GW we show individually the rates for the radio (solid), optical (dashed), and X (dotted) bands. The saturation point of the curves indicates the sensitivity required to detect all the EM+GW events, resulting in a corresponding detection rate for the GRB afterglow and KN (see Figure 6.8) of $0.34^{+0.34}_{-0.20}$ yr^{-1} for the O4 run and $2.13^{+2.19}_{-1.25}$ yr^{-1} for the O5 run (assuming the SFHo EoS and $\chi_{BH} = 0$).

In order to provide additional information about the sky localization, in Figure 6.8 we show the detection rates as function of the detection limit for the KN+GW (in the g band) and GRB afterglow+GW (in the radio band), considering all the detectable

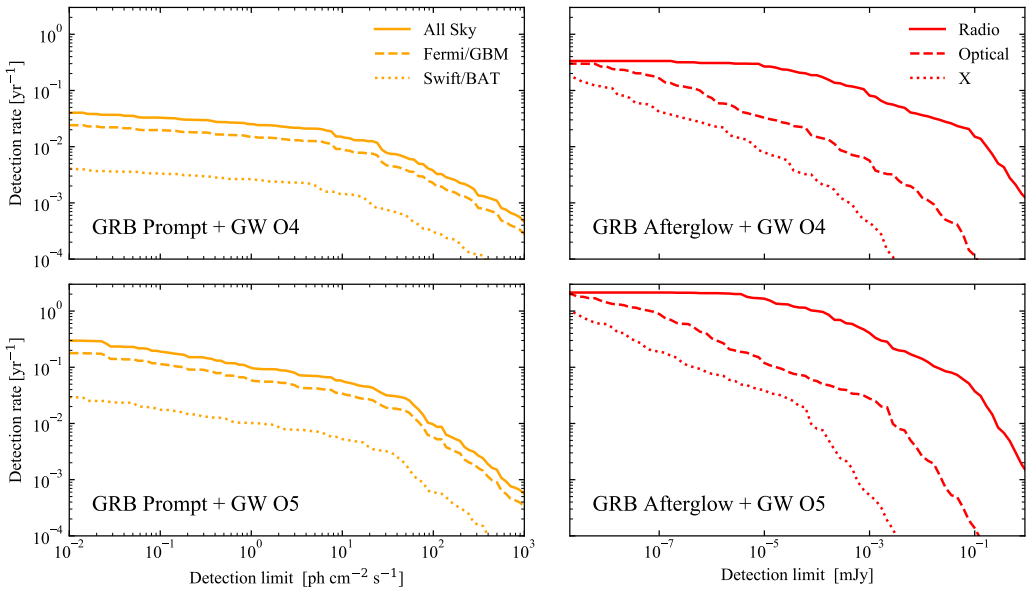

FIGURE 6.7: Detection rate as a function of detection limit threshold for our fiducial BHNS population. In the top panel we assume the LVK O4 detectors network, while in the lower panel we assume the LVKI O5 detectors, both with a 70% duty cycle for each detector. The orange and red colors indicate respectively the GRB prompt+GW and the GRB afterglow+GW detectable binaries. In the left panel, the solid line indicates an all-sky field of view with a 100% duty cycle, the dashed and dotted lines account for the *Fermi*/GBM and Swift/BAT duty cycle and field of view, respectively. In the right panel, the solid, dashed, and dotted lines indicate the radio, optical, and X bands, respectively.

binaries (solid lines), the detectable binaries with $\Delta\Omega_{90\%} < 100$ deg^2 (dashed lines) and the ones with $\Delta\Omega_{90\%} < 10$ deg^2 (dotted lines). In the top panel we assume the LVK O4 detectors network (colored lines) and a network consisting of only two aLIGO (black lines), while in the lower panel the LVKI O5 detectors network (colored lines) and the same network without LIGO–India (black lines).

In O4, as expected, there is a significant degradation in sky localization assuming a GW network without Virgo and KAGRA. However, the detection rates are still low for a complete network, due to the intrinsic challenges that we discussed previously, posed by the BHNS population. Regarding the O5 run, assuming the LVKI network, the sky localization is excellent, with nearly all events having $\Delta\Omega_{90\%} < 100$ deg^2. Furthermore, in the absence of LIGO-India, the presence of Virgo and KAGRA at their design sensitivities would result in only a twofold reduction in the rate relative to 100 square degrees, yielding a KN+GW rate of ~ 1 yr^1.

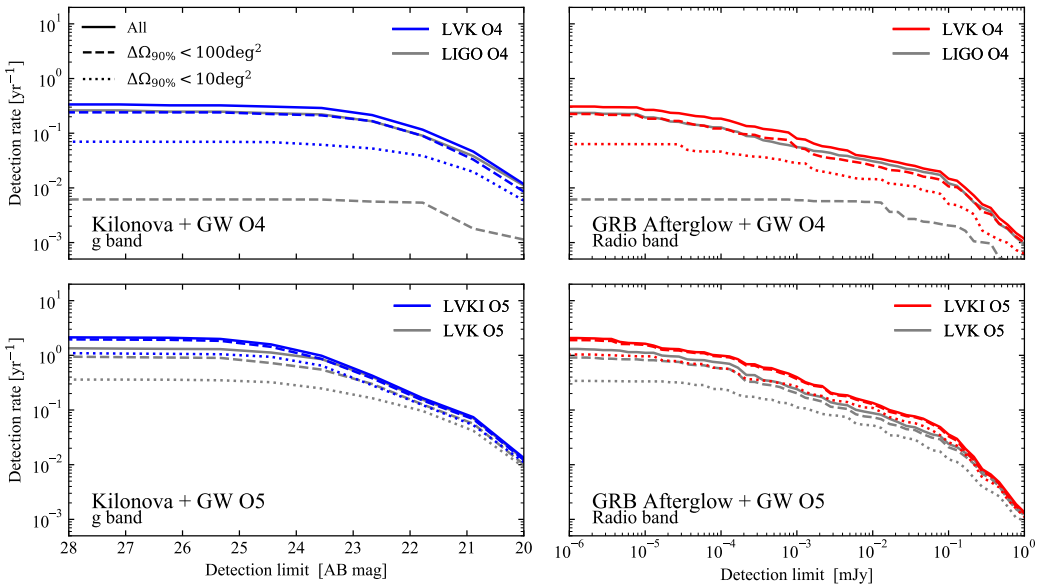

FIGURE 6.8: Detection rate as a function of detection limit threshold for our fiducial BHNS population. In the top panel we assume the LVK O4 detectors network (colored lines) and a network consisting of only two aLIGO (grey lines). In the lower panel we assume the LVKI O5 detectors network (colored lines) and the same network without LIGO–India (black lines). Every network is assumed with a 70% duty cycle for each detector. The blue and red colors indicate respectively the kilonova+GW (g band) and the GRB afterglow+GW (radio band) detectable binaries. The solid line indicates all the detectable binaries, the dashed and dotted lines the detectable binaries with $\Delta\Omega_{90\%} < 100\mathrm{deg}^2$ and the ones with $\Delta\Omega_{90\%} < 10\mathrm{deg}^2$, respectively.

6.6 Discussion

6.6.1 Comparison with other works with similar goals

As pointed out by Boersma and van Leeuwen [62], the distribution of BH spins plays a crucial role in determining the prospects of MM detections of BHNS mergers. This role is more important than the NS EoS, and the uncertainty due to the unknown spin distribution surpasses the uncertainty on the intrinsic BHNS merger rate. However, in contrast to Boersma and van Leeuwen [62], we find that the prospects for radio afterglow detections in the upcoming runs of the Ligo-Virgo-generation of GW interferometers are not that poor, assuming the radio instruments follow their planned development. In the O5 run with a limiting radio sensitivity of 0.01 mJy, the detection rate is no lower than 1 every few years in the fiducial model where BHs are non spinning, and can reach order 1 yr^{-1} in the case BHs are endowed with a moderate spin (see Tab. 6.1). The issue of localizing the source in order to discover the afterglow remains since we find that the likeliness of detecting a short GRB counterpart is low, as in Boersma and van Leeuwen [62], and more so in O5 than in O4. Even with the current generation of IFOs, the coming online of more GW detectors will decrease the expected size of the GW skymaps, and the deployment of more optimized follow-up strategies can help to meet the challenge of covering them.

In their KN modeling, Zhu et al. [315] follow an approach similar to ours when informing the parameters of a semi-analytical model (e.g., mass and opacity of various ejecta components) with numerical simulations. For the O5 run, we find a similar limiting magnitude of 23–24 in the visible bands found by Zhu et al. [315] to recover half of the KN counterparts, with the spinning-BH hypothesis (see Tab. 6.1). We also share their conclusion of the fast decay of these signals, possibly hindering their detection even three days post-merger. A possible way to circumvent this issue is to search for the afterglow using wide-FoV instruments to tile the GW skymap, as suggested in the X-rays by Ronchini et al. [258] and as we will discuss in Section 6.6.2.

Conversely, Zhu et al. [316] find a much larger rate of combined GW, GRB prompt and KN detections in O4 and O5 than we do. Interestingly, their study follows a very different method, which relies on the parameter inference of three long-duration GRBs that are hypothesized to be of BHNS-merger origin. Their analysis suggests massive-BH and highly-spinning BH progenitors, which could explain their much higher detection rates. Of course, this conclusion is highly dependent on the emission model they use to infer the properties of the progenitors of these three bursts. In any case, the comparison of our formation-channel-based work with studies such as Zhu et al. [316] underlines the importance of considering BHNS systems in all of their manifestations: as GW triggers with EM counterparts but also as the progenitors of a fraction of SGRBs ([129], or even some LGRBs, [recently, e.g., 249, 179]), for which the longer observation history can be an advantage over the GW triggers as a tool to study the population of BHNS mergers.

6.6.2 Direct searches for the radio afterglow with a titling strategy

In Section 6.3, we studied the detectability of the radio afterglow of merging BHNS systems at a fixed detection threshold of the radio flux. In practice, this criterion assumes knowing the location of the source, e.g., thanks to a detection of the KN before the afterglow searches. In the O2 and O3 GW observing runs, searching for the KN signal was seen as a stepping-stone to locate the event before performing deep searches for other EM counterparts, such as the relativistic jet's afterglow. Efforts in

TABLE 6.2: Relative number of GW-detectable systems with detectable GRB afterglows (radio band), with and without detectable KN, for our fiducial population model, in an O5-type run, and the two jet opening angle hypotheses. The threshold for GRB radio afterglow detection considered was 0.01 mJy. KN detection is defined by detection in g (24) or in z (22.5), see text for more details.

Fractions of GW triggers with detectable radio afterglow, among which:	$\theta_j = 3.4°$ O5	$\theta_j = 15°$ O5
KN detectable	67%	74 %
KN undetectable	33%	26%
KN undetectable & GRB prompt undetectable	12 %	15%

developing large-FoV optical instruments and networks of instruments were partly driven by the wish to ensure this KN detection, overcoming the potentially large uncertainties of GW skymaps.

However, as shown in the O3 run, and for those events likely hosting a NS, covering the GW skymaps in optical searches is challenging (we refer to GW190425 and the two BHNS systems; see Section 6.1 and, e.g., [83, 22]). In addition, our results show that most KNæ associated to BHNS systems remain undetectable for the majority of the GW triggers (see Tab. 6.1 and Figure 6.4). This should also be the case for BNS systems [e.g. 78]. Furthermore, detecting a KN is challenging considering its fast decay. This limitation motivates the development of new follow-up strategies to detect the afterglow emission without having first acquired the source's location thanks to the KN detection.

Luckily, the long duration of the radio afterglows due to the system's off-axis inclination angles, as exemplified in Figure 6.5, represents a significant advantage over the shorter-lived KNæ suggesting the direct search of the afterglow counterpart after a GW trigger with optimized follow-up strategies.

To quantify the gain in discovering the afterglow in absence of a KN counterpart we show in Tab. 6.2 the number of detectable BHNS afterglows with and without a detectable KN in an O5-type run. We considered a radio afterglow threshold of 0.01 mJy for O5 as in Section 6.3 and KN limits of 24 in g and 22.5 in z. In Section 6.3, we had considered a g-magnitude limit of 26 respectively for O5, representing the performance of a single deep instrument. However, due to limitations in sky coverage and instrument availability, it is likely that networks of optical instruments with shallower imagery will continue to play a significant role in kilonova discovery searches. Therefore, a more realistic estimate of the overall follow-up performance in O5 is a shallower limit of 24 in g.

The table shows that, in O5, 33% of GW triggers with a detectable afterglow do not present a detectable KN for $\theta_j = 3.4°$, and 26% for $\theta_j = 15°$. This suggests that relying on the KN as a stepping-stone for afterglow searches limits the potential for afterglow detection. As expected, inspection of this subclass of events shows that the afterglows without KN are mostly high-distance events with low inclination angles, close to the GW horizon. In addition, 12-15% of these afterglows present neither a KN nor a detectable GRB prompt emission, prohibiting the GRB prompt from providing localization data.

To bypass this dependence on the KN signal, we explore the possibility that large-FoV radio instruments can tile the GW skymap in search for the afterglow, as already considered for future radio arrays by Dobie et al. [92] and in the X-ray band for upcoming large-FoV instruments by Ronchini et al. [258]. In Figure 6.9,

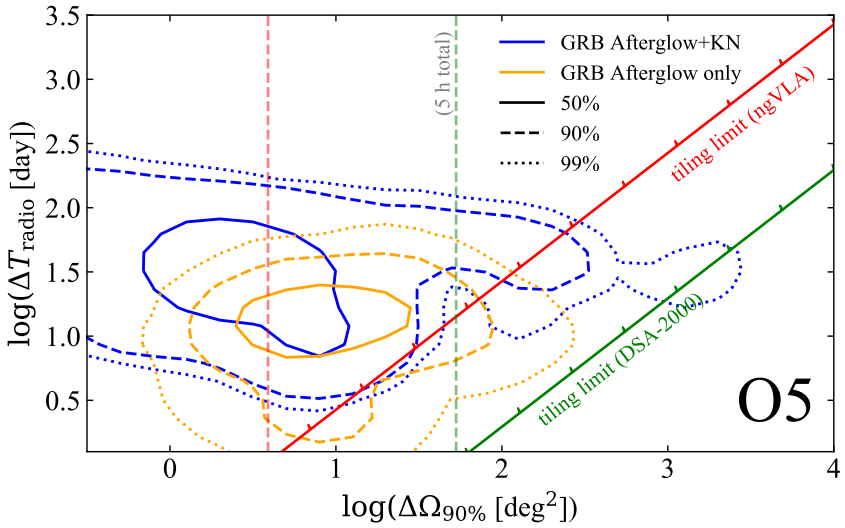

FIGURE 6.9: Population contours of the GW-detectable events in O5 with detectable radio afterglow in the plane of detectability interval of the afterglow versus 90%-confidence GW skymap size. We distinguish the events with a detectable (blue) or undetectable (orange) KN. The limiting fluxes and magnitudes for the radio afterglows and KN are as in Tab. 6.2. The green and red lines indicate the limit above which the tiling strategy is viable for the DSA-2000 and the ngVLA, respectively. That is, the GW skymap can be covered at least 5 times by tiles over the afterglow time of observability (Eq. 6.3). The vertical lines indicate the GW skymap sizes that require a total observing time of one and five hours to cover by the two instruments, using the same color code.

we show the contours of GW triggers with detectable radio afterglows in O5 runs, by distinguishing those with and without detectable KN, using the same radio and KN limits as in Tab. 6.2. The orange contours corresponds to the KN-less afterglows discussed in Tab. 6.2, which could be the target of this radio tiling strategy.

In this plot, a tiled search for the afterglow is only viable under the following condition:

$$\frac{\Delta T_{\rm radio}}{\Delta t_{\rm tile}} > N \times \frac{\Delta\Omega_{\rm GW}}{\Delta\Omega_{\rm FoV}} \tag{6.3}$$

such that the GW skymap of size $\Delta\Omega_{\rm GW}$ can be covered entirely at least N times by tiles of size $\Delta\Omega_{\rm FoV}$ in the time that the afterglow is detectable. Being able to cover the GW skymap more than once ensures to acquire enough photometry points to identify the afterglow among various transient sources. We added this integer N, that increases the observation time required to tile a GW skymap, also to capture the unmodelled effects of overheads in observations and gaps in instrument availability; one can consider a fiducial value of $N = 5$. Here, $\Delta t_{\rm tile}$ is the tiling period, that is, the time interval between two tiles, which we take to be the integration time for radio imagery, neglecting repointing time and similar overheads. $\Delta T_{\rm radio}$ is the afterglow detectability time interval, i.e., the time length during which the afterglow flux is above the radio threshold of the given instrument, as determined from our afterglow model (Section 6.2.3).

This tiling strategy is especially interesting for large-FoV instruments. We follow Dobie et al. [92] in considering the DSA-2000 [143] and the Next-Generation VLA (ngVLA, [279]), both instrument concepts with plans for a target-of-opportunity program. The DSA-2000 is a survey instrument with a single-image FoV of $\Delta\Omega_{\rm FoV} = 10.6\,{\rm deg}^2$ that can reach an rms sensitivity of 1 μJy in $\Delta t_{\rm tile} = 1$ h in the 2 GHz band

[143]. The ngVLA is a general-purpose radio array with a smaller FoV of $\Delta\Omega_{\rm FoV} = 0.13\,{\rm deg}^2$ and a shorter time of $\Delta t_{\rm tile} = 10\,{\rm min}$ to reach $1\,\mu{\rm Jy}$[5] in the same band.

In the radio tiling strategy, the critical factor is the tiling speed down to a given sensitivity:

$$\Sigma = \frac{\Delta\Omega_{\rm FoV}}{\Delta t_{\rm tile}}, \tag{6.4}$$

which, is $\Sigma_{\rm DSA} = 10.6\,{\rm deg}^2/{\rm h}$ and $\Sigma_{\rm ngVLA} = 0.78\,{\rm deg}^2/{\rm h}$ for the two instruments, respectively, down to $1\,\mu{\rm Jy}$.

In Figure 6.9, the green and red lines show the tiling limit according to Eq. 6.3 for the DSA-2000 and ngVLA. The dashed vertical lines indicate the GW skymap sizes that can be covered in five hours of total tiling observation by these instruments. We find that all of the KN-less GRB afterglows are in reach of the tiling strategy of DSA-2000 and most of them are in reach for ngVLA, thanks to their large tiling speeds. The limits of $1\,\mu{\rm Jy}$ for DSA-2000 and ngVLA, an order of magnitude deeper than the detection limits applied in Figure 6.9, would allow these instruments to make a good sampling of the light curves and identify the GRB afterglow transient. We note that, similarly to KN searches, once a transient candidate is identified by the radio searches, these candidates can be announced and monitored by other instruments, sharing the load of follow-up observations. In this scenario, the monitoring of radio candidates identified early enough can even lead to the KN detection through optical searches.

In O5, we find that these KN-less GRB afterglows will be detectable for up to tens of days, leaving more than enough time to tile the skymaps. The prominence of the KN-less afterglows at larger skymap sizes over the afterglows with KN further motivates this strategy. We note that, even in O4 where the KNæ are in principle detectable, this strategy opens an alternate channel for counterpart discovery in the case that the optical network did not detect the detectable KN beforehand, e.g., for lack of instrument availability or ToO program time. In O5, most of the GRB radio afterglows are discoverable with a total observing time of less than 5 hours for DSA-2000, corresponding to 5 tiles of DSA-2000. A significant fraction of events are discoverable within 5 hours by ngVLA, corresponding to 30 tiles for this instrument.

The potential for radio tiling to improve the outcome of EM searches is critical for systems such as BHNSs for which the detection prospects are tight (see Section 6.3). The DSA-2000 and ngVLA concepts project to carry out target-of-opportunity programs. This ToO time could be used for the GRB afterglow discovery of already-localized events, as was the case for radio arrays for GW170817. Alternatively, this time could be condensed into the tiling of GW skymaps. With this second option, a radio array can allow the discovery of up to 100% more GRB afterglow counterparts than if the community relies on the detection of the KN first.

In any case, like all tiling strategies, the radio tiling strategy requires archival images of the sky to flux limits as deep as the follow-up searches. This is required to carry out difference-imaging and identify the transient sources. To our knowledge, such archival images do not exist in the GHz band. However, the instruments that are best fit for tiling strategies are survey instruments, such as the upcoming DSA-2000, which could then rely on its own survey images for the searches in its ToO program.

Whether targeting the KN or the GRB afterglow, the choice of events to follow up and when to start tiling could benefit from low-latency release of GW constraints on the binary parameters. In particular, the early publication of the binary masses

[5]The announced performance for the ngVLA is 0.41 μJy in one hour [279, Tab. 1], equivalent to 1 μJy in 10 min, considering $F_{\rm lim} \propto t^{-1/2}$.

would help determine the expected afterglow flux, and information on the inclination angle would help predict the peak time or optimal interval for observation. For the KN, follow-up teams have already developed models to generate the light curved likely to arise from a source, given the binary parameters [41, 92]. A similar tool for afterglows could help optimize searches, if the GW constraints on the binary systems are released in low latency.

6.7 Summary and conclusions

In this Chapter, we studied the MM detectability of merging BHNS binaries in the O4 and O5 runs of the global GW detector network. BHNS systems are MM sources and here we explored their observability by characterizing their multi-frequency EM emission and computing the cumulative MM detection rates. We started by constructing a synthetic population based on the binary evolution models from Broekgaarden et al. [68], assuming two different BH spin prescriptions and two variations of the NS EoS. We computed the expected properties of the material expelled during and after the coalescence using fitting formulae calibrated on a large set of relativistic hydrodynamical simulations. We then used this information as input to semi-analytical models to compute the observable properties of the associated KN, multi-wavelength GRB afterglow and GRB prompt emission. This allowed us to construct the distributions of the EM observables for O4 and O5 GW-detectable events.

Overall, the prospects for O4 are poor, with less than one detectable KN counterpart every few years when assuming non-spinning BHs in the binaries. Under the assumption that BHs can have spins up to $\chi_{\rm BH} = 0.5$, the prospects are of the order of one detectable counterpart per year, the effect of the spin distribution on the rate of detectable counterparts being larger than that of the EoS.

As of O5, the prospects for MM observations will be brighter, thanks to the improved performance of the GW and EM instruments. We expect one detectable KN counterpart per year assuming non-spinning BHs, and about ten per year if the BHs are spinning. The prospects for detectable radio GRB afterglows follow the same trend, with one detectable counterpart assuming spinning BHs in O5.

The strong effect of the spin distribution on the EM counterparts opens the way to constraining the formation channels of the BHNS systems since these channels determine the distribution of binary parameters. However, it is only as of O5, when the potential detection rates will be significant, that the constraining power of MM observations will appear.

In any case, even when the KNæ are detectable, their observation should remain challenging due to their fast dimming, and the large GW skymap sizes. This motivates tailored observing strategies aiming to provide an alternative channel to discover afterglow counterparts directly in the radio band, leveraging the afterglow's long duration, in case the KN was not detected. Large field-of-view radio arrays, such as the projected DSA-2000 and ngVLA, can effectively carry out a tiling of the GW skymap during their target-of-opportunity program. This radio tiling strategy could allow to recover up to twice as more GRB afterglow counterparts of BHNS systems than if one relies on first detecting the KN.

The data produced in this Chapter are publicly available on Zenodo through the link https://zenodo.org/doi/10.5281/zenodo.10700748. The scripts and files to reproduce the main figures in the text are publicly available at https://github.com/acolombo140/O4O5BHNS.

Chapter 7

Multi-Messenger Observations in the Einstein Telescope Era

In this Chapter, we present preliminary prospects for multi-messenger observations of binary neutron star and black hole - neutron star mergers in the Einstein Telescope era. The model used is the one described in Chapters 5 and 6, based on Colombo et al. [78, 79]. Part of the results presented here will be included in the Chapter of the Einstein Telescope Blue Book dedicated to multi-messenger observations. Since the following Chapter is not based on a peer-reviewed work, the results presented here should be treated with caution.

7.1 Introduction

The first detection of gravitational waves (GW) from a binary neutron star (NSNS) merger, GW170817, by Advanced LIGO [1] and Virgo [24] marked a significant milestone in multi-messenger (MM) astronomy. This event, characterized by both GW and electromagnetic (EM) emissions, substantially enhanced our understanding of EM transients originating from NSNS mergers [9, 11, 8].

Despite the improved sensitivity in the O3 and the first half of the O4 observing runs, no new EM counterpart detections were reported. The challenges in EM follow-up campaigns were often attributed to either the inadequate sky localization of GW signals or the considerable distance of the events.

Recent detections of black hole-neutron star (BHNS) mergers through their GW emission have opened new possibilities [22]. Although EM emissions have not yet been confidently associated with these mergers, the subject remains of keen interest.

The forthcoming third-generation (3G) GW observatories, such as the Einstein Telescope (ET; [242]) and Cosmic Explorer (CE; [251]), promise remarkable advancements. Compared to current detectors, these observatories are expected to offer an order of magnitude improvement in sensitivity and an expanded bandwidth, both at lower and higher frequencies. This enhancement will significantly boost the potential for discoveries in astrophysics, cosmology, and fundamental physics.

The current design of ET incorporates several innovative features compared to the second-generation LIGO-Virgo detectors. Notably, ET is planned as a unique triangular observatory located 200-300 meters underground, a strategic decision aimed at reducing seismic noise. Its triangular layout, comprising three nested detectors with arms stretching 10-15 km, is designed to offer redundancy, the capability to distinguish GW polarizations, and the creation of a null stream for disturbance rejection. Additionally, ET's xylophone configuration is a distinctive aspect. Each detector consists of two interferometers: one optimized for high frequencies with high laser power, and the other for low frequencies, operating at cryogenic temperatures and low laser power.

In this preliminary study, we analyze the expected observational characteristics of EM emissions from NSNS and BHNS mergers detectable by ET, with a focus on kilonova (KN) and jet-related emissions. We constructed a synthetic population of merging NSNS and BHNS binaries, calculating the expected properties of their ejecta and accretion disks using numerical-relativity-informed fitting formulae. Employing these properties as inputs, we then computed the observable features of their associated KN, GRB prompt, and GRB afterglow emissions using a suite of semi-analytical models. This approach enabled us to construct distributions of EM observables for ET-detectable events, providing a comprehensive view of this new era in astronomy.

7.2 GW-EM models

For the analysis conducted in this Chapter, we assumed two populations of merging compact objects, one of NSNS and one of BHNS.

The NSNS population was the same as assumed in Chapter 5 (based on [78]), in which the mass distribution was calibrated with current observational data from GW detections and Galactic NSNS systems, assuming a cosmic merger rate density derived by convolving a delay time distribution ($P(t_{\rm d}) \propto t_{\rm d}^{-1}$), with a minimal delay of $t_{\rm d,min} = 50\,$Myr, with the cosmic star formation rate as per [185] (refer to Appendix A for details). This was normalized to align with the local rate density $R_0 = 347^{+536}_{-256}\,{\rm Gpc^{-3}\,yr^{-1}}$, ensuring a consistent match with the observed frequency of significant NSNS mergers [17] (see Appendix A.1.3).

For BHNS we assumed the fiducal population described in Chapter 6 (based on [79]). Specifically, we relied on the BH and NS mass distributions from the standard parameter set (model A) detailed in Broekgaarden et al. [68]. We also incorporated the fiducial metallicity-specific star formation rate density from the same study, grounded in the phenomenological model of Neijssel et al. [214]. This approach was normalized to match an empirically derived merger rate density of $R_0 = 149^{+153}_{-87}{\rm Gpc^{-3}yr^{-1}}$ at redshift $z = 0$, accurately reflecting the four BHNS events observed with FAR ≤ 1 ${\rm yr^{-1}}$ as reported in [17]. The normalization process followed methodologies similar to those in Appendix A.1.3. For the BH spin distribution we fixed the conservative model where $\chi_{\rm BH} = 0$ for all the binaries.

For both the populations we assumed the soft SFHo EoS ([146]), predicting a maximum non-rotating NS mass of $M_{\rm TOV} = 2.06\,{\rm M_\odot}$ and a radius of $R_{1.4} = 11.30\,$km for a $1.4\,{\rm M_\odot}$ NS.

For each merging event within our study, we have calculated the expected signal-to-noise ratio (S/N) for ET using a matched-filter approach. Additionally, we calculated the 90% credible area for sky localization $\Delta\Omega_{90\%}$ for each detected signal (for BHNS only for the events with an EM counterpart, $m_{\rm out} > 0$). For ET we assumed the triangle configuration with 10 km arms, locating the detector in Sardinia. We considered the ET-D sensitivity curve and we incorporated a 85% uncorrelated duty cycle for each detector, aligning with the standard set in [64].

The computations of S/N and sky localization were performed via the `GWFAST` software package [155, 154], utilizing the `IMRPhenomNSBH` waveform model [225, 89] for BHNS and `IMRPhenomD_NRTidalv2` [89] for NSNS. This model in `GWFAST` depends on several parameters, including the detector-frame chirp mass, mass ratio, dimensionless spins of the binary components, luminosity distance, sky position, binary inclination angle, polarization angle, time and phase of coalescence, and the neutron star's tidal deformability [155]. For parameters not explicitly discussed previously, values were drawn from non-informative priors within their physically relevant

ranges, as detailed in Iacovelli et al. [155]. For an in-depth discussion on this topic and a comparison of different inversion methods, we refer to Section 6.2.2 in the previous Chapter and Section 2 and Appendix D of Iacovelli et al. [154].

Our population analysis included computations of expected ejecta mass, average velocity, and accretion disk mass, utilizing numerical-relativity-informed fitting formulae [41, 171, 245]. For BHNS we calculated the accretion disk mass as $M_{\rm disk} = m_{\rm out} - m_{\rm dyn}$, where $m_{\rm out}$ is the mass remaining external to the remnant BH for each event in our compact object population [116]. We also implemented a condition where if $m_{\rm dyn}$ exceeded half of $m_{\rm out}$ as predicted by these formulas, we set $m_{\rm dyn}$ to its maximum value $m_{\rm dyn}^{\rm max}(m_{\rm out}) = 0.5 m_{\rm out}$, following the guidelines of Foucart et al. [113] and Rees [250] (see Chapter 2).

These results served as inputs for calculating the EM counterparts observable features for each binary in our population. Specifically, we computed the KN light curves in the g (484 nm), z (900 nm), and J (1250 nm) bands, using the anisotropic multi-component model of Breschi et al. [66], which is based on Perego et al. [230].

For NSNS, in scenarios where the merger results in a remnant mass $M_{\rm rem} \geq 1.2 M_{\rm TOV}$, indicative of either immediate or delayed collapse into a BH, we hypothesized the launch of a relativistic jet. For BHNS, the formation of a relativistic jet with energy $E_{\rm c}$ was presumed if $M_{\rm disk} > 0$. We assumed that if the jet energy surpasses a certain threshold (based on [97]), it successfully penetrates the ejecta, leading to GRB prompt and afterglow emissions.

For both the populations, we adopted a jet angular structure motivated by the one of GRB170817A [125], fixing the median interstellar medium density and microphysical parameters representative of GW170817. We computed the GRB afterglow light curves over 0.1 to 1000 days in the radio, optical, and X-ray spectrums.

Our methodology for GRB prompt emissions employed a model approach akin to [44] and [266]. A constant fraction $\eta_\gamma = 0.15$ of the jet energy density, restricted to regions with a bulk Lorentz factor $\Gamma \geq 10$, was assumed to be emitted as photons. The resulting observed spectrum was an integration of this radiation over the jet's solid angle, incorporating relativistic beaming effects.

For NSNS systems observed within a viewing angle $\theta_{\rm v} \leq 60^\circ$, we also included a cocoon shock breakout component, modeled following GRB170817A [8], featuring a luminosity and spectrum characteristic of this event. In BHNS we did not consider this additional emission, because off the lack of observing constraints from this kind of sources.

Finally, photon fluxes in specific energy bands were calculated, assuming a standard burst duration, and considering the observational constraints of *Fermi*/GBM and *Swift*/BAT. Further details and model specifics were elaborated in Chapter 4. Our calculations of GRB prompt emission detection rates also accounted for the limited field of view and duty cycle of these instruments, as quantified by [71].

7.2.1 Multi-messenger detection criteria

In this analysis, we focused on NSNS and BHNS systems detectable through GW and MM observations, considering the capabilities of upcoming observational facilities. In order to facilitate the comparison with the previous Chapters and to avoid facility-specific simulations of the GW localization and of the actual search strategy, we assumed the O5 detection thresholds described in Section 6.2.4

For GW signal detection, we implemented a S/N threshold of 12. This relatively stringent S/N threshold also enhances the reliability of the parameter estimation forecasts based on the `GWFAST` Fisher-information-matrix [154].

Regarding EM follow-up, we anticipated substantial improvements in radio and optical search depths, owing to new instrumentation. In the radio spectrum, we expect a tenfold sensitivity increase to 0.01 mJy [92] respect to our limits in O4, achievable by next-generation instruments like the SKA2 [65], Next-Generation VLA [81], or DSA-2000 [143]. In optical observations, advancements are anticipated with large FoV instruments like the Vera Rubin Observatory [156]. We considered magnitude thresholds of 26 in the g band and 24.4 in the z band, corresponding to the Rubin Observatory's target-of-opportunity program [35]. For X-ray we assumed a flux limit of $10^{-13}\,\mathrm{erg/cm^2/s/keV}$ at 1 keV, achievable by Chandra or XMM-Newton with extended exposures [192, 85]; and a gamma-ray detection threshold for GRB prompt emission of $4\,\mathrm{ph\,cm^{-2}\,s^{-1}}$ in the 10-1000 keV range, derived from *Fermi*/GBM GRB flux distributions [78].

As in the previous Chapters, it is crucial to note that our analysis is predicated on the assumption that the GW sky localization areas for NSNS and BHNS mergers will be thoroughly surveyed to the outlined detection thresholds by a coordinated effort of various observatories. This assumption is based on the EM counterpart searches following the BNS event GW190425 [83, 150, 36]. A more comprehensive analysis of practical detection rates would require simulations mimicking the search strategies of individual observatories.

7.3 Multi-messenger prospects with ET

In the left panel of Figure 7.1, we present our forecasts for the NSNS EM counterpart detection scenario in conjunction with ET, based on the limits established in the previous Section. The light grey line, labeled "All NSNS", depicts the intrinsic cumulative merger rate, with the corresponding light grey band illustrating its uncertainty. This uncertainty originates from Poissonian fluctuations in the rate density normalization, considering our mass distribution (detailed in Appendix A.1.3). This uncertainty propagates as a constant relative error to all subsequent rate estimates, displayed in the Figure as colored bands.

The black line, denoted as "GW ET", represents our estimated cumulative detection rate of NSNS mergers assuming an ET triangle 10 km configuration. The colored lines – blue for KNæ and GW joint detections ("Kilonova+GW"), red for GW and GRB radio afterglows ("GRB Afterglows+GW"), and orange for GW and GRB prompt emissions ("GRB Prompt+GW") – indicate all-sky cumulative rates, with the exception of the GRB prompt detection, that is based on observations by *Fermi*/GBM. Results for other spectral bands are summarized in Table 7.1. The dashed lines represent the cumulative detection rates assuming only binaries with a sky localization $\Delta\Omega_{90\%} < 100\mathrm{deg}^2$.

Our analysis suggests that NSNS merger will be GW detectable by ET up to approximately $z \sim 1.5$, translating to a detection rate of 21402^{+33059}_{-15789} events per year. Joint GW+EM detection rates for various counterparts are detailed in Table 7.1.

These rates imply that, up to redshift $z \sim 0.4$, the majority of KNæ associated with ET events will likely exceed the brightness thresholds at their peaks, hence falling within the capabilities of Vera Rubin, with a detection rate of $4698^{+7257}_{-3466}\ \mathrm{yr}^{-1}$. The large number of detectable events and the rapid evolution of these sources poses significant challenges for the choice of the GW events to follow and the subsequent EM identification. The ability of ET to localize the sky position significantly influences the effectiveness of the search for a counterpart by determining how many pointings EM instruments need to adequately cover the GW signal location, as discussed by [64].

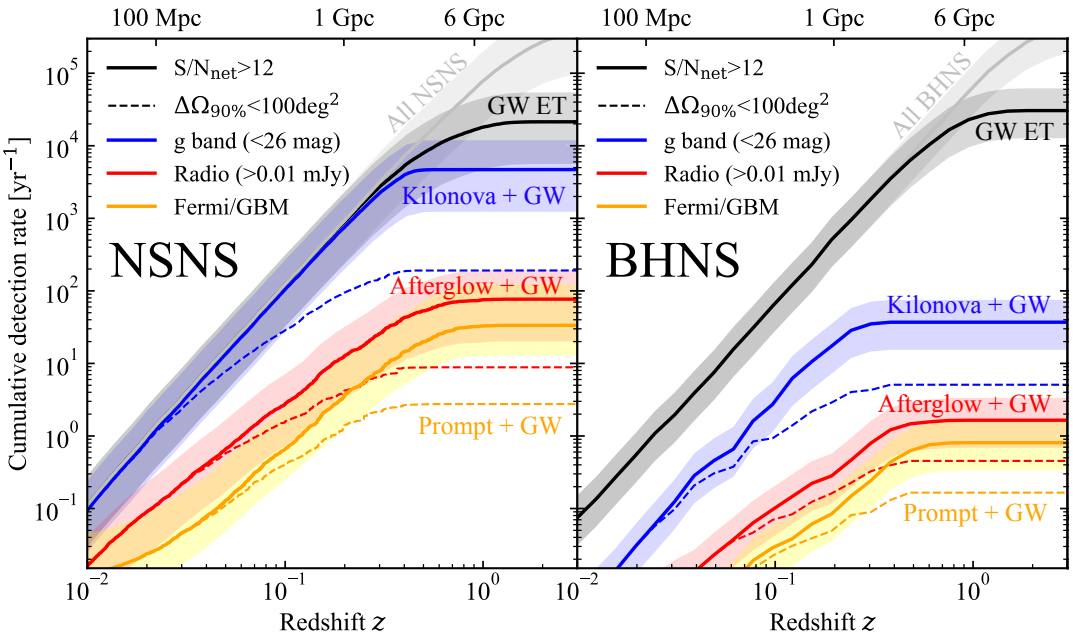

FIGURE 7.1: Cumulative MM detection rates as a function of redshift (luminosity distance) for our fiducial NSNS and BHNS population (SFHo EoS, non-spinning BHs) and assuming a jet core half-opening angle $\theta_j = 3.4^\circ$ for the jet-related emissions. *Left-hand panel*: assumes the ET triangle 10 km configuration. The light grey line ("All NSNS") represents the intrinsic merger rate for the NSNS population, with the grey band showing its uncertainty due to the local merger rate. This uncertainty propagates as a constant relative error to all the other rates. The black ("GW ET") line is the cumulative GW detection rate (events per year with network S/N $\geq$ 12). The blue ("Kilonova+GW"), red ("Afterglow+GW") and orange ("Prompt+GW") lines are the cumulative detection rates for the joint detection of ET GW plus either a KN, a GRB afterglow or a GRB prompt (all-sky except for the orange line, which accounts for the *Fermi*/GBM duty cycle and field of view). The dashed lines are the cumulative detection rates assuming only the binaries with $\Delta\Omega_{90\%} < 100\text{deg}^2$. The assumed thresholds are shown in the legend. *Right-hand panel:* same as the left-hand panel, but for the BHNS population.

TABLE 7.1: Detection limits and predicted detection rates for NSNS and BHNS, assuming ET triangle 10 km. We report in parenthesis the detection rates assuming $\Delta\Omega_{90\%} < 100\text{deg}^2$. The GW detection limits refer to the SNR_{net} threshold. Near infrared and optical limiting magnitudes are in the AB system; radio limiting flux densities are in mJy @ 1.4 GHz; X-ray limiting flux densities are in erg cm^{-2} s^{-1} keV^{-1} @ 1 keV; gamma-ray limiting photon fluxes are in photons cm^{-2} s^{-1} in the 15–150 keV (*Swift*/BAT) or 10–1000 keV (*Fermi*/GBM) band. Detection rates are in yr^{-1}. The reported errors, given at the 90% credible level, stem from the uncertainty on the overall merger rate, while systematic errors are not included.

	GW ET	KN + GW			GRB Afterglow + GW			GRB Prompt + GW	
		J	z	g	Radio	Optical	X-rays	*Swift*/BAT	*Fermi*/GBM
NSNS									
Limit	12	21	24.4	26	0.01	26	10^{-13}	3.5	4
Rate	21402^{+33059}_{-15789}	$4.5^{+7.0}_{-3.3}$	500^{+772}_{-369}	4698^{+7257}_{-3466}	77^{+119}_{-57}	63^{+97}_{-47}	108^{+166}_{-79}	$5.2^{+8.1}_{-3.8}$	34^{+91}_{-21}
($\Delta\Omega_{90\%} < 100\text{deg}^2$)		$(3.4^{+5.2}_{-2.5})$	$(77.9^{+120.4}_{-57.5})$	(191^{+295}_{-141})	$(8.8^{+13.7}_{-6.5})$	$(3.2^{+4.9}_{-2.3})$	$(4.6^{+7.2}_{-3.4})$	$(0.49^{+0.76}_{-0.36})$	$(2.8^{+4.3}_{-2.0})$
BHNS									
Limit	12	21	24.4	26	0.01	26	10^{-13}	3.5	4
Rate	30535^{+31354}_{-17829}	$0.09^{+0.10}_{-0.05}$	$7.7^{+7.9}_{-4.5}$	$37.0^{+38.0}_{-21.6}$	$1.6^{+1.7}_{-1.0}$	$4.2^{+4.3}_{-2.4}$	$4.8^{+4.9}_{-2.8}$	$0.12^{+0.12}_{-0.07}$	$0.81^{+0.83}_{-0.47}$
($\Delta\Omega_{90\%} < 100\text{deg}^2$)		$(0.07^{+0.08}_{-0.04})$	$(1.7^{+1.7}_{-1.0})$	$(5.1^{+5.2}_{-3.0})$	$(0.45^{+0.47}_{-0.26})$	$(0.41^{+0.42}_{-0.24})$	$(0.42^{+0.43}_{-0.25})$	$(0.03^{+0.03}_{-0.02})$	$(0.17^{+0.17}_{-0.10})$

For this reason in Table 7.1 we also report the detections rates for the best localized binaries, having $\Delta\Omega_{90\%} < 100\text{deg}^2$. In this case the KN detection rates decrease to a more realistic value of 191^{+295}_{-141} yr^{-1}.

As discussed in the previous Chapters, the high proportion (97%) of off-axis jets makes the predicted joint GW and GRB rates comparatively lower, with a detection rate of 77^{+119}_{-57} yr^{-1} for GRB radio afterglows and 34^{+91}_{-21} yr^{-1} for GRB prompt (for the best localized events the rates decrease to $8.8^{+13.7}_{-6.5}$ yr^{-1} and $2.8^{+4.3}_{-2.0}$ yr^{-1}, respectively). According to this analysis, the majority of sGRB currently detected by *Fermi*/GBM will have a GW detectable counterpart, in accordance with [258]. Moreover, differently from the close KN population, the jet related emissions will constitute a unique population to study MM astronomy in the distant Universe, with an EM horizon set by the ET GW detection up to redshift $z \sim 1.5$.

In the left panel of Figure 7.1, we report the same cumulative detection rates for the BHNS population. We expect a GW detection rate of 30535^{+31354}_{-17829} yr^{-1}, detectable up to redshift $z \sim 2$. For these events, we expect that only about 2% will manage to emit material during the coalescence ($m_{\rm out} > 0$), potentially powering an EM counterpart. This results in significantly lower rates compared to the NSNS population.

In particular, we find a KN detection rate of $37.0^{+38.0}_{-21.6}$ yr^{-1}, that decreases to $5.1^{+5.2}_{-3.0}$ yr^{-1} considering only the events with $\Delta\Omega_{90\%} < 100\text{deg}^2$. The KN horizon is the same as the NSNS case around $z \sim 0.4$.

GW-detectable systems with an observable radio afterglow and GRB prompt are forecasted to achieve a total rate of $1.6^{+1.7}_{-1.0}$ yr^{-1} and $0.81^{+0.83}_{-0.47}$ yr^{-1} ($0.45^{+0.47}_{-0.26}$ yr^{-1} and $0.17^{+0.17}_{-0.10}$ yr^{-1} for the well localized events). Their EM horizon is sensibly smaller than the GW one respect to the NSNS case. This occurs because only events with lower BH masses, and consequently with a reduced intrinsic S/N, have the capacity to generate an EM counterpart, as discussed in Chapter 6. Consequently, the combined GW+EM detection horizon is defined by the GW detection of events involving BHs below a specific mass threshold.

Although the detection rates for the BHNS population are significantly lower compared to NSNS cases, it is important to note that we are considering the most conservative population scenario, with non-rotating BHs and a soft EoS for NSs. Relative to the O5 run, the detection rates increase by more than a factor of 10, ensuring the identification of EM counterparts from these types of sources. Thus, ET could represent a pivotal advancement for MM astronomy in the context of BHNS observations.

7.4 EM properties

7.4.1 Kilonova

In Figure 7.2, we display the temporal progression of KNæ apparent AB magnitude in the g band for ET-detectable binary systems in our NSNS (left column) and BHNS (right column) populations. The filled color regions shows the ranges encompassing 50%, 90%, and 99% of the light curves over time, considering all the ET-detectable binaries (upper panels) and only the binaries with $\Delta\Omega_{90\%} < 100\text{deg}^2$. For comparison, we also report the observed data of AT2017gfo [307] at the median distance of the GW-detectable events, for NSNS ~ 2.3 Gpc (~ 1 Gpc for the well-localized events) and for BHNS ~ 2.7 Gpc (~ 1.3 Gpc for the well-localized events).

For the NSNS population we find that, considering all the ET-detectable binaries, the KN peaks span from an apparent AB magnitude of 22 down to 28, while the

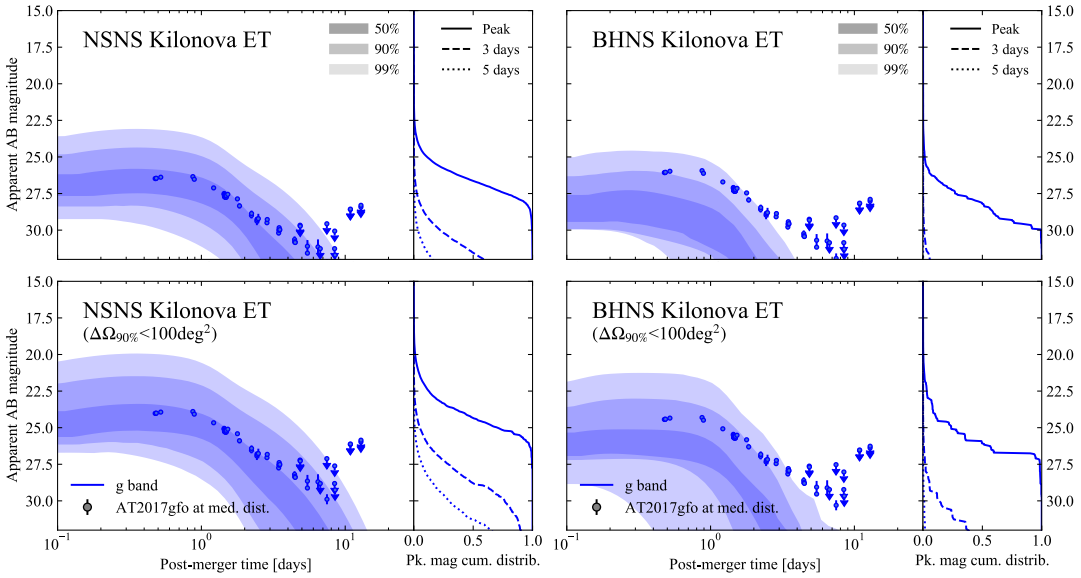

FIGURE 7.2: Distribution of ET otical KNæ as a function of time for our NSNS (left column) and BHNS (right column) population. The left-hand panel shows the apparent AB magnitude versus post-merger time for our simulated KN light curves, restricting to ET GW-detectable sources. The shaded regions contain 50%, 90% and 99% of the KN light curves in the g (484 nm) band. Colored circles show extinction-corrected AT2017gfo data rescaled to the median distance of our populations.The right-hand panel shows the cumulative distributions of apparent magnitude at peak, at 3 days and at 5 days after the merger (solid, dashed and dotted lines, respectively). The lower panels show the same but restricted to the binaries with $\Delta\Omega_{90\%} < 100\text{deg}^2$.

.

50% is concentrated in the 24.5-26.5 interval. Considering the constraint on the sky localization, the majority of peaks are found in the 23-25 interval, making almost all the KNæ accessible to Vera Rubin.

For the BHNS population, we generally observe magnitudes that are two orders of magnitude higher. This is partly due to the greater average distance of this population compared to the NSNS one. Additionally, in comparison to observational data, this population of KNæ appears to be less luminous than GW170817, whose data exceed the 90% curves, whereas for NSNS, it is above the 50% ones.

With the lines in the right panels, we indicate the cumulative distributions of apparent magnitudes at their peak (solid line), and also at 3 and 5 days post-merger (dashed and dotted lines), showcasing their rapid brightness decline, particularly for the BHNS population. As described in Section 6.6.2, a possible effective strategy to counteract the challenge of rapidly dimming KNæ involves directly seeking out non-thermal counterparts, like radio afterglows, using tiling instruments. This approach is well-suited for upcoming radio surveys, enabling a possible efficient search for these transient events.

7.4.2 GRB afterglow

In Figure 7.3, we illustrate the properties of GRB afterglows associated to GW detectable NSNS (upper panel) and BHNS (lower panel) binaries. The figure presents contours encompassing 50% (solid lines) and 90% (dashed lines) of the peak values of GRB afterglows on the flux (F_ν) versus time (t) plane. Additionally, the right side of the figure provides the corresponding apparent AB magnitude and νF_ν at 1 keV.

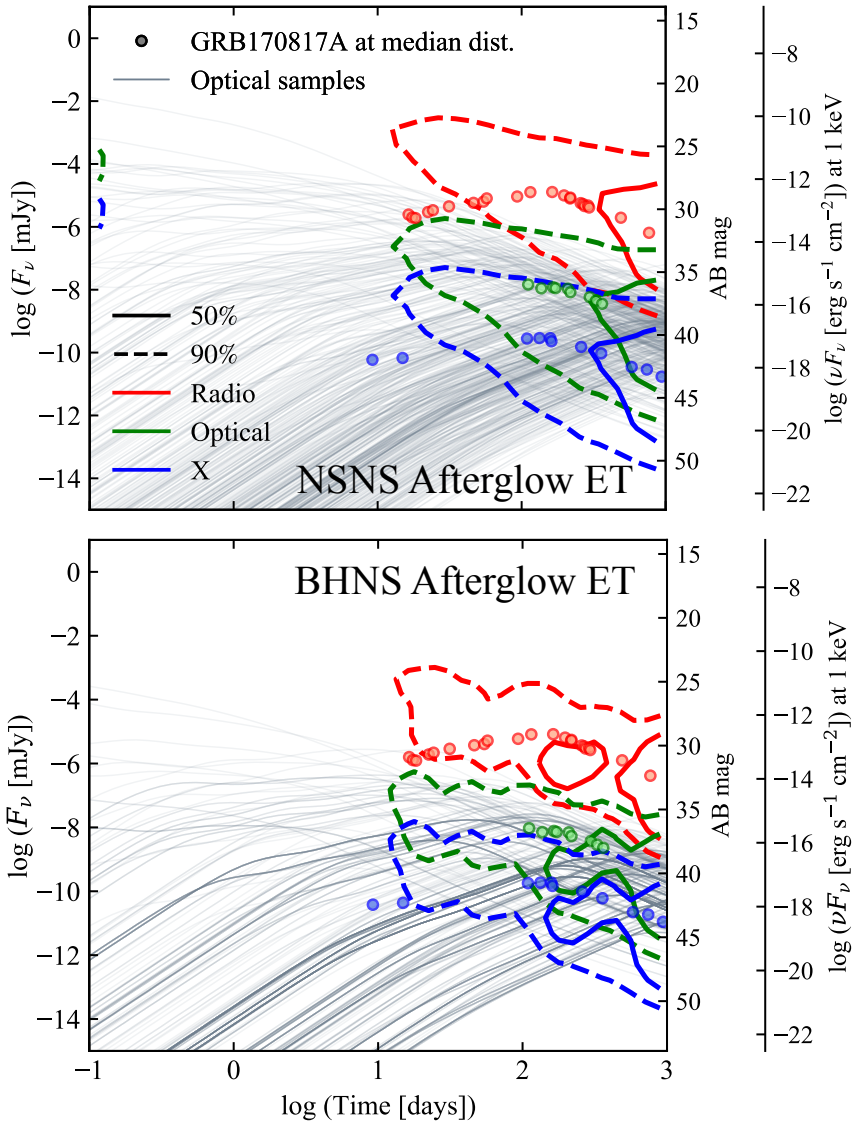

FIGURE 7.3: F_ν, AB magnitude and νF_ν versus time for the GRB afterglow light curves associated to ET-detectable NSNS (upper panel) and BHNS (lower panel) mergers. Solid and dashed contours contain 50% and 90% of the peaks, respectively. Red, green and blue colors indicate the radio (1.4×10^9Hz), optical (4.8×10^{14}Hz), X-ray (2.4×10^{17}Hz) bands, respectively. The colored circles represent the observed data of GRB170817A [188], scaled to the median distance of our population. The grey lines in the background are a random sample of optical light curves. We assume for both the populations the same jet half-opening angle $\theta_j = 3.4$ deg.

.

The depicted red, green, and blue colors correspond to the radio, optical, and X-ray bands, respectively. Most of the peak occurrences are beyond 10^2 days, noting that light curve calculations were restricted between 10^{-1} and 10^3 rest-frame days, and exhibit a distribution extending to shorter peak times. To enhance visualization of the underlying light curve behavior, we have included a sample of randomly chosen optical light curves (thin grey lines) in the background. For context, we also include GRB170817A data [188, small circles] at the median distance of our populations.

These observations are largely influenced by the strong dependency of GRB afterglow light curves on the viewing angle, combined with the viewing angle distribution skewed by GW detection (tending towards smaller angles compared to an isotropic distribution, with a peak at about 30° – [278]). As a result, the majority of peaks occur several months to years post-GW event, with a minority peaking earlier (around hours) in the optical and X-rays, exhibiting notably bright emissions due to closer viewing angles.

7.4.3 GRB prompt

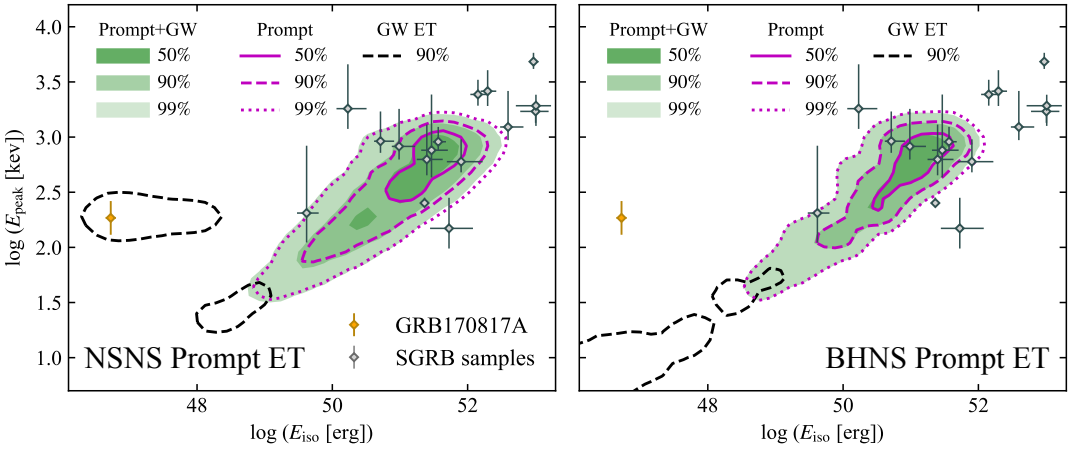

FIGURE 7.4: Rest-frame SED peak photon energy E_{peak} versus the isotropic-equivalent energy E_{iso} for our NSNS (left panel) and BHNS (right panel) populations. The filled green colored regions contain 50%, 90% and 99% of the binaries both GRB Prompt- and ET-detectable. The magenta lines contain 50%, 90% and 99% (solid, dashed and dotted, respectively) of the GRB Prompt-detectable binaries. The black dashed line contains 90% of the ET-detectable binaries. The black dots with error bars represent a sGRB sample for comparison [268]. The orange dot is GRB170817A. We assume for both the populations the same jet half-opening angle $\theta_j = 3.4$ deg.

.

In Figure 7.4, we present for NSNS (left panel) and BHNS (right panel) the distribution of rest-frame spectral energy distribution (SED) peak energy E_{peak} versus isotropic-equivalent energy E_{iso} for events that meet our detection criteria for both the GW signal and GRB prompt emission.

The green shaded areas encompass 50%, 90%, and 99% of the binary systems detectable by both *Fermi*/GBM and the ET. The magenta lines, varying in style from solid to dashed to dotted, represent the 50%, 90%, and 99% containment levels, respectively, of binary systems that are detectable through GRB prompt emission without the requirement of ET detection.

To contextualize *Fermi*/GBM-detected GRB prompt events within the broader cosmological population, we incorporate a sample of sGRBs with known redshift,

symbolized by gray diamonds [268]. The specific case of GRB 170817A is marked as an orange diamond on the plot, serving as a reference point.

A dashed black line is included to denote the 90% confidence region for binaries detectable by ET, independent of the GRB prompt emission detectability constraint. This curve displays the most significant differences between the two populations. For NSNS, the curve shows a bimodal distribution, as we also consider a cocoon shock breakout component for events with a viewing angle less than 60 degrees, replicating the properties of GRB170817A. This component is predominant for particularly close events (within 100 Mpc), thus it is not as relevant in comparison to the cosmological population of sGRBs. Since our BHNS population lacks this cocoon shock breakout component, the black curve does not intersect with the cocoon shock breakout event cluster and extends into lower $E_{\rm iso}$ values.

7.5 Conclusions

In this Chapter, we presented a preliminary study of the potential of MM astronomy during the ET era, focusing on NSNS and BHNS mergers. In particular, we explored the observability of these sources by characterizing their different EM emissions and computing the cumulative MM detection rates. These forecasts stem from a simulated set of NSNS events characterized by a mass distribution and event rate density derived from observational data, and a set of BHNS events based on the binary evolution models from Broekgaarden et al. [68] with non-spinning BHs. For these populations, we calculated the GW S/N, KN light curves, GRB afterglow light curves, and prompt emission peak photon fluxes. This approach allows for a direct assessment of the detectability of each emission component for each individual event within the population.

For the NSNS population, we find that these events can be detected up to a redshift $z \sim 1.5$, with an annual detection rate of the order of 10^4 per year. The KN population can be detected by an instrument like the Vera Rubin Observatory up to a redshift of $z \sim 0.4$, ensuring several tens detections per year, even when considering only the best-localized events. The rates for prompt and afterglow emissions are of the order of ~ 10, but this population is limited only by the gravitational horizon up to $z \sim 1.5$. Specifically, we find that most sGRBs detected by *Fermi*/GBM will likely have a GW counterpart.

The rates for the BHNS population are less promising, as only a small fraction of these can emit a counterpart. However, the rates are more than tenfold higher compared to the O5 era, ensuring a few KN detections per year, and jet-related emissions every few years.

In the near future we plan to expand this study, in particular, we will investigate how changes in the properties of NSNS and BHNS populations, such as different EoS, BH spins, mass distributions and redshift evolution might affect the detectability and characteristics of GW and EM counterparts. Moreover, we will also analyze how different configurations of the ET, as well as potential collaboration with other observatories like Cosmic Explorer, could enhance GW detection and localization, thereby improving MM observations. The versatility of our model will also enable us to study the prospects of specific EM facilities, providing clear guidelines to maximize the scientific yield of the ET era in the field of MM astronomy.

Chapter 8

Summary

In this thesis, I presented our forecasts for the electromagnetic (EM) emissions associated with binary neutron star (NSNS) [78] and black hole - neutron star (BHNS) [79] mergers, observable in the current and forthcoming observing runs O4 and O5 of the LIGO, Virgo and KAGRA Collaboration (LVK), as well as by third-generation (3G) gravitational wave (GW) observatories such as the Einstein Telescope (ET; [242]) and Cosmic Explorer (CE; [251]).

To accomplish this, we constructed a synthetic population of NSNS binaries, guided by GW observations and data from Galactic NSNS systems, in conjunction with a BHNS population derived from the fiducial model in [68]. We computed the signal-to-noise ratios for the GW signals of each binary system within these detectors and estimated the GW-based sky localizations utilizing the `GWFAST` software [154].

Subsequently, we computed for each binary the properties of the material expelled during the coalescence, namely the mass and velocity of the dynamical ejecta and the mass of the accretion disk, using fitting formulae informed by numerical relativity [163, 245, 171, 114]. Utilizing this information, we evaluated the detectable features of the corresponding kilonova (KN), gamma-ray burst (GRB) prompt, and GRB afterglow emissions via a suite of semi-analytical models, enhancing the methodology delineated in Barbieri et al. [44]. This model allowed us to map the distributions of EM observables for events that are detectable in the O4, O5 runs, and by 3G GW observatories. As a result, this investigation contributes to several critical areas, providing a fundamental insight into the present and future of multi-messenger (MM) astronomy.

In Chapter 5 we presented our prospects for MM observations of NSNS in the O4 and O5 runs, finding a GW detection rate of $7.4^{+11.3}_{-5.5}$ yr^{-1} and $67.1^{+104}_{-49.5}$ yr^{-1}, respectively. Among these events, KNæ are generated in 77% of the mergers, with the rest leading to massive events that culminate in an immediate black hole formation, lacking both a disk and ejecta. Our analysis reveals light curves resembling AT2017gfo, albeit generally less luminous. Despite being at a greater median distance compared to those detected in earlier runs, in most instances, their apparent magnitude will surpass the conventional limits of previous optical counterpart explorations, albeit for a shorter duration, restricted to the first and second night. This renders the identification and observation of these sources more challenging than that of AT2017gfo. We infer that the majority of O4 and O5 KNæ will be observable within the current typical EM counterpart search sensitivity thresholds, corroborating findings from Chase et al. [74], Setzer et al. [280], and Sagués Carracedo et al. [262].

Relativistic jets manifest in 53% of the events in our population. The GRB prompt emissions from these jets surpass our defined thresholds in only a fraction of cases, with a negligible enhancement even when considering more sensitive gamma-ray detector data searches. For O4, a more efficacious approach to associating a GRB with a NSNS event might be through a sub-threshold GW event search following a

gamma-ray trigger, yielding a joint detection rate of $0.90^{+1.38}_{-0.66}$ per year in our model, aided by the expanded GW horizon.

Radio wavelengths are optimal for detecting the relativistic jet afterglow in a precisely localized event. Approximately one-tenth of the simulated events produce radio afterglows brighter than our 'candidate monitoring' threshold, translating to a detection rate of $0.77^{+1.23}_{-0.57}$ per year (assuming all candidates are pinpointed to arc-second precision via their KN emission). These projections suggest the feasible discovery of a new relativistic jet counterpart in O4, a valuable addition to our understanding of these phenomena, though not a certainty.

Regarding the discernible attributes of these relativistic jet counterparts, if a propitious GRB prompt emission event is observed, it will likely be dominated by the cocoon shock breakout emission for closer events (within $\sim$ 100 Mpc), or by emissions from the slower, less powerful material encircling the jet core. This latter scenario assumes a mechanism akin to that responsible for the prompt emissions of cosmological GRBs extends to about two to three times the jet core's opening angle. However, it's important to note the uncertainties surrounding the prompt emission mechanisms of GRBs outside the jet core and the limited understanding of shock breakout emissions in highly anisotropic and relativistic scenarios. The anticipated GRB afterglows are expected to show properties akin to GRB170817A, characterized by a gradual increase in flux density over several months post-merger, followed by a peak and a swift decline. Nonetheless, a small percentage of detectable events in our population might peak earlier, indicating a narrower viewing angle and providing a unique study case that bridges the gap between the viewing angles of cosmological GRBs and GRB170817A. In conclusion, our findings suggest that GRB170817A was an exceptionally fortuitous occurrence (aligning with, for instance, [205], but also see [231]), unlikely to recur soon. The strong alignment of our model predictions with the cumulative peak flux distribution of short GRBs observed by *Fermi*/GBM and *Swift*/BAT lends credence to this assertion.

In Chapter 6 we presented our prospects for BHNS MM observations in O4 and O5, with a GW detection rate of $15.0^{+15.4}_{-8.8}$ yr^{-1} and 140^{+143}_{-81} yr^{-1}, respectively. In brief, the forecast for O4 is not promising, with an expectation of less than one KN counterpart detectable every few years, particularly under the assumption of non-rotating BHs in binary systems. However, if we assume BHs with spins up to $\chi_{\rm BH} = 0.5$, the detection prospects improve to approximately one counterpart annually, indicating that the impact of spin distribution on detectable rates exceeds that of the NS EoS.

Looking ahead to O5, the outlook for MM observations becomes more optimistic due to enhancements in both GW and EM detection capabilities. Assuming non-spinning BHs, the rate of detectable KN counterparts should reach one per year, and this could escalate to around ten yearly if the BHs are spinning. The detection prospects for radio GRB afterglows exhibit a similar pattern, with an expectation of one discernible counterpart in O5, assuming spinning BHs.

The pronounced influence of spin distribution on EM counterpart detections paves the way for more precise constraints on the formation channels of BHNS systems, as these mechanisms govern the distribution of binary parameters. Nonetheless, it is only from O5 onwards, with potentially higher detection rates, that the constraining potential of MM observations will truly manifest.

Nonetheless, even when KNæ are within detection range, their observation remains challenging due to rapid fading and extensive GW skymap areas. This scenario necessitates specialized observational strategies, particularly focusing on an alternative route to identify afterglow counterparts directly in the radio spectrum. This

approach would exploit the prolonged duration of afterglows, especially in instances where the KN was not observed. Advanced, wide-field radio arrays like the proposed DSA-2000 and ngVLA are well-suited to implement a tiling strategy across the GW skymap within their target-of-opportunity programs. Such a radio tiling approach could potentially double the recovery rate of GRB afterglow counterparts from BHNS systems compared to relying solely on initial KN detections.

Finally, in Chapter 7 we presented our preliminary prospects for MM observations in the ET era, assuming our joint population of NSNS and BHNS mergers.

In examining the NSNS population, we find that such events are detectable up to redshift $z \sim 1.5$, boasting an annual detection rate of the order of 10^4 events per year. For the KN population, detection by a facility like the Vera Rubin Observatory is feasible up to a redshift of $z \sim 0.4$, compatible with [64]. This translates into numerous detections yearly, even when focusing on events with the most precise localizations, making the selection of GW events to follow up on crucial. The occurrence rates for both prompt and afterglow emissions are of the order of ~ 10 per year, yet this estimation is contingent solely on the GW horizon, extending up to $z \sim 1.5$. Notably, we ascertain that the majority of sGRBs identified by *Fermi*/GBM are likely to have an associated GW signal, aligning with [258].

Conversely, the detection prospects for the BHNS population appear less encouraging, as only a limited fraction of these events are expected to produce observable counterparts. Nevertheless, the detection rates show a significant increase, more than tenfold, compared to the O5 era. This implies the likelihood of several KN detections each year and emissions related to jets occurring every few years.

In the works presented in this thesis, we operated under the premise that the GW sky localization regions for NSNS and BHNS mergers will invariably be comprehensively scanned by EM counterpart searches, down to our designated representative sensitivity thresholds. While this level of coverage is impractical for individual observatories (owing to constraints in sky accessibility and the time allocation for each search), it's important to recognize that the collective efforts of multiple facilities can effectively survey extensive localization areas. This approach has been exemplified in the search for EM counterparts of the single-detector event GW190425, as highlighted in works like [36, 83, 183, 150]. A more nuanced evaluation of the actual detection rates achievable would necessitate facility-specific simulations of GW localization and the corresponding search strategies, akin to the analysis conducted in [119]. However, such detailed simulations fall beyond the scope of this current work.

It is also crucial to acknowledge that all our projections are founded on broadly-defined observational parameters and are subject to systematic uncertainties, which have only been partially examined due to the complexities inherent in comprehensive population modeling. The forthcoming collaborations between GW and EM communities in future observational runs are anticipated to yield richer and richer results, thereby gradually honing our understanding of the true physics underlying these extraordinary astrophysical phenomena.

Appendix A

NSNS and BHNS populations

A.1 NSNS population model

A.1.1 Mass distribution

The mass distribution of merging binary neutron stars is currently not well constrained. Observations of galactic pulsars in double neutron star binaries historically pointed to a narrow distribution centered around $1.33\,\mathrm{M}_\odot$ [218, 219], but recent studies hint at a bimodal distribution being more likely [104], and the existence of a sub-population detectable with current radio facilities cannot be dismissed [e.g. 238]. Selection effects in GW observations are much simpler, but the only two detections so far (GW170817, [9]; and GW190425, [4]) are insufficient to constrain the shape of the mass distribution. Still, analyses of GW-detected NSs [e.g. 174, 20], combined to GW+pulsar analyses [123], and arguments based on the incidence of jets [270], clearly point to a relatively broad distribution. With the aim of defining a simple mass distribution informed only by merging NSNS binaries (as opposed to those obtained by including also the masses of neutron stars in BHNS binaries, [174, 20]), we devised the following ad-hoc method, which we adopted mainly because of its simplicity, in absence of strong observational constraints. We assumed the component mass probability distribution to be factorized into the chirp mass $\mathcal{M}_c$ probability and the probability of the mass ratio $q = M_2/M_1$ (assumed independent of each other), namely

$$P(M_1, M_2) = JP(\mathcal{M}_c)P(q) \tag{A.1}$$

where $J(M_1, M_2) = \mathcal{M}_c/M_1^2$ is the Jacobian that relates the two parametrizations [72]. We then adopted a parametrization for each of these unknown probability distributions, that is

$$P(\mathcal{M}_c \,|\, \mathcal{M}_{c,\min}, \alpha) = \Theta(\mathcal{M}_c - \mathcal{M}_{c,\min})\Theta(\mathcal{M}_{c,\max} - \mathcal{M}_c)\frac{(1-\alpha)\mathcal{M}_c^{-\alpha}}{\mathcal{M}_{c,\max}^{1-\alpha} - \mathcal{M}_{c,\min}^{1-\alpha}} \tag{A.2}$$

and

$$P(q \,|\, \beta) = (1+\beta)q^\beta, \tag{A.3}$$

where Θ is the Heaviside step function and α and β are free parameters. We fixed $\mathcal{M}_{c,\max} = 2\,\mathrm{M}_\odot$, which for an equal-mass binary corresponds to $M_1 = M_2 = 2.3\,\mathrm{M}_\odot$ (but we note that this choice does not impact our results significantly). We then looked for maximum-a-posteriori estimates for $\mathcal{M}_{c,\min}$ and α given the observed chirp masses of the two GW-detected events GW170817 ($\mathcal{M}_{c,1} = 1.186 \pm 0.001\,\mathrm{M}_\odot$, [9]) and GW190425 ($\mathcal{M}_{c,2} = 1.44 \pm 0.02\,\mathrm{M}_\odot$, [4]). Following [189], assuming a simple $\mathcal{M}_c^{5/2}$ scaling for the effective searched time-volume and neglecting the small measurement

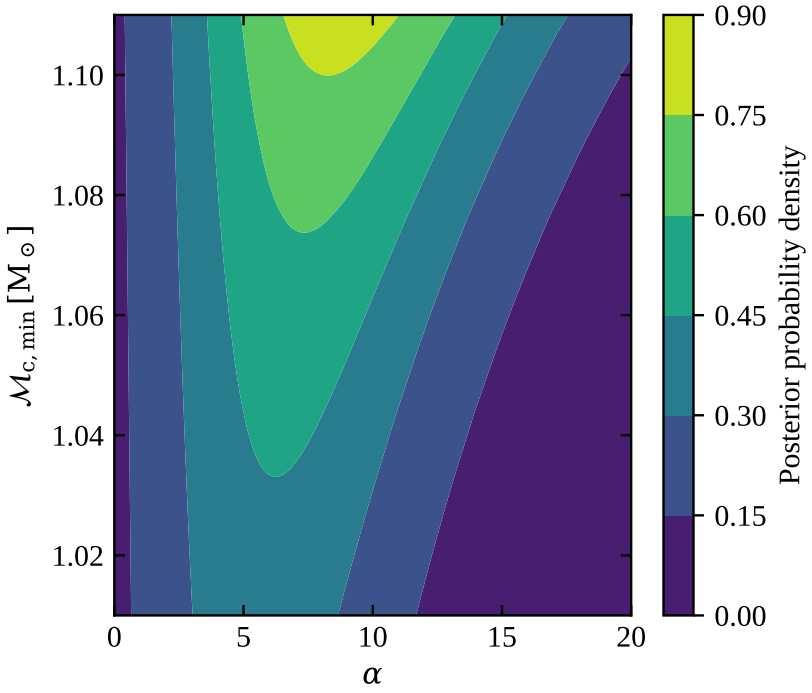

FIGURE A.1: Posterior probability density on our chirp mass probability distribution parameters $\mathcal{M}_{c,\mathrm{min}}$ and α. Filled contours show the two-dimensional posterior probability density, with lighter colors corresponding to larger values, as defined in the colorbar.

uncertainties, the posterior probability on our two parameters can be written as

$$P(\mathcal{M}_{c,\mathrm{min}},\alpha\,|\,\mathcal{M}_{c,1},\mathcal{M}_{c,2}) \propto \pi(\mathcal{M}_{c,\mathrm{min}})\pi(\alpha)\frac{P(\mathcal{M}_{c,1}\,|\,\mathcal{M}_{c,\mathrm{min}},\alpha)P(\mathcal{M}_{c,2}\,|\,\mathcal{M}_{c,\mathrm{min}},\alpha)}{\left[\int_{\mathcal{M}_{c,\mathrm{min}}}^{\mathcal{M}_{c,\mathrm{max}}} P(\mathcal{M}_c\,|\,\mathcal{M}_{c,\mathrm{min}},\alpha)\mathcal{M}_c^{5/2}\,\mathrm{d}\mathcal{M}_c\right]^2}, \tag{A.4}$$

where $\pi(\mathcal{M}_{c,\mathrm{min}})$ and $\pi(\alpha)$ are the adopted priors. Given that the smallest observed chirp mass in a merging Galactic NSNS system is $\sim 1.11\,\mathrm{M}_\odot$ (the chirp mass of J1756-2251, [106]), we set $\pi(\mathcal{M}_{c,\mathrm{min}}) = \Theta(1.11\,\mathrm{M}_\odot - \mathcal{M}_{c,\mathrm{min}})$, while we adopted a broad uniform prior on α in the range $0 \leq \alpha \leq 20$. The resulting posterior probability density is shown in Figure A.1, which shows that the maximum a posteriori probability density is at $\alpha = 8.67$ and $\mathcal{M}_{c,\mathrm{min}} = 1.1\,\mathrm{M}_\odot$, the latter being located on the edge of the prior support (which is based on the lowest chirp mass observed in Galactic NSNS binaries). This tells us that the estimate of $\mathcal{M}_{c,\mathrm{min}}$ is informed by EM Galactic NSNS observations, in addition to GW NSNS merger observations: in that sense, this is a multi-messenger estimate.

In order to constrain the mass ratio distribution parameter β, we used instead the observed Galactic NSNS mass posteriors from [104]. Their sample comprises $N = 10$ NSNSs that will merge within a Hubble time, for each of which they provide $N_s = 10^4$ component mass posterior samples. We constructed mass ratio posterior samples $\{q_{i,j}\}_{i=1,...N;\,j=1,..,N_s}$ from these samples, adopting the appropriate mass ordering to ensure $q \leq 1$ for each posterior sample pair. The posterior probability on the β

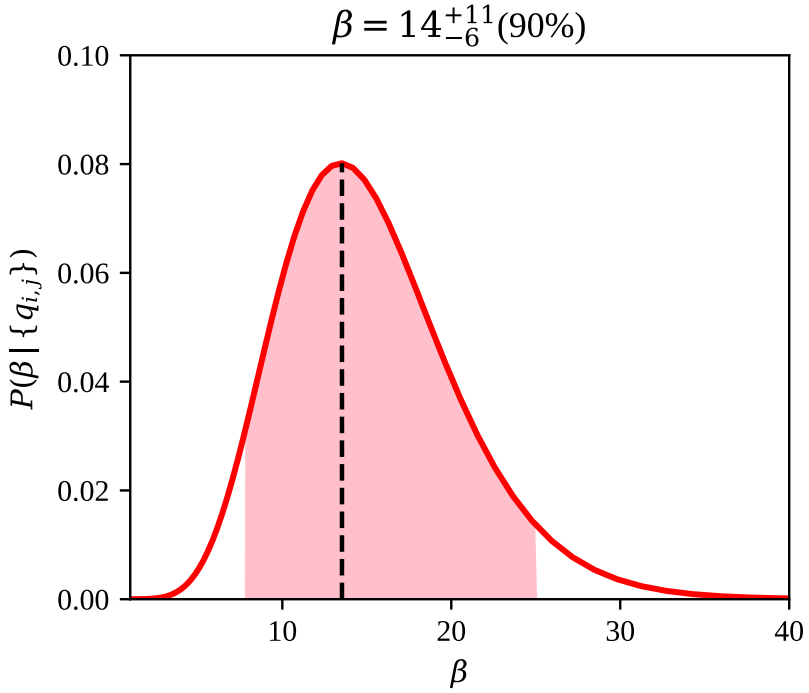

FIGURE A.2: Posterior probability density on the β parameter of our assumed mass ratio probability distribution parametrization. The red solid curve shows the result of Eq. A.5 using the mass information on 10 Galactic NSNS binaries that merge within a Hubble time from Farrow et al. [104]. The pink shaded area shows the 90% credible interval, while the vertical dashed line marks the maximum *a posteriori*.

parameter based on these samples is then

$$P(\beta \mid \{q_{i,j}\}) \propto \pi(\beta) \prod_{i=1}^{N} \frac{1+\beta}{N_s} \sum_{j=1}^{N_s} q_{i,j}^{\beta}. \tag{A.5}$$

We adopted a uniform prior $\pi(\beta)$ in the range $0 \leq \beta \leq 40$.

The resulting posterior probability distribution is shown in Figure A.2, which shows a large uncertainty, but a well-defined peak at $\beta = 14$.

Figure A.3 compares the observed Galactic NSNS mass ratio cumulative distribution and our mass ratio distribution model $P(q \mid \beta)$ with the maximum-a-posteriori value $\beta = 14$.

Figure A.4 compares the resulting $P(M_1, M_2 \mid \mathcal{M}_{c,\min}, \alpha, \beta)$ model of the mass distribution with the observations on the (M_1, M_2) plane. It also shows iso-contours of ejecta and accretion disk mass obtained with our adopted fitting formulae [171, 43] and equation of state (EoS) SFHo (left panel) and DD2 (right panel), which helps in visualizing the absence of EM counterparts for events in the upper right corner of the plane, and the general trends in the distribution of ejecta and disk masses in the population. We also show with a pink line the condition for a HMNS remnant ($M_{\rm rem} > 1.2 M_{\rm TOV}$) and so the condition to launch a relativistic jet.

We note that changing the chirp mass parametrization to either an exponential $P(\mathcal{M}_c) \propto \Theta(\mathcal{M}_c - \mathcal{M}_{c,\min}) \exp(-\mathcal{M}_c / \mathcal{M}_{c,\rm scale})$ or a Gaussian tail $P(\mathcal{M}_c) \propto \Theta(\mathcal{M}_c - \mathcal{M}_{c,\min}) \exp\left[-(\mathcal{M}_c / \mathcal{M}_{c,\rm scale})^2\right]$ does not alter significantly our results, as demonstrated in Figure A.5 (left-hand panel).

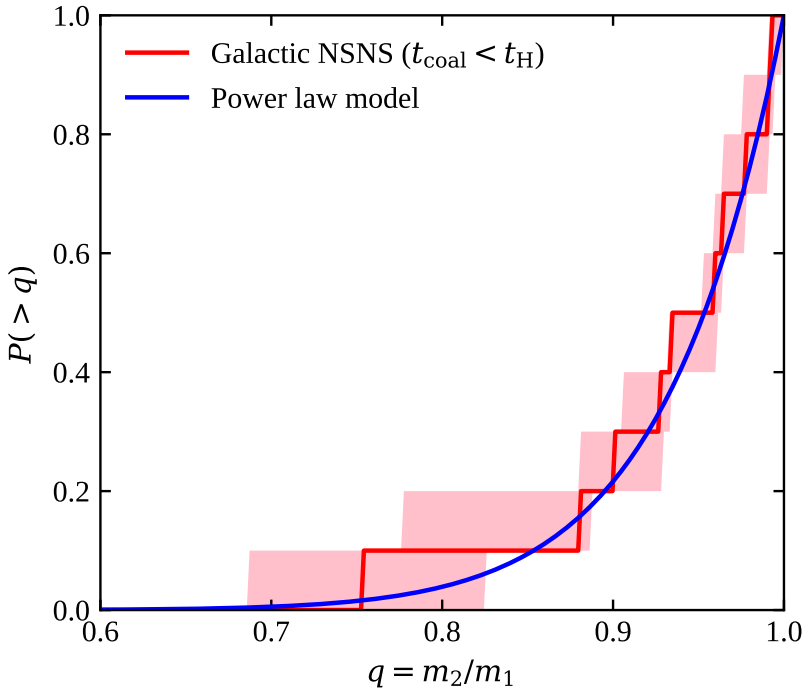

FIGURE A.3: Cumulative mass ratio probability density in our mass distribution model (blue solid line), compared to the observed Galactic NSNS (with coalescence time less than the Hubble time) mass ratio cumulative distribution (red line: median; pink area: 90% uncertainty region – based on the data from [104]).

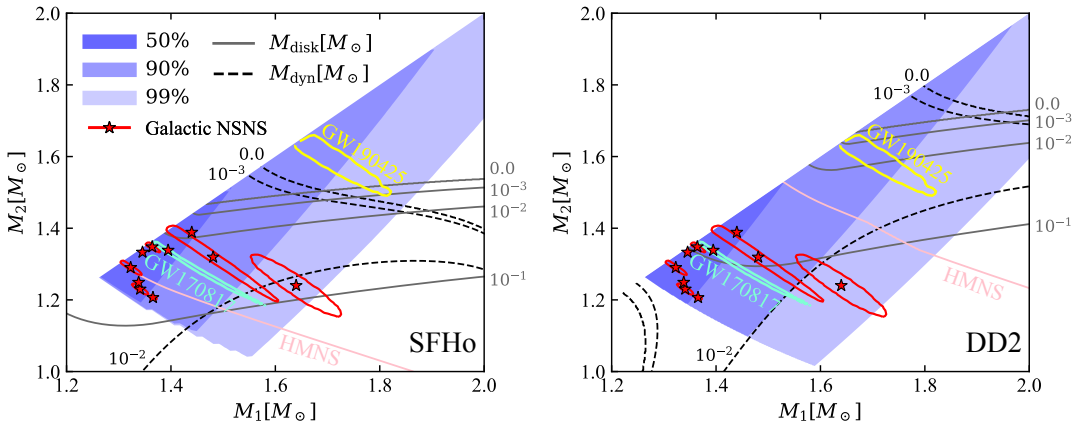

FIGURE A.4: M_1, M_2 plane showing the mass distribution for our NSNS population. The filled blue colored regions contain 50%, 90% and 99% of the binaries. The black dashed lines and the grey lines represent respectively the contours for the predicted dynamical ejecta and disk mass, assuming the SFHo EoS (left panel) and the DD2 EoS (right panel). The pink line indicates the condition for a HMNS remnant ($M_{rem} > 1.2M_{TOV}$). Red stars and contours show the best fit and 90% credible regions for the known Galactic NSNS [217, 104] systems that merge within a Hubble time. Yellow and aquamarine lines represent the 50% confidence regions for the component masses in GW190425 [4] and GW170817 [7], both constructed using the publicly available low-spin-prior posterior samples.

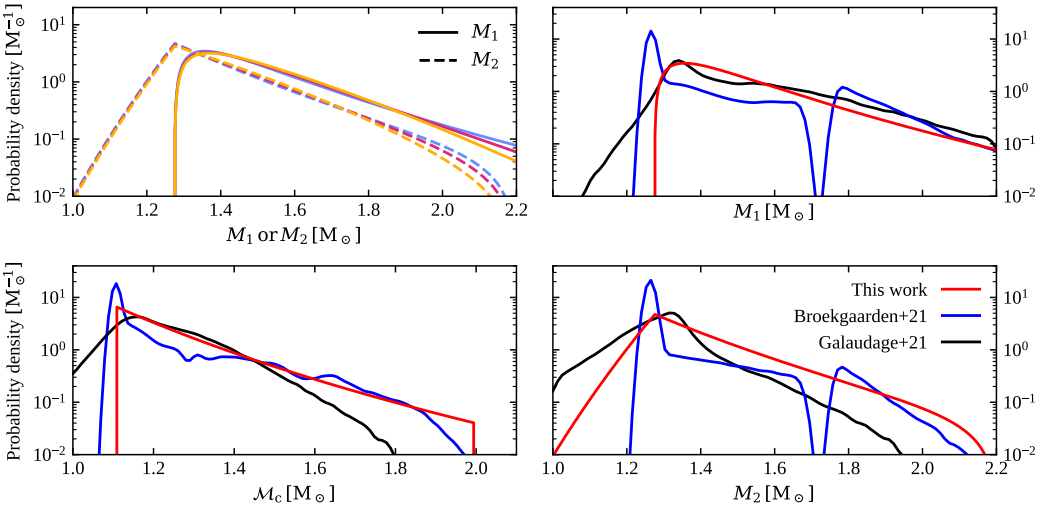

FIGURE A.5: Component mass probability distribution comparisons. Upper-left panel: NSNS component mass probability distributions (solid lines: primary mass; dashed lines: secondary mass) from our model, assuming three different parametrizations of the chirp mass probability distribution, namely a power law (purple – the fiducial model described in the text), a decreasing exponential (orange) and a Gaussian tail (light blue). Other panels: comparison of our component mass (top-right: primary; bottom-right: secondary) and chirp mass (lower-left) probability distributions (red lines) with those from a state-of-the-art population synthesis model [the fiducial model from 68, blue lines] and of an observational study that combines Galactic and GW NSNS measurements [123, black lines, obtained considering their median distributions].

It is instructive to compare our mass probability distribution with others in the literature. To that purpose, we show in the right-hand panels of Figure A.5 a comparison of the probability distributions of component and chirp masses implied by our result (red lines) with the corresponding distributions from a recently published population synthesis model [68, their fiducial model] based on the COMPAS code [254], and with the result of the study by [123], which models the Galactic NSNS population and the GW-detected NSNS binaries together. These comparisons show that, despite the large uncertainties and the simplifying assumptions, our results fall in a reasonably similar range as other results based on more refined methodologies. Last, but not least, our mass distribution combined with our choice of the EoS leads to a large fraction of remnants that satisfy the basic requirements for the launch of a relativistic jet by the [60] process, namely a hyper-massive NS or a BH remnant and a non-negligible accretion disk, as required by the high observed incidence of jets [see 270, who discuss this argument and the implied mass distribution constraints in detail].

A.1.2 Redshift distribution

Merging binary neutron stars are thought to form either from isolated stellar binaries or in dense stellar environments such as stellar clusters, in which dynamical interactions can play a non-negligible role in their formation and evolution [288, 290, 240, 56]. Taking into account the strong dependence of the GW-driven coalescence timescale $t_{c,GW}$ on the binary separation a, $t_{c,GW} \propto a^4$, and expressing the probability distribution of a as a power law with index x, namely $dP/da \propto a^x$, the probability distribution of the delay time between the start of the GW-driven inspiral and the

coalescence is $\mathrm{d}P/\mathrm{d}t_{\mathrm{c,GW}} = (\mathrm{d}P/\mathrm{d}a)(\mathrm{d}a/\mathrm{d}t_{\mathrm{c,GW}}) \propto t_{\mathrm{c,GW}}^{-3/4+x/4}$ [235]. Being the result of a diverse and complex range of processes, it is reasonable to expect the separation distribution $\mathrm{d}P/\mathrm{d}a$ to be close to uniform in the logarithm, and hence $x \sim -1$. This translates into a delay time distribution $\mathrm{d}P/\mathrm{d}t_{\mathrm{c,GW}}$ that is also close to uniform-in-log, and the $x/4$ dependence ensures that this remains approximately true unless x is very large in absolute value. When the coalescence timescale $t_{\mathrm{c,GW}}$ is longer than t_{SN2}, the time elapsed between the birth of the binary and the formation of the second neutron star, then the delay t_{d} between the binary formation and its coalescence also follows the same power law; conversely, for very short GW coalescence timescales, the delay time $t_{\mathrm{d}} \sim t_{\mathrm{SN2}}$. These arguments lead to a delay time distribution of the form

$$\frac{\mathrm{d}P}{\mathrm{d}t_{\mathrm{d}}} \propto \begin{cases} t_{\mathrm{d}}^{-1} & t_{\mathrm{d}} \geq \langle t_{\mathrm{SN2}} \rangle \\ 0 & t_{\mathrm{d}} < \langle t_{\mathrm{SN2}} \rangle \end{cases}, \tag{A.6}$$

where $\langle t_{\mathrm{SN2}} \rangle$ is the mean time to the second supernova, which we take as $\langle t_{\mathrm{SN2}} \rangle = 50\,\mathrm{Myr}$, appropriate for the lightest neutron star progenitors. This distribution is broadly consistent with the results of detailed binary stellar population synthesis models [e.g. 93]. With the further simplifying assumption of a constant fraction of stellar mass going into binaries that end up as double neutron stars throughout the history of the Universe, the cosmic NSNS merger rate density can be then modelled as

$$\dot{\rho}(t) = \frac{\mathrm{d}^2 N}{\mathrm{d}V\mathrm{d}t} \propto \int_t^{\infty} \dot{\rho}_\star(t') \frac{\mathrm{d}P}{\mathrm{d}t_{\mathrm{d}}}(t'-t)\mathrm{d}t', \tag{A.7}$$

where $t = t(z)$ is the lookback time corresponding to redshift z, $\mathrm{d}V$ is the comoving volume element, and $\dot{\rho}_\star$ is the cosmic star formation rate density, for which we adopt the analytical form given in [185].

A.1.3 Local rate density

The normalization of the assumed NSNS merger rate density, namely the local neutron star merger rate density $\dot{\rho}(0) = R_0$, was set based on self-consistency of the total number of NSNS detections in the three past observing runs of the advanced GW detector network and the number expected given our chosen mass and redshift distributions. To do this in practice, we needed to estimate the effective time-volume searched by the LIGO-Virgo network during the three observing runs O1, O2 and O3, which can be defined as [e.g. 297]

$$V_{\mathrm{eff}} = f_{\mathrm{det}}(< z_{\mathrm{max}}) \int_0^{z_{\mathrm{max}}} \frac{\dot{\rho}(z)}{\dot{\rho}(0)} \frac{\mathrm{d}V}{\mathrm{d}z} \frac{\mathrm{d}z}{1+z}, \tag{A.8}$$

where $\vec{\lambda}_{\mathrm{pop}} = (\mathcal{M}_{\mathrm{c,min}}, \alpha, \beta, \langle t_{\mathrm{SN}} \rangle)$ is our population model parameter vector, $\mathrm{d}V/\mathrm{d}z$ is the differential comoving volume [149], z_{max} is any redshift beyond the O3 GW detectability horizon, and $f_{\mathrm{det}}(< z_{\mathrm{max}})$ is the fraction of detectable NSNS mergers within z_{max}. To estimate the latter, we took the publicly available LVK Collaboration O1+O2+O3 sensitivity study Monte Carlo samples [181], we re-sampled them to reflect our assumed mass and redshift distributions, and then computed $f_{\mathrm{det}}(< z_{\mathrm{max}})$ as the fraction of events that satisfied our detectability cut $\mathrm{SNR}_{\mathrm{net}} \geq 12$ over the total within z_{max}. This resulted in $V_{\mathrm{eff}} = 5.1 \times 10^{-3}\,\mathrm{Gpc}^3$. Given the actual number $N_{\mathrm{obs}} = 2$ of observed NSNS events that satisfy the same cut (i.e. GW170817 and GW190425), and given the total O1+O2+O3 effective observing time $T = 1.23\,\mathrm{yr}$ [17, representing the total time span of observing periods with at least one active detector],

we obtained the posterior on the local merger rate density R_0 (conditional on our assumed mass and redshift distribution)

$$P(R_0 \mid N_{\rm obs}) \propto R_0^{N_{\rm obs}} \exp\left(-R_0 V_{\rm eff} T\right) \pi(R_0), \tag{A.9}$$

where we adopted the Jeffreys prior $\pi(R_0) = R_0^{-1/2}$. The resulting median and symmetric 90% credible interval are $R_0 = 347^{+536}_{-256}\,{\rm Gpc}^{-3}\,{\rm yr}^{-1}$, which therefore includes the statistical Poisson uncertainty stemming from the small number of observed events, but not any model systematic uncertainty (which would result in a larger uncertainty, probably more akin to the ones from [20]), which is not explored here.

A.2 BHNS population model

In Figure A.6, we present similar information of Figure A.4, but for the BHNS population. The figure display in the $M_{\rm NS} - M_{\rm BH}$ plane our BHNS fiducial mass distribution at redshift z = 0 [68]. The filled blue colored regions contain 50%, 90% and 99% of the binaries. The figure also features iso-contours of ejecta and accretion disk masses, calculated using fitting formulae from Krüger and Foucart [171] and Kawaguchi et al. [163], considering two EoS, SFHo (upper panel) and DD2 (right panel), and assuming three different spin configurations for the BHs, $\chi_{\rm BH} = 0$, $\chi_{\rm BH} = 0.5$, $\chi_{\rm BH} = 0.9$. The plot highlights the general trends in the distribution of ejecta and disk masses across our population and show the strong dependence between the BH spin and the ejecta production.

A.2.1 Mass distribution comparison

It is informative to compare the mass probability distribution of our population model of BHNS systems with the one inferred from the GW data. Therefore, we show in Fig. A.7 a comparison of the probability distribution of primary (left panel) and secondary (right panel) component masses based on the population synthesis fiducial model from Broekgaarden et al. [68] assumed in this work (red lines) with the corresponding distributions obtained by Biscoveanu, Landry, and Vitale [57] (blue lines) using an approach driven by the population of four candidate BHNS events detected in GW so far with a FAR rate $\leq 1\ {\rm yr}^{-1}$. In particular the solid blue line represent the posterior predictive distribution and the shaded blue regions the 50% and 90% credible intervals, under a Gaussian mass ratio model.

In the BH mass range of interest in this work $M_{\rm BH} \lesssim 11 M_\odot$, corresponding to systems that can power EM counterparts in our optimistic scenario (see Sec. 6.2.1), the mass distribution from Broekgaarden et al. [68] lies within the 90% credible interval inferred from the GW data. Moreover, the requirement of having systems with $M_{\rm BH} \lesssim 5 M_\odot$ in our fiducial scenario is not in contrast with the distribution predicted by Biscoveanu, Landry, and Vitale [57]. The NS mass distribution inferred from the GW data is flatter than the one used in this work and they both fall off sharply at the maximum mass. The two peaks in the red curve are caused by the choice of supernovae remnant mass prescription in [68] and it is common to all the variations performed in the work.

Overall, we can conclude that the mass distributions of our BHNS population model are consistent with the first constraints deduced from GW data, lending credit to the basis of our MM study.

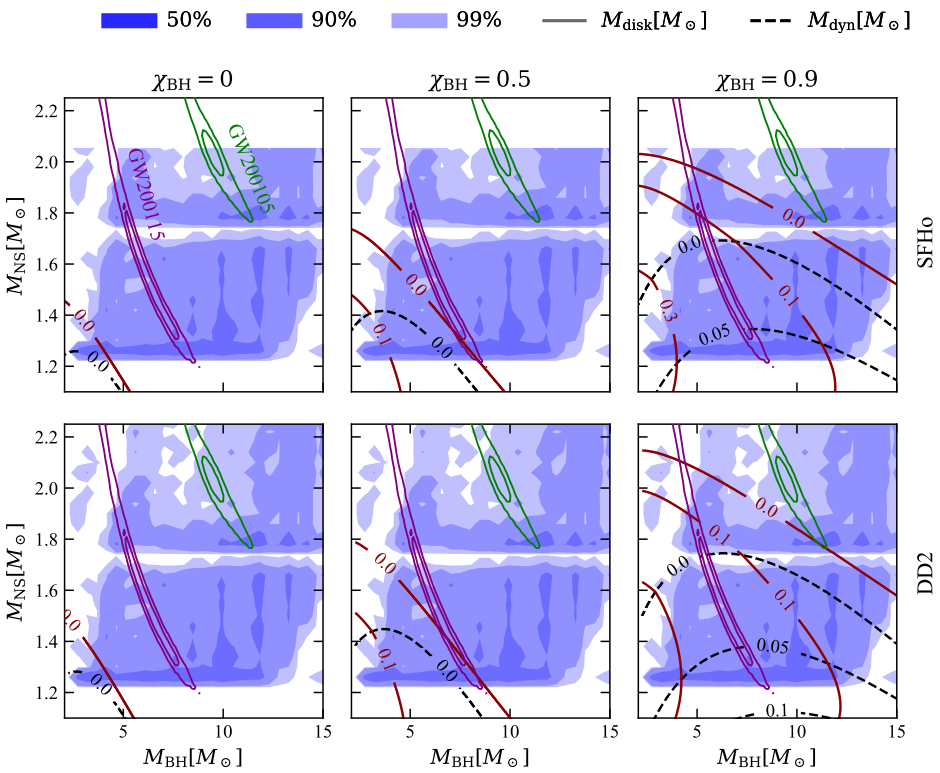

FIGURE A.6: $M_{\rm NS}, M_{\rm BH}$ plane showing the mass distribution for our BHNS population at redshift $z = 0$ (fiducial model in [68]). The filled blue colored regions contain 50%, 90% and 99% of the binaries. The black dashed lines and the dark red lines represent respectively the contours for the predicted dynamical ejecta and disk mass, assuming the SFHo EoS (upper panel) and the DD2 EoS (lower panel). Violet and green lines represent the 50% and 90% confidence regions for the component masses in GW200115 and GW200105 [22], both constructed using the publicly available low-spin-prior posterior samples.

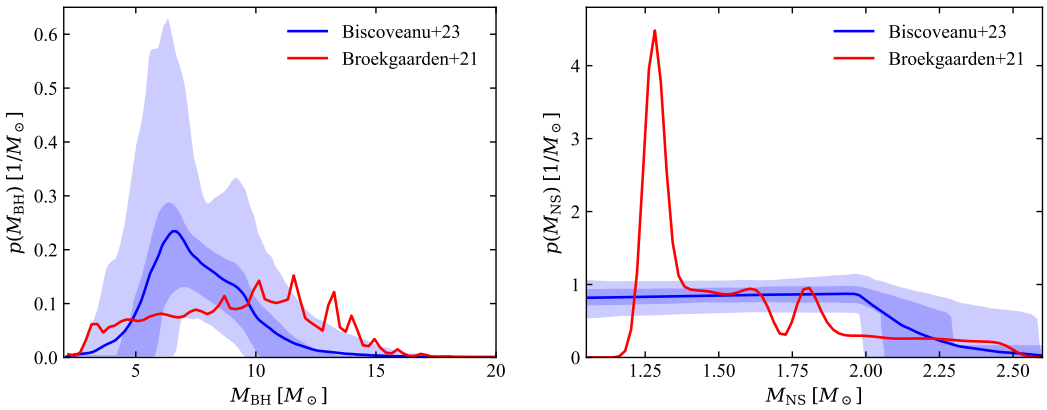

FIGURE A.7: Component mass probability distribution comparisons. Component masses (left panel: BH; right panel: NS) probability distribution (red lines) for the fiducial model in [68] used in this work and posterior predictive distributions (solid blue), 50% and 90% credible intervals (shaded blue) inferred from the population of four candidate BHNS events detected in GW with a FAR rate $\leq 1\ {\rm yr}^{-1}$ [57].

Bibliography

[1] J. Aasi et al. "Advanced LIGO". In: *Classical and Quantum Gravity* 32.7, 074001 (Apr. 2015), p. 074001. DOI: 10.1088/0264-9381/32/7/074001. arXiv: 1411.4547 [gr-qc].

[2] J. Aasi et al. "Characterization of the LIGO detectors during their sixth science run". In: *Classical and Quantum Gravity* 32.11, 115012 (June 2015), p. 115012. DOI: 10.1088/0264-9381/32/11/115012. arXiv: 1410.7764 [gr-qc].

[3] B. P. Abbott, R. Abbott, T. D. Abbott, et al. "Search for Gravitational Waves Associated with Gamma-Ray Bursts during the First Advanced LIGO Observing Run and Implications for the Origin of GRB 150906B". In: *ApJ* 841.2, 89 (June 2017), p. 89. DOI: 10.3847/1538-4357/aa6c47. arXiv: 1611.07947 [astro-ph.HE].

[4] B. P. Abbott, LIGO Scientific Collaboration, and Virgo Collaboration. "GW190425: Observation of a Compact Binary Coalescence with Total Mass $\sim 3.4 M_{\odot}$". In: *arXiv e-prints*, arXiv:2001.01761 (Jan. 2020), arXiv:2001.01761. arXiv: 2001.01761 [astro-ph.HE].

[5] B. P. Abbott, LIGO Scientific Collaboration, and Virgo Collaboration. "GWTC-1: A Gravitational-Wave Transient Catalog of Compact Binary Mergers Observed by LIGO and Virgo during the First and Second Observing Runs". In: *Phys. Rev. X* 9 (3 2019), p. 031040. DOI: 10.1103/PhysRevX.9.031040. URL: https://journals.aps.org/prx/abstract/10.1103/PhysRevX.9.031040.

[6] B. P. Abbott, LIGO Scientific Collaboration, and Virgo Collaboration. "Multi-messenger Observations of a Binary Neutron Star Merger". In: *Astrophys. J.* 848.2 (2017), p. L12. DOI: 10.3847/2041-8213/aa91c9. arXiv: 1710.05833 [astro-ph.HE].

[7] B. P. Abbott, LIGO Scientific Collaboration, and Virgo Collaboration. "Properties of the Binary Neutron Star Merger GW170817". In: *Physical Review X* 9.1, 011001 (Jan. 2019), p. 011001. DOI: 10.1103/PhysRevX.9.011001. arXiv: 1805.11579 [gr-qc].

[8] B. P. Abbott et al. "Gravitational Waves and Gamma-Rays from a Binary Neutron Star Merger: GW170817 and GRB 170817A". In: *ApJ* 848.2, L13 (Oct. 2017), p. L13. DOI: 10.3847/2041-8213/aa920c. arXiv: 1710.05834 [astro-ph.HE].

[9] B. P. Abbott et al. "GW170817: Observation of Gravitational Waves from a Binary Neutron Star Inspiral". In: *Phys. Rev. Lett.* 119.16, 161101 (Oct. 2017), p. 161101. DOI: 10.1103/PhysRevLett.119.161101. arXiv: 1710.05832 [gr-qc].

[10] B. P. Abbott et al. "GWTC-1: A Gravitational-Wave Transient Catalog of Compact Binary Mergers Observed by LIGO and Virgo during the First and Second Observing Runs". In: *Physical Review X* 9.3, 031040 (July 2019), p. 031040. DOI: 10.1103/PhysRevX.9.031040. arXiv: 1811.12907 [astro-ph.HE].

[11] B. P. Abbott et al. "Multi-messenger Observations of a Binary Neutron Star Merger". In: *ApJ* 848.2, L12 (Oct. 2017), p. L12. DOI: 10.3847/2041-8213/aa91c9. arXiv: 1710.05833 [astro-ph.HE].

[12] B. P. Abbott et al. "Observation of Gravitational Waves from a Binary Black Hole Merger". In: *Phys. Rev. Lett.* 116.6, 061102 (Feb. 2016), p. 061102. DOI: 10.1103/PhysRevLett.116.061102. arXiv: 1602.03837 [gr-qc].

[13] B. P. Abbott et al. "Prospects for observing and localizing gravitational-wave transients with Advanced LIGO, Advanced Virgo and KAGRA". In: *Living Reviews in Relativity* 21.1, 3 (Apr. 2018), p. 3. DOI: 10.1007/s41114-018-0012-9. arXiv: 1304.0670 [gr-qc].

[14] B. P. Abbott et al. "Prospects for observing and localizing gravitational-wave transients with Advanced LIGO, Advanced Virgo and KAGRA". In: *Living Reviews in Relativity* 23.1 (Sept. 2020). ISSN: 1433-8351. DOI: 10.1007/s41114-020-00026-9. URL: http://dx.doi.org/10.1007/s41114-020-00026-9.

[15] R. Abbott, LIGO Scientific Collaboration, and Virgo Collaboration. "GWTC-2: Compact Binary Coalescences Observed by LIGO and Virgo During the First Half of the Third Observing Run". In: *Phys. Rev. X* 11 (2 2021), p. 021053. DOI: 10.1103/PhysRevX.11.021053. URL: https://journals.aps.org/prx/abstract/10.1103/PhysRevX.11.021053.

[16] R. Abbott, LIGO Scientific Collaboration, and Virgo Collaboration. "GWTC-2.1: Deep Extended Catalog of Compact Binary Coalescences Observed by LIGO and Virgo During the First Half of the Third Observing Run". In: *arXiv e-prints* (Aug. 2021). arXiv: 2108.01045 [gr-qc].

[17] R. Abbott, LIGO Scientific Collaboration, and Virgo Collaboration. "GWTC-3: Compact Binary Coalescences Observed by LIGO and Virgo During the Second Part of the Third Observing Run". In: *arXiv e-prints*, arXiv:2111.03606 (Nov. 2021), arXiv:2111.03606. arXiv: 2111.03606 [astro-ph.HE].

[18] R. Abbott, LIGO Scientific Collaboration, and Virgo Collaboration. "Observation of Gravitational Waves from Two Neutron Star–Black Hole Coalescences". In: *ApJ* 915, L5 (June 2021), p. L5. DOI: 10.3847/2041-8213/ac082e. arXiv: 2106.15163 [astro-ph.HE].

[19] R. Abbott, LIGO Scientific Collaboration, and Virgo Collaboration. "Search for Gravitational Waves Associated with Gamma-Ray Bursts Detected by Fermi and Swift During the LIGO-Virgo Run O3b". In: *arXiv e-prints* (Nov. 2021). arXiv: 2111.03608 [astro-ph.HE].

[20] R. Abbott, LIGO Scientific Collaboration, and Virgo Collaboration. "The population of merging compact binaries inferred using gravitational waves through GWTC-3". In: *arXiv e-prints* (Nov. 2021). arXiv: 2111.03634 [astro-ph.HE].

[21] R. Abbott et al. "GW190814: Gravitational Waves from the Coalescence of a 23 Solar Mass Black Hole with a 2.6 Solar Mass Compact Object". In: *The Astrophysical Journal Letters* 896.2 (June 2020), p. L44. ISSN: 2041-8213. DOI: 10.3847/2041-8213/ab960f. URL: http://dx.doi.org/10.3847/2041-8213/ab960f.

[22] R. Abbott et al. "Observation of Gravitational Waves from Two Neutron Star-Black Hole Coalescences". In: *ApJ* 915.1, L5 (July 2021), p. L5. DOI: 10.3847/2041-8213/ac082e. arXiv: 2106.15163 [astro-ph.HE].

[23] R. Abbott et al. "Population of Merging Compact Binaries Inferred Using Gravitational Waves through GWTC-3". In: *Physical Review X* 13.1, 011048 (Jan. 2023), p. 011048. DOI: 10.1103/PhysRevX.13.011048.

[24] F. Acernese et al. "Advanced Virgo: a second-generation interferometric gravitational wave detector". In: *Classical and Quantum Gravity* 32.2, 024001 (Jan. 2015), p. 024001. DOI: 10.1088/0264-9381/32/2/024001. arXiv: 1408.3978 [gr-qc].

[25] F. Acernese et al. "Advanced Virgo: a second-generation interferometric gravitational wave detector". In: *Classical and Quantum Gravity* 32.2, 024001 (Jan. 2015), p. 024001. DOI: 10.1088/0264-9381/32/2/024001. arXiv: 1408.3978 [gr-qc].

[26] K. Ackley et al. "Observational constraints on the optical and near-infrared emission from the neutron star-black hole binary merger candidate S190814bv". In: *A&A* 643, A113 (Nov. 2020), A113. DOI: 10.1051/0004-6361/202037669. arXiv: 2002.01950 [astro-ph.SR].

[27] Ricard Aguilera-Miret et al. "Turbulent magnetic-field amplification in the first 10 milliseconds after a binary neutron star merger: Comparing high-resolution and large-eddy simulations". In: *Phys. Rev. D* 102.10, 103006 (Nov. 2020), p. 103006. DOI: 10.1103/PhysRevD.102.103006. arXiv: 2009.06669 [gr-qc].

[28] K. D. Alexander et al. "A Late-time Galaxy-targeted Search for the Radio Counterpart of GW190814". In: *ApJ* 923.1, 66 (Dec. 2021), p. 66. DOI: 10.3847/1538-4357/ac281a. arXiv: 2102.08957 [astro-ph.HE].

[29] L. Amati et al. "Intrinsic spectra and energetics of BeppoSAX Gamma-Ray Bursts with known redshifts". In: *A&A* 390 (July 2002), pp. 81–89. DOI: 10.1051/0004-6361:20020722. arXiv: astro-ph/0205230 [astro-ph].

[30] L. Amati et al. "The THESEUS space mission: science goals, requirements and mission concept". In: *Experimental Astronomy* 52.3 (Dec. 2021), pp. 183–218. DOI: 10.1007/s10686-021-09807-8. arXiv: 2104.09531 [astro-ph.IM].

[31] Shreya Anand et al. "Optical follow-up of the neutron star-black hole mergers S200105ae and S200115j". In: *Nature Astronomy* 5 (Jan. 2021), pp. 46–53. DOI: 10.1038/s41550-020-1183-3. arXiv: 2009.07210 [astro-ph.HE].

[32] Igor Andreoni et al. "Constraining the Kilonova Rate with Zwicky Transient Facility Searches Independent of Gravitational Wave and Short Gamma-Ray Burst Triggers". In: *ApJ* 904.2, 155 (Dec. 2020), p. 155. DOI: 10.3847/1538-4357/abbf4c. arXiv: 2008.00008 [astro-ph.HE].

[33] Igor Andreoni et al. "Fast-transient Searches in Real Time with ZTFReST: Identification of Three Optically Discovered Gamma-Ray Burst Afterglows and New Constraints on the Kilonova Rate". In: *ApJ* 918.2, 63 (Sept. 2021), p. 63. DOI: 10.3847/1538-4357/ac0bc7. arXiv: 2104.06352 [astro-ph.HE].

[34] Igor Andreoni et al. "GROWTH on S190814bv: Deep Synoptic Limits on the Optical/Near-infrared Counterpart to a Neutron Star-Black Hole Merger". In: *ApJ* 890.2, 131 (Feb. 2020), p. 131. DOI: 10.3847/1538-4357/ab6a1b. arXiv: 1910.13409 [astro-ph.HE].

[35] Igor Andreoni et al. "Target-of-opportunity Observations of Gravitational-wave Events with Vera C. Rubin Observatory". In: *ApJS* 260.1, 18 (May 2022), p. 18. DOI: 10.3847/1538-4365/ac617c. arXiv: 2111.01945 [astro-ph.HE].

[36] S. Antier et al. "The first six months of the Advanced LIGO's and Advanced Virgo's third observing run with GRANDMA". In: *MNRAS* 492.3 (Mar. 2020), pp. 3904–3927. DOI: 10.1093/mnras/stz3142. arXiv: 1910.11261 [astro-ph.HE].

[37] A. Arcones, H. Th. Janka, and L. Scheck. "Nucleosynthesis-relevant conditions in neutrino-driven supernova outflows. I. Spherically symmetric hydrodynamic simulations". In: *A&A* 467.3 (June 2007), pp. 1227–1248. DOI: 10.1051/0004-6361:20066983. arXiv: astro-ph/0612582 [astro-ph].

[38] Yoichi Aso et al. "Interferometer design of the KAGRA gravitational wave detector". In: *Phys. Rev. D* 88.4, 043007 (Aug. 2013), p. 043007. DOI: 10.1103/PhysRevD.88.043007. arXiv: 1306.6747 [gr-qc].

[39] Auger, Gerard and Plagnol Eric. *An Overview of Gravitational Waves. Theory, Sources and Detection*. World Scientific, 2017. ISBN: 978-981-3141-77-3. DOI: https://doi.org/10.1142/10082.

[40] Leor Barack and Curt Cutler. "LISA capture sources: Approximate waveforms, signal-to-noise ratios, and parameter estimation accuracy". In: *Phys. Rev. D* 69 (2004), p. 082005. DOI: 10.1103/PhysRevD.69.082005. arXiv: gr-qc/0310125.

[41] C. Barbieri et al. "Electromagnetic counterparts of black hole-neutron star mergers: dependence on the neutron star properties". In: *European Physical Journal A* 56.1, 8 (Jan. 2020), p. 8. DOI: 10.1140/epja/s10050-019-00013-x. arXiv: 1908.08822 [astro-ph.HE].

[42] C. Barbieri et al. "Exploring the nature of ambiguous merging systems: GW190425 in low latency". In: *A&A* 654, A12 (Oct. 2021), A12. DOI: 10.1051/0004-6361/202037778.

[43] C. Barbieri et al. "Filling the Mass Gap: How Kilonova Observations Can Unveil the Nature of the Compact Object Merging with the Neutron Star". In: *ApJ* 887.2, L35 (Dec. 2019), p. L35. DOI: 10.3847/2041-8213/ab5c1e. arXiv: 1912.03894 [astro-ph.HE].

[44] C. Barbieri et al. "Light-curve models of black hole - neutron star mergers: steps towards a multi-messenger parameter estimation". In: *A&A* 625, A152 (May 2019), A152. DOI: 10.1051/0004-6361/201935443. arXiv: 1903.04543 [astro-ph.HE].

[45] James M. Bardeen, William H. Press, and Saul A. Teukolsky. "Rotating Black Holes: Locally Nonrotating Frames, Energy Extraction, and Scalar Synchrotron Radiation". In: *ApJ* 178 (Dec. 1972), pp. 347–370. DOI: 10.1086/151796.

[46] Jennifer Barnes and Daniel Kasen. "Effect of a High Opacity on the Light Curves of Radioactively Powered Transients from Compact Object Mergers". In: *ApJ* 775.1, 18 (Sept. 2013), p. 18. DOI: 10.1088/0004-637X/775/1/18. arXiv: 1303.5787 [astro-ph.HE].

[47] Thomas W. Baumgarte, Stuart L. Shapiro, and Masaru Shibata. "On the Maximum Mass of Differentially Rotating Neutron Stars". In: *ApJ* 528.1 (Jan. 2000), pp. L29–L32. DOI: 10.1086/312425. arXiv: astro-ph/9910565 [astro-ph].

[48] A. Bauswein, S. Goriely, and H. T. Janka. "Systematics of Dynamical Mass Ejection, Nucleosynthesis, and Radioactively Powered Electromagnetic Signals from Neutron-star Mergers". In: *ApJ* 773.1, 78 (Aug. 2013), p. 78. DOI: 10.1088/0004-637X/773/1/78. arXiv: 1302.6530 [astro-ph.SR].

[49] K. Belczynski et al. "Evolutionary roads leading to low effective spins, high black hole masses, and O1/O2 rates for LIGO/Virgo binary black holes". In: *A&A* 636, A104 (Apr. 2020), A104. DOI: 10.1051/0004-6361/201936528. arXiv: 1706.07053 [astro-ph.HE].

[50] Krzysztof Belczynski et al. "Missing Black Holes Unveil the Supernova Explosion Mechanism". In: *ApJ* 757.1, 91 (Sept. 2012), p. 91. DOI: 10.1088/0004-637X/757/1/91. arXiv: 1110.1635 [astro-ph.GA].

[51] Enis Belgacem et al. "Cosmology and dark energy from joint gravitational wave-GRB observations". In: *Journal of Cosmology and Astroparticle Physics* 2019.08 (Aug. 2019), 015–015. ISSN: 1475-7516. DOI: 10.1088/1475-7516/2019/08/015. URL: http://dx.doi.org/10.1088/1475-7516/2019/08/015.

[52] Paz Beniamini, Lara Nava, and Tsvi Piran. "A revised analysis of gamma-ray bursts' prompt efficiencies". In: *MNRAS* 461.1 (Sept. 2016), pp. 51–59. DOI: 10.1093/mnras/stw1331. arXiv: 1606.00311 [astro-ph.HE].

[53] Paz Beniamini and Alexander J. van der Horst. "Electrons' energy in GRB afterglows implied by radio peaks". In: *MNRAS* 472.3 (Dec. 2017), pp. 3161–3168. DOI: 10.1093/mnras/stx2203. arXiv: 1706.07817 [astro-ph.HE].

[54] E. Berger, W. Fong, and R. Chornock. "An r-process Kilonova Associated with the Short-hard GRB 130603B". In: *ApJ* 774.2, L23 (Sept. 2013), p. L23. DOI: 10.1088/2041-8205/774/2/L23. arXiv: 1306.3960 [astro-ph.HE].

[55] Sebastiano Bernuzzi et al. "Accretion-induced prompt black hole formation in asymmetric neutron star mergers, dynamical ejecta, and kilonova signals". In: *MNRAS* 497.2 (Sept. 2020), pp. 1488–1507. DOI: 10.1093/mnras/staa1860. arXiv: 2003.06015 [astro-ph.HE].

[56] D. Bhattacharya and E. P. J. van den Heuvel. "Formation and evolution of binary and millisecond radio pulsars". In: *Phys. Rep.* 203.1-2 (Jan. 1991), pp. 1–124. DOI: 10.1016/0370-1573(91)90064-S.

[57] Sylvia Biscoveanu, Philippe Landry, and Salvatore Vitale. "Population properties and multimessenger prospects of neutron star-black hole mergers following GWTC-3". In: *MNRAS* 518.4 (Feb. 2023), pp. 5298–5312. DOI: 10.1093/mnras/stac3052. arXiv: 2207.01568 [astro-ph.HE].

[58] Luc Blanchet. "Gravitational Radiation from Post-Newtonian Sources and Inspiralling Compact Binaries". In: *Living Reviews in Relativity* 17.1, 2 (Dec. 2014), p. 2. DOI: 10.12942/lrr-2014-2. arXiv: 1310.1528 [gr-qc].

[59] R. D. Blandford and C. F. McKee. "Fluid dynamics of relativistic blast waves". In: *Physics of Fluids* 19 (Aug. 1976), pp. 1130–1138. DOI: 10.1063/1.861619.

[60] R. D. Blandford and R. L. Znajek. "Electromagnetic extraction of energy from Kerr black holes." In: *MNRAS* 179 (May 1977), pp. 433–456. DOI: 10.1093/mnras/179.3.433.

[61] S. I. Blinnikov et al. "Exploding Neutron Stars in Close Binaries". In: *Soviet Astronomy Letters* 10 (Apr. 1984), pp. 177–179. DOI: 10.48550/arXiv.1808.05287. arXiv: 1808.05287 [astro-ph.HE].

[62] Oliver M. Boersma and Joeri van Leeuwen. "Investigating the detection rates and inference of gravitational-wave and radio emission from black hole neutron star mergers". In: *A&A* 664, A160 (Aug. 2022), A160. DOI: 10.1051/0004-6361/202243267. arXiv: 2202.02181 [astro-ph.HE].

[63] Luke Bovard et al. "r -process nucleosynthesis from matter ejected in binary neutron star mergers". In: *Phys. Rev. D* 96.12, 124005 (Dec. 2017), p. 124005. DOI: 10.1103/PhysRevD.96.124005. arXiv: 1709.09630 [gr-qc].

[64] Marica Branchesi et al. "Science with the Einstein Telescope: a comparison of different designs". In: *J. Cosmology Astropart. Phys.* 2023.7, 068 (July 2023), p. 068. DOI: 10.1088/1475-7516/2023/07/068. arXiv: 2303.15923 [gr-qc].

[65] Robert Braun et al. "Anticipated Performance of the Square Kilometre Array – Phase 1 (SKA1)". In: *arXiv e-prints*, arXiv:1912.12699 (Dec. 2019), arXiv:1912.12699. DOI: 10.48550/arXiv.1912.12699. arXiv: 1912.12699 [astro-ph.IM].

[66] Matteo Breschi et al. "AT2017gfo: Bayesian inference and model selection of multicomponent kilonovae and constraints on the neutron star equation of state". In: *MNRAS* 505.2 (Aug. 2021), pp. 1661–1677. DOI: 10.1093/mnras/stab1287. arXiv: 2101.01201 [astro-ph.HE].

[67] Cosima Breu and Luciano Rezzolla. "Maximum mass, moment of inertia and compactness of relativistic stars". In: *MNRAS* 459.1 (June 2016), pp. 646–656. DOI: 10.1093/mnras/stw575. arXiv: 1601.06083 [gr-qc].

[68] Floor S. Broekgaarden et al. "Impact of massive binary star and cosmic evolution on gravitational wave observations - II. Double compact object rates and properties". In: *MNRAS* 516.4 (Nov. 2022), pp. 5737–5761. DOI: 10.1093/mnras/stac1677. arXiv: 2112.05763 [astro-ph.HE].

[69] Omer Bromberg et al. "The Propagation of Relativistic Jets in External Media". In: *ApJ* 740.2, 100 (Oct. 2011), p. 100. DOI: 10.1088/0004-637X/740/2/100. arXiv: 1107.1326 [astro-ph.HE].

[70] E. Margaret Burbidge et al. "Synthesis of the Elements in Stars". In: *Reviews of Modern Physics* 29.4 (Jan. 1957), pp. 547–650. DOI: 10.1103/RevModPhys.29.547.

[71] Eric Burns et al. "Do the Fermi Gamma-Ray Burst Monitor and Swift Burst Alert Telescope see the Same Short Gamma-Ray Bursts?" In: *ApJ* 818.2, 110 (Feb. 2016), p. 110. DOI: 10.3847/0004-637X/818/2/110. arXiv: 1512.00923 [astro-ph.HE].

[72] T. A. Callister. "A Thesaurus for Common Priors in Gravitational-Wave Astronomy". In: *arXiv e-prints*, arXiv:2104.09508 (Apr. 2021), arXiv:2104.09508. arXiv: 2104.09508 [gr-qc].

[73] A. G. W. Cameron. "Nuclear Reactions in Stars and Nucleogenesis". In: *PASP* 69.408 (June 1957), p. 201. DOI: 10.1086/127051.

[74] Eve A. Chase et al. "Kilonova Detectability with Wide-field Instruments". In: *The Astrophysical Journal* 927.2 (Mar. 2022), p. 163. DOI: 10.3847/1538-4357/ac3d25. URL: https://doi.org/10.3847%2F1538-4357%2Fac3d25.

[75] R. Chornock et al. "The Electromagnetic Counterpart of the Binary Neutron Star Merger LIGO/Virgo GW170817. IV. Detection of Near-infrared Signatures of r-process Nucleosynthesis with Gemini-South". In: *ApJ* 848.2, L19 (Oct. 2017), p. L19. DOI: 10.3847/2041-8213/aa905c. arXiv: 1710.05454 [astro-ph.HE].

[76] Riccardo Ciolfi. "Collimated outflows from long-lived binary neutron star merger remnants". In: *MNRAS* 495.1 (June 2020), pp. L66–L70. DOI: 10.1093/mnrasl/slaa062. arXiv: 2001.10241 [astro-ph.HE].

[77] Riccardo Ciolfi and Jay Vijay Kalinani. "Magnetically Driven Baryon Winds from Binary Neutron Star Merger Remnants and the Blue Kilonova of 2017 August". In: *ApJ* 900.2, L35 (Sept. 2020), p. L35. DOI: 10.3847/2041-8213/abb240. arXiv: 2004.11298 [astro-ph.HE].

[78] Alberto Colombo et al. "Multi-messenger Observations of Binary Neutron Star Mergers in the O4 Run". In: *ApJ* 937.2, 79 (Oct. 2022), p. 79. DOI: 10.3847/1538-4357/ac8d00. arXiv: 2204.07592 [astro-ph.HE].

[79] Alberto Colombo et al. "Multi-messenger prospects for black hole - neutron star mergers in the O4 and O5 runs". In: *arXiv e-prints*, arXiv:2310.16894 (Oct. 2023), arXiv:2310.16894. DOI: 10.48550/arXiv.2310.16894. arXiv: 2310.16894 [astro-ph.HE].

[80] Monica Colpi and Alberto Sesana. "Gravitational Wave Sources in the Era of Multi-Band Gravitational Wave Astronomy". In: *An Overview of Gravitational Waves: Theory*. 2017, pp. 43–140. DOI: 10.1142/9789813141766_0002.

[81] Alessandra Corsi et al. "Astro2020 Science White Paper: Radio Counterparts of Compact Object Mergers in the Era of Gravitational-Wave Astronomy". In: *arXiv e-prints*, arXiv:1903.10589 (Mar. 2019), arXiv:1903.10589. DOI: 10.48550/arXiv.1903.10589. arXiv: 1903.10589 [astro-ph.IM].

[82] E. Costa et al. "Discovery of an X-ray afterglow associated with the γ-ray burst of 28 February 1997". In: *Nature* 387.6635 (June 1997), pp. 783–785. DOI: 10.1038/42885. arXiv: astro-ph/9706065 [astro-ph].

[83] Michael W. Coughlin and Tim Dietrich. "Can a black hole-neutron star merger explain GW170817, AT2017gfo, and GRB170817A?" In: *Phys. Rev. D* 100.4, 043011 (Aug. 2019), p. 043011. DOI: 10.1103/PhysRevD.100.043011. arXiv: 1901.06052 [astro-ph.HE].

[84] D. A. Coulter et al. "Swope Supernova Survey 2017a (SSS17a), the optical counterpart to a gravitational wave source". In: *Science* 358.6370 (Dec. 2017), pp. 1556–1558. DOI: 10.1126/science.aap9811. arXiv: 1710.05452 [astro-ph.HE].

[85] P. D'Avanzo et al. "The evolution of the X-ray afterglow emission of GW 170817/ GRB 170817A in XMM-Newton observations". In: *A&A* 613, L1 (May 2018), p. L1. DOI: 10.1051/0004-6361/201832664.

[86] M. B. Davies et al. "Merging Neutron Stars. I. Initial Results for Coalescence of Noncorotating Systems". In: *ApJ* 431 (Aug. 1994), p. 742. DOI: 10.1086/174525. arXiv: astro-ph/9401032 [astro-ph].

[87] Kishalay De et al. "Palomar Gattini-IR: Survey Overview, Data Processing System, On-sky Performance and First Results". In: *PASP* 132.1008, 025001 (Feb. 2020), p. 025001. DOI: 10.1088/1538-3873/ab6069. arXiv: 1910.13319 [astro-ph.IM].

[88] L. Dessart et al. "Neutrino Signatures and the Neutrino-Driven Wind in Binary Neutron Star Mergers". In: *ApJ* 690.2 (Jan. 2009), pp. 1681–1705. DOI: 10.1088/0004-637X/690/2/1681. arXiv: 0806.4380 [astro-ph].

[89] Tim Dietrich et al. "Improving the NRTidal model for binary neutron star systems". In: *Phys. Rev. D* 100.4, 044003 (Aug. 2019), p. 044003. DOI: 10.1103/PhysRevD.100.044003.

[90] S. G. Djorgovski et al. "Spectroscopy of the Host Galaxy of the Gamma-Ray Burst 980703". In: *ApJ* 508.1 (Nov. 1998), pp. L17–L20. DOI: 10.1086/311729. arXiv: astro-ph/9808188 [astro-ph].

[91] D. Dobie et al. "A comprehensive search for the radio counterpart of GW190814 with the Australian Square Kilometre Array Pathfinder". In: *MNRAS* 510.3 (Mar. 2022), pp. 3794–3805. DOI: 10.1093/mnras/stab3628. arXiv: 2109.08452 [astro-ph.HE].

[92] Dougal Dobie et al. "Radio afterglows from compact binary coalescences: prospects for next-generation telescopes". In: *MNRAS* 505.2 (Aug. 2021), pp. 2647–2661. DOI: 10.1093/mnras/stab1468. arXiv: 2105.08933 [astro-ph.HE].

[93] Michal Dominik et al. "Double Compact Objects. I. The Significance of the Common Envelope on Merger Rates". In: *ApJ* 759.1, 52 (Nov. 2012), p. 52. DOI: 10.1088/0004-637X/759/1/52. arXiv: 1202.4901 [astro-ph.HE].

[94] P. Drozda et al. "Black hole-neutron star mergers: The first mass gap and kilonovae". In: *A&A* 667, A126 (Nov. 2022), A126. DOI: 10.1051/0004-6361/202039418. arXiv: 2009.06655 [astro-ph.HE].

[95] Matthew D. Duez et al. "Equation of state effects in black hole-neutron star mergers". In: *Classical and Quantum Gravity* 27.11, 114106 (June 2010), p. 114106. DOI: 10.1088/0264-9381/27/11/114106. arXiv: 0912.3528 [astro-ph.HE].

[96] Paul C. Duffell, Eliot Quataert, and Andrew I. MacFadyen. "A Narrow Short-duration GRB Jet from a Wide Central Engine". In: *ApJ* 813.1, 64 (Nov. 2015), p. 64. DOI: 10.1088/0004-637X/813/1/64. arXiv: 1505.05538 [astro-ph.HE].

[97] Paul C. Duffell et al. "Jet Dynamics in Compact Object Mergers: GW170817 Likely Had a Successful Jet". In: *ApJ* 866.1, 3 (Oct. 2018), p. 3. DOI: 10.3847/1538-4357/aae084. arXiv: 1806.10616 [astro-ph.HE].

[98] Robert C. Duncan, Stuart L. Shapiro, and Ira Wasserman. "Neutrino-driven Winds from Young, Hot Neutron Stars". In: *ApJ* 309 (Oct. 1986), p. 141. DOI: 10.1086/164587.

[99] Ulyana Dupletsa et al. "gwfish: A simulation software to evaluate parameter-estimation capabilities of gravitational-wave detector networks". In: *Astron. Comput.* 42 (2023), p. 100671. DOI: 10.1016/j.ascom.2022.100671. arXiv: 2205.02499 [gr-qc].

[100] R. Duque, F. Daigne, and R. Mochkovitch. "Radio afterglows of binary neutron star mergers: a population study for current and future gravitational wave observing runs". In: *A&A* 631, A39 (Nov. 2019), A39. DOI: 10.1051/0004-6361/201935926. arXiv: 1905.04495 [astro-ph.HE].

[101] Raphaël Duque et al. "Probing binary neutron star mergers in dense environments using afterglow counterparts". In: *A&A* 639, A15 (July 2020), A15. DOI: 10.1051/0004-6361/201937115. arXiv: 1911.03302 [astro-ph.HE].

[102] David Eichler et al. "Nucleosynthesis, neutrino bursts and γ-rays from coalescing neutron stars". In: *Nature* 340.6229 (July 1989), pp. 126–128. DOI: 10.1038/340126a0.

[103] Will M. Farr et al. "The Mass Distribution of Stellar-mass Black Holes". In: *ApJ* 741.2, 103 (Nov. 2011), p. 103. DOI: 10.1088/0004-637X/741/2/103. arXiv: 1011.1459 [astro-ph.GA].

[104] N. Farrow et al. "The Mass Distribution of Galactic Double Neutron Stars". In: *ApJ* 876, 18 (Dec. 2019), p. 18. DOI: 10.3847/1538-4357/ab12e3. arXiv: 1902.03300 [astro-ph.HE].

[105] Stephen M. Feeney et al. "Prospects for Measuring the Hubble Constant with Neutron-Star-Black-Hole Mergers". In: *Phys. Rev. Lett.* 126.17, 171102 (Apr. 2021), p. 171102. DOI: 10.1103/PhysRevLett.126.171102. arXiv: 2012.06593 [astro-ph.CO].

[106] R. D. Ferdman et al. "PSR J1756-2251: a pulsar with a low-mass neutron star companion". In: *MNRAS* 443.3 (Sept. 2014), pp. 2183–2196. DOI: 10.1093/mnras/stu1223. arXiv: 1406.5507 [astro-ph.SR].

[107] Rodrigo Fernández and Brian D. Metzger. "Delayed outflows from black hole accretion tori following neutron star binary coalescence". In: *MNRAS* 435.1 (Oct. 2013), pp. 502–517. DOI: 10.1093/mnras/stt1312. arXiv: 1304.6720 [astro-ph.HE].

[108] Rodrigo Fernández et al. "Dynamics, nucleosynthesis, and kilonova signature of black hole—neutron star merger ejecta". In: *Classical and Quantum Gravity* 34.15, 154001 (Aug. 2017), p. 154001. DOI: 10.1088/1361-6382/aa7a77. arXiv: 1612.04829 [astro-ph.HE].

[109] Rodrigo Fernández et al. "Long-term GRMHD simulations of neutron star merger accretion discs: implications for electromagnetic counterparts". In: *MNRAS* 482.3 (Jan. 2019), pp. 3373–3393. DOI: 10.1093/mnras/sty2932. arXiv: 1808.00461 [astro-ph.HE].

[110] F. Fiore et al. "The HERMES-technologic and scientific pathfinder". In: *Space Telescopes and Instrumentation 2020: Ultraviolet to Gamma Ray*. Ed. by Jan-Willem A. den Herder, Shouleh Nikzad, and Kazuhiro Nakazawa. Vol. 11444. Society of Photo-Optical Instrumentation Engineers (SPIE) Conference Series. Dec. 2020, 114441R, 114441R. DOI: 10.1117/12.2560680. arXiv: 2101.03078 [astro-ph.HE].

[111] Éanna É. Flanagan and Tanja Hinderer. "Constraining neutron-star tidal Love numbers with gravitational-wave detectors". In: *Phys. Rev. D* 77.2, 021502 (Jan. 2008), p. 021502. DOI: 10.1103/PhysRevD.77.021502. arXiv: 0709.1915 [astro-ph].

[112] W. Fong et al. "A Decade of Short-duration Gamma-Ray Burst Broadband Afterglows: Energetics, Circumburst Densities, and Jet Opening Angles". In: *ApJ* 815.2, 102 (Dec. 2015), p. 102. DOI: 10.1088/0004-637X/815/2/102. arXiv: 1509.02922 [astro-ph.HE].

[113] F. Foucart et al. "Numerical simulations of neutron star-black hole binaries in the near-equal-mass regime". In: *Phys. Rev. D* 99.10, 103025 (May 2019), p. 103025. DOI: 10.1103/PhysRevD.99.103025. arXiv: 1903.09166 [astro-ph.HE].

[114] Francois Foucart. "A brief overview of black hole-neutron star mergers". In: *Frontiers in Astronomy and Space Sciences* 7, 46 (July 2020), p. 46. DOI: 10.3389/fspas.2020.00046. arXiv: 2006.10570 [astro-ph.HE].

[115] Francois Foucart. "Black-hole-neutron-star mergers: Disk mass predictions". In: *Phys. Rev. D* 86.12, 124007 (Dec. 2012), p. 124007. DOI: 10.1103/PhysRevD.86.124007. arXiv: 1207.6304 [astro-ph.HE].

[116] Francois Foucart, Tanja Hinderer, and Samaya Nissanke. "Remnant baryon mass in neutron star-black hole mergers: Predictions for binary neutron star mimickers and rapidly spinning black holes". In: *Phys. Rev. D* 98.8, 081501 (Oct. 2018), p. 081501. DOI: 10.1103/PhysRevD.98.081501. arXiv: 1807.00011 [astro-ph.HE].

[117] Giacomo Fragione. "Black-hole-Neutron-star Mergers Are Unlikely Multi-messenger Sources". In: *ApJ* 923.1, L2 (Dec. 2021), p. L2. DOI: 10.3847/2041-8213/ac3bcd. arXiv: 2110.09604 [astro-ph.HE].

[118] D. A. Frail et al. "The radio afterglow from the γ-ray burst of 8 May 1997". In: *Nature* 389.6648 (Sept. 1997), pp. 261–263. DOI: 10.1038/38451.

[119] Danielle Frostig et al. "An Infrared Search for Kilonovae with the WINTER Telescope. I. Binary Neutron Star Mergers". In: *The Astrophysical Journal* 926.2 (Feb. 2022), p. 152. DOI: 10.3847/1538-4357/ac4508. URL: https://doi.org/10.3847%2F1538-4357%2Fac4508.

[120] Chris L. Fryer et al. "Compact Remnant Mass Function: Dependence on the Explosion Mechanism and Metallicity". In: *ApJ* 749.1, 91 (Apr. 2012), p. 91. DOI: 10.1088/0004-637X/749/1/91. arXiv: 1110.1726 [astro-ph.SR].

[121] Jim Fuller and Linhao Ma. "Most Black Holes Are Born Very Slowly Rotating". In: *ApJ* 881.1, L1 (Aug. 2019), p. L1. DOI: 10.3847/2041-8213/ab339b. arXiv: 1907.03714 [astro-ph.SR].

[122] Leo W. H. Fung, Tom Broadhurst, and George F. Smoot. "Pure Gravitational Wave Estimation of Hubble's Constant using Neutron Star-Black Hole Mergers". In: *arXiv e-prints*, arXiv:2308.02440 (Aug. 2023), arXiv:2308.02440. DOI: 10.48550/arXiv.2308.02440. arXiv: 2308.02440 [astro-ph.CO].

[123] Shanika Galaudage et al. "Heavy Double Neutron Stars: Birth, Midlife, and Death". In: *ApJ* 909.2, L19 (Mar. 2021), p. L19. DOI: 10.3847/2041-8213/abe7f6. arXiv: 2011.01495 [astro-ph.HE].

[124] N. Gehrels et al. "A short γ-ray burst apparently associated with an elliptical galaxy at redshift z = 0.225". In: *Nature* 437.7060 (Oct. 2005), pp. 851–854. DOI: 10.1038/nature04142. arXiv: astro-ph/0505630 [astro-ph].

[125] G. Ghirlanda et al. "Compact radio emission indicates a structured jet was produced by a binary neutron star merger". In: *Science* 363.6430 (Mar. 2019), pp. 968–971. DOI: 10.1126/science.aau8815. arXiv: 1808.00469 [astro-ph.HE].

[126] Bruno Giacomazzo and Rosalba Perna. "Formation of Stable Magnetars from Binary Neutron Star Mergers". In: *ApJ* 771.2, L26 (July 2013), p. L26. DOI: 10.1088/2041-8205/771/2/L26. arXiv: 1306.1608 [astro-ph.HE].

[127] Bruno Giacomazzo et al. "Producing Magnetar Magnetic Fields in the Merger of Binary Neutron Stars". In: *ApJ* 809.1, 39 (Aug. 2015), p. 39. DOI: 10.1088/0004-637X/809/1/39. arXiv: 1410.0013 [astro-ph.HE].

[128] A. Goldstein et al. "An Ordinary Short Gamma-Ray Burst with Extraordinary Implications: Fermi-GBM Detection of GRB 170817A". In: *ApJ* 848.2, L14 (Oct. 2017), p. L14. DOI: 10.3847/2041-8213/aa8f41. arXiv: 1710.05446 [astro-ph.HE].

[129] B. P. Gompertz, A. J. Levan, and N. R. Tanvir. "A Search for Neutron Star-Black Hole Binary Mergers in the Short Gamma-Ray Burst Population". In: *ApJ* 895.1, 58 (May 2020), p. 58. DOI: 10.3847/1538-4357/ab8d24.

[130] B. P. Gompertz et al. "Constraints on compact binary merger evolution from spin-orbit misalignment in gravitational-wave observations". In: *MNRAS* 511.1 (Mar. 2022), pp. 1454–1461. DOI: 10.1093/mnras/stac029. arXiv: 2108.10184 [astro-ph.HE].

[131] J. Goodman. "Are gamma-ray bursts optically thick?" In: *ApJ* 308 (Sept. 1986), p. L47. DOI: 10.1086/184741.

[132] Stephane Goriely, Andreas Bauswein, and Hans-Thomas Janka. "r-process Nucleosynthesis in Dynamically Ejected Matter of Neutron Star Mergers". In: *ApJ* 738.2, L32 (Sept. 2011), p. L32. DOI: 10.1088/2041-8205/738/2/L32. arXiv: 1107.0899 [astro-ph.SR].

[133] Ore Gottlieb and Ehud Nakar. "The propagation of relativistic jets in expanding media". In: *MNRAS* 517.2 (Dec. 2022), pp. 1640–1666. DOI: 10.1093/mnras/stac2699. arXiv: 2106.03860 [astro-ph.HE].

[134] Ore Gottlieb, Ehud Nakar, and Tsvi Piran. "Detectability of neutron star merger afterglows". In: *MNRAS* 488.2 (Sept. 2019), pp. 2405–2411. DOI: 10.1093/mnras/stz1906. arXiv: 1903.08173 [astro-ph.HE].

[135] Ore Gottlieb et al. "A cocoon shock breakout as the origin of the γ-ray emission in GW170817". In: *MNRAS* 479.1 (Sept. 2018), pp. 588–600. DOI: 10.1093/mnras/sty1462. arXiv: 1710.05896 [astro-ph.HE].

[136] J. O. Goussard, P. Haensel, and J. L. Zdunik. "Rapid differential rotation of protoneutron stars and constraints on radio pulsars periods". In: *A&A* 330 (Feb. 1998), pp. 1005–1016. DOI: 10.48550/arXiv.astro-ph/9711347. arXiv: astro-ph/9711347 [astro-ph].

[137] M. J. Graham et al. "Candidate Electromagnetic Counterpart to the Binary Black Hole Merger Gravitational-Wave Event S190521g*". In: *Phys. Rev. Lett.* 124.25, 251102 (June 2020), p. 251102. DOI: 10.1103/PhysRevLett.124.251102. arXiv: 2006.14122 [astro-ph.HE].

[138] Jonathan Granot and Pawan Kumar. "Constraining the Structure of Gamma-Ray Burst Jets through the Afterglow Light Curves". In: *ApJ* 591.2 (July 2003), pp. 1086–1096. DOI: 10.1086/375489. arXiv: astro-ph/0212540 [astro-ph].

[139] Jonathan Granot and Re'em Sari. "The Shape of Spectral Breaks in Gamma-Ray Burst Afterglows". In: *ApJ* 568.2 (Apr. 2002), pp. 820–829. DOI: 10.1086/338966. arXiv: astro-ph/0108027 [astro-ph].

[140] Jonathan Granot and Alexander J. van der Horst. "Gamma-Ray Burst Jets and their Radio Observations". In: *PASA* 31, e008 (Feb. 2014), e008. DOI: 10.1017/pasa.2013.44.

[141] Doron Grossman et al. "The long-term evolution of neutron star merger remnants - II. Radioactively powered transients". In: *MNRAS* 439.1 (Mar. 2014), pp. 757–770. DOI: 10.1093/mnras/stt2503. arXiv: 1307.2943 [astro-ph.HE].

[142] G. Hallinan et al. "A radio counterpart to a neutron star merger". In: *Science* 358.6370 (Dec. 2017), pp. 1579–1583. DOI: 10.1126/science.aap9855. arXiv: 1710.05435 [astro-ph.HE].

[143] Gregg Hallinan et al. "The DSA-2000 — A Radio Survey Camera". In: *Bulletin of the American Astronomical Society*. Vol. 51. Sept. 2019, 255, p. 255. DOI: 10.48550/arXiv.1907.07648. arXiv: 1907.07648 [astro-ph.IM].

[144] Hamid Hamidani and Kunihito Ioka. "Jet propagation in expanding medium for gamma-ray bursts". In: *MNRAS* 500.1 (Jan. 2021), pp. 627–642. DOI: 10.1093/mnras/staa3276. arXiv: 2007.10690 [astro-ph.HE].

[145] Ming-Zhe Han et al. "Is GW190425 Consistent with Being a Neutron Star-Black Hole Merger?" In: *ApJ* 891.1, L5 (Mar. 2020), p. L5. DOI: 10.3847/2041-8213/ab745a. arXiv: 2001.07882 [astro-ph.HE].

[146] M. Hempel et al. "New Equations of State in Simulations of Core-collapse Supernovae". In: *ApJ* 748.1, 70 (Mar. 2012), p. 70. DOI: 10.1088/0004-637X/748/1/70. arXiv: 1108.0848 [astro-ph.HE].

[147] Tanja Hinderer. "Tidal Love Numbers of Neutron Stars". In: *ApJ* 677.2 (Apr. 2008), pp. 1216–1220. DOI: 10.1086/533487. arXiv: 0711.2420 [astro-ph].

[148] Tanja Hinderer et al. "Tidal deformability of neutron stars with realistic equations of state and their gravitational wave signatures in binary inspiral". In: *Phys. Rev. D* 81.12, 123016 (June 2010), p. 123016. DOI: 10.1103/PhysRevD.81.123016. arXiv: 0911.3535 [astro-ph.HE].

[149] David W. Hogg. "Distance measures in cosmology". In: *arXiv e-prints*, astro-ph/9905116 (May 1999), astro–ph/9905116. arXiv: astro-ph/9905116 [astro-ph].

[150] G. Hosseinzadeh et al. "Follow-up of the Neutron Star Bearing Gravitational-wave Candidate Events S190425z and S190426c with MMT and SOAR". In: *ApJ* 880.1, L4 (July 2019), p. L4. DOI: 10.3847/2041-8213/ab271c. arXiv: 1905.02186 [astro-ph.HE].

[151] Kenta Hotokezaka et al. "Remnant massive neutron stars of binary neutron star mergers: Evolution process and gravitational waveform". In: *Phys. Rev. D* 88.4, 044026 (Aug. 2013), p. 044026. DOI: 10.1103/PhysRevD.88.044026. arXiv: 1307.5888 [astro-ph.HE].

[152] E. J. Howell et al. " Joint gravitational wave - gamma-ray burst detection rates in the aftermath of GW170817". In: *MNRAS* 485 (May 2019), pp. 1435–1447. DOI: 10.1093/mnras/stz455. arXiv: astro-ph/1811.09168 [astro-ph].

[153] R. A. Hulse and J. H. Taylor. "Discovery of a pulsar in a binary system." In: *ApJ* 195 (Jan. 1975), pp. L51–L53. DOI: 10.1086/181708.

[154] Francesco Iacovelli et al. "Forecasting the Detection Capabilities of Third-generation Gravitational-wave Detectors Using GWFAST". In: *ApJ* 941.2, 208 (Dec. 2022), p. 208. DOI: 10.3847/1538-4357/ac9cd4. arXiv: 2207.02771 [gr-qc].

[155] Francesco Iacovelli et al. "GWFAST: A Fisher Information Matrix Python Code for Third-generation Gravitational-wave Detectors". In: *ApJS* 263.1, 2 (Nov. 2022), p. 2. DOI: 10.3847/1538-4365/ac9129.

[156] Z. Ivezic et al. "Large Synoptic Survey Telescope: From Science Drivers To Reference Design". In: *Serbian Astronomical Journal* 176 (June 2008), pp. 1–13. DOI: 10.2298/SAJ0876001I.

[157] J. D. Jackson and Ronald F. Fox. "Classical Electrodynamics, 3rd ed." In: *American Journal of Physics* 67.9 (Sept. 1999), pp. 841–842. DOI: 10.1119/1.19136.

[158] O. Just et al. "Comprehensive nucleosynthesis analysis for ejecta of compact binary mergers". In: *MNRAS* 448.1 (Mar. 2015), pp. 541–567. DOI: 10.1093/mnras/stv009. arXiv: 1406.2687 [astro-ph.SR].

[159] Vicky Kalogera et al. "The Next Generation Global Gravitational Wave Observatory: The Science Book". In: *arXiv e-prints*, arXiv:2111.06990 (Nov. 2021), arXiv:2111.06990. DOI: 10.48550/arXiv.2111.06990. arXiv: 2111.06990 [gr-qc].

[160] Daniel Kasen, N. R. Badnell, and Jennifer Barnes. "Opacities and Spectra of the r-process Ejecta from Neutron Star Mergers". In: *ApJ* 774.1, 25 (Sept. 2013), p. 25. DOI: 10.1088/0004-637X/774/1/25. arXiv: 1303.5788 [astro-ph.HE].

[161] Daniel Kasen, Rodrigo Fernández, and Brian D. Metzger. "Kilonova light curves from the disc wind outflows of compact object mergers". In: *MNRAS* 450.2 (June 2015), pp. 1777–1786. DOI: 10.1093/mnras/stv721. arXiv: 1411.3726 [astro-ph.HE].

[162] Kyohei Kawaguchi et al. "Black hole-neutron star binary merger: Dependence on black hole spin orientation and equation of state". In: *Phys. Rev. D* 92.2, 024014 (July 2015), p. 024014. DOI: 10.1103/PhysRevD.92.024014. arXiv: 1506.05473 [astro-ph.HE].

[163] Kyohei Kawaguchi et al. "Models of Kilonova/Macronova Emission from Black Hole-Neutron Star Mergers". In: *ApJ* 825.1, 52 (July 2016), p. 52. DOI: 10.3847/0004-637X/825/1/52. arXiv: 1601.07711 [astro-ph.HE].

[164] Kenta Kiuchi et al. "Efficient magnetic-field amplification due to the Kelvin-Helmholtz instability in binary neutron star mergers". In: *Phys. Rev. D* 92.12, 124034 (Dec. 2015), p. 124034. DOI: 10.1103/PhysRevD.92.124034. arXiv: 1509.09205 [astro-ph.HE].

[165] Kenta Kiuchi et al. "Revisiting the Lower Bound on Tidal Deformability Derived by AT 2017gfo". In: *ApJ* 876.2, L31 (May 2019), p. L31. DOI: 10.3847/2041-8213/ab1e45. arXiv: 1903.01466 [astro-ph.HE].

[166] Ray W. Klebesadel, Ian B. Strong, and Roy A. Olson. "Observations of Gamma-Ray Bursts of Cosmic Origin". In: *ApJ* 182 (June 1973), p. L85. DOI: 10.1086/181225.

[167] Kazunori Kohri, Ramesh Narayan, and Tsvi Piran. "Neutrino-dominated Accretion and Supernovae". In: *ApJ* 629.1 (Aug. 2005), pp. 341–361. DOI: 10.1086/431354. arXiv: astro-ph/0502470 [astro-ph].

[168] S. S. Komissarov. "Direct numerical simulations of the Blandford-Znajek effect". In: *MNRAS* 326.3 (Sept. 2001), pp. L41–L44. DOI: 10.1046/j.1365-8711.2001.04863.x.

[169] O. Korobkin et al. "On the astrophysical robustness of the neutron star merger r-process". In: *MNRAS* 426.3 (Nov. 2012), pp. 1940–1949. DOI: 10.1111/j.1365-2966.2012.21859.x. arXiv: 1206.2379 [astro-ph.SR].

[170] Matthias U. Kruckow et al. "Progenitors of gravitational wave mergers: binary evolution with the stellar grid-based code COMBINE". In: *MNRAS* 481.2 (Dec. 2018), pp. 1908–1949. DOI: 10.1093/mnras/sty2190. arXiv: 1801.05433 [astro-ph.SR].

[171] Christian J. Krüger and Francois Foucart. "Estimates for disk and ejecta masses produced in compact binary mergers". In: *Phys. Rev. D* 101.10, 103002 (May 2020), p. 103002. DOI: 10.1103/PhysRevD.101.103002. arXiv: 2002.07728 [astro-ph.HE].

[172] Koutarou Kyutoku et al. "On the Possibility of GW190425 Being a Black Hole-Neutron Star Binary Merger". In: *ApJ* 890.1, L4 (Feb. 2020), p. L4. DOI: 10.3847/2041-8213/ab6e70. arXiv: 2001.04474 [astro-ph.HE].

[173] Benjamin D. Lackey et al. "Extracting equation of state parameters from black hole-neutron star mergers: Nonspinning black holes". In: *Phys. Rev. D* 85.4, 044061 (Feb. 2012), p. 044061. DOI: 10.1103/PhysRevD.85.044061. arXiv: 1109.3402 [astro-ph.HE].

[174] Philippe Landry and Jocelyn S. Read. "The Mass Distribution of Neutron Stars in Gravitational-wave Binaries". In: *ApJ* 921.2, L25 (Nov. 2021), p. L25. DOI: 10.3847/2041-8213/ac2f3e. arXiv: 2107.04559 [astro-ph.HE].

[175] J. M. Lattimer and M. Prakash. "Neutron Star Structure and the Equation of State". In: *ApJ* 550.1 (Mar. 2001), pp. 426–442. DOI: 10.1086/319702. arXiv: astro-ph/0002232 [astro-ph].

[176] J. M. Lattimer and D. N. Schramm. "Black-Hole-Neutron-Star Collisions". In: *ApJ* 192 (Sept. 1974), p. L145. DOI: 10.1086/181612.

[177] J. M. Lattimer and D. N. Schramm. "The tidal disruption of neutron stars by black holes in close binaries." In: *ApJ* 210 (Dec. 1976), pp. 549–567. DOI: 10.1086/154860.

[178] A. Levan et al. *JWST detection of heavy neutron capture elements in a compact object merger*. 2023. arXiv: 2307.02098 [astro-ph.HE].

[179] Andrew J. Levan et al. "A long-duration gamma-ray burst of dynamical origin from the nucleus of an ancient galaxy". In: *Nature Astronomy* 7 (Aug. 2023), pp. 976–985. DOI: 10.1038/s41550-023-01998-8. arXiv: 2303.12912 [astro-ph.HE].

[180] Li-Xin Li and Bohdan Paczyński. "Transient Events from Neutron Star Mergers". In: *ApJ* 507.1 (Nov. 1998), pp. L59–L62. DOI: 10.1086/311680. arXiv: astro-ph/9807272 [astro-ph].

[181] LIGO Scientific Collaboration, Virgo Collaboration, and KAGRA Collaboration. *GWTC-3: Compact Binary Coalescences Observed by LIGO and Virgo During the Second Part of the Third Observing Run — O1+O2+O3 Search Sensitivity Estimates*. 2021. DOI: 10.5281/zenodo.5636816. URL: https://doi.org/10.5281/zenodo.5636816.

[182] Nathan P. Lourie et al. "The wide-field infrared transient explorer (WINTER)". In: *Ground-based and Airborne Instrumentation for Astronomy VIII*. Ed. by Christopher J. Evans, Julia J. Bryant, and Kentaro Motohara. Vol. 11447. Society of Photo-Optical Instrumentation Engineers (SPIE) Conference Series. Dec. 2020, 114479K, 114479K. DOI: 10.1117/12.2561210. arXiv: 2102.01109 [astro-ph.IM].

[183] M. J. Lundquist et al. "Searches after Gravitational Waves Using ARizona Observatories (SAGUARO): System Overview and First Results from Advanced LIGO/Virgo's Third Observing Run". In: *ApJ* 881.2, L26 (Aug. 2019), p. L26. DOI: 10.3847/2041-8213/ab32f2. arXiv: 1906.06345 [astro-ph.HE].

[184] J. D. Lyman et al. "The optical afterglow of the short gamma-ray burst associated with GW170817". In: *Nature Astronomy* 2 (July 2018), pp. 751–754. DOI: 10.1038/s41550-018-0511-3. arXiv: 1801.02669 [astro-ph.HE].

[185] Piero Madau and Mark Dickinson. "Cosmic Star-Formation History". In: *Annual Review of Astronomy and Astrophysics* 52 (Aug. 2014), pp. 415–486. DOI: 10.1146/annurev-astro-081811-125615. arXiv: 1403.0007 [astro-ph.CO].

[186] Michele Maggiore. *Gravitational Waves. Vol. 1: Theory and Experiments*. Oxford University Press, 2008. ISBN: 978-0-19-171766-6, 978-0-19-852074-0. DOI: 10.1093/acprof:oso/9780198570745.001.0001.

[187] Michele Maggiore et al. "Science case for the Einstein telescope". In: *J. Cosmology Astropart. Phys.* 2020.3, 050 (Mar. 2020), p. 050. DOI: 10.1088/1475-7516/2020/03/050. arXiv: 1912.02622 [astro-ph.CO].

[188] S. Makhathini et al. "The Panchromatic Afterglow of GW170817: The Full Uniform Data Set, Modeling, Comparison with Previous Results, and Implications". In: *ApJ* 922.2, 154 (Dec. 2021), p. 154. DOI: 10.3847/1538-4357/ac1ffc. arXiv: 2006.02382 [astro-ph.HE].

[189] Ilya Mandel, Will M. Farr, and Jonathan R. Gair. "Extracting distribution parameters from multiple uncertain observations with selection biases". In: *MNRAS* 486.1 (June 2019), pp. 1086–1093. DOI: 10.1093/mnras/stz896. arXiv: 1809.02063 [physics.data-an].

[190] Ilya Mandel et al. "Distinguishing types of compact-object binaries using the gravitational-wave signatures of their mergers". In: *MNRAS* 450.1 (June 2015), pp. L85–L89. DOI: 10.1093/mnrasl/slv054. arXiv: 1503.03172 [astro-ph.HE].

[191] Ben Margalit and Brian D. Metzger. "Constraining the Maximum Mass of Neutron Stars from Multi-messenger Observations of GW170817". In: *ApJ* 850.2, L19 (Dec. 2017), p. L19. DOI: 10.3847/2041-8213/aa991c. arXiv: 1710.05938 [astro-ph.HE].

[192] R. Margutti et al. "The Electromagnetic Counterpart of the Binary Neutron Star Merger LIGO/Virgo GW170817. V. Rising X-Ray Emission from an Off-axis Jet". In: *ApJ* 848.2, L20 (Oct. 2017), p. L20. DOI: 10.3847/2041-8213/aa9057.

[193] D. Martin et al. "Neutrino-driven Winds in the Aftermath of a Neutron Star Merger: Nucleosynthesis and Electromagnetic Transients". In: *ApJ* 813.1, 2 (Nov. 2015), p. 2. DOI: 10.1088/0004-637X/813/1/2. arXiv: 1506.05048 [astro-ph.SR].

[194] Joel de Jesús Mendoza-Temis et al. "Nuclear robustness of the r process in neutron-star mergers". In: *Phys. Rev. C* 92.5, 055805 (Nov. 2015), p. 055805. DOI: 10.1103/PhysRevC.92.055805. arXiv: 1409.6135 [astro-ph.HE].

[195] P. Mészáros. "Gamma-ray bursts". In: *Reports on Progress in Physics* 69.8 (Aug. 2006), pp. 2259–2321. DOI: 10.1088/0034-4885/69/8/R01. arXiv: astro-ph/0605208 [astro-ph].

[196] B. D. Metzger, A. L. Piro, and E. Quataert. "Time-dependent models of accretion discs formed from compact object mergers". In: *MNRAS* 390.2 (Oct. 2008), pp. 781–797. DOI: 10.1111/j.1365-2966.2008.13789.x. arXiv: 0805.4415 [astro-ph].

[197] B. D. Metzger et al. "Electromagnetic counterparts of compact object mergers powered by the radioactive decay of r-process nuclei". In: *MNRAS* 406.4 (Aug. 2010), pp. 2650–2662. DOI: 10.1111/j.1365-2966.2010.16864.x. arXiv: 1001.5029 [astro-ph.HE].

[198] B. D. Metzger et al. "The protomagnetar model for gamma-ray bursts". In: *MNRAS* 413.3 (May 2011), pp. 2031–2056. DOI: 10.1111/j.1365-2966.2011.18280.x. arXiv: 1012.0001 [astro-ph.HE].

[199] Brian D. Metzger. "Kilonovae". In: *Living Reviews in Relativity* 23.1, 1 (Dec. 2019), p. 1. DOI: 10.1007/s41114-019-0024-0. arXiv: 1910.01617 [astro-ph.HE].

[200] Brian D. Metzger and Rodrigo Fernández. "Red or blue? A potential kilonova imprint of the delay until black hole formation following a neutron star merger". In: *MNRAS* 441.4 (July 2014), pp. 3444–3453. DOI: 10.1093/mnras/stu802. arXiv: 1402.4803 [astro-ph.HE].

[201] Brian D. Metzger, Todd A. Thompson, and Eliot Quataert. "A Magnetar Origin for the Kilonova Ejecta in GW170817". In: *ApJ* 856.2, 101 (Apr. 2018), p. 101. DOI: 10.3847/1538-4357/aab095. arXiv: 1801.04286 [astro-ph.HE].

[202] M. R. Metzger et al. "Spectral constraints on the redshift of the optical counterpart to the γ-ray burst of 8 May 1997". In: *Nature* 387.6636 (June 1997), pp. 878–880. DOI: 10.1038/43132.

[203] Jonah M. Miller et al. "Full transport model of GW170817-like disk produces a blue kilonova". In: *Phys. Rev. D* 100.2, 023008 (July 2019), p. 023008. DOI: 10.1103/PhysRevD.100.023008. arXiv: 1905.07477 [astro-ph.HE].

[204] M. C. Miller et al. "The Radius of PSR J0740+6620 from NICER and XMM-Newton Data". In: *ApJ* 918.2, L28 (Sept. 2021), p. L28. DOI: 10.3847/2041-8213/ac089b. arXiv: 2105.06979 [astro-ph.HE].

[205] R. Mochkovitch et al. "Prospects for kilonova signals in the gravitational-wave era". In: *A&A* 651, A83 (July 2021), A83. DOI: 10.1051/0004-6361/202140689. arXiv: 2103.00943 [astro-ph.HE].

[206] K. Mogushi, Marco Cavaglià, and Siellez Karelle. "Jet Geometry and Rate Estimate of Coincident Gamma-Ray Burst and Gravitational-wave Observations". In: *ApJ* 880, 55 (July 2019). DOI: 10.3847/1538-4357/ab1f76. arXiv: 1811.08542 [astro-ph.HE].

[207] K. P. Mooley and S. Mooley. "LIGO/Virgo GW170817: X-ray observations confirm prediction made from radio data." In: *GRB Coordinates Network* 22211 (Jan. 2017), p. 1.

[208] K. P. Mooley et al. "A mildly relativistic wide-angle outflow in the neutron-star merger event GW170817". In: *Nature* 554.7691 (Feb. 2018), pp. 207–210. DOI: 10.1038/nature25452. arXiv: 1711.11573 [astro-ph.HE].

[209] Elias R. Most et al. "Signatures of Quark-Hadron Phase Transitions in General-Relativistic Neutron-Star Mergers". In: *Phys. Rev. Lett.* 122.6, 061101 (Feb. 2019), p. 061101. DOI: 10.1103/PhysRevLett.122.061101. arXiv: 1807.03684 [astro-ph.HE].

[210] Philipp Mösta et al. "A Magnetar Engine for Short GRBs and Kilonovae". In: *ApJ* 901.2, L37 (Oct. 2020), p. L37. DOI: 10.3847/2041-8213/abb6ef. arXiv: 2003.06043 [astro-ph.HE].

[211] Kirpal Nandra et al. "The Hot and Energetic Universe: A White Paper presenting the science theme motivating the Athena+ mission". In: *arXiv e-prints*, arXiv:1306.2307 (June 2013), arXiv:1306.2307. DOI: 10.48550/arXiv.1306.2307. arXiv: 1306.2307 [astro-ph.HE].

[212] L. Nava et al. "Clustering of LAT light curves: a clue to the origin of high-energy emission in gamma-ray bursts". In: *MNRAS* 443.4 (Oct. 2014), pp. 3578–3585. DOI: 10.1093/mnras/stu1451. arXiv: 1406.6693 [astro-ph.HE].

[213] Vsevolod Nedora et al. "Spiral-wave Wind for the Blue Kilonova". In: *ApJ* 886.2, L30 (Dec. 2019), p. L30. DOI: 10.3847/2041-8213/ab5794. arXiv: 1907.04872 [astro-ph.HE].

[214] Coenraad J. Neijssel et al. "The effect of the metallicity-specific star formation history on double compact object mergers". In: *MNRAS* 490.3 (Dec. 2019), pp. 3740–3759. DOI: 10.1093/mnras/stz2840. arXiv: 1906.08136 [astro-ph.SR].

[215] M. Nicholl et al. "The Electromagnetic Counterpart of the Binary Neutron Star Merger LIGO/Virgo GW170817. III. Optical and UV Spectra of a Blue Kilonova from Fast Polar Ejecta". In: *ApJ* 848.2, L18 (Oct. 2017), p. L18. DOI: 10.3847/2041-8213/aa9029. arXiv: 1710.05456 [astro-ph.HE].

[216] Samaya Nissanke et al. "Determining the Hubble constant from gravitational wave observations of merging compact binaries". In: *arXiv e-prints*, arXiv:1307.2638 (July 2013), arXiv:1307.2638. DOI: 10.48550/arXiv.1307.2638. arXiv: 1307.2638 [astro-ph.CO].

[217] F. Özel and P. Freire. "Masses, Radii, and the Equation of State of Neutron Stars". In: *ARA&A* 54 (Sept. 2016), pp. 401–440. DOI: 10.1146/annurev-astro-081915-023322. arXiv: 1603.02698 [astro-ph.HE].

[218] F. Özel et al. "On the Mass Distribution and Birth Masses of Neutron Stars". In: *ApJ* 757, 55 (Sept. 2012), p. 55. DOI: 10.1088/0004-637X/757/1/55. arXiv: 1201.1006 [astro-ph.HE].

[219] Feryal Özel, Gordon Baym, and Tolga Güver. "Astrophysical measurement of the equation of state of neutron star matter". In: *Phys. Rev. D* 82.10, 101301 (Nov. 2010), p. 101301. DOI: 10.1103/PhysRevD.82.101301. arXiv: 1002.3153 [astro-ph.HE].

[220] B. Paczynski. "Gamma-ray bursters at cosmological distances". In: *ApJ* 308 (Sept. 1986), pp. L43–L46. DOI: 10.1086/184740.

[221] K. L. Page et al. "Swift-XRT follow-up of gravitational wave triggers during the third aLIGO/Virgo observing run". In: *MNRAS* 499.3 (Dec. 2020), pp. 3459–3480. DOI: 10.1093/mnras/staa3032. arXiv: 2009.13804 [astro-ph.HE].

[222] A. Panaitescu and P. Kumar. "Analytic Light Curves of Gamma-Ray Burst Afterglows: Homogeneous versus Wind External Media". In: *ApJ* 543.1 (Nov. 2000), pp. 66–76. DOI: 10.1086/317090. arXiv: astro-ph/0003246 [astro-ph].

[223] Francesco Pannarale. "Black hole remnant of black hole-neutron star coalescing binaries". In: *Phys. Rev. D* 88.10, 104025 (Nov. 2013), p. 104025. DOI: 10.1103/PhysRevD.88.104025. arXiv: 1208.5869 [gr-qc].

[224] Francesco Pannarale and Frank Ohme. "Prospects for Joint Gravitational-wave and Electromagnetic Observations of Neutron-star-Black-hole Coalescing Binaries". In: *ApJ* 791.1, L7 (Aug. 2014), p. L7. DOI: 10.1088/2041-8205/791/1/L7. arXiv: 1406.6057 [gr-qc].

[225] Francesco Pannarale et al. "Aligned spin neutron star-black hole mergers: A gravitational waveform amplitude model". In: *Phys. Rev. D* 92.8, 084050 (Oct. 2015), p. 084050. DOI: 10.1103/PhysRevD.92.084050.

[226] Barbara Patricelli et al. "Prospects for multi-messenger detection of binary neutron star mergers in the fourth LIGO-Virgo-KAGRA observing run". In: *Monthly Notices of the Royal Astronomical Society* (Apr. 2022). DOI: 10.1093/mnras/stac1167. URL: https://doi.org/10.1093%2Fmnras%2Fstac1167.

[227] L. Pavan et al. "The long helical jet of the Lighthouse nebula, IGR J11014-6103". In: *A&A* 562, A122 (Feb. 2014), A122. DOI: 10.1051/0004-6361/201322588. arXiv: 1309.6792 [astro-ph.HE].

[228] Asaf Pe'er. "Dynamical Model of an Expanding Shell". In: *ApJ* 752.1, L8 (June 2012), p. L8. DOI: 10.1088/2041-8205/752/1/L8. arXiv: 1203.5797 [astro-ph.HE].

[229] A. Perego et al. "Neutrino-driven winds from neutron star merger remnants". In: *MNRAS* 443.4 (Oct. 2014), pp. 3134–3156. DOI: 10.1093/mnras/stu1352. arXiv: 1405.6730 [astro-ph.HE].

[230] Albino Perego, David Radice, and Sebastiano Bernuzzi. "AT 2017gfo: An Anisotropic and Three-component Kilonova Counterpart of GW170817". In: *ApJ* 850.2, L37 (Dec. 2017), p. L37. DOI: 10.3847/2041-8213/aa9ab9. arXiv: 1711.03982 [astro-ph.HE].

[231] Rosalba Perna et al. "Host galaxies and electromagnetic counterparts to binary neutron star mergers across the cosmic time: detectability of GW170817-like events". In: *MNRAS* 512.2 (May 2022), pp. 2654–2668. DOI: 10.1093/mnras/stac685. arXiv: 2112.05202 [astro-ph.HE].

[232] P. C. Peters. "Gravitational Radiation and the Motion of Two Point Masses". In: *Physical Review* 136.4B (Nov. 1964), pp. 1224–1232. DOI: 10.1103/PhysRev.136.B1224.

[233] P. Petrov et al. "Data-driven expectations for electromagnetic counterpart searches based on LIGO/Virgo public alerts". In: *arXiv e-prints* (Aug. 2021). arXiv: 2108.07277 [astro-ph.HE].

[234] E. Pian et al. "Spectroscopic identification of r-process nucleosynthesis in a double neutron-star merger". In: *Nature* 551.7678 (Nov. 2017), pp. 67–70. DOI: 10.1038/nature24298. arXiv: 1710.05858 [astro-ph.HE].

[235] Tsvi Piran. "The Implications of the Compton (GRO) Observations for Cosmological Gamma-Ray Bursts". In: *ApJ* 389 (Apr. 1992), p. L45. DOI: 10.1086/186345.

[236] Tsvi Piran. "The physics of gamma-ray bursts". In: *Reviews of Modern Physics* 76.4 (Oct. 2004), pp. 1143–1210. DOI: 10.1103/RevModPhys.76.1143. arXiv: astro-ph/0405503 [astro-ph].

[237] Planck Collaboration et al. "Planck 2015 results. XIII. Cosmological parameters". In: *A&A* 594, A13 (Sept. 2016), A13. DOI: 10.1051/0004-6361/201525830. arXiv: 1502.01589.

[238] Nihan Pol, Maura McLaughlin, and Duncan R. Lorimer. "Future Prospects for Ground-based Gravitational-wave Detectors: The Galactic Double Neutron Star Merger Rate Revisited". In: *ApJ* 870.2, 71 (Jan. 2019), p. 71. DOI: 10.3847/1538-4357/aaf006. arXiv: 1811.04086 [astro-ph.HE].

[239] Robert Popham, S. E. Woosley, and Chris Fryer. "Hyperaccreting Black Holes and Gamma-Ray Bursts". In: *ApJ* 518.1 (June 1999), pp. 356–374. DOI: 10.1086/307259. arXiv: astro-ph/9807028 [astro-ph].

[240] S. F. Portegies Zwart and L. R. Yungelson. "Formation and evolution of binary neutron stars". In: *A&A* 332 (Apr. 1998), pp. 173–188. arXiv: astro-ph/9710347 [astro-ph].

[241] Jason Pruet, Todd A. Thompson, and R. D. Hoffman. "Nucleosynthesis in Outflows from the Inner Regions of Collapsars". In: *ApJ* 606.2 (May 2004), pp. 1006–1018. DOI: 10.1086/382036. arXiv: astro-ph/0309278 [astro-ph].

[242] M. Punturo et al. "The Einstein Telescope: a third-generation gravitational wave observatory". In: *Classical and Quantum Gravity* 27.19, 194002 (Oct. 2010), p. 194002. DOI: 10.1088/0264-9381/27/19/194002.

[243] Y. Z. Qian. "Supernovae versus Neutron Star Mergers as the Major R-Process Sources". In: *ApJ* 534.1 (May 2000), pp. L67–L70. DOI: 10.1086/312659. arXiv: astro-ph/0003242 [astro-ph].

[244] G. Raaijmakers et al. "Constraints on the Dense Matter Equation of State and Neutron Star Properties from NICER's Mass-Radius Estimate of PSR J0740+6620 and Multimessenger Observations". In: *ApJ* 918.2, L29 (Sept. 2021), p. L29. DOI: 10.3847/2041-8213/ac089a. arXiv: 2105.06981 [astro-ph.HE].

[245] David Radice et al. "Binary Neutron Star Mergers: Mass Ejection, Electromagnetic Counterparts, and Nucleosynthesis". In: *ApJ* 869.2, 130 (Dec. 2018), p. 130. DOI: 10.3847/1538-4357/aaf054. arXiv: 1809.11161 [astro-ph.HE].

[246] David Radice et al. "Dynamical mass ejection from binary neutron star mergers". In: *MNRAS* 460.3 (Aug. 2016), pp. 3255–3271. DOI: 10.1093/mnras/stw1227. arXiv: 1601.02426 [astro-ph.HE].

[247] Carolyn A. Raithel, Feryal Özel, and Dimitrios Psaltis. "Tidal Deformability from GW170817 as a Direct Probe of the Neutron Star Radius". In: *ApJ* 857.2, L23 (Apr. 2018), p. L23. DOI: 10.3847/2041-8213/aabcbf. arXiv: 1803.07687 [astro-ph.HE].

[248] Enrico Ramirez-Ruiz et al. "Compact Stellar Binary Assembly in the First Nuclear Star Clusters and r-process Synthesis in the Early Universe". In: *ApJ* 802.2, L22 (Apr. 2015), p. L22. DOI: 10.1088/2041-8205/802/2/L22. arXiv: 1410.3467 [astro-ph.GA].

[249] Jillian C. Rastinejad et al. "A kilonova following a long-duration gamma-ray burst at 350 Mpc". In: *Nature* 612.7939 (Dec. 2022), pp. 223–227. DOI: 10.1038/s41586-022-05390-w. arXiv: 2204.10864 [astro-ph.HE].

[250] Martin J. Rees. "Tidal disruption of stars by black holes of 10^6-10^8 solar masses in nearby galaxies". In: *Nature* 333.6173 (June 1988), pp. 523–528. DOI: 10.1038/333523a0.

[251] David Reitze et al. "Cosmic Explorer: The U.S. Contribution to Gravitational-Wave Astronomy beyond LIGO". In: *Bulletin of the American Astronomical Society*. Vol. 51. Sept. 2019, 35, p. 35. DOI: 10.48550/arXiv.1907.04833. arXiv: 1907.04833 [astro-ph.IM].

[252] Sherwood Richers et al. "Monte Carlo Neutrino Transport through Remnant Disks from Neutron Star Mergers". In: *ApJ* 813.1, 38 (Nov. 2015), p. 38. DOI: 10.1088/0004-637X/813/1/38. arXiv: 1507.03606 [astro-ph.HE].

[253] K. Riles. "Gravitational waves: Sources, detectors and searches". In: *Progress in Particle and Nuclear Physics* 68 (Jan. 2013), pp. 1–54. DOI: 10.1016/j.ppnp.2012.08.001. arXiv: 1209.0667 [hep-ex].

[254] Jeff Riley et al. "Rapid Stellar and Binary Population Synthesis with COMPAS". In: *ApJS* 258.2, 34 (Feb. 2022), p. 34. DOI: 10.3847/1538-4365/ac416c.

[255] L. F. Roberts, Sanjay Reddy, and Gang Shen. "Medium modification of the charged-current neutrino opacity and its implications". In: *Phys. Rev. C* 86.6, 065803 (Dec. 2012), p. 065803. DOI: 10.1103/PhysRevC.86.065803. arXiv: 1205.4066 [astro-ph.HE].

[256] Jaime Román-Garza et al. "The Role of Core-collapse Physics in the Observability of Black Hole Neutron Star Mergers as Multimessenger Sources". In: *ApJ* 912.2, L23 (May 2021), p. L23. DOI: 10.3847/2041-8213/abf42c. arXiv: 2012.02274 [astro-ph.HE].

[257] Isobel M. Romero-Shaw et al. "On the origin of GW190425". In: *MNRAS* 496.1 (July 2020), pp. L64–L69. DOI: 10.1093/mnrasl/slaa084. arXiv: 2001.06492 [astro-ph.HE].

[258] S. Ronchini et al. "Perspectives for multimessenger astronomy with the next generation of gravitational-wave detectors and high-energy satellites". In: *A&A* 665, A97 (Sept. 2022), A97. DOI: 10.1051/0004-6361/202243705. arXiv: 2204.01746 [astro-ph.HE].

[259] S. Rosswog, T. Piran, and E. Nakar. "The multimessenger picture of compact object encounters: binary mergers versus dynamical collisions". In: *MNRAS* 430.4 (Apr. 2013), pp. 2585–2604. DOI: 10.1093/mnras/sts708. arXiv: 1204.6240 [astro-ph.HE].

[260] S. Rosswog et al. "Detectability of compact binary merger macronovae". In: *Classical and Quantum Gravity* 34.10, 104001 (May 2017), p. 104001. DOI: 10.1088/1361-6382/aa68a9. arXiv: 1611.09822 [astro-ph.HE].

[261] S. Rosswog et al. "Mass ejection in neutron star mergers". In: *A&A* 341 (Jan. 1999), pp. 499–526. DOI: 10.48550/arXiv.astro-ph/9811367. arXiv: astro-ph/9811367 [astro-ph].

[262] A. Sagués Carracedo et al. "Detectability of kilonovae in optical surveys: post-mortem examination of the LVC O3 run follow-up". In: *MNRAS* 504.1 (June 2021), pp. 1294–1303. DOI: 10.1093/mnras/stab872. arXiv: 2004.06137 [astro-ph.HE].

[263] Kailash C. Sahu et al. "The optical counterpart to γ-ray burst GRB970228 observed using the Hubble Space Telescope". In: *Nature* 387.6632 (May 1997), pp. 476–478. DOI: 10.1038/387476a0. arXiv: astro-ph/9705184 [astro-ph].

[264] O. S. Salafia and B. Giacomazzo. "Accretion-to-jet energy conversion efficiency in GW170817". In: *A&A* 645, A93 (Jan. 2021), A93. DOI: 10.1051/0004-6361/202038590. arXiv: 2006.07376 [astro-ph.HE].

[265] O. S. Salafia et al. "Gamma-ray burst jet propagation, development of angular structure, and the luminosity function". In: *A&A* 636, A105 (Apr. 2020), A105. DOI: 10.1051/0004-6361/201936335. arXiv: 1907.07599 [astro-ph.HE].

[266] O. S. Salafia et al. "On-axis view of GRB 170817A". In: *A&A* 628, A18 (Aug. 2019), A18. DOI: 10.1051/0004-6361/201935831. arXiv: 1905.01190 [astro-ph.HE].

[267] O. S. Salafia et al. "Structure of gamma-ray burst jets: intrinsic versus apparent properties". In: *MNRAS* 450.4 (July 2015), pp. 3549–3558. DOI: 10.1093/mnras/stv766. arXiv: 1502.06608 [astro-ph.HE].

[268] O. S. Salafia et al. "The short gamma-ray burst population in a quasi-universal jet scenario". In: *arXiv e-prints*, arXiv:2306.15488 (June 2023), arXiv:2306.15488. DOI: 10.48550/arXiv.2306.15488. arXiv: 2306.15488 [astro-ph.HE].

[269] Om Sharan Salafia and Giancarlo Ghirlanda. "The Structure of Gamma Ray Burst Jets". In: *Galaxies* 10.5 (Aug. 2022), p. 93. DOI: 10.3390/galaxies10050093.

[270] Om Sharan Salafia et al. "Constraints on the merging binary neutron star mass distribution and equation of state based on the incidence of jets in the population". In: *A&A* 666, A174 (Oct. 2022), A174. DOI: 10.1051/0004-6361/202243260. arXiv: 2202.01656 [astro-ph.HE].

[271] M. Saleem. "Prospects of joint detections of neutron star mergers and short GRBs with Gaussian structured jets". In: *MNRAS* 493 (Apr. 2020), pp. 1633–1639. DOI: 10.1093/mnras/staa303. arXiv: astro-ph/arXiv:1905.00314 [astro-ph].

[272] M. Saleem et al. "Rates of short-GRB afterglows in association with binary neutron star mergers". In: *MNRAS* 475 (Mar. 2018), pp. 699–707. DOI: 10.1093/mnras/stx3108.

[273] Filippo Santoliquido et al. "The cosmic merger rate density of compact objects: impact of star formation, metallicity, initial mass function, and binary evolution". In: *MNRAS* 502.4 (Apr. 2021), pp. 4877–4889. DOI: 10.1093/mnras/stab280. arXiv: 2009.03911 [astro-ph.HE].

[274] Re'em Sari, Tsvi Piran, and Ramesh Narayan. "Spectra and Light Curves of Gamma-Ray Burst Afterglows". In: *ApJ* 497.1 (Apr. 1998), pp. L17–L20. DOI: 10.1086/311269. arXiv: astro-ph/9712005 [astro-ph].

[275] B. S. Sathyaprakash and Bernard F. Schutz. "Physics, Astrophysics and Cosmology with Gravitational Waves". In: *Living Reviews in Relativity* 12.1, 2 (Dec. 2009), p. 2. DOI: 10.12942/lrr-2009-2. arXiv: 0903.0338 [gr-qc].

[276] V. Savchenko, A. Neronov, and T. J. L. Courvoisier. "Timing properties of gamma-ray bursts detected by SPI-ACS detector onboard INTEGRAL". In: *A&A* 541, A122 (May 2012), A122. DOI: 10.1051/0004-6361/201218877. arXiv: 1203.1344 [astro-ph.HE].

[277] B. F. Schutz. "Determining the Hubble constant from gravitational wave observations". In: *Nature* 323.6086 (Sept. 1986), pp. 310–311. DOI: 10.1038/323310a0.

[278] Bernard F. Schutz. "Networks of gravitational wave detectors and three figures of merit". In: *Classical and Quantum Gravity* 28.12, 125023 (June 2011), p. 125023. DOI: 10.1088/0264-9381/28/12/125023. arXiv: 1102.5421 [astro-ph.IM].

[279] Robert J. Selina et al. "The Next-Generation Very Large Array: a technical overview". In: *Ground-based and Airborne Telescopes VII*. Ed. by Heather K. Marshall and Jason Spyromilio. Vol. 10700. Society of Photo-Optical Instrumentation Engineers (SPIE) Conference Series. July 2018, 107001O, 107001O. DOI: 10.1117/12.2312089. arXiv: 1806.08405 [astro-ph.IM].

[280] Christian N. Setzer et al. "Modelling Populations of Kilonovae". In: *arXiv e-prints*, arXiv:2205.12286 (May 2022), arXiv:2205.12286. arXiv: 2205.12286 [astro-ph.HE].

[281] Stuart L. Shapiro. "Black holes, disks, and jets following binary mergers and stellar collapse: The narrow range of electromagnetic luminosities and accretion rates". In: *Phys. Rev. D* 95.10, 101303 (May 2017), p. 101303. DOI: 10.1103/PhysRevD.95.101303. arXiv: 1705.04695 [astro-ph.HE].

[282] Stuart L. Shapiro and Saul A. Teukolsky. *Black holes, white dwarfs and neutron stars. The physics of compact objects*. 1983. DOI: 10.1002/9783527617661.

[283] Masaru Shibata and Keisuke Taniguchi. "Merger of binary neutron stars to a black hole: Disk mass, short gamma-ray bursts, and quasinormal mode ringing". In: *Phys. Rev. D* 73.6, 064027 (Mar. 2006), p. 064027. DOI: 10.1103/PhysRevD.73.064027. arXiv: astro-ph/0603145 [astro-ph].

[284] Daniel M. Siegel. "GW170817 -the first observed neutron star merger and its kilonova: Implications for the astrophysical site of the r-process". In: *European Physical Journal A* 55.11, 203 (Nov. 2019), p. 203. DOI: 10.1140/epja/i2019-12888-9. arXiv: 1901.09044 [astro-ph.HE].

[285] Daniel M. Siegel and Brian D. Metzger. "Three-Dimensional General-Relativistic Magnetohydrodynamic Simulations of Remnant Accretion Disks from Neutron Star Mergers: Outflows and r -Process Nucleosynthesis". In: *Phys. Rev. Lett.* 119.23, 231102 (Dec. 2017), p. 231102. DOI: 10.1103/PhysRevLett.119.231102. arXiv: 1705.05473 [astro-ph.HE].

[286] Leo P. Singer and Larry R. Price. "Rapid Bayesian position reconstruction for gravitational-wave transients". In: *Phys. Rev. D* 93.2, 024013 (Jan. 2016), p. 024013. DOI: 10.1103/PhysRevD.93.024013. arXiv: 1508.03634 [gr-qc].

[287] Lorenzo Sironi and Dimitrios Giannios. "A Late-time Flattening of Light Curves in Gamma-Ray Burst Afterglows". In: *ApJ* 778.2, 107 (Dec. 2013), p. 107. DOI: 10.1088/0004-637X/778/2/107. arXiv: 1307.3250 [astro-ph.HE].

[288] L. L. Smarr and R. Blandford. "The binary pulsar: physical processes, possible companions, and evolutionary histories." In: *ApJ* 207 (July 1976), pp. 574–588. DOI: 10.1086/154524.

[289] S. J. Smartt et al. "A kilonova as the electromagnetic counterpart to a gravitational-wave source". In: *Nature* 551.7678 (Nov. 2017), pp. 75–79. DOI: 10.1038/nature24303. arXiv: 1710.05841 [astro-ph.HE].

[290] G. Srinivasan. "Pulsars: their origin and evolution". In: *A&A Rev.* 1.3-4 (Nov. 1989), pp. 209–260. DOI: 10.1007/BF00873079.

[291] Andrew W. Steiner, James M. Lattimer, and Edward F. Brown. "The Neutron Star Mass-Radius Relation and the Equation of State of Dense Matter". In: *ApJ* 765.1, L5 (Mar. 2013), p. L5. DOI: 10.1088/2041-8205/765/1/L5. arXiv: 1205.6871 [nucl-th].

[292] E. Symbalisty and D. N. Schramm. "Neutron Star Collisions and the r-Process". In: *Astrophys. Lett.* 22 (Jan. 1982), p. 143.

[293] K. Takahashi, J. Witti, and H. T. Janka. "Nucleosynthesis in neutrino-driven winds from protoneutron stars II. The r-process". In: *A&A* 286 (June 1994), pp. 857–869.

[294] Masaomi Tanaka and Kenta Hotokezaka. "Radiative Transfer Simulations of Neutron Star Merger Ejecta". In: *ApJ* 775.2, 113 (Oct. 2013), p. 113. DOI: 10.1088/0004-637X/775/2/113. arXiv: 1306.3742 [astro-ph.HE].

[295] N. R. Tanvir et al. "A 'kilonova' associated with the short-duration γ-ray burst GRB 130603B". In: *Nature* 500.7464 (Aug. 2013), pp. 547–549. DOI: 10.1038/nature12505. arXiv: 1306.4971 [astro-ph.HE].

[296] Alexander Tchekhovskoy, Ramesh Narayan, and Jonathan C. McKinney. "Magnetohydrodynamic simulations of gamma-ray burst jets: Beyond the progenitor star". In: *New A* 15.8 (Nov. 2010), pp. 749–754. DOI: 10.1016/j.newast.2010.03.001. arXiv: 0909.0011 [astro-ph.HE].

[297] Vaibhav Tiwari. "Estimation of the sensitive volume for gravitational-wave source populations using weighted Monte Carlo integration". In: *Classical and Quantum Gravity* 35.14 (June 2018), p. 145009. DOI: 10.1088/1361-6382/aac89d. URL: https://doi.org/10.1088/1361-6382/aac89d.

[298] E. Troja et al. "The X-ray counterpart to the gravitational-wave event GW170817". In: *Nature* 551.7678 (Nov. 2017), pp. 71–74. DOI: 10.1038/nature24290. arXiv: 1710.05433 [astro-ph.HE].

[299] Ryo Tsutsui et al. "Possible existence of the E_p-L_p and E_p-E_{iso} correlations for short gamma-ray bursts with a factor 5-100 dimmer than those for long gamma-ray bursts". In: *MNRAS* 431.2 (May 2013), pp. 1398–1404. DOI: 10.1093/mnras/stt262. arXiv: 1208.0429 [astro-ph.HE].

[300] C. S. Unnikrishnan. "IndIGO and Ligo-India Scope and Plans for Gravitational Wave Research and Precision Metrology in India". In: *International Journal of Modern Physics D* 22.1, 1341010 (Jan. 2013), p. 1341010. DOI: 10.1142/S0218271813410101. arXiv: 1510.06059 [physics.ins-det].

[301] Michele Vallisneri. "Use and abuse of the Fisher information matrix in the assessment of gravitational-wave parameter-estimation prospects". In: *Phys. Rev. D* 77.4, 042001 (Feb. 2008), p. 042001. DOI: 10.1103/PhysRevD.77.042001.

[302] Freeke van de Voort et al. "Neutron star mergers and rare core-collapse supernovae as sources of r-process enrichment in simulated galaxies". In: *MNRAS* 494.4 (June 2020), pp. 4867–4883. DOI: 10.1093/mnras/staa754. arXiv: 1907.01557 [astro-ph.GA].

[303] J. van den Eijnden et al. "An evolving jet from a strongly magnetized accreting X-ray pulsar". In: *Nature* 562.7726 (Sept. 2018), pp. 233–235. DOI: 10.1038/s41586-018-0524-1. arXiv: 1809.10204 [astro-ph.HE].

[304] Hendrik van Eerten, Alexander van der Horst, and Andrew MacFadyen. "Gamma-Ray Burst Afterglow Broadband Fitting Based Directly on Hydrodynamics Simulations". In: *ApJ* 749.1, 44 (Apr. 2012), p. 44. DOI: 10.1088/0004-637X/749/1/44. arXiv: 1110.5089 [astro-ph.HE].

[305] Jan van Paradijs, Chryssa Kouveliotou, and Ralph A. M. J. Wijers. "Gamma-Ray Burst Afterglows". In: *ARA&A* 38 (Jan. 2000), pp. 379–425. DOI: 10.1146/annurev.astro.38.1.379.

[306] J. Veitch et al. "Parameter estimation for compact binaries with ground-based gravitational-wave observations using the LALInference software library". In: *Phys. Rev. D* 91.4, 042003 (Feb. 2015), p. 042003. DOI: 10.1103/PhysRevD.91.042003. arXiv: 1409.7215 [gr-qc].

[307] V. A. Villar et al. "The Combined Ultraviolet, Optical, and Near-infrared Light Curves of the Kilonova Associated with the Binary Neutron Star Merger GW170817: Unified Data Set, Analytic Models, and Physical Implications". In: *ApJ* 851.1, L21 (Dec. 2017), p. L21. DOI: 10.3847/2041-8213/aa9c84. arXiv: 1710.11576 [astro-ph.HE].

[308] N. E. White et al. "The Gamow Explorer: a Gamma-Ray Burst Observatory to study the high redshift universe and enable multi-messenger astrophysics". In: *UV, X-Ray, and Gamma-Ray Space Instrumentation for Astronomy XXII*. Ed. by Oswald H. Siegmund. Vol. 11821. Society of Photo-Optical Instrumentation Engineers (SPIE) Conference Series. Aug. 2021, 1182109, p. 1182109. DOI: 10.1117/12.2599293. arXiv: 2111.06497 [astro-ph.HE].

[309] Ryan T. Wollaeger et al. "Impact of ejecta morphology and composition on the electromagnetic signatures of neutron star mergers". In: *MNRAS* 478.3 (Aug. 2018), pp. 3298–3334. DOI: 10.1093/mnras/sty1018. arXiv: 1705.07084 [astro-ph.HE].

[310] Zepei Xing et al. "From ZAMS to Merger: Detailed Binary Evolution Models of Coalescing Neutron Star-Black Hole Systems at Solar Metallicity". In: *arXiv e-prints*, arXiv:2309.09600 (Sept. 2023), arXiv:2309.09600. DOI: 10.48550/arXiv.2309.09600. arXiv: 2309.09600 [astro-ph.HE].

[311] Jiming Yu et al. "Multimessenger Detection Rates and Distributions of Binary Neutron Star Mergers and Their Cosmological Implications". In: *The Astrophysical Journal* 916.1 (July 2021), p. 54. ISSN: 1538-4357. DOI: 10.3847/1538-4357/ac0628. URL: http://dx.doi.org/10.3847/1538-4357/ac0628.

[312] Francesco Zappa et al. "Gravitational-Wave Luminosity of Binary Neutron Stars Mergers". In: *Phys. Rev. Lett.* 120.11, 111101 (Mar. 2018), p. 111101. DOI: 10.1103/PhysRevLett.120.111101. arXiv: 1712.04267 [gr-qc].

[313] Michael Zevin et al. "Exploring the Lower Mass Gap and Unequal Mass Regime in Compact Binary Evolution". In: *ApJ* 899.1, L1 (Aug. 2020), p. L1. DOI: 10.3847/2041-8213/aba74e. arXiv: 2006.14573 [astro-ph.HE].

[314] J.-P. Zhu et al. "Kilonova and Optical Afterglow from Binary Neutron Star Mergers. II. Optimal Search Strategy for Serendipitous Observations and Target-of-opportunity Observations of Gravitational-wave Triggers". In: *arXiv e-prints*, arXiv:2110.10469 (Oct. 2021). arXiv: 2110.10469 [astro-ph.HE].

[315] Jin-Ping Zhu et al. "Kilonova Emission from Black Hole-Neutron Star Mergers. II. Luminosity Function and Implications for Target-of-opportunity Observations of Gravitational-wave Triggers and Blind Searches". In: *ApJ* 917.1, 24 (Aug. 2021), p. 24. DOI: 10.3847/1538-4357/abfe5e.

[316] Jin-Ping Zhu et al. "Long-duration Gamma-Ray Burst and Associated Kilonova Emission from Fast-spinning Black Hole-Neutron Star Mergers". In: *ApJ* 936.1, L10 (Sept. 2022), p. L10. DOI: 10.3847/2041-8213/ac85ad. arXiv: 2207.10470 [astro-ph.HE].